Enhancive Robotic Exoskeleton Design Methodology Based on Link Cross-section Geometry and Length Optimization for Specific Tasks

Pourshid Jan Fani

Submitted in accordance with the requirements for the degree of
Ph.D.

The University of Leeds
Institute of Design Robotics and Optimization
School of Mechanical Engineering

September, 2018

The candidate confirms that the work submitted is his/her own and that appropriate credit has been given where reference has been made to the work of others.

This copy has been supplied on the understanding that it is copyright material and that no quotation from the thesis may be published without proper acknowledgement.

The right of Pourshid Jan Fani to be identified as Author of this work has been asserted by him in accordance with the Copyright, Designs and Patents Act 1988.

Acknowledgements

I offer my sincerest thanks and gratitude to my supervisor *Professor Abbas Dehghani* for his unyielding support, reassurance and fighting spirit throughout the entire PhD Study*.

I would also like to extend my gratitude to *Mr Rob* Bloomfield as well as *Prof. Dehghani* for allowing me to partake in the exoskeleton journey*.

I would like to thank my co-supervisors, *Dr Osvaldo Querin* and *Dr Peter Brooks* for their tireless support and expertise and *Dr Neil Messenger* for his support with the motion capture.

I am also grateful to my friends and co-researchers *Maciej Napora, Thomas Magill* and *Konstantinos Drosos* for their support and sharing this journey with me. No greater partners could be chosen to be stuck in the middle with.

I would like to thank my family, *Hedieh Shamsi, Farshid Fani, Omid Fani* and *Parvin Sadravi,* and friends *Jonathan Kidane, Nazanin Zarei, Amine Eloucham, Nicholaus Lobulu, Patryk Turzyniecki, Sara* and *David Kaye, Sara* and *Harri Halonen* and *Melody Sadeghi* back home for their encouragement and support. I would also like to give a special thanks to my very dear friends *Shahab Showman* and *Arman Karim*. We made it.

A special thanks goes out to my comrades and champions, the University of Leeds American Football team, for embracing me into the family.

Abstract

The use of exoskeletons can aid in the performance of tasks by adding strength and structural support to the human body. The usage of enhancive exoskeletons lies within search and rescue operations, heavy material handling, aiding daily activities, muscle regeneration and control of tele operated robots. The classification of exoskeletons can be made based on the purpose, control strategy and structural design of the exoskeleton; Enhancive, Assistive, Rehabilitation and Telecommunication and Force Feedback Exoskeletons.

The research shows that there is a gap in exoskeleton design methodologies which take into consideration a wider span of human motions. Specifically optimal design of the exoskeleton's link lengths for specific tasks considering the power consumption.

The research presents the development of a design methodology for designing optimally exoskeletons to perform given tasks. By obtaining motion capture data of motions that the exoskeleton is expected to perform, computer models can be built which are faithful to the motions.

Two motions are used to verify the design methodology, 'Object Lifting', using predominantly the legs, and 'Object Raising' using predominantly the arms. The model for the exoskeleton with a rigid back is developed and it is found that the rigid back will significantly alter the hip and shoulder trajectories of the exoskeleton in comparison to the humans, when performing the same motions. The motion data of the markers used to capture data is incorporated in geometric optimizations of the rigid back structure obtain the smallest shape for the exoskeleton back structure. Furthermore the link cross-sections are optimized for minimum mass. In comparing hollow and solid cylinder links it is found that for the required external load of 90 kg, the effects of the links masses are negligible on joint torques.

Link lengths are also optimized to obtain minimum power consumption during motions. It is found that for 'Object Lifting' motion, the ideal leg structure is one with longer thigh and shorter shin; and for 'Object Raising' motion the ideal arm structure is one with longer upper arms and shorter forearms.

The work demonstrates that the optimization for the exoskeleton link geometric properties with respect to given motions is needed in order to obtain the most efficient design.

Table of Contents

List of Tables

List of Figures

Nomenclature

Marker Names

C6	Sixth cervical vertebra marker
Head_Peak	Cap Anterior marker
L_1st_Dist	Left foot first metatarsal distal marker
L_1st_Prox	Left foot first metatarsal proximal marker
L_5th_Dist	Left foot fifth metatarsal distal marker
L_5th_Prox	Left foot fifth metatarsal proximal marker
L_Acrom_Sup	Left acromion supinated marker
L_Arcrom_Post	Left acromion posterior marker
L_Arm1	Left arm cluster marker 1
L_Arm2	Left arm cluster marker 2
L_Arm3	Left arm cluster marker 3
L_Arm4	Left arm cluster marker 4
L_But	Left buttocks marker
L_Calc_lat	Left foot calcaneus lateral marker
L_Calc_Med	Left foot calcaneus medial marker
L_Calc_Post	Left foot calcaneus posterior marker
L_Cond_Lat	Left knee condyle lateral marker
L_Cond_Med	Left knee condyle medial marker
L_Coracoid	Left coracoid marker
L_Epicon_Lat	Left arm epicondyle lateral marker
L_Epicon_Med	Left arm epicondyle medial marker
L_Foot	Left foot marker
L_Hand	Left hand marker
L_Head_Post	Left head posterior marker
L_Iliac	Left iliac marker
L_Mall_Lat	Left ankle malleolus lateral marker
L_Mall_Med	Left ankle malleolus medial marker

L_Sac	Left sacrum marker
L_Shank1	Left shank cluster marker 1
L_Shank2	Left shank cluster marker 2
L_Shank3	Left shank cluster marker 3
L_Shank4	Left shank cluster marker 4
L_Temple	Left head temple marker
L_Thigh1	Left thigh cluster marker 1
L_Thigh2	Left thigh cluster marker 2
L_Thigh3	Left thigh cluster marker 3
L_Thigh4	Left thigh cluster marker 4
L_Thoriac	Left thoriac marker
L_Wrist	Left wrist marker
L_Wrist_Rad	Left wrist radial marker
L_Wrist_Uln	Left wrist ulnar marker
L3	Third lumbar vertebra marker
R_1st_Dist	Right foot first metatarsal distal marker
R_1st_Prox	Right foot first metatarsal proximal marker
R_5th_Dist	Right foot fifth metatarsal distal marker
R_5th_Prox	Right foot fifth metatarsal proximal marker
R_Acrom_Sup	Right acromion supinated marker
R_Arcrom_Post	Right acromion posterior marker
R_Arm1	Right arm cluster marker 1
R_Arm2	Right arm cluster marker 2
R_Arm3	Right arm cluster marker 3
R_Arm4	Right arm cluster marker 4
R_But	Right buttocks marker
R_Calc_lat	Right foot calcaneus lateral marker
R_Calc_Med	Right foot calcaneus medial marker
R_Calc_Post	Right foot calcaneus posterior marker

R_Cond_Lat	Right knee condyle lateral marker
R_Cond_Med	Right knee condyle medial marker
R_Coracoid	Right coracoid marker
R_Epicon_Lat	Right arm epicondyle lateral marker
R_Epicon_Med	Right arm epicondyle medial marker
R_Foot	Right foot marker
R_Hand	Right hand marker
R_Head_Post	Right head posterior marker
R_Iliac	Right iliac marker
R_Mall_Lat	Right ankle malleolus lateral marker
R_Mall_Med	Right ankle malleolus medial marker
R_Sac	Right sacrum marker
R_Shank1	Right shank cluster marker 1
R_Shank2	Right shank cluster marker 2
R_Shank3	Right shank cluster marker 3
R_Shank4	Right shank cluster marker 4
R_Temple	Right head temple marker
R_Thigh1	Right thigh cluster marker 1
R_Thigh2	Right thigh cluster marker 2
R_Thigh3	Right thigh cluster marker 3
R_Thigh4	Right thigh cluster marker 4
R_Thoriac	Right thoriac marker
R_Wrist	Right wrist marker
R_Wrist_Rad	Right wrist radial marker
R_Wrist_Uln	Right wrist ulnar marker
Sternum	Sternum marker
T12	Twelfth thoracic vertebra maker
T3	Third thoracic vertebra marker

Gait keys

Hs	Heel strike
To	Toe-off
Hc	Heel contact
Tc	Toe contact
Rhs	Right heel strike
Lhs	Left heel strike
Rto	Right toe-off
Lto	Left toe-off

Geometries and Physical Properties

C	Circle
R	Rectangle
S	Square
m	Mass
ρ	Density
l	Length
b	Base
h	Height
r	Radius
th	Thickness
A	Area
V	volume
I_{2nd}	Second Moment of Area
o	Outer
i	inner
x	X axis
y	Y axis
δ	Beam Deflection
F	Force (linear)

| M | Moment |
| E | Young's modulus |

Chapter 1
Introduction

1.1 Background

The beginning of robots, as they have been created in Karel Capek play Rossums Universal Robots (R.U.R), are as slaves (Čapek and Playfair 1923). Human-like creations of humans, an experiment at the expense of mankind. This 1920 science fiction play introduces the English language to the word Robot. Close to one hundred years later, mankind has realized the fictive attempts to be makers of species, quite literally. With the mechanical, electrical and computational expansion that has followed Capek's days, technology and information has altered the landscape of human innovation and creation drastically.

Although a philosophical debate may ensue, what is it that gives sentient beings consciousness? What is the prime mover in a human's ability to make choices? This thesis is merely an analysis and presentation of a design methodology of a machines frame. The machine that is of interest, the robotic exoskeleton, is one that is designed to follow its users command input, which the reader will see is the physical inputs of the human movement. There can be a sense of irony found in this comparison between Capek's robots and exoskeleton robots; Capek's robots were slaves that rebelled from a man-made bondage, exoskeletons are literally robots bound to the human who controls it with his/her every movement.

Early research into exoskeletons was made by General Electric in the 1960-70's (Mosher 1967). This effort started in 1965 as a joint Army-Navy (USA) program in November 1965. The design of the Hardiman was based on having two exoskeletons, one acting as the slave, and one as the master. The user would control the slave, which was designed to reflect the working force of the master exoskeleton back to the user, reduced by a factor of 25. In turn the slave would control the master exoskeleton which would interact with the outside world. The research resulted in an exoskeleton with optimized servo motors and an unstable control system, though the upper segment operated fine, the lower segment and gait remained an issue (Fick and Makinson 1971).

The current state of exoskeleton research is heavily dominated in the aspects of rehabilitation and assistive form. It turns out that certain static exoskeletons can be used to aid rehabilitating people with various injuries, primarily neural-damage

which limits movement. Such exoskeletons based on the literature not worn wholly by the user as they tend to be fixed, for example to the ground. As an aid, robotic exoskeletons can also aid humans who are paralysed to walk, although with some higher level of artificial intelligence (AI) involved.

The functionality of robotic exoskeletons as an assistive tool has been researched with a more symbiotic relationship to the user. Whereby the user provides the structure for loads to be transmitted to the ground and the exoskeleton acts principally as muscle enhancers. The control system for such exoskeletons have been developed with EMG sensors (Sankai 2006). The assistive classification can be considered a halfway point of sorts between rehabilitative and enhancive exoskeletons.

The primary focus of this research is the design of enhancive exoskeletons. The current state of enhancive exoskeleton research can be viewed as divided between full-body and partially-covering enhancive exoskeletons. As for the design aspect of exoskeletons, BLEEX, a lower-body task-specific exoskeleton has been developed at Berkley University. The starting point of the design of this exoskeleton is an investigation into clinical gait analysis (CGA) data, as the purpose of the exoskeleton is to carry a back-mounted load for walking soldiers (Kazerooni and Steger 2006). A method of design by biological analogy is implanted by normalizing the CGA data to the weight of the subjects, therefor an estimation can be made by scaling. This is then used to design actuation systems, both hydraulic linear systems and electric motors with harmonic drives have been investigated.

Current full-body enhancive exoskeletons developed are Raytheon Sarco's XOS 2 (Army-Technology.com 2014) and at the PERCO Lab of Scuolo Superiore S.Anna of Pisa, Italy (Marcheschi *et al.* 2011). Consequently, the information on the XOS 2 is scars as it is a company prototype. The PERCO team have named robotic exoskeletons with the purpose of enhancing or augmenting the human strength and carrying capacities, body power extenders (BE), as such their exoskeleton will be referred to as the BE in this thesis. These afore mentioned exoskeletons are prime examples of quasi-anthropomorphic robot exoskeletons being designed with typical human shapes and dimensions in mind. They differ predominantly in their actuation system, the XOS 2 being hydraulic and the BE purely electric (Bergamasco *et al.* 2010). The BE proposes a design methodology which aims to achieve ideal transparency, i.e. the devices presence does not affect the natural motor habit of the user. The design methodology proposes to do this via two conditions. The first reflecting the equilibrium of the

systems weight distribution so the user does not have to alter his/her natural movement to compensate for the devices balance, CAD model dynamic simulations are used for calculating the coordinates of the Zero Moment Point which is used to verify the support polygon. The second condition is related to the tracking force, i.e. the force interaction between where the user is connected and the exoskeleton sensor. This is verified by the development of the complete dynamic model including the actuation control laws as well as by experimental study into the disturbance forces (Marcheschi *et al.* 2011).

This research will investigate a multitude of available variations that arise from varying link geometric parameters, link length and cross-section dimensions. As mentioned before the exoskeleton is bound by the user. Therefore, this research will present a design methodology which at its core will define a human not by the flesh and bones, nor by its thoughts and feelings but by its range of motion and the lifting capacity. Although, investigations in mimicking the functionality of individual human joints will be presented as well. Then the human is looked at as the crucial points which it interacts with the world around it. These are simplified to its hands and feet and some space inside, in the context of designing an enhancive exoskeleton the space will be designated 'design-space'.

The defined 'design-space' is where the robot will mimic the human, but in a way better than the human. Just as the human is could be thought of as being the optimum developed by its environment over tens of thousands of years, the 'design-space' becomes the environment in which the exoskeleton will be developed. Much analogous to the changing surroundings of the human, to which it had to conform, the changing space of the robot forces the structure to conform. The more spaces that the robot must conform to, the more general will the structure be of the final machine.

1.2 Motivation

This research is a part of an industrial collaboration between University of Leeds and Mechatec to research and develop exoskeleton technologies for usage in future applications such as, but not limited to: search and rescue, construction site, emergency repairs and space exploration. This includes research into areas of enhancive exoskeleton design, electric and hydraulic actuation within enhancive exoskeletons, control of enhancive exoskeletons, control of assistive exoskeletons and assistive exosksleton design. Some documents have been developed together with the industrial partner regarding the requirements of the exoskeleton. The development of these requirements and metrics are beyond

the scope of this research and will therefore not be discussed in detail. These documents are, the Exoskeleton Tasks (found in APPENDIX A), the Customer Needs Documents (found in APPENDIX B), the Customer Requirements Document (found in APPENDIX C) and the Metrics Document (found in APPENDIX D).

The current research into enhancive exoskeletons have mainly been focused on purely anthropomorphising the exoskeleton design (Kazerooni and Steger 2005; Marcheschi *et al.* 2011; Army-Technology.com 2014). This has led to the main motivation of this research, to focus on the alternate designs which may be optimal for specific tasks of operation for the exoskeleton.

1.3 Aims and Objectives

1.3.1 Aims

The aims of this PhD are to:

- carry out research in finding the relationship between structural geometries of an exoskeleton and power and torque when following the key trajectories of a human motion
- obtain the optimum geometries which correspond to minimum power expenditure and peak torque for the joints relevant for the exoskeleton to perform a human mimicking movement with an external load.

1.3.2 Objectives

The following objectives have been set for this research to achieve the above aims.

1. To develop a design methodology for an exoskeleton structure with relaxed anthropomorphic constraints.
2. To obtain motion data via motion capture experiments and identify key patterns, furthermore to use the data as a basis of exoskeleton motion simulation.
3. Implement cross-section optimization of links based on bending criteria and compare the results with FEA of the links measuring the difference in deflection.
4. Obtain and compare torque data from joints considering the effects link-masses have with and without external exoskeleton loading.

5. Obtain the ratio between link-lengths and in extension map the effects varying ratio has on the power and torque characteristics of the exoskeleton model when following the required trajectories.

1.4 Contribution of This Research

The research will contribute to the power enhancing field of research in exoskeletons with the focus on principally sagittal plane motions and the combined effects of various motions expected to be performed by the exoskeleton.

The contributions are summarized as follows

1. Development of a design methodology for exoskeletons intended for specific load carrying tasks.
2. Data collection and investigation into a greater spectrum of human motions to be mimicked by exoskeletons by use of motion capture.
3. Demonstrate by comparison to FEA results that using a simple beam bending equation as a constraint within cross-section optimization is feasible.
4. Evaluation of the cross-sections role in the effects of link masses and in turn their effects on the overall power and torque characteristics of the exoskeleton joints.
5. Optimal ratio of link lengths when considering a simple sagittal plane exoskeleton model for two load-carrying tasks. For lifting object from ground the exoskeleton's thigh-link ratio should be larger and for raising an object from hip height to shoulder height the upper-arm-link ratio should be larger.

1.5 Scope

The research scope is to investigate geometric parameters of the exoskeleton frame linkages and their effects on parameters which are related to actuation design and operational power consumption. The design methodology could potentially be implemented in a workflow for designing the entire exoskeleton, including but not limited to design of actuation systems, placement of electronic hardware, optimized cabling and wiring, and power systems integration.

1.6 Outline of Thesis

The thesis is outlined in such a way that each chapter build on the previous. Therefor there is a gradual build-up of relevant information. This gradual development of the work is culminated in the last two chapters presenting the optimization and component design. Each chapter is briefly discussed below.

Chapter 1, the introductory chapter covers the background, the motivation, the aims and objectives, the contribution and the scope of the research of design parameters of the exoskeleton frame.

Chapter 2 presents a literature review on the human biomechanics including an overview of human anatomy and terminology which will be used in this thesis as well as considering human gait and research on human object lifting. Then aspects of anthropomorphic robot design will be looked at, namely kinematic modelling, contact and impact modelling and legged robot kinematic optimization for biped walking. Once the ground material for humans and humanoid robots have been covered the exoskeleton robot classifications will be discussed and the relevant research will be presented. Certain design challenges of anthropomorphic nature in robot design, primarily in exoskeleton robots, will be reviewed. The effects of actuation on exoskeleton design will review various actuation methods used in exoskeleton design with focus on enhancive exoskeletons. The review of current research known will culminate in the enhancive exoskeleton robot design section which will review known successful enhancive exoskeletons. The last sections will discuss and summarise the literature review.

Chapter 3 highlights the gaps in current exoskeleton knowledge and continues to present a design methodology from this. Furthermore, the simulation environment relevant to this research and terminology associated with the environment is presented. This includes a review of the inverse kinematics of two-link model and the comparison of the practicality of using numeric and analytical approaches of solving the inverse kinematics.

Chapter 4 presents the motion-capture pilot study. Included is the protocol for the experiment as well as a review of the software and hardware used, moreover to filter the motion data Winter's residual analysis method is employed (Winter 2009a), and this is discussed as well. The motion-capture model and the data extracted from the software is presented for gait, object lifting and object raising. The gait data is verified by comparing to known CGA data published. In this chapter analysis is also done on the interaction point trajectory data from the

motion capture study to identify if the model could be considered connected with the ground or moving. The new model trajectories are presented. Patterns in the ground reaction force data of the motions 'Object Lifting' and 'Object Raising' are also considered. Signal filtering and smoothing techniques are presented and compared, and a sample model is presented where the trajectory, pattern and signal process analysis combined, and the results discussed.

Chapter 5 presents the methodology by witch the planar 2D exoskeleton is modelled. Firstly, the chapter reviews the exoskeleton subdivisions based on the design methodology. Secondly the model development is presented by analysing the back-structure orientation and trajectories and minimizing the back-structure for a given motion, and finally the forward and backward kinematics is derived using the Denavit-Hartenberg notation.

Chapter 6 starts by presenting a relationship between the cross-sections of simple geometries, cylinders, squares and rectangles. The methodology used in the optimization is presented as an example of a simple pendulum with a mass attached to the free end. Full system cross-section optimization is performed on 'Object Lifting' and 'Object Raising' motions for both cylinder and hollow tube links. The results are compared with FEA of the found geometric values. This is followed by a geometry reselection example. The last part of the optimizations looks at the effects of the link lengths on the power and torque of the exoskeleton for each motion. This optimization takes into account the variation of the link geometries as the link lengths change to adapts for the varying bending moment the links undergo.

Chapter 7 summarises and concludes the research and discusses the future works.

Chapter 2
Literature review

2.1 Introduction

As the exoskeleton is a machine intended for use around the human body it is first necessary to understand the basic structure of the human. Then, human motions relevant to this research are presented, including gait and object lifting.

Legged robots are presented by looking at optimization aspects. This is discussed from the perspective of links and their lengths and impact on power consumption.

The anatomy of a robotic exoskeleton will be discussed in short and will serve as an introductory platform for the exoskeleton classifications section. Some key developments in enhancive exoskeletons will be presented. An overview of other exoskeleton classifications will serve to enhance the properties of the enhancive exoskeletons.

Design challenges and their solutions within exoskeleton research are presented, drawing from all classifications. This is then followed up by presenting various actuation methods in exoskeletons.

The chapter is discussed, and strengths and gaps are presented in general. This is followed up by a summary focusing on the gaps in the research.

2.2 The Human Biomechanics

2.2.1 General Anatomy of the Human

A human body consists of (but not limited to) skeletal, muscular, cardiovascular, digestive, endocrine, nervous, respiratory, and immune/lymphatic systems. For the purpose of this work an overview of the muscular and skeletal (musculoskeletal) systems of a healthy human being is sufficient. The skeletal system can be seen Figure 2.1.

For both males and females, the body consists of five extremities, two arms, two legs and one head, as well as one torso that all the extremities protrude from. The upper limb bones consist of the clavicle, scapula, humerus, radius, ulna, carpal bones, metacarpal bones and phalanges. The corresponding joints are sternoclavicular, acromioclavicular, shoulder (glenohumeral) elbow and superior radioulnar joints. From the forearm there are the inferior radioulnar, radiocarpal, midcarpal joints. In the hand the joints are carpometacarpal, metacarpophalangeal, interphalangeal (Palastanga, Soames and Palastanga 2008).

The lower limb bones consist of the sacrum, coccyx, innominate, femur, patella, tibia, fibula, talus, calcaneus, cuboid, navicular, cuneiforms, metatarsals and phalanges. The corresponding joints are sacroiliac, hip joint, knee joint, superior tibiofibular, ankle joint and inferior tibiofibular joint (Palastanga, Soames and Palastanga 2008).

The human joints are extremely complex in that they do not move in a fixed manner. That is the degrees of freedom of a joint, although might seem like one, can actually be represented as six (Palastanga, Soames and Palastanga 2008). The elbow is one such example, where its primary movement occurs as flexion and extension but by doing so it moves in an intricate double frustum pattern (Vitiello *et al.* 2013).

Although all (healthy) humans possess the aforementioned structures, the dimensions of each human vary. In terms of volume, each human is again unique as daily activities and nutritional intake play major roles in how much fat and muscle tissues are present in the human. These factors make for each human to be truly unique with respect to volume and mass distribution coupled with position of joints and ranges of motion (Pheasant 1996).
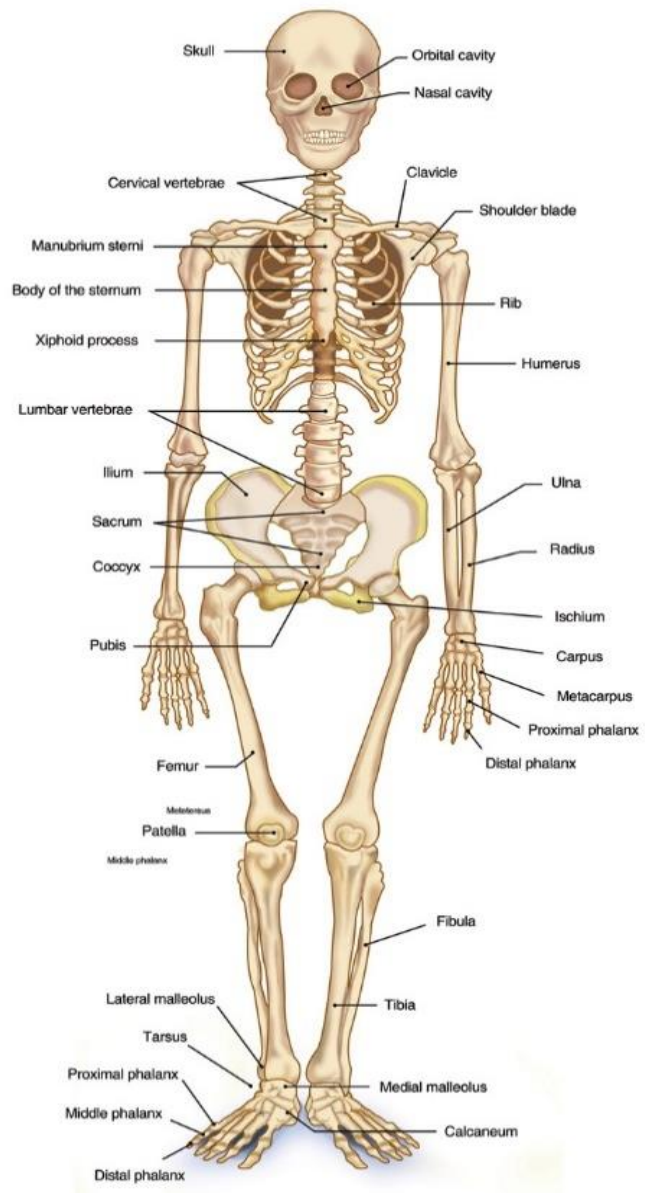
Figure 2.1 Human Skeleton (Health 2013)

2.2.2 Human Gait Analysis

The human gait cycle is well studied and in most enhancive exoskeleton designs has served as a basis for design as this is the principle mode by which humans transport themselves. As it will be referred to many times in other studies and in part used for experimental validation in this research, the vital aspects of human gait will be presented here.

The gait cycle can be split into phases for each leg, as seen in Figure 2.2. The primary phases are the stance and the swing phases, it should be noted that in the human gait there exists an instance where both feet are on the ground simultaneously. The stance phase can be further split into crucial moments:

- Initial Contact
- Heel Strike
- Foot Flat
- Heel Rise/Off
- Toe Off
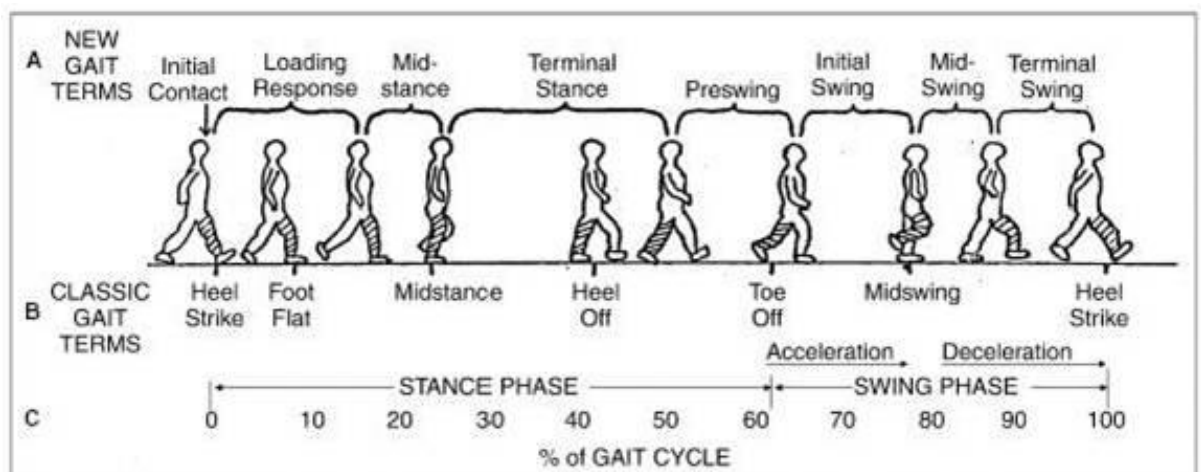
Figure 2.2 – Human gait cycle, starts from heel strike and ends with the heel strike on the same side. (Singh)

Research into identifying the various key instances is very important specifically for use of prosthetic devises which can be actuated. These robotic prosthetics control systems use the gait patterns to work in tandem with the user's healthy leg (Maqbool *et al.* 2017).

Some research, which will be presented in the Exoskeleton Classification section of this chapter, will show that designs of exoskeletons can also use human motion data as a starting point of the exoskeleton design.

2.2.3 Human Lifting

As this thesis is concerned about lifting items from the ground it will be considered in this section. 'Lifting' will refer only to the activity which results in a load or item being picked up from ground level. Various research has been made into human lifting. Some research focuses on athletic lifts in competitions (Escamilla *et al.* 2000), and some into material handling in workplaces (Gallagher and Unger 1990).

Research into athletic lifting methods have derived kinematic and kinetic models (Brown and Abani 1985). Some later studies have used motion capture technologies to record the athletes in their lifts (Escamilla *et al.* 2000). The primary purpose of these studies has been to identify optimal lifting motions (squats and deadlifts) for strength athletes.

Other research into lifting has been related to back issues that may arise due to manual labour. Some studies look at the spine and the stress between the vertebrae (Anderson and Chaffin 1986) and some into more detailed work inside mines where the working space is narrow (Gallagher and Unger 1990). Research into the effects of squats vs. stoops for lifting items from the ground has also been performed with back health as focus, Figure 2.3.

At the current stage of this research, no research is known that incorporates lifting data is in the exoskeleton designs.
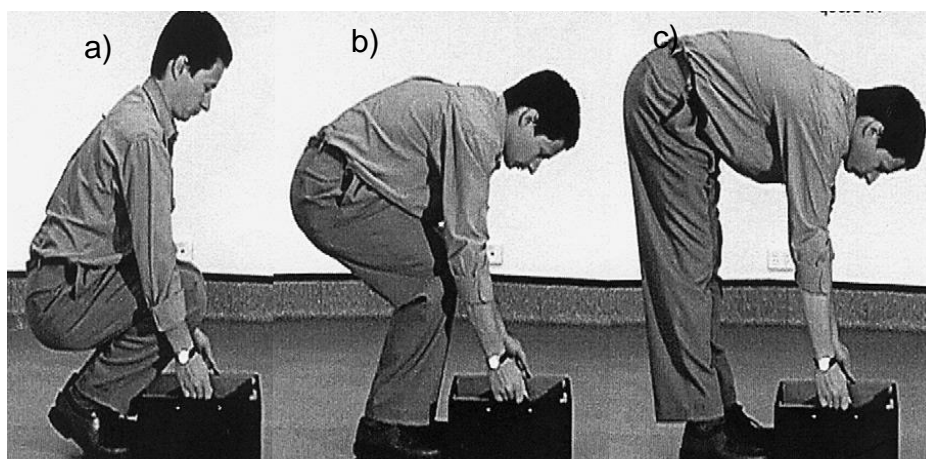
Figure 2.3 – a) Squat, b) Semi Squat and c) Stoop postures when lifting a box from the ground. (Burgess-Limerick 2003)

2.3 Legged Robot Kinematic Optimization for Walking Robots

In order to aid in the kinematic design level of legged robots work has been carried out on mechanical antagonism (Abate, Hurst and Hatton 2016). It is presented that power quality, the difference between the squared sum of powers and the sum of squared powers (Equation 2-1), can be used when determining the overall structure of the robot in question to minimize antagonism in actuators. An example is shown in Figure 2.4. The presented methodology is independent of the type of actuation as it is concerned with the power about the joints of the kinematic system.
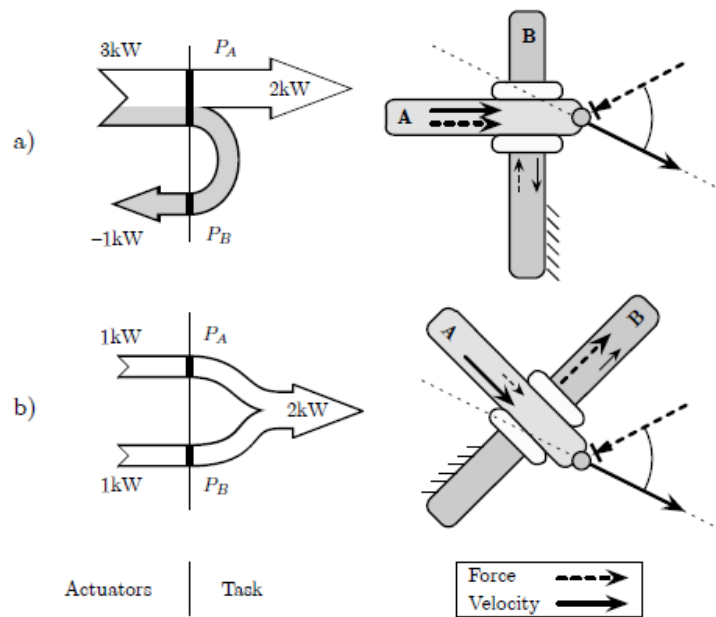
Figure 2.4 - Example of mechanical antagonism producing the same net power, however in a) 1kW of power is lost and in b) due to the change in configuration no loss occurs (Abate, Hurst and Hatton 2016)

$$Q(\boldsymbol{P}) = \left(\sum P_i\right)^2 - \sum (P_i^2)$$

Equation 2-1

In a letter for energy efficient locomotion the use of direct drive motors in legged robots is compared within various legged robots of varying size and weight, most of which are multi legged with more than two legs (Kenneally, De and Koditschek 2016). Three different mechanisms for the legs are analysed with respect to proprioceptive sensitivity (force sensing at the joints), force production and thermal cost of force (Figure 2.5). Some benefits are shown for the direct drive system in smaller robots as well as using symmetric five bar mechanisms for the legged robots as shown in Figure 2.6.
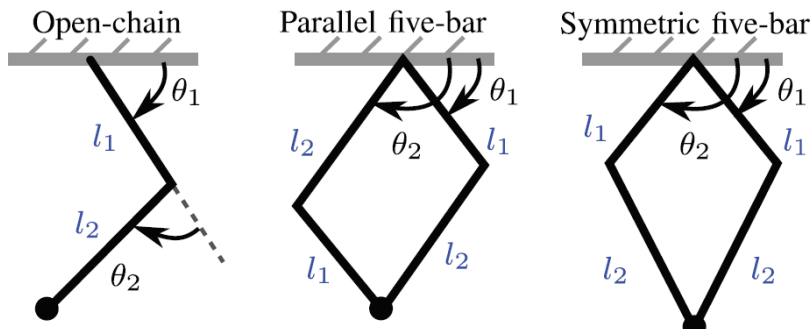
Figure 2.5 – Leg designs considered in the research on direct drive actuation on smaller scale quadruped robot (Kenneally, De and Koditschek 2016).
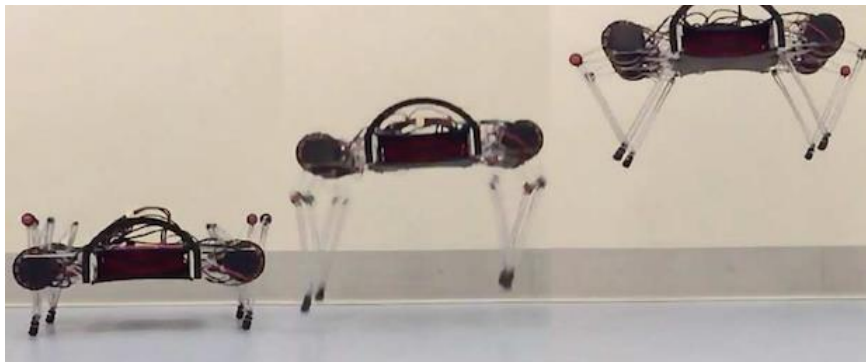
Figure 2.6 - Minitaur, one of the robots considered in the research on direct drive actuation on smaller scale quadruped robot, performing a jump (Kenneally, De and Koditschek 2016).

Research in optimizing link lengths with respect to two costs of transports, mechanical and total (which is representative of energy used in electric motors) has been done (Bhounsule, Pusey and Moussouni 2016). The model that is developed uses hip and knee to optimise the structure, but ignores ankle. It is known from biomechanics (Winter 2009b; Nordin and Frankel 2001) and humanoid mimicking robotics (Zoss, Kazerooni and Chu 2006b; Cenciarini and Dollar 2011) that the ankle in fact experiences torque. As is known during gait the human foot passes through a multitude of phases and a simple point contact model is not indicative of the true nature of humanlike biped gait (Whittle 2014). This research generates human gait like trajectories by simplifying the trajectory to that of an inverted pendulum shown in Figure 2.7. The research here might have assumed that the foot was in point contact. The swing phase of the leg is omitted in the research. The research also looks at a cost of transport which is associated with electric motors.
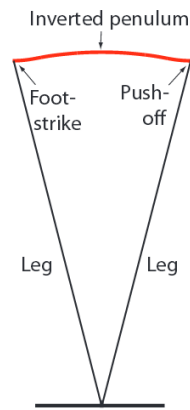
Figure 2.7 – Inverted pendulum model trajectory
(Bhounsule, Pusey and Moussouni 2016).

The above-mentioned researches (Kenneally, De and Koditschek 2016; Bhounsule, Pusey and Moussouni 2016; Abate, Hurst and Hatton 2016) do not consider structural properties of the mechanisms they evaluate. The basis of the torque and force relations are in the Jacobian matrix. Bending, buckling, torsion, mass and mass distribution are factors which affect the inertial properties of the models. This in turn affects the torques and powers required about the joints.

Although some biped robots use point contact for their walking (Ramezani *et al.* 2013) the development of current biped humanoid robots is based on using some form of platform as feet, some robots gait movements are less human like due to lacking toe joint control (Chestnutt *et al.* 2005) however more current research is focusing on dynamic gait (Zhao *et al.* 2014).

2.4 Anatomy of Robotic Exoskeletons

A robotic exoskeleton designed for human use follow certain similarities irrespective of its applications. Key components are: actuation system, electrical system, sensory system, joints and links. For example, systems are developed that are stationary and work as a robot manipulator used for rehabilitation, systems are also developed to carry its own weight autonomously and interact with the user such that they perform a user defined motion. Research also shows that the need for an active actuation system can be minimized and in some cases completely omitted in favour of a gravity compensating spring system (Zhou *et al.* 2012). Thus, the components of the anatomy of exoskeletons are very general and heavily dependent on the classifications they fall into.

2.5 Exoskeleton Classification

Although definitions of exoskeleton types have not been made formally, in order to better understand the scope of this project this section will classify exoskeletons based on their application and functionality as they have been presented.

When exoskeletons are designed for the purpose of power augmentation and load carrying they are considered as being enhancive. Outside of the scope of enhancive, exoskeletons fall into one of three categories: assistive, rehabilitative or haptic.

2.5.1 Enhancive Exoskeletons

Exoskeletons designed with the purpose of enhancing human strength by adding a powered interface between the external load and the human fall specifically into this category. The main purpose of these exoskeletons is to allow the user to perform tasks and/or carry loads beyond natural human strength without transmitting the load through the musculoskeletal system. The uses of such exoskeletons range from military applications (Army-Technology.com 2014) to heavy material handling (Marcheschi *et al.* 2011). The stated definition of an enhancive exoskeleton also includes lower body exoskeletons which only allow for load carrying support, such as a backpack (Zoss, Kazerooni and Chu 2006b).

Sarcos XOS-2 is a military funded exoskeleton (Army-Technology.com 2014) and can be seen in Figure 2.8 (a). It follows from the patent application that it can be defined as a load bearing structure (Jacobsen and Olivier 2009).

The BE in Figure 2.8 (b), is an exoskeleton developed for human power augmentation. It is developed for heavy material handling in unconstructed environments (Marcheschi *et al.* 2011). As such it is deduces that the reaction forces between the exoskeleton and the object it interacts with must be transferred to the ground. For the BE, a full body exoskeleton intended for material handling, the degrees of freedom of each limb needs to be complete and independently actuated such that no joint is unactuated and dependencies in motion between joints do not exist. It is further concluded that due to this the structure is likely to be relatively bulky and complex. The design methodology of the BE is based on achieving ideal transparency, that is the exoskeleton's presence shall not affect the natural motor habit of the user (Lucchesi *et al.* 2010). To achieve this there are two conditions set. First, the equilibrium of the system, that is, the weight distribution of the system should be maintained such that the system is not unbalanced forcing the user to alter his/her natural

movement. Second, relating to the tracking forces, the forces of the contact points that the user has with the exoskeleton, should be minimized and therefor excessive tracking forces can lead to unwanted distorted movements. Although it seems that the second design condition is related to the control of the exoskeleton which has impacts on the design.

The lower body exoskeleton BLEEX, seen in Figure 2.8 (c), differs from the BE in that it is highly task specific. Its design is based on CGA from which kinematic and dynamic data is derived and gathered (Zoss, Kazerooni and Chu 2006b). Due to it being highly constrained a minimum set of active actuators are implemented, the rest being passive. These are found using the CGA data by analysing the torque and power consumption during gait. Only the hip, knee and ankle joints are actuated in the sagittal plane.
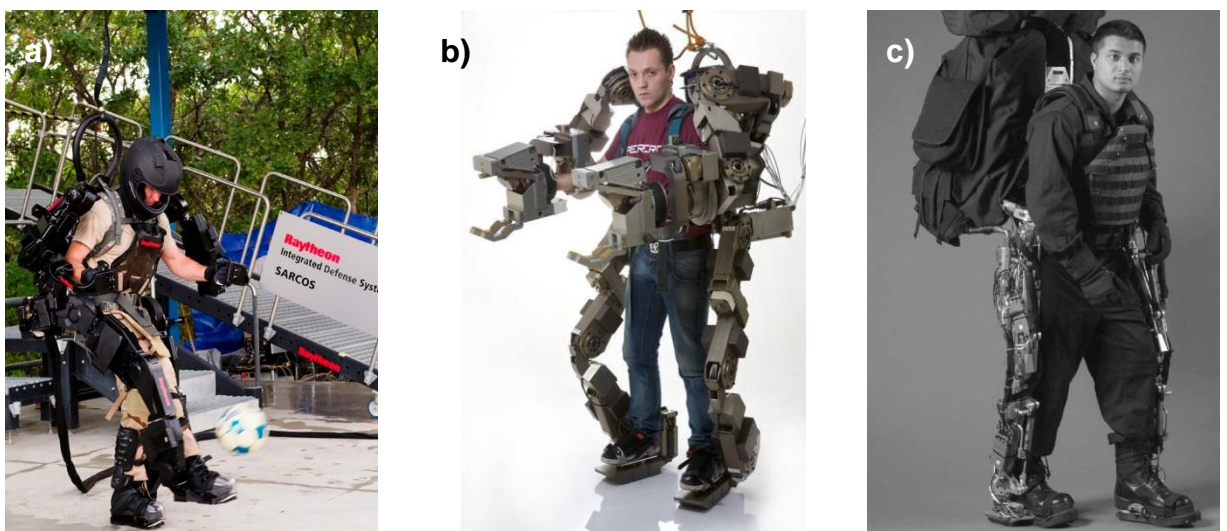
Figure 2.8 - Various known enhancive exoskeletons a) Sarcos XOS-2 (Army-Technology.com 2014) b) Body Extender (Marcheschi *et al.* 2011) c) BLEEX (Kazerooni and Steger 2006)

2.5.2 Assistive Exoskeletons

Assistive devices are those that focus on aiding human skeletal muscle functions specifically without having the exoskeleton acting as an interface between the user and the external load. This includes people who have lesser muscle functions than a healthy human including elderly people (Kiguchi *et al.* 2008). This means that the exoskeletons need to support load is omitted and it is therefore carried through the humans musculoskeletal system. The system, that specifically supports muscular power, such as HAL (Hayashi, Kawamoto and

17

Sankai 2005), allows for the users own force output to be added to the exoskeletons force output.

2.5.3 Rehabilitative Exoskeletons

Rehabilitative exoskeletons come in two forms stationary and mobile. This is true for both lower body (Low 2011) and upper body (Gopura, Kiguchi and Bandara 2011; Nef *et al.* 2007). An example of a stationary rehabilitation device is the Armin shown in Figure 2.9. They allow for people who have neural damages to train certain functions, typically walking or arm movement respectively. Rehabilitation devices can differ significantly in size and structure due to the lack of spatial limitations.

Figure 2.9 - Armin exoskeleton for
rehabilitation purposes (Nef *et al.* 2007)

2.5.4 Telecommunication and Force feedback exoskeletons

Exoskeletons have also been researched in the use of telecommunication operation of robotic devices with force feedback systems incorporated. These systems are not load bearing structures and as such resemble more motion tracking units rather than enhancing exoskeletons.

2.6 Design Challenges of Anthropomorphic Nature in Exoskeletons

2.6.1 Misalignment

Misalignment is a crucial problem in assistive, rehabilitative and haptic devices. The exoskeleton and the human kinematics differ. One way of solving this problem is by introducing several passive elements into the joint architecture. Another is to introduce connections between limb and machine that limits the level of uncontrolled forces that are generated by hyperstaticity (Jarrasse *et al.* 2012). The problem has also been tackled by decoupling the joint rotations and translations (Cempini *et al.* 2013). For dealing with elbow-joint misalignment an introduced misalignment in the exoskeleton is proposed (Malosio *et al.* 2011). A detailed analysis methodology is presented to aid in the issue of self-alignment. The outcome of the research presents a methodology to evaluate the joint number and types that should be controlled in order to provide self-alignment and torque transmission for assistive devices (Cempini *et al.* 2013). The presented method is intended for analytical purposes and it is stated that it is not sufficient for how the self-alignment chain should be constructed. Due to the neglecting of external loads, mass and inertial load effects are not considered. Correct alignment is generally accepted as being unachievable without complex imaging techniques (Vitiello *et al.* 2013)

2.6.2 Glenohumeral and Hip Joint

The hip joint and the glenohumeral joint are two main joints that can be described as ball and socket joints. By intersecting three axes at the point of the internal joint the three degrees of freedom of that joint can be represented externally. The hip differs from the glenohumeral joint in that its rotational axis runs inside the human, whereas the glenohumeral joint axis is free above the shoulder.

2.6.2.1 Glenohumeral joint

Research has shown that a gimbal structure external to the glenohumeral joint can be used to move singularities within the workspace of a rehabilitation exoskeleton arm and closer to the edge (Liszka 2006). The exoskeleton is shown being used in Figure 2.10.
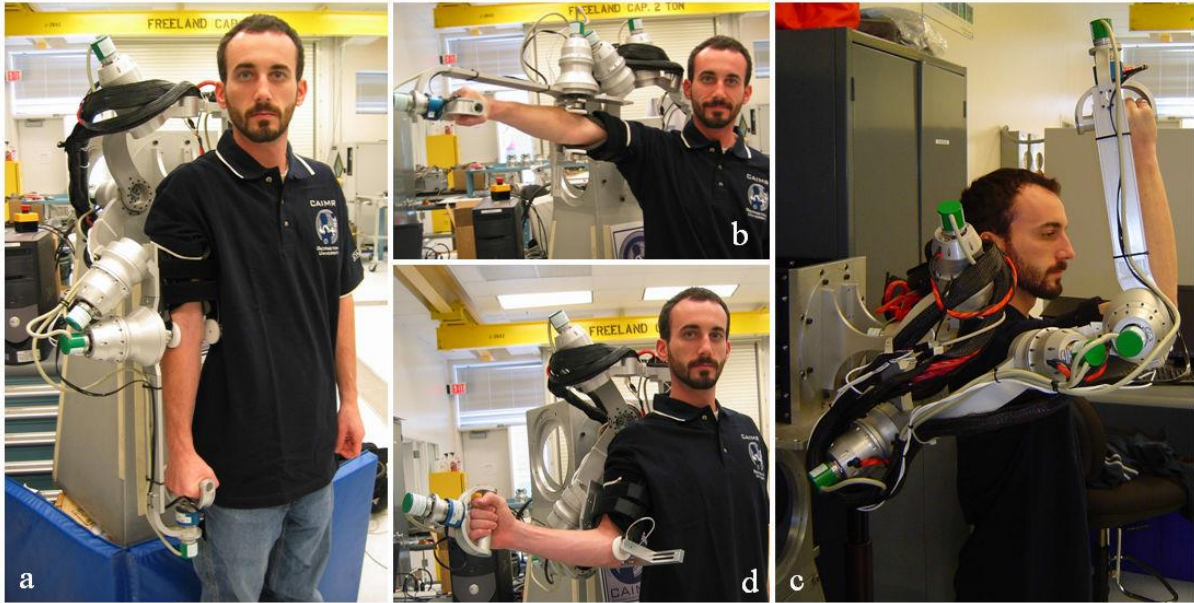
Figure 2.10 - Using a gimbal design various postures are shown, a) arm relaxed, b) abduction, c) rotation during abduction and d) medial rotation (Liszka 2006)

Similar to the gimbals structure it has been shown in Figure 2.11 in a haptic exoskeleton that a third rotational DoF located around the upper arm can also be used to move all singularities in the frontal plane to the edges of the workspace (Letier *et al.* 2008).
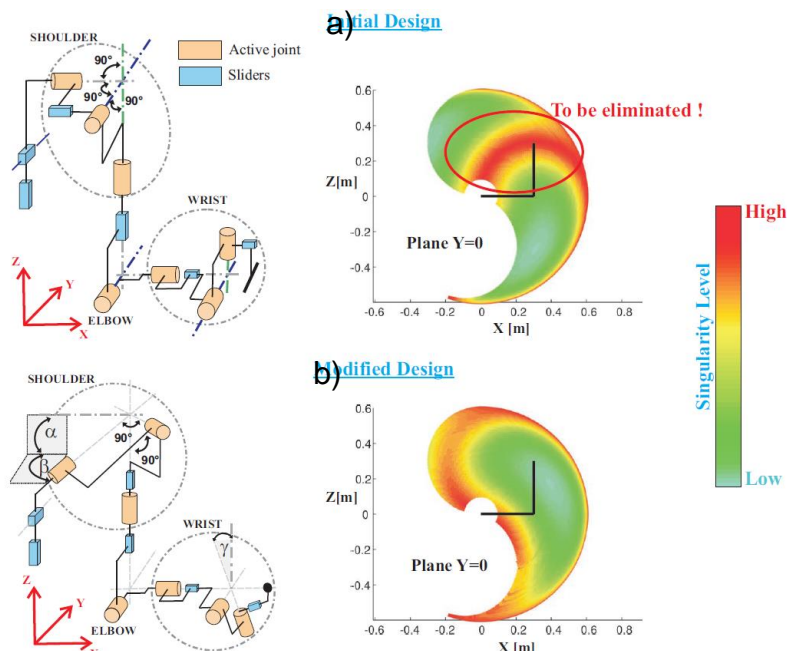
Figure 2.11 - a) The initial design of a shoulder exoskeleton and b) the modified version (Letier *et al.* 2008)

Figure 2.12 shows a complex haptic exoskeleton intended for tele operation in space is designed by completely omitting a structure around the shoulder (Schiele and Hirzinger 2011). A prismatic joint was used to connect the arm to the chest level of the user. The workspace was optimized to minimize singularities and thus does not find itself in a singularity position (Schiele and van der Helm 2006).
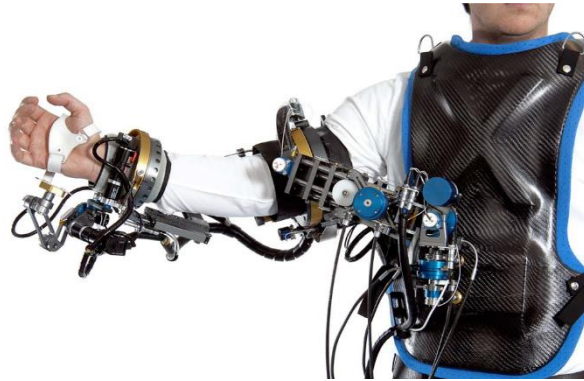
Figure 2.12 - Exoskeleton intended for tele operations in space programs (Schiele and Hirzinger 2011)

2.6.2.2 Hip

BLEEX has solved the issue of singularity by not aligning the three axis of the hip with the user (Zoss, Kazerooni and Chu 2006b) as seen in Figure 2.13. The un-actuated rotation joint was initially located above the exoskeleton leg but relocated to behind the users back due to large moments created. The rotation joint is spring loaded. No quantitative data is presented to affirm this work.
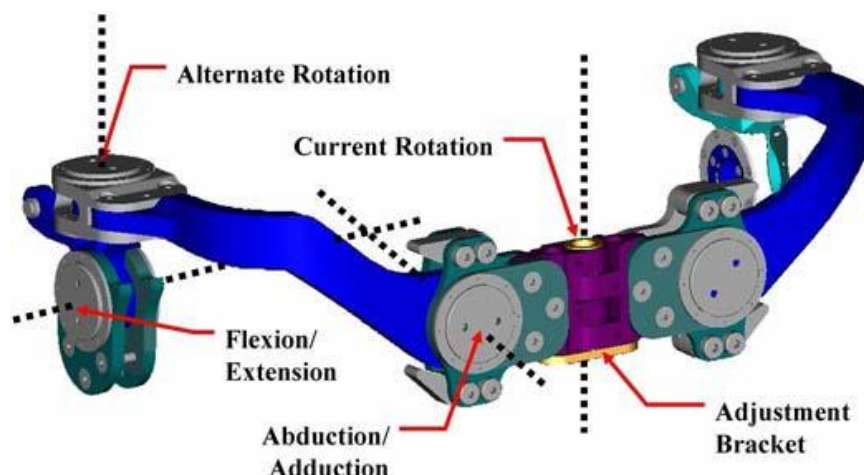
Figure 2.13 - The BLEEX hip structure (Zoss, Kazerooni and Chu 2005)

Unlike BLEEX, in the MIT exoskeleton seen in Figure 2.14, the rotation of the leg above the knee (Cenciarini and Dollar 2011). The effectiveness has not been quantified.

Figure 2.14 - MIT exoskeleton (Cenciarini and Dollar 2011)

2.6.3 Scapular motion representation

The clavicle and scapula add complexity to the glenohumeral joint motion. The shoulder girdle motions that are considered are the dominant ones, retraction/protraction and elevation/depression (Donghan *et al.* 2011). Extension/flexion, abduction/adduction and internal/external rotation are all functions of the shoulder joint motion however moving the humerus is coupled with scapular movement, called the scapulohumeral rhythm (Ergin and Patoglu 2012). Due to this the scapular motion also needs to be represented in designs.

Specific research in measuring the centre of rotation displacement of the human shoulder has led to a rehabilitation exoskeleton attached to the ground which allows for actuated flexion/extension and abduction/adduction of the upper-limb (Kiguchi, Kado and Hayashi 2011). Only simulations verify the design.

Figure 2.15 shows the assistOn-se, which is a rehabilitation device that is firmly attached to the ground. It incorporates a complex 3 DoF (3RRP) self-aligning joint. The joint design permits two planar translations and one perpendicular

rotation (Ergin and Patoglu 2012). An early prototype workspace analysis is performed which yielded positive results.
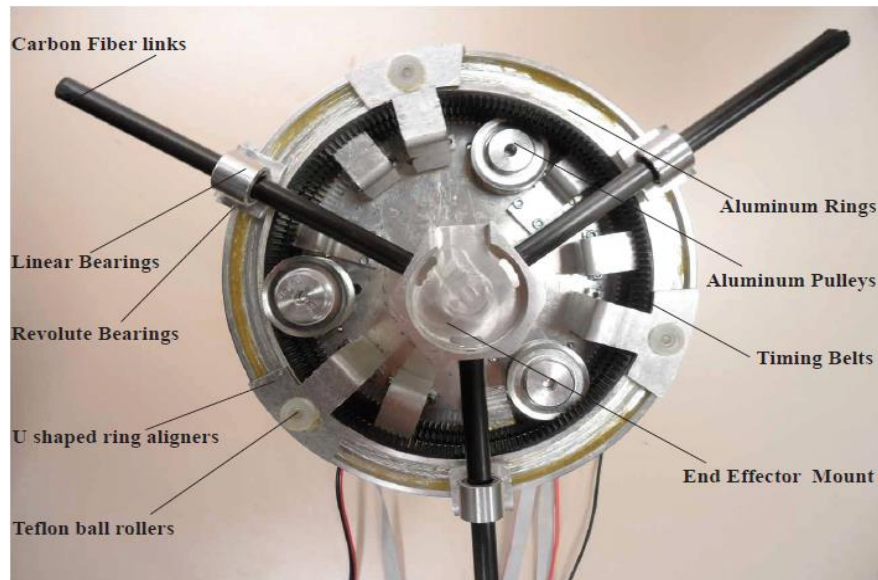
Figure 2.15 - The AssistON-se rehabilitation device's shoulder mechanism which allows for scapular representation (Ergin and Patoglu 2012)

Following a review of existing exoskeletons for rehabilitation that allow for shoulder girdle movement a proposed exoskeleton based on the limitations is presented (Donghan *et al.* 2011). The rehabilitation devises are all connected to ground and the proposed model incorporates 6 DoF to allow for all the major movements of the shoulder joint and girdle which differs from the existing rehabilitation devises presented.

2.6.4 Knee and Elbow

Elbows and knees have very similar structures, they both connect one bone to two other and they both predominantly allow for motion about one plane.

NEUROExos is a rehabilitation exoskeleton for the elbow joint. By thorough analysis the joint motion is presented in three dimensional space and a passive mechanism comprising 13 passive joints was developed (Vitiello *et al.* 2013). The actuation system transmits force via Bowden cables. As seen in Figure 2.16 the device attaches to the human using four shells, two for the upper parts of the arm and two for the lower. This allows the forces to be distributed over a larger area.
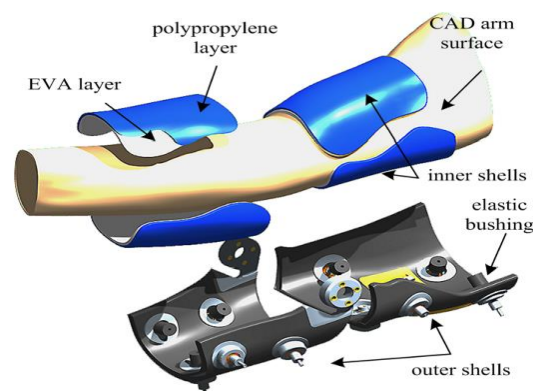
Figure 2.16 - The NEUROExos exoskeleton primary parts (Vitiello *et al.* 2013)

Researchers presented a kinematic algorithm based on geometry constraints and optimization which was used to simulate tibia rolling/sliding on the femur (Donghai *et al.* 2014).

From simulation, adaptive knee joint design solutions are proposed, and results of various combinations of pin, slider and cam configurations are presented. Experimental findings suggest that using pin slider/cam mechanism can minimize internal joint forces and torques. This mechanism shown in Figure 2.17 however only considers the sagittal plane.
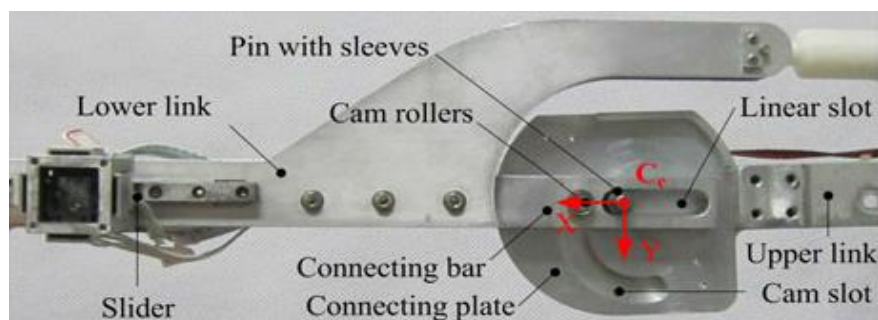
Figure 2.17 - Cam roller design for a knee exoskeleton (Donghai *et al.* 2014)

2.7 Discussion

2.7.1 Discussion on Structural Optimization in Legged Robots

The current research in robotics that focuses on structural optimization is limited to relatively simple kinematics of legs in robots. The work produced is fundamental, the effects of link physical properties are omitted. The weight of the actuation systems and their impact are also omitted. Furthermore, it is assumed that for legged systems there is no ankle joint, therefore the investigations lack the torque and power effects on what can be considered as ankle joint.

2.7.2 Discussion on Exoskeleton Classifications

The different classifications of exoskeletons are primarily tied into how they work around the user. An enhancive exoskeleton not only increases the users lifting capacity, but also omits the need to use the users own musculoskeletal system as a load carrying structure. Generally, this is achieved by force control methods (Kazerooni and Steger 2006; Steger, Kim and Kazerooni 2006; Jacobsen and Olivier 2014). Undeniably, however, the mechanical design needs to accommodate for this as well.

The assistive device aims to aid in human functionality whether this is in supporting or controlling capacity. This becomes a crucial difference in how the assistive systems are intended to function when compared to enhancive systems. There is a lesser symbiotic nature in the enhancive system with the user as it function as an interface between the users movement and the external world. Assistive systems, however, are not intented to function as a separate entity but in unison with the users movement as an external force generator.

In contrast to both assistive and enhancive exoskeletons, the rehabilitative device is built to support human functionality through tasks for training purposes where little or no muscle control exists.There is, however, a greater grey area between assistive and rehabilitation designs, than there is between enhancive and assistive designs. Due to the close relationship between the former pair, certain devices can be built to cover the range of both (Gopura, Kiguchi and Bandara 2011; Perry, Rosen and Burns 2007). As for the latter case the way in which the exoskeleton allows the user to interact with the environment determines whether it in fact enhances or assists the user. HAL is a great example of this, as it acts as a muscle enhancer but is used by people within a wider spectrum of capacities (Hayashi, Kawamoto and Sankai 2005; Kawamoto and Sankai 2002).

A design difference, which is the outcome of the classifications seen above, is how joint alignment and size adaptability is solved. As rehabilitative and assistive devices are supposed to aid the human motion, the target to minimize misalignment between machine and human joints become crucial. Size adjustment needs to be incorporated into the design. The same issue is presented in haptic feedback exoskeletons, which are developed for tele operating machinery. As they mimic the user's body they too need to be considerate of this (Schiele and van der Helm 2006).

For enhancive exoskeleton devices these issues have been solved by the near-anthropomorphic structures. There are minimum points of contact the between user and the machine which is sufficient to control the shape of the exoskeleton in a desired manner (Zoss, Kazerooni and Chu 2005). This allows the interconnecting links between the contact points to orientate irrespective of the human's links.

The differences can best be likened to common two wheeled vehicles: Motorcycles (enhancive), bicycle (assistive), bicycle with support wheels (Assistive/Rehabilitation) and training cycles without pedals (Rehabilitative). In this analogy the main functions are the same, to use the sense of balance to stay upright whilst moving forward using a two-wheeled vehicle.

Motorcycles have built-in engines that produce all the force irrespective of human muscle strength and are mainly dependant on the driver's sense of balance and direction. Bicycles have pedals and work with the user input force to roll forward whilst relying on the user's own balance. Bicycles with support wheels and training cycles without pedals are used for the user to learn to work their balance to a level where they can utilise it without support.

2.7.3 Predominant issues in designing exoskeleton structures

2.7.3.1 Joint misalignment

Several researches have been undertaken to deal with misalignment on specific joint sections, but as seen only one deals with presenting a structure for any joint. All the misalignment issues show that representing the human joint motions necessitates implementation of multiple DoFs. Due to the complex nature of the joints, even in simpler ones such as elbow joints that commonly are simplified as pin joints, misalignment becomes a critical factor when the level of anthropomorphic likeness increases. These multiple DoFs create the need for complex structures that can solve the issues.

For enhancive exoskeletons the misalignment is a not as great of an issue, as the exoskeleton structures can be designed so that there is space between the user and the machine. Therefore misalignment can be viewed as non-consequential where the exoskeleton is not connected to the user.

2.7.3.2 Scapular representation in exoskeletons

The shoulder girdle movement is predominantly researched regarding rehabilitation devices. As they are most commonly fixed to the ground they allow for a large workspace to be used supporting larger designs with actuation systems for many degrees of freedom. Such a system is not feasible for the application of mobile devices.

2.7.3.3 Force transmission and interaction

One common theme along all the passive joints that were developed is that force transmission from machine to human was considered. Such that the passive joints would not hinder this to occur but to allow for it to occur comfortably by complying with the joints they are supporting. No mention or analysis is made on interactions with external forces on the mechanism, which is crucial for an enhancive device.

2.7.3.4 Design considerations for enhancive exoskeletons

As can be seen various solution methods are used to solve issues arising from joint alignment. More notably each joint presents an in-depth area of research specifically these are for assistive and rehabilitation exoskeletons whereas in enhancive exoskeletons some general representation of an anthropomorphic structure is used for joint positions.

At several instances we see upper extremity exoskeletons being designed utilising gimbal type joints (three rotational joints with intersecting axes of rotation) for the shoulder joints. These are all optimized such that their workspace to minimize the location of singularities. None however have actively sought to tackle the problem from the sternoclavicular joint. This means that the scapular motion is not taken into consideration in the shoulder movement.

The design for the BE uses a general anthropomorphic structure as the base, the goal being to keep the centre of mass in the same location to the user. This omits the needs for the user to alter his/her natural movement to satisfy the stability of the exoskeleton. The actuation system of the BE is modular, the actuators are designed only once but used in all planes of motion except wrist

rotation along the forearm. The risk for the actuator being over-engineered at certain joints increases.

No literature was found to provide details on how Sarcos XOS2 has been designed.

The BLEEX being a lower body exoskeleton that is used for load carrying, has not dealt with the hip joint in the manner where all joint axes align with the hip joint in the human. This has also not been done with the ankle joint either. Therefor the system does present misalignments and inconsistencies with the human wearer on a fundamental level. Furthermore, the design of the exoskeleton initially started with an investigation into CGA data. This was then scaled to what was expected to be the exoskeletons weight. The result being that the torque-angle graphs of the exoskeleton differs from that of the CGA curves indicating that the kinematics and dynamics of the exoskeleton do not fully match the humans (Zoss, Kazerooni and Chu 2006a).

2.8 Summary

What can be seen from this literature review is that there is a gap in optimizing link lengths for biped robots as well as exoskeletons, especially with respect to the effects of mass and structural considerations of links and actuation systems.

A whole systems approach to the mechanical design of an enhancing exoskeleton, in terms of the effects of the links on the power consumption of the exoskeleton is also lacking.

The importance of making the machine universally usable has potentially led to the relatively bulky sizes of known enhancive systems. Modularity in components and link sizes and strengths has not been researched. By making the links changeable the semi anthropomorphic nature of the enhancive exoskeleton could become less bulky as each link could fit closer to the user.

Another factor is that the system actuation integration is not yet developed into an optimized state. Although remote location of actuators has been implemented in the BE (to a small degree) and some hypotheses are made with regards to the BLEEX exoskeleton, the full potential of remote location actuation in exoskeleton design has not been researched. By utilizing cable driven actuation systems, the exoskeleton could be developed to be less bulky as well as potentially lowering the power consumption of the system during certain tasks.

Chapter 3
Design Paradigm and Simulation Environment

3.1 Introduction

This chapter is divided into two main sections. The first section will present the design paradigm by discussing the limitations in current research, leading to a design theory and a design methodology for optimized enhancive exoskeletons. This is followed by a review of simulation environments, this includes the choice of analytical and numerical methods for solving the inverse kinematics of an exoskeleton model.

In the first section of the chapter design limitations and gaps in the previous chapter, which will form the bases of this research, are presented. The difference in enhancive and assistive exoskeletons in terms of model and kinematic representations are shown by presenting the transformation matrices which describe the kinematics of a human and an exoskeleton that are connected. It will be shown that in certain scenarios alternative representations of kinematic models are feasible. Therefore, the trajectories of a body whose kinematic structure is unknown can also be equated to the mimicking trajectories of the exoskeleton, whose kinematics are known. Following this, 'task specific design' in exoskeletons is discussed. Based on the insight that is built a design theory is derived from which four postulations are presented. This is used to present an overall design methodology which concludes the first section.

The second section looks in more detail at the simulation and modelling environment specifically by comparing analytical and numerical methods of computing the inverse kinematics. First a general two-link model is presented. This is followed by an overview of Maple software and an analytical computing approach. The algorithm for a numeric solutions approach in MATLAB and SimScape is presented next. The two methods are compared, and a potential hybrid solution is discussed.

The sections are discussed individually in the discussions section and the chapter is concluded with a summary of everything presented.

3.2 Design Limitations, Theory and Proposed Methodology

As seen in the literature review, analytical methods have been proposed for designing assistive exoskeletons tackling the misalignment issue which arises (Cempini *et al.* 2013). Research has also been made to avoid uncontrollable forces in assistive devices where it interfaces to the user (Jarrasse *et al.* 2012). These researches have clearly shown that for an assistive device there needs to be several passive (un-actuated) degrees of freedom apart from the actuated ones.

The research albeit sound is specifically geared towards the key issues of assistive exoskeletons, the alignment of joints and controlling assisting forces. These are not prerequisites for an enhancing exoskeleton. As such there is no known research that tackles the problem of an enhancive exoskeleton for a full-body application which entails the optimisation of link lengths, degrees of freedom and joint locations with respect to the human workspace and the exoskeletons interaction with the user.

3.2.1 Limitations in Current Research

The enhancive full-body exoskeletons are not designed taking into consideration specific tasks, therefore underlying understanding of the structure mimicking human movement is not developed, meaning:

1. Full-body enhancive exoskeletons have been designed based on a semi-anthropomorphic geometry. Therefore, optimal power consumption of the exoskeleton in terms of lengths of links for specific tasks have not been considered.
2. The relationship in terms of power consumption between the effects of link masses and external work load has not been developed.
3. As an extension to, and combination of, 1 and 2 above, the effects of actuators masses on power consumption during an optimization of link lengths is also not considered.
4. Though CGA data has been used as a design basis for BLEEX scalable design methodology and some motions being simulated for the design of the BE to verify COM, the methodologies so far have not incorporated any human motion trajectories as the basis of their design as control input to the exoskeleton.

These four points are gaps in the current enhancive exoskeleton knowledge that this research will focus and expand on. The following sub-sections will expand

on these topics in order to present a design theory, postulations and a methodology.

3.2.2 Alternative Representations of Degrees of Freedom

By considering the equations that represent the human enhancive exoskeleton interaction system's kinematic chain represented in Figure 3.1, some insight is found into how to minimize the degrees of freedom (DoF) required.
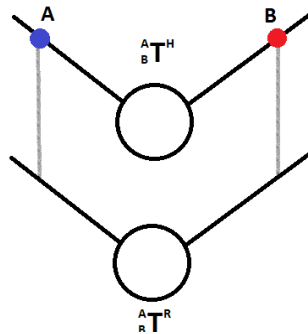
Figure 3.1 - An arbitrary human joint represented by T^H linked to a robotic joint T^R connected at two points A and B

The link between human and machine from point A to point B can be equated shown in Equation 3-1.

$${}_{B}^{A}T^{H} = {}_{B}^{A}T^{R}$$

Equation 3-1

Where the robot transformation expression can be known, shown in Equation 3-2.

$${}_{B}^{A}T^{R} = {}_{n}^{A}T^{R}\,{}_{m}^{n}T^{R}\,{}_{B}^{m}T^{R}$$

Equation 3-2

${}_{m}^{n}T^{R}$ is the transformation of the joint being represented. ${}_{n}^{A}T^{R}$ and ${}_{B}^{m}T^{R}$ are shown in Equation 3-3 and Equation 3-4 respectively. They are the required joints needed to mimic the human motion.

$${}_{n}^{A}T^{R} = \prod_{A=0}^{n-1} {}_{A+1}^{A}T^{R}$$

Equation 3-3

$${}_{B}^{m}T^{R} = \prod_{m}^{B} {}_{m+1}^{m}T^{R}$$

Equation 3-4

Note that:

$$A, \ldots, n-1, n, n+1 = m,\ m+1, \ldots, B$$

Equation 3-5

The transfer functions $^A_nT^R$ and $^m_BT^R$ are both unset. If $^A_BT^H$ = simple rotation, then both $^A_nT^R$ and $^m_BT^R$ will be identity matrices.

The human transfer function is however significantly more complex as it represents a joint (Vitiello *et al.* 2013). Joints of each human create a trajectory of the bone which is unique. The complexity is also partially due to several degrees of freedom in a single joint.

The transfer functions motions can be represented as the trajectory of a point B with respect to point A, shown in Equation 3-6.

$$^A_BT^H = f_A(\alpha, \beta, \gamma, x, y, z)$$

Equation 3-6

Note:

α, β, γ are rotations about x, y and z axis; x, y, z are translations along x, y and z axes.

The motion of two links created by a single human joint can be represented as a 6 DoF joint, 3 translations + 3 rotations as it moves two links in 3D space relative to eachother. When the motion is constrained to a 2D plane, the same joint will have a motion represented by 3 DoF. 2 DoF will locate the end point of the link in the correct location and the third DoF will ensure the orientation of the end point is correct. This can be in the form of: 2 translations and 1 Rotation, 1 rotation and 1 translation and 1 rotation or 3 rotations only, as seen in Figure 3.2.
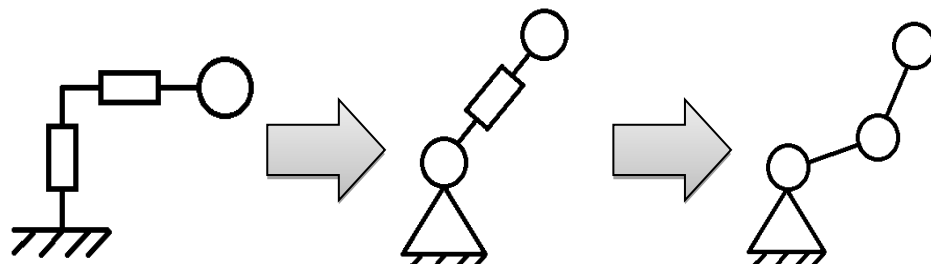
Figure 3.2 - 3 DoFs represented in one plane of action in several ways, rectangles are translational joints and circles rotational

If several links would be connected via such 3 DoF joints their end positions with respect to the base could still be represented by a 3 DoF joint as seen visually in Figure 3.3.
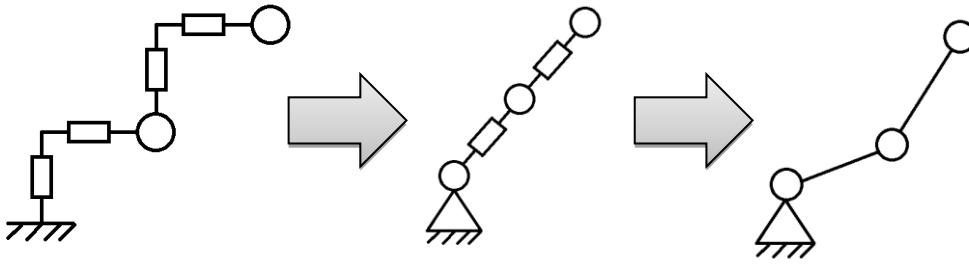
Figure 3.3 - Visual comparison between Multiple DoF in a plane and
the minimum DoF needed to represent the same motion

It is evident that the same orientation and position in space can be represented by 3 DoFs if only the end effectors are concerned. This is the key difference in enhancive and assistive exoskeleton design. It is therefore reasonable to assume that there might be a structure that has a complex chain of links and joints, such as the spine, but this could be minimized to a smaller representation.

3.2.3 Task Motion Specific Design

Tasks can be broken down into a set of motions (or actions) such that the cost of the task can be minimized or maximised with respect to one or many parameters. For example, the task of picking up a box and dropping it off elsewhere, could be subdivided into smaller motions:

1. First motion, walking to the box
2. Second motion, picking up the box
3. Third motion, walking with the box
4. Fourth motion, placing the box

Unless the set of tasks is clearly defined the solution will be of some general form and can become over or under engineered. This particularly holds true for the assistive and rehabilitation exoskeletons as they operate intimately with the user. The same may not hold so true for some enhancive exoskeletons. BLEEX, although classified as an enhancing exoskeleton, is a highly task specific system, where the analysis is made on assumptions of scalability based on actual joint data. Methods of changing link-length dimensions, for example, would not be feasible. It may be the case that the BE and the XOS-2 fall into a larger domain where a vast array of tasks needs to be performed. Yet motion, in the case of BE, is only used for verification. It should be noted that it is unclear if the motion of BE is derived from human motion data.

Looking at the human performing certain motions and mimicking the conditions of them for an exoskeleton will limit the exoskeleton to the human performing said motion/s. Thus, to design an exoskeleton for the human, as generally as

possible, this 'generality' needs to be defined in such a way that a wide enough spectrum of human performances as possible can best be encompassed. Therefore, a singular motion cannot be looked at as a foundation for a fully capable exoskeleton design. Singular motions can however be used as measuring and comparison tools, for example in user power increase vs. energy consumption.

It can be assumed that some optimal structure may vary depending on the task. As an extension to this, the optimal structure of a full-body enhancive exoskeleton designed to perform several tasks or motions may not be an anthropomorphic one, if there is a distinct primary motion.

3.2.4 Design Theory and Postulations

From these observations a general theory of optimal enhancive exoskeleton design structure arises. An enhancive exoskeleton robot whose purpose is to mimic and enhance the user motions can be designed by finding an optimal configuration of joints and link dimensions such that the same task is performed as far as the trajectories of the connecting points between the exoskeleton and the human are concerned. This theory is subdivided into the following four postulations:

First postulation: Within a pre-defined space, confined by a group of peripheral points (points on the border of that space), that are connected to one another via a common point (or way-point) that is not peripheral with some number of links and joints in succession, there may be an optimal configuration of number of these links and joints that will minimize the cost of movement of the combined structure for a set of given tasks.

Second postulation: By similarity, it should also be true that for an enhancive exoskeleton robot where the peripheral points are the extremities of the robot that are connected to the human and the way point is also connected to the human but in between the peripheral points, there may be an optimal structure not akin to the human for the set of given tasks it is expected to perform.

Third postulation: For the first postulation to be true it must have no less than two peripheral points and one way-point and for the second postulation, being a derivation of the first must have no less than four peripheral points and one-way points for a healthy human being.

Fourth postulation: For the second postulation to be feasible a practical criterion must be met. The robot must not obstruct the users natural motion, and nor must it interfere with the user.

3.2.5 Design-Space and Design-Variables of Enhancive Exoskeletons

From the previous sections it can be seen that the design of an enhancive exoskeleton can be viewed as a shape optimization problem inside a contrained dynamic space, a design-space. The design-space is defined around the user. The exoskeleton should not interferere with the user, the users body is therefor the minimum boundary where the exoskeleton can exist. The exoskeleton needs to interactive with the user at certain points, and therefor there are some locations where exoskeleton needs to exists.

As mentioned the design-space is dynamic, this is an inherited property of the user, as the user moves the design-space alters shape, it can therefor be said that the design-space is dynamic and/or a function of the tasks the user is intented to perform in the exoskeleton the greater the number of defined tasks the user is intended to perform in the exoskeleton, the greater the dimension of the design-space. It can be argued then that an exoskeleton that is not designed to a certain task, should have a design space that is infinite in dimension as it must allow for all possible motions the user can perform. This is however a topic beyond the scope of this thesis.

The design-variables of the exoskeleton, for the shape optimization in this research, are identified to be the shapes of the links. Specifically this would mean the lengths. The bulkiness of the system is also a design-variable, which at component level is represented by the the cross-section geometry of the links.

Other design-variables which effect the design of the chassi for enhancive exoskeletons include actuation type and method (effects of actuation in exoskeleton design can be read in APPENDIX F). Having direct drive or remote location could effect the structure of the links. Similarly if the actuation type is lnear or rotary can also effect the design of the links and exoskeleton joints. Also, the selection and shape of sensors and their locations and cabling on or through exoskeleton links impose constraints which can be translated to design-variables. These are considered higher level design variables which are beyond the scope of this research. This research will focus only on the link-length and cross-section geometry as design-variables and it is left for future work to integrate sensory and actuation knowledge into the design methodology, presented below.

3.2.6 Proposed Design Methodology for Inclusion of Optimization of Link Parameters

The proposed design methodology for the exoskeleton design with focus on link geometry dimension optimization is presented in Figure 3.4. The design methodology presented here is focused on incorporating the link optimization into designing an enhancive exoskeleton. The segments are related to the chapters in this thesis as follows:

- Core Motion and Optimization Analysis
    - Obtain Trajectory Data (motion capture) (Chapter 4)
    - Analyse and Filter Trajectory Data (Chapter 4)
    - Model Definition and Generation (Chapter 5)
    - Optimization of Model (Chapter 5 and Chapter 6)
- Exoskeleton Component Design
    - Design of Components (Chapter 7)

Building and testing of components for the greater research project is mentioned in APPENDIX H and the future works section in Chapter 7 the usage of this research is discussed in context of adding component design in the design loop. This thesis is not concerned with the manufacturing and assembly of the exoskeleton in the design methodology.

Figure 3.4 – Proposed sequence of the design methodology for the enhancive exoskeleton design with focus on link geometry dimension optimization for specific tasks. The process starts with the gathering of relevant trajectory data and ends with component design before manufacturing, assembly and testing.

Taking a closer look at the optimization segment and expanding it, shown in Figure 3.5 the process of selecting components by informed model data presents itself. By first optimizing the links without external considerations during loaded conditions, key components can be selected. The inclusion of external design elements, i.e. selection of fundamental components based on optimization and known data (this research will be limited to bearings and actuators) will then yield results which will further inform the designer of the correct link parameters needed to be considered.
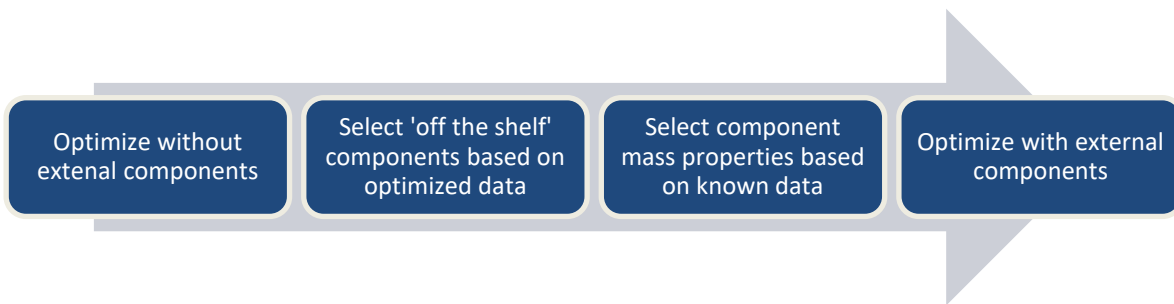
Figure 3.5 - Optimization segment of this methodology expanded, the initial starting point is to optimize the exoskeleton without any consideration of the material properties, locations and effects of external components such as, bearings, sensors, cabling, actuators, ECU's etc. The data obtained will be used together with already known data or estimated data from known research to select basic off the shelf components whose properties will be considered when rerunning the optimization.

The optimization segment could potentially be altered such that it becomes an iterative element within the sequential design methodology. The optimization process would then be as shown in Figure 3.6. The process would start with an optimization of the model, the data would be used to select or alter the appropriate components, the model would then be rebuilt and re-optimized. This would continue to some given iteration tolerance or a satisfactory result is obtained.
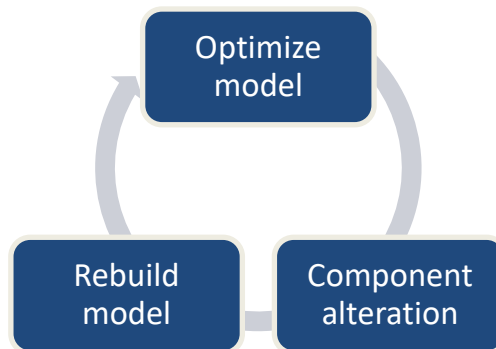
Figure 3.6 – Iterative optimization segment flow chart. The process is the same as in Figure 3.5 with the exception that the process is repeated such that the components selected are also updated in each iteration to satisfy the torques and reaction forces at the link joints.

3.3 Simulation Environment

When the relevant trajectory points from the motion capture have been analysed and a description of the model has been established, a method of finding the inverse kinematics of the model becomes required. This is because part of the goal of this work is to identify the effects when changing the link length parameters in the exoskeleton. Previous works have had a static description of the model they have been developing (Marcheschi *et al.* 2011). In some cases, the system kinematics have been likened to that of a human (Kazerooni and Steger 2006). Intuitively, once the link lengths change one would expect this to change as well and therefor the new kinematics need to be derived.

To assess two methods (analytical and numerical) of inverse kinematics most applicable to this case, a simple two link planar model with revolute joints is looked at. As a double pendulum, the subject is greatly studied. First, the forward kinematics of the simple model is derived, then Maple's analytical method is used to obtain inverse kinematic expressions for the system. The analytical results will also be used in Chapter 5 when analysing gradient and smoothing methods for derivation of velocity and acceleration data. Following this MATLAB's vpasolve function is explored for obtaining the inverse kinematics solutions by numeric methods. The detailed analysis and the comparison between Maple and MATLAB model can be found in APPENDIX M.

Using the numeric approach removes the mathematical hurdles but presents a time cost problem. The specific method used in MATLAB, vpasolve function, may, as seen, require an unknown amount of iterations to find the second solution.

As for the difference in the results using the two various methods, the order of magnitude is no greater than 10^-6.

3.3.1 Kinematics Model Equations of Two Link System

Kinematic equations for a two-link model relating the joint angles to the end effector position are shown in Equation 3-7 and Equation 3-8.

$$Dx = Px + L_1 \cos(\theta_1 + k_1) + L_2 \cos(\theta_1 + k_1 + \theta_2 + k_2) \qquad \text{Equation 3-7}$$

$$Dy = Py + L_1 \sin(\theta_1 + k_1) + L_2 \sin(\theta_1 + k_1 + \theta_2 + k_2) \qquad \text{Equation 3-8}$$

Equation 3-9 and Equation 3-10 are the results when the frame of reference is rotated 90 degrees counter clockwise for k_1 and remains 0 for k_2.

$$Dx = Px - L_1 \sin(\theta_1) - L_2 \sin(\theta_1 + \theta_2)$$

<div style="text-align: right">Equation 3-9</div>

$$Dy = Py + L_1 \cos(\theta_1) + L_2 \cos(\theta_1 + \theta_2)$$

<div style="text-align: right">Equation 3-10</div>

This change in reference frame is performed so that the change in the two-link systems first joint is analogues with the ankle and is measured from 0 when standing straight, similar to the human standing. This will ease comparison with literature and with experimental motion capture data performed for this research.

3.3.2 Hybrid Inverse Kinematics

The two methods can be used separately and both have their strengths and weaknesses. To compensate for eachother a hybrid algorithm can be written to solve for the inverse kinematics if and only if the analytical equation returns undefined answer.

Due to the decision from the University of Leeds and MechaTech to not proceed with Maple and MapleSim solution this research will use the numeric method of calculating the inverse kinematics.

3.4 Discussion

3.4.1 Design Paradigm

The four gaps in the current research highlighted in this chapter can, for full-body enhancive exoskeletons, be argued to be artefacts of limited research in the field. But can also, as in the case of XOS-2, be a result of patent being chosen over publication. It remains, whatever the case, that alternative optimized link-length full-body exoskeleton structures have not been researched. In the case of BE the justification is that similar anthropomorphic structure at kinematic level will yield in similar CoM at full structure level, furthermore, that this is crucial in the design of an exoskeleton in terms of its control by validation through ZMP. Although a sound hypothesis which was proven for the BE, the question remains if this is true for a higher level of task specificity full-body exoskeleton designs.

Though the goal of this research is not to investigate the difference in enhancive and assistive exoskeletons, it shows itself in the broad overview of the mathematics behind the kinematics or transformation matrix notation analysis of two connected chains, where one is the human and the other the robot. It has been shown that indeed any two points connected via a complex structure can be represented as a relative trajectory between the points for a given motion and that this can be followed by a minimized set of joint-link numbers. Therefore, the kinematic chain can be reduced and thus decreasing complexity. For an exoskeleton however, this alone does not mean that the minimization is an optimum as the design still needs to consider obstruction to the user, which is a criterion identified in previous research (Kazerooni and Steger 2006; Lucchesi *et al.* 2010). This does however yield credence to research the variety of link-lengths for exoskeletons as a precursor to optimal joint locations/orientations, types and combinations.

Research in task specific exoskeletons has previously used CGA data as the basis for the structural design (Kazerooni and Steger 2006). Verification of designs has also been done using simulated motions (Lucchesi *et al.* 2010). However, kinematic data has not been directly used as input signals to a model, whereby the model is forced to adapt its shape to said inputs. As mentioned in section 3.2.3 the optimal structure of a full-body enhancive exoskeleton may vary from anthropomorphic one if it is task or motion biased. Using the trajectory data as input signals for the optimization would allow for finding this optimal structure by simulation.

The human enhancive exoskeleton design paradigm takes shape in the form of a design theory, which is presented with four postulations based on the gaps found from the literature review. The design postulations state the need of having certain points which are in the case of the enhancive exoskeleton connected to the human such that the exoskeleton performs the same tasks. There are criterions for number of these connection points and for non-interference with the human. No criterion for balance is presented, as a falling exoskeleton technically is performing the motion of falling when the user is not, therefor it is not satisfying the second postulation.

The key variables that this research will focus on are identified alongside and as an extension to an explanation of the design-space in which the exoskeleton can be defined in. The design-variables are link lengths and cross-section geometry. Although other variables could be considered which are results or more detailed designs This research will focus on using the two mentioned. Other variables are considered too dependent on other components, actuation systems, sensory systems and cabling.

To aid the workflow a sequential design methodology with potential iterative elements is also presented. The focus of the design process is the optimization. The methodology will be the procedure which will be used in this research to investigate and analyse the design theory and postulations.

3.4.2 Simulation Environment

The Inverse kinematic approach for finding the joint trajectories for planar case is developed. Two methods, symbolic and numeric, using Maple and MATLAB are compared to eachother. It is found that the time taken to derive the inverse kinematics for two-link planar system, is faster by first deriving the inverse kinematics using the symbolic approach and substituting the values. However, the issue of denominators arises which demands extra consideration.

It can be speculated that the analytical approach might not always be feasible as the complexity of the equations increases when the system is larger (in terms of unknown joint variables). However, as will be shown in Chapter 5 by breaking up the exoskeleton into segments the overall complexity, as far as the kinematics is concerned, is decreased considerably.

3.5 Summary

The chapter reviewed the gaps and limitations found in the literature review in the current research. Specifically, four limitations where presented; the semi-anthropomorphic designs of full-body enhancive exoskeletons not being optimized to power consumption for specific tasks; relationship between power consumption, link-masses and external load; the effect of actuator mass on power consumption during link-length optimization; and the utilization of human motion trajectories as inputs for the exoskeleton models.

It is shown through transformation notation that the simplified robot structure can follow motion trajectories of a more complication human structure. Furthermore, that the trajectories that the robot will follow, namely the human tasks, can be subdivided into motions. It is also discussed that an optimal structure confined by the trajectories which are used as inputs (and therefor govern the model) may be different than that of an anthropomorphic enhancive exoskeleton.

The design theory is presented as: An enhancive exoskeleton robot whose purpose is to mimic and enhance the user motions can be designed by finding an optimal configuration of joints and link dimensions such that the same task is performed as far as the trajectories of the connecting points between the exoskeleton and the human are concerned. Four postulations which will be used as guidelines to aid the design are also presented. The first regarding the optimality of connected links in a structure with peripheral points and some midpoints (way-points), the second postulation relates the first postulation to exoskeletons specifically by connecting the peripheral and way-points to human interaction points, the third presents a minimal condition for the number of points and the fourth is a non-collision constraint for the second postulation.

A methodology is presented which will be the basis for the thesis structure and how the research is conducted, as a process of verification of the theory and the postulations.

The simulation environment is discussed. To simulate the model, which will be changing, there is a need to find the inverse kinematics of the equations of the exoskeleton which can be found for example by the transformations presented in 3.2.2 Alternative Representations of Degrees of Freedom. Maple and MATLAB are looked at as platforms for this work. Maple, for its analytical engine, and MATLAB for its numeric methods. When comparing the two it is found that there are in some instances issues with using analytical methods, for example the equations might return undefined results. Numeric solvers do not have this

problem, however present a higher cost in time. Furthermore, it possesses a potential overhead as the function used in MATLAB to solve the inverse kinematics may return the same result, forcing an iterative approach to rerun the function until all solutions are found.

Some hybrid solution would seem to be the best approach but this research is limited to the use of MATLAB on the basis of decisions outside the control of the research.

Chapter 4
Motion Capture and Ground Reaction Force Pilot Study and Analysis of Planar Motion Data

4.1 Introduction

This chapter focuses on the motion capture pilot study. This study is used in this thesis but was developed for use in the entire high powered enhancive exoskeleton project at University of Leeds, which this PhD is a part of. As such the purpose of the study is broader than just for the work presented here.

The work was carried out to obtain marker trajectories during certain motions. This will be used to simulate the trajectories the exoskeleton is expected to follow. The work that will be presented here will also be used as a means to verify that the motions agree with clinical data, such as gait. As an extension beyond this however the data will contribute motion capture and ground reaction force data to the scientific community, albeit in the form of a pilot study.

First the protocol of the pilot study will be outlined, the ethical approval required to perform the study can be found in APPENDIX G. This is followed by an overview of the software used to extract and post-process the data. The methodology used to build the motion capture model is described and the motions are shown with visual still-images. The filtering method used for motion capture data is also presented together with the found cut-off frequencies for each joint. The filtered and time-normalized data for the joint angles as well as relevant marker and joint location trajectories are presented in this chapter. The full filtered results of the motion capture data can be found in APPENDIX N.

This chapter will introduce the methodology for analysing the motion data of points derived from the motion capture. The aim is to simplify the model being built to such a degree that interaction points between the exoskeleton and the world become manageable for usage in the simulation environment.

Firstly the trajectory of relevant points will be looked at and static periods identified in order to simplify the model. Second, methods of signal filtering, derivation and smoothing will be considered to remove signal noise and spikes. Third, an appropriate workflow will be established for derivation of angular velocity and acceleration from the inverse kinematics results, by comparing the order in which smoothing and signal derivation will occur. All of this will be

performed on a sample example of the data obtained in the motion capture pilot study. Finally the work will be discussed and summarised.

4.2 Motion Capture Protocol

4.2.1 Purpose

The purpose of this experimental study for this thesis is to:

- develop a 3D human model to be used for proof of concept evaluation of the effects of design parameters of a full-body modular power enhancing exoskeleton.
- optimize the design parameters with respect to the motion data gathered and human model generated
- collect motion capture data for justification purposes of manufacturing of prototypes and validation of physical experimental results

4.2.2 Materials and Equipment

In order to measure the 3D kinetics and kinematics for the test subject the following items was required:

- 13 camera motion analysis system (Qualysis).
- 2 force plates integrated into the floor
- Reflective markers
- Visual3D software for inverse dynamics and data analysis
- 1 healthy male has participated in te study to perform tasks outlined in Table 4-2. The subject is 182 cm tall and weighs approximately 95 kg.

During the experiment various tasks required the use of mock equipment to simulate real life interaction scenarios, such as opening doors. These are given in Table 4-1 with the corresponding unique identifier of the task they are used with. The unique identifiers are used in the exoskeleton project as a standardised method of identification.

Table 4-1 – Table of equipment built for use in motion capture experiment

No.	Equipment	Associated Task	Unique Identifier
1.	Valve stand	NA-43, NA-44	NE-1
2.	Door stand	NA-42	NE-2
3.	Box load[1]	NA-40, NA-11, NA-45, NA-22, NA-54	NE-3
4.	Cylindrical load[2]	NA-53	NE-4
5.	Small diameter cylindrical swing item[3]	NA-55	NE-5
6.	Chair without wheels	NA-56	NE-6

4.2.3 Methodology

Testing took place in the biomechanics laboratory, Faculty of Biological sciences. The procedure took approximately 4 hours. During the motion capture the subject wore shorts that do not cover the thigh, shoes and upper garments are not to be worn. Reflective markers (used for motion tracking) was placed on the subject following the recommended marker placement found in Figure 4.1.

The usage of one healthy subject for this pilot study was deemed satisfactory as the goal is to prove the design methodology explained in Chapter 3. As such the impact on the design when considering a greater is considered future work which will build on the optimization algorithm in this thesis.

The markers placed on the subject facilitate two functions and are divided therefor into two groups: individual and clusters. Individual markers are placed on anatomical key positions for geometry definition. Clusters are placed on top of the segments to track movements (position and orientation) and are attached on the subject as bands with plates of four markers as well as on the head wear.

---

[1] 2 different shapes of loads: 1) large – 120 cm x 80 cm x 80 cm empty cardboard box, 2) medium – 61 cm x 46 cm x 46 cm empty cardboard box
[2] A cylindrical cardboard and wood tube of dimensions: 30 cm in diameter x 1 m long
[3] A wooden cylinder of dimensions: 5cm in diameter x 1 meter in length

Figure 4.1 – Motion Capture marker placement on the test subject, cluster markers seen attached to the arms and legs of the subject are used for segment orientation.

4.2.4 Procedure

The procedure of the experiment is outlined below:

1. The motions are reviewed with the subject and a trial of each motion is performed within the testing environment (approximately 20 minutes).
2. The markers are placed on the subject according to the placement arrangement described in Appendix B (approximately 30 minutes).
3. The motion capture system will be initialized including the force platforms (approximately 10 minutes).
4. The height and weight of the subject is recorded (approximately 5 minutes)..
5. The technician starts the recording.
6. The subject performs given task.
7. The technician stops the recording and saves it
8. Steps 5-7 are repeated for the activities outlined in section 4.2.5 each repetition should take no more than 1 minute. Three 15 minute breaks are allocated and spaced out evenly during the recoding process.

4.2.5 Activities

The activities performed are shown in Table 4-2 and are derived from the Customer Needs Document.

Table 4-2 – Table of activities to be captured during motion capture experiment

No.	Activity	Unique Identifier
1.	Walk on level ground forwards	NA-1
2.	Walk on level ground backwards	NA-30
3.	Turning 90 deg whilst walking	NA-34
4.	Run forwards	NA-3
5.	Pick up load from ground (deadlift)	NA-40
6.	Walk on level ground with load forwards	NA-11
7.	Walk on level ground with load backwards	NA-45
8.	Walk on level ground whilst crouching with load	NA-53
9.	Turning 90 deg with load whilst walking	NA-46

10.	Lift load above shoulder height from hip level	NA-22
11.	Lift load to shoulder height from hip level	NA-54
12.	Swing arms from above head downwards holding a cylindrical object ending at hip level. Performed at angles (from sagital plane) 0 and 45 degrees with arms above head, and 90 degrees swinging from one side and ending at the other.	NA-55
13.	Turning valves horizontally	NA-43
14.	Turning valves vertically	NA-44
15.	Get up from a fallen position laying on stomach	NA-39
16.	Walk on level ground – sidestep	NA-31
17.	Opening doors	NA-42
18.	Vertical jump from standing pushing with two legs	NA-47
19.	Sitting down on chair and getting up	NA-56

4.2.6 Motions Results

The motions used from the pilot study in this research are limited to NA-1 (walking on level ground forward, 'Simple Gait'), which will be used as a gauge to compare the subjects gait with already established clinical data to verify the experiment. It will also be used for the purposes of developing and illustrating Interaction Point Trajectory Analysis and Trajectory Simplification From Motion Capture Data in Section 4.5 . The two motions NA-40 ('Object Lifting' - pick up load from ground) and NA-54 ('Object Raising', lift load to shoulder height from hip level) are chosen as they are representative of human lifting activites and interactions with loads. NA-40 due to it predominantly using the legs and NA-54 due to it predominantly using arms. Therefore the analysis will be done on tasks which correlate with the motivations and scope of the grander exoskeleton project explained in Section 1.2 Motivation. Therefore only the results from these motions will be presented and discussed in this thesis.

The number of trials for the three selected motions can be seen in Table 4-3. The filtered results which are relevant to the simulation and model generation will be presented in the following sections.

Table 4-3 – Number of trials for selected motions

Motions	NA01 – Walking	NA40 – Object Lifting	NA – 54 – Object Raising
Number of trials	5	3	2

4.3 Motion Capture Software and Signal Processing

The motion data is collected using Qualysis and post processed using Visual3D. The raw results of the Visual3D model is then further processed on MATLAB. Using Winters residual analysis the cut-off frequencies are found.

In this section the software used for data extraction and post-process will be reviewed. The model generated in Visual3D will be presented and the Winters residual analysis explained before presenting the filtered motion capture results.

4.3.1 Qualysis and Visual3D v6

Qualysis motion capture technology allows for recording of motion data. It uses cameras that pick up marker positions for motion capturing. The motion data is collected using Qualysis track manager, the software can be integrated with force platforms to collect ground reaction force data.

Visual3D v6 is an analysis tool for biomechanics measurement of movement and force data. Visual 3D is compatible with the motion capture and force data collected from Qualysis. It contains the necessary tools for kinematic and kinetic calculations.

Using Visual3D a model can be built from the data that has been tracked with Qualysis. There are various methods of building models using motion capture data depending on which marker combinations are used and the purpose of the model. The model was developed using the marker guidelines found in Visual 3Ds marker guidelines help page (C-Motion) in conjunction with expert advice from Dr. Niel Messenger, Lecturer in Biomechanics at the School of Biomedical Sciences at the University of Leeds.

4.3.2 Motion Capture Model and Motions

The first segment created in the model is the hip. The relevant markers can be seen in Figure 4.2. With the creation of this segment virtual markers for the hip joints are also made. Following this the segments for the legs can be made in succession. The thigh segments markers are shown in Figure 4.3. Using the Medial and Lateral Condyle markers seen in Figure 4.1, the virtual knee joints are created. Figure 4.4 shows the marker setup that is required to create the shank segments.
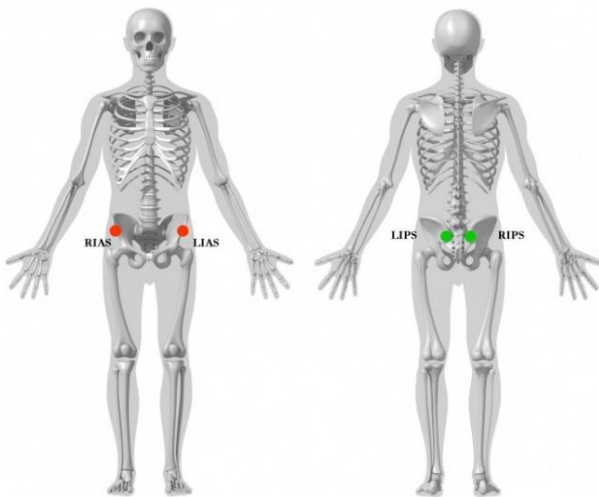
Figure 4.2 – Marker guideline for pelvis (Coda). Although not shown in the figure the generation of the Coda pelvis creates landmarks for virtual hips which is used when generating the thigh segments
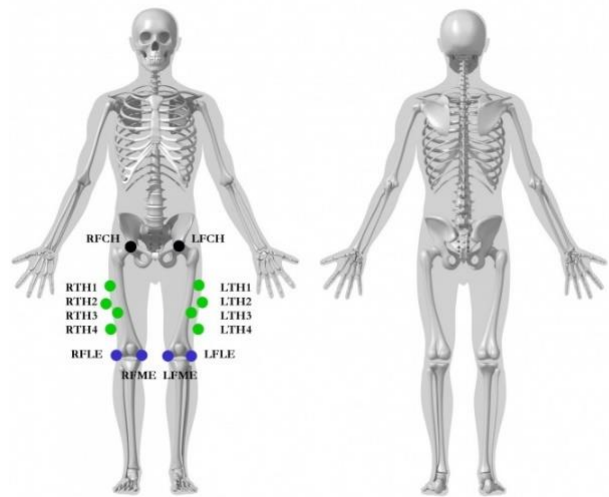
Figure 4.3 – Marker guidelines for the thigh segments. The Hip virtual joints are created when the hip segment is created. The RFLE, RFME and LFLE LFME are equal to the Medial and Lateral Condyle markers in Figure 5.1 and are used to create the virtual knee joints
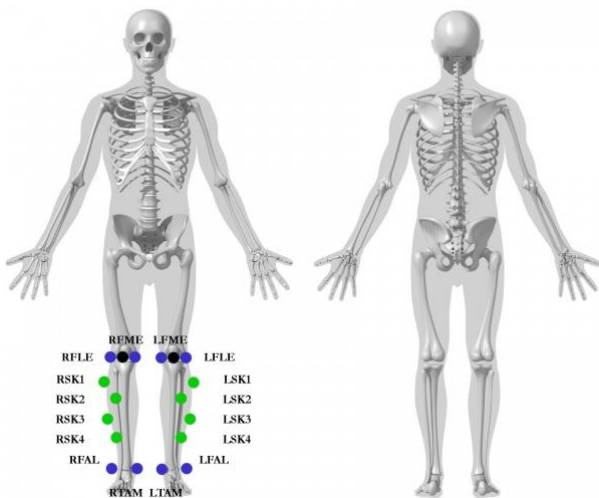
Figure 4.4 – Marker guidelines for shank segment. Using the virtual knee joint the shank segments can be created.

The remaining segments are created referring only to Figure 4.1.

The foot segment is created by first creating a virtual ankle joint with the malleolus medial and lateral markers. Furthermore a toe joint marker is created using the calcaneus posterior the 5th distal, the 1st distal and the foot marker. The foot segment can now be created using the virtual ankle and toe joints in conjunction with the 5th distal (to define the orientation of the segment) and the 1st and 5th distal, posterior calcaneus and foot markers for tracking the segment.

In order to create the arm and the thorax/abdomen segments certain joints virtual joints need to be created first. The shoulder joints use the acromion posterior and coracoid markers. The virtual elbow joints were created using the lateral and medial epicondyle markers. The virtual wrist joint was created by using the ulnar wrist and radial wrist markers.

The Thorax/Abdomen segment is created using the shoulder and hip virtual joints. The shoulder joint markers, the C6 marker, the left and right acromion superior markers and the left and right sacrum markers are used for tracking the segment

The upper arm segment is created using the virtual shoulder markers and the epicondyle markers in conjunction with arm marker clusters seen in Figure 4.1. The forearm segments were created using the virtual wrist markers and the epicondyle markers. The hand segment is created using the ulnar wrist, radial wrist and the hand markers.

4.3.2.1 Motion Capture Still Images and Coordinates

Though there were several trials to capture statistic data for the pilot study, one recording from each of the trials has been used to capture still images capturing the essence of each motion. Figure 4.5 shows the finished calibrated model with all the segments represented as general geometric shapes. Figure 4.6 shows the key events in the 'Simple Gait' motion. Figure 4.7 shows the key events in 'Object Lifting' motion. Figure 4.8 shows the key events in 'Object Raising' motion. It should be noted that for 'Object Lifting' a box was used with minimal weight (approx. 2kg). This was not used in 'Object Raising' instead a stick was used to force the arms to stay equidistant.

As the joint angles of interest in this research are the ones corresponding to a planar (sagittal) rotation, the results shown in the 'Motion Capture Data Results of Simple Gait, Object Lifting and Object Raising' section below are all joint angle data about the local x-axis (red axial line in graphs below). As explained earlier the relevancy of this is due to the 2-D scope of this research.

The data captured in the motion capture lab follows the coordinates of the lab seen clearly in Figure 4.6, Figure 4.7 and Figure 4.8 on the ground. In order to capture ground reaction force data from both feet in all three movements, the force platforms (represented by white rectangles on the ground in the images below) were kept in the same location. The subject however rotated 90 degrees when performing 'Object Lifting' and 'Object Raising'. This negated the cumbersome task of relocation and recalibration of the laboratory equipment. It does however mean that the coordinates of the results for 'Simple Gait' landmark data corresponds as following: x-axis is the lateral movement and y-axis is the horizontal movement. For 'Object Lifting' and 'Object Raising' the coordinates correspond as following: x-axis is the horizontal movement and z-axis is the lateral movement.
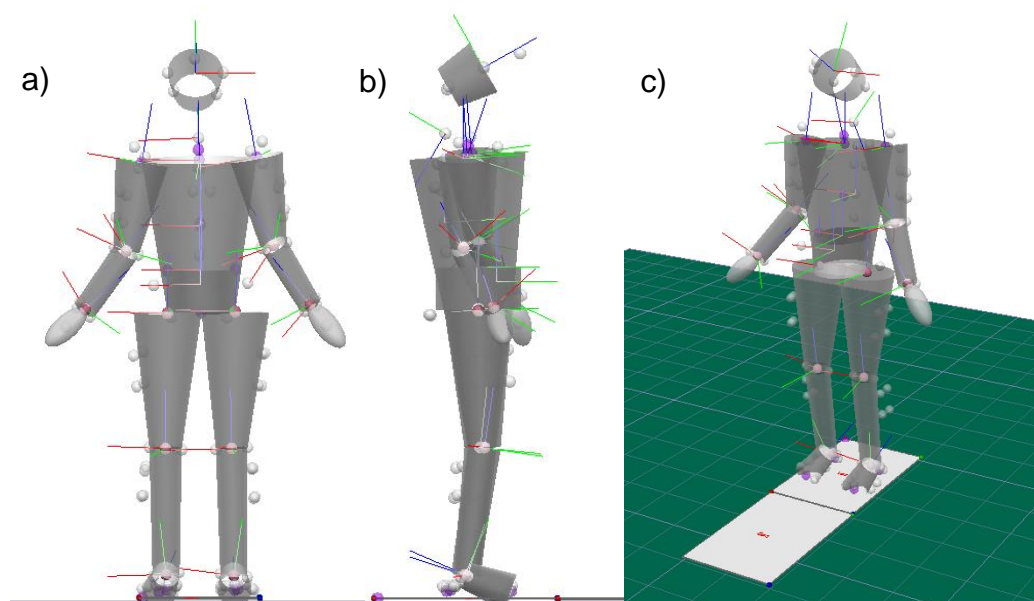
Figure 4.5 – the calibrated model used for motion capture data. The segments are represented by geometric shapes, a) frontal view, b) sagittal view and c) perspective view, showing the two force platforms.

54
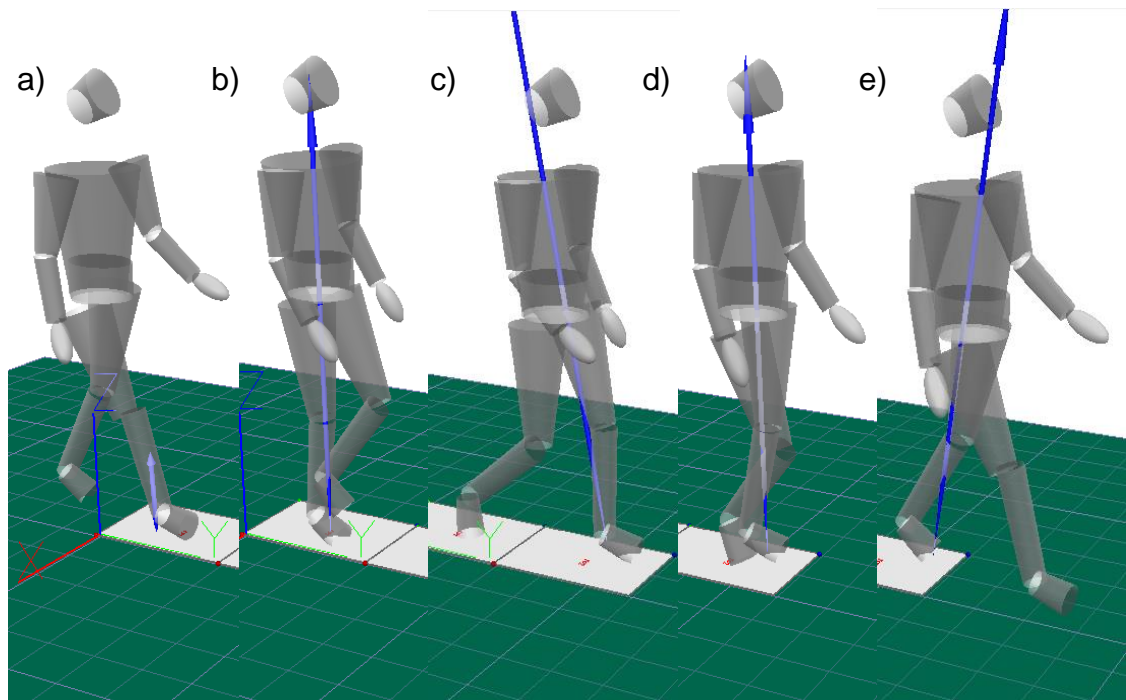
Figure 4.6 – Stills from the motion NA01 'Simple Gait', in perspective view. The blue arrow showing the vector force from the force platforms. a) initial heel strike, right leg, or heel on (platform), b) swing phase for left leg, midstance, c) heel strike, left leg, d) swing phase for right leg, midstance, e) prior to toe-off from force platforms for left leg.
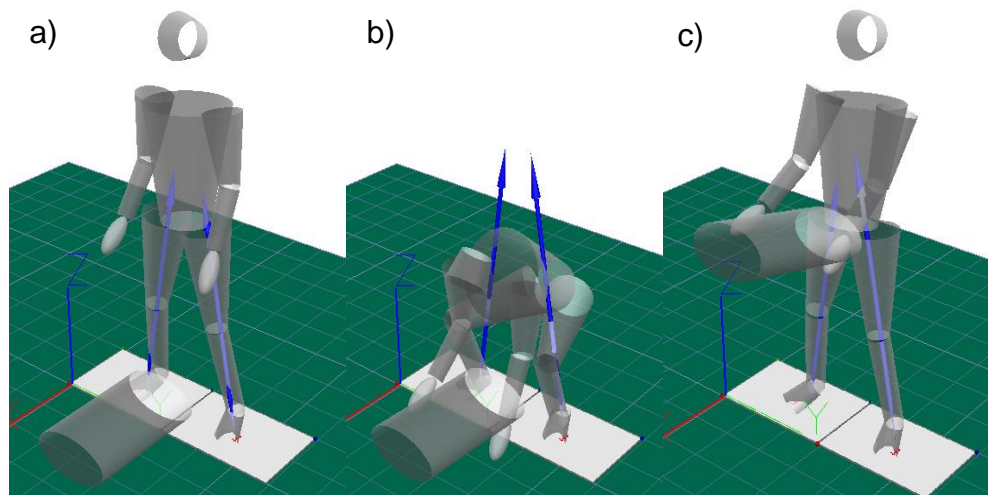
Figure 4.7 – Stills from the motion NA40 'Object Lifting', in perspective view. The blue arrows showing the force vector from the force platforms. a) stance without load, where the subject is standing in position ready to commence, b) fully squatted, grabbed the object to be lifted, c) loaded stance, where the subject is standing straight again but with object in hands. The motion cycle is repeated but with the object being placed back on the ground and subject returning to stance without object.
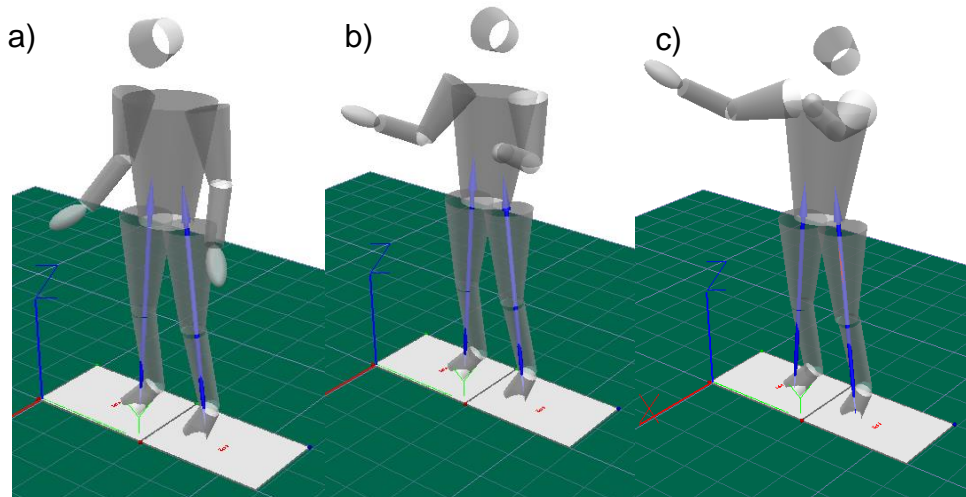
Figure 4.8 – Stills from the motion NA54 'Object Raising', in
perspective view. The blue arrows showing the force vector
from the force platforms. a) stance with object (not included in
simulated environment) in hands, where the subject is standing
in position ready to commence, b) mid-lift, object is being raised,
c) raised stance, where the subject is standing straight with
object raised out. The motion cycle is reversed but with the
object being lowered.

4.3.3 Winters Residual Analysis

The raw results of the motion data undergoes a filtering to remove noise utilising a method known as residual analysis, developed by Winter (Winter 2009b). The method is used to find the cut-off frequency (fc) for the motion capture data using Equation 4-1. By performing a residual analysis of the difference between filtered and unfiltered signals over a wide range of cut-off frequencies the fc can be found, this is shown in a theoretical plot in Figure 4.9.

$$R(f_c) = \sqrt{\frac{\sum_{1=1}^{N}(x_i - \hat{x}_i)^2}{N}}$$ Equation 4-1

Where

R = Residual

N = Maximum number of samples

f_c = cut-off frequency of the fourth-order dual-pass filter

x_i = raw data at i[th] sample

$\hat{x}_i$ = filtered data at the ith sample using fourth-order zero-lag filter

The choice of cut-off frequency using the residual analysis method can be made by plotting a line which represents the noise residual to the residual axis, point a. From point a, a horizontal line is projected to intersect the residual line at point b. From point b a vertical line is projected on to the frequency axis and fc is obtained. This is the simplest method whereby the trade-off between signal distortion and noise passed through are estimated to be equal.
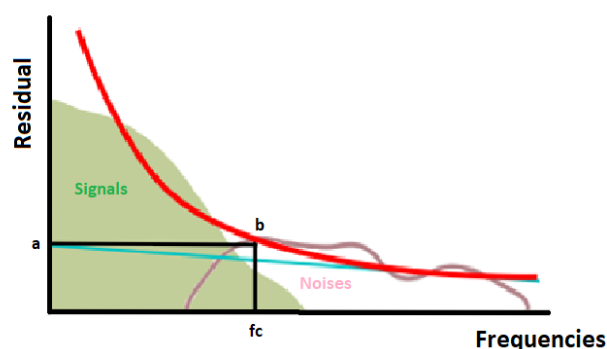
Figure 4.9 – Residual analysis choice of cut-off frequency (fc)

Using this method the cut-off frequency can be found for all the joints in the various motions. The mean frequency and the standard deviations are shown in Table 4-4 for 'Simple Gait, Table 4-5 for 'Object Lifting' and Table 4-6 for 'Object Raising'.

Table 4-4 – NA01 Simple gait mean cut-off frequencies and standard deviation results using winters residual analysis for joint angle data.

	AngleX mean	AngleX std	AngleY mean	AngleY std	AngleZ mean	AngleZ std
Ankle R	7.8	0.45	7.2	0.84	8	0.71
Knee R	8	0	8	0	8.4	0.55
Hip R	8.2	0.45	8	0.71	8	0
Shoulder R	8	0.71	8.4	0.55	8.8	0.45
Elbow R	8	0.71	8.4	0.55	7.6	0.55
Wrist R	7	0.71	6	1	7	1
Ankle L	7.2	0.45	5.4	0.55	7.2	0.84
Knee L	7.6	0.55	7.6	0.55	7.2	0.84
Hip L	8	0	7.6	0.55	7.6	0.55
Shoulder L	8.4	0.55	8.4	0.55	9	0
Elbow L	8	0.71	8.2	0.45	7.8	0.45
Wrist L	8.4	0.55	8.8	0.45	7.6	0.55
Thorax	8.8	0.45	8.6	0.55	9	0

Table 4-5 – NA40 Object Lifting mean cut-off frequencies and standard deviation results using winters residual analysis for joint angle data.

	AngleX mean	AngleX std	AngleY mean	AngleY std	AngleZ mean	AngleZ std
Ankle R	6.33	0.58	6.67	0.58	6.33	0.58
Knee R	7	0	7	0	7.67	0.58
Hip R	7.33	0.58	8	0	8	0
Shoulder R	8	0	7.33	0.58	8.33	0.58
Elbow R	7.67	0.58	8	0	7.33	0.58
Wrist R	7.33	0.58	7.67	0.58	7	0
Ankle L	7	0	6.67	0.58	8	0
Knee L	7.33	0.58	7.33	0.58	7	0
Hip L	7.33	0.58	7	0	7.33	0.58
Shoulder L	7.67	0.58	7.67	0.58	8.33	0.58
Elbow L	7.67	0.58	8.33	0.58	7.33	0.58
Wrist L	7.33	1.15	7.33	0.58	7	1
Thorax	7.33	0.58	8	0	8	0

Table 4-6 – NA54 Object Raising mean cut-off frequencies and standard deviation results using winters residual analysis for joint angle data.

	AngleX mean	AngleX std	AngleY mean	AngleY std	AngleZ mean	AngleZ std
Ankle R	6.5	0.71	5.5	0.71	7	0
Knee R	7	0	6.5	0.71	6.5	0.71
Hip R	7.5	0.71	6.5	0.71	7	0
Shoulder R	7.5	0.71	7.5	0.71	7.5	0.71
Elbow R	8	0	7.5	0.71	6.5	0.71
Wrist R	7.5	0.71	7.5	0.71	5.5	0.71
Ankle L	6.5	0.71	6.5	0.71	7	0
Knee L	6.5	0.71	6.5	0.71	7	0
Hip L	7	0	6.5	0.71	6.5	0.71
Shoulder L	7	0	6.5	0.71	6.5	0.71
Elbow L	8	0	6.5	0.71	6.5	0.71
Wrist L	7.5	0.71	7.5	0.71	7	0
Thorax	8	0	6.5	2.12	7.5	0.71

Using the frequencies the data is filtered, example of this can be seen in Figure 4.10, filtering done for the knee joint in NA01 – Walking trial. It can be seen that some noise is reduced and that the joint angle data is smoother. This is done for all data.

Non-Filtered vs Filtered Data for Right Knee Data During NA01 - Walking
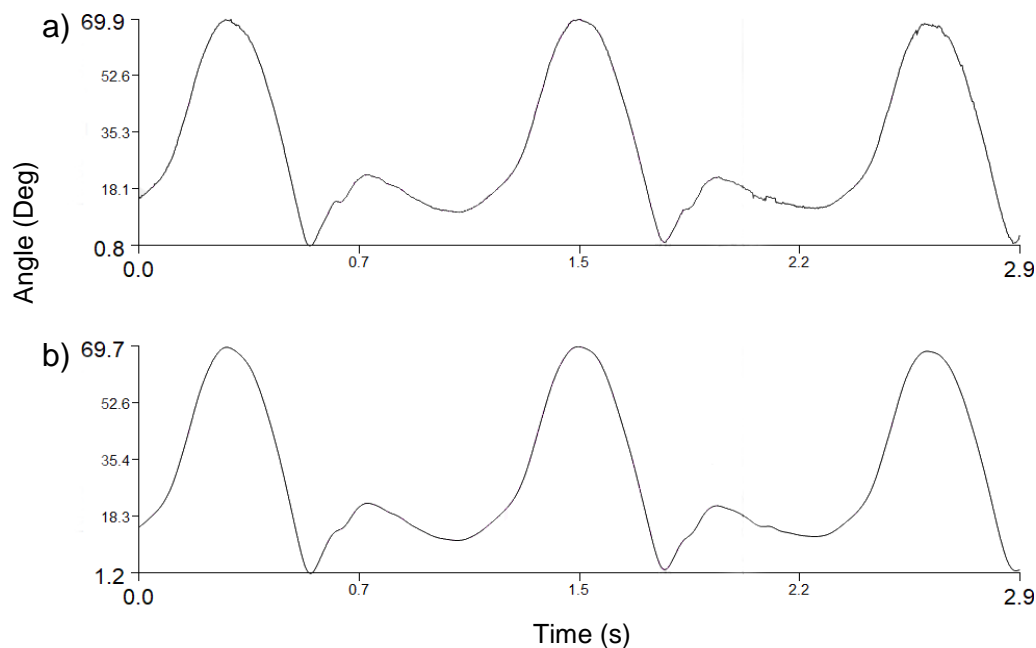
Figure 4.10 – Comapring data before (a) and after (b) filtering using the cut-off frequency found by means of Winters Residual Analysis

4.4 Motion Capture Data Results of Simple Gait, Object Lifting and Object Raising

In this section selected results on joint angles and marker positions from the motion capture trials are presented. They are also compared with known data as a means of verification. Where there is a gap in the knowledge, this pilot study cannot compare the data but others may use the results for comparison and further research. It should be noted that as this research is interested in a 2D simplified model of the exoskeleton, only the results in the sagittal plane to the human will be presented in these results. The full range of 2D results can be found in APPENDIX N (this includes the trajectories of specific landmarks that will be used when calculating inverse kinematics of the exoskeleton model and orientation of the back structure).

The data is filtered using a lowpass filter with a maximum cut-off frequency found. This allows the use of a single cut-off frequency for all joints which encompasses the ranges found using the winters residual analysis method in previous section.

The data are also time normalized to the start and end of the motion. For 'Simple Gait' motion the start is at heel-strike of right leg and end again at heel-strike of the right leg following one full cycle. The 'Object Lifting' motion starts when the user bends down (from standing) to pick up the object. When this occurs the hip angle starts to decrease. The end of the motion occurs when the hip angle returns to zero again.

The joint angle results for 'Simple Gait' can be seen in Figure 4.11. It can be seen that the standard deviation curves follow the motion curves closely. The same can be seen in the joint location trajectory data for Ankle and Hip joints in Figure 4.12 and Figure 4.13.

As there is no motion capture data research known to the author pertaining to 'Object Lifting' and 'Object Raising' motions the use of joint angle data for comparative purposes is not possible. The joint angle results are omitted in this section and are instead included in APPENDIX N. The figures for joint location trajectories, Figure 4.14 to Figure 4.21, show that there is a greater variability in the motion as represented by the larger and more fluctuating standard deviation bands. It is possible that this is due to the variance of the motions, such as inconsistencies with where on the object the subject grabbed hold on when picking it up for 'Object Lifting' motion. Similar for 'Object Raising' motion, differences in where the objects end position was could lead to variances in motion. This is seen in the figures for Wrist joint trajectories Figure 4.16 and Figure 4.20. The overall

lack of training in these motions which would lead to non-uniformity in the data is clear.

Figure 4.14 and Figure 4.18 show that the feet are quite static. For the 'Object Lifting' we however see a small increase in the vertical position suggesting that some joint location shifting occurs even in this rather static motion. This is in contrast to 'Object Raising' motion where the lover chain of the human is relatively static.

For 'Object Lifting' the inverse bell shape for hip, wrist and shoulder joint trajectories is seen in Figure 4.15, Figure 4.16 and Figure 4.17, this is due to the raising and lowering of the body. Similarly for 'Object Raising' in Figure 4.19 and Figure 4.20 for hip and wrist joint trajectories the predominant patterns emerge.
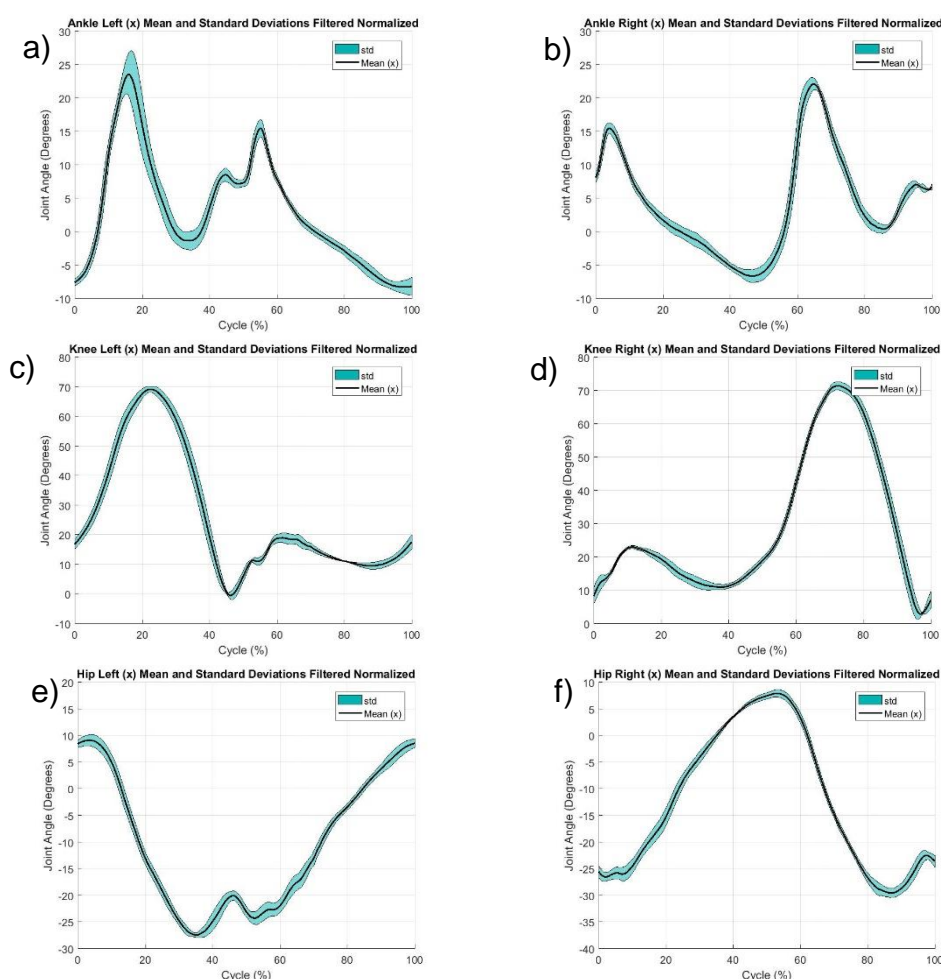
Figure 4.11 – Joint angles mean and standard deviations for 'Simple Gait' for a) ankle right and b) left, c) knee right and d) left, e) hip right and f) left.
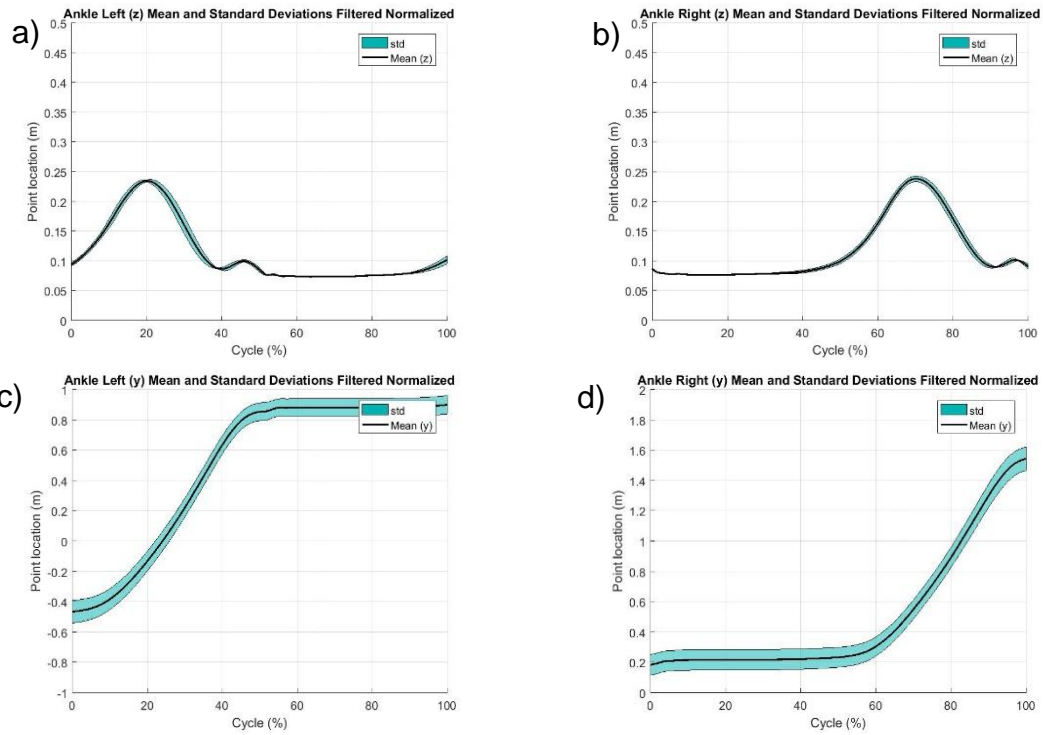
Figure 4.12 – Data for ankle joint location during 'Simple Gait' motion
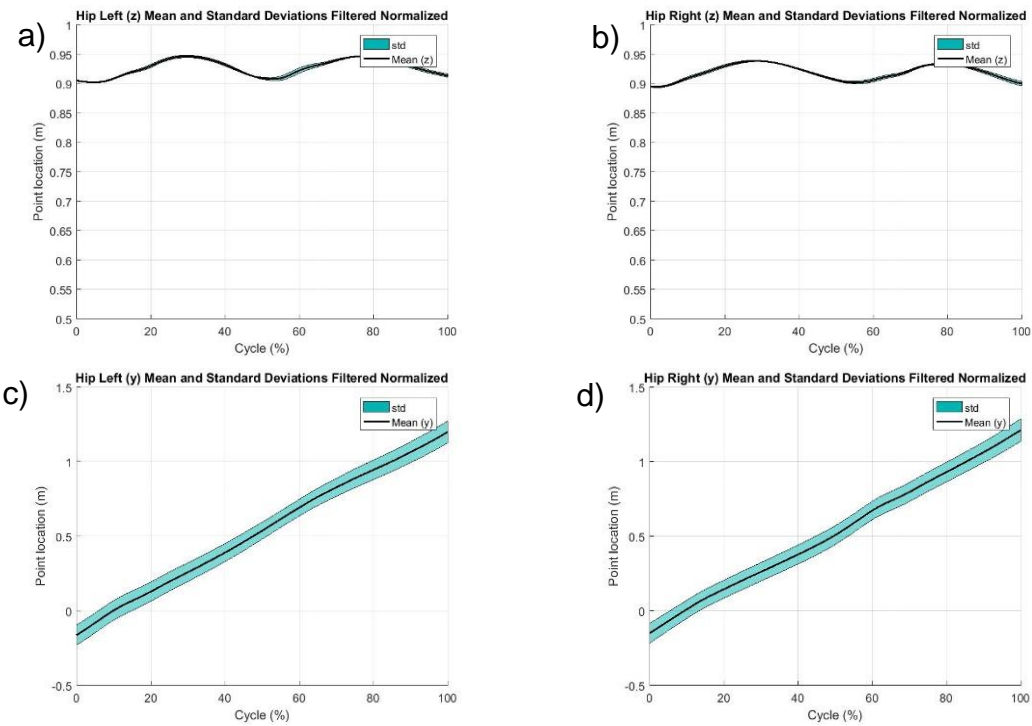
Figure 4.13 – Data for Hip joint trajectories during 'Simple Gait' motion
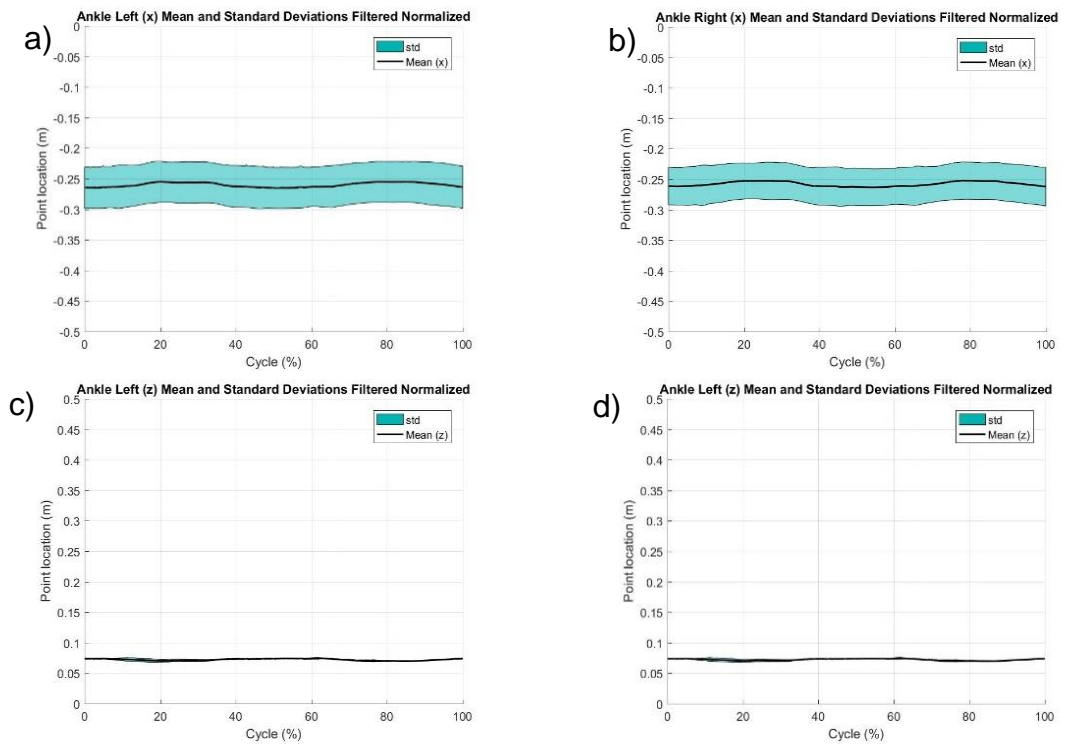
Figure 4.14 – Data for ankle joint trajectories during 'Object Lifting' motion
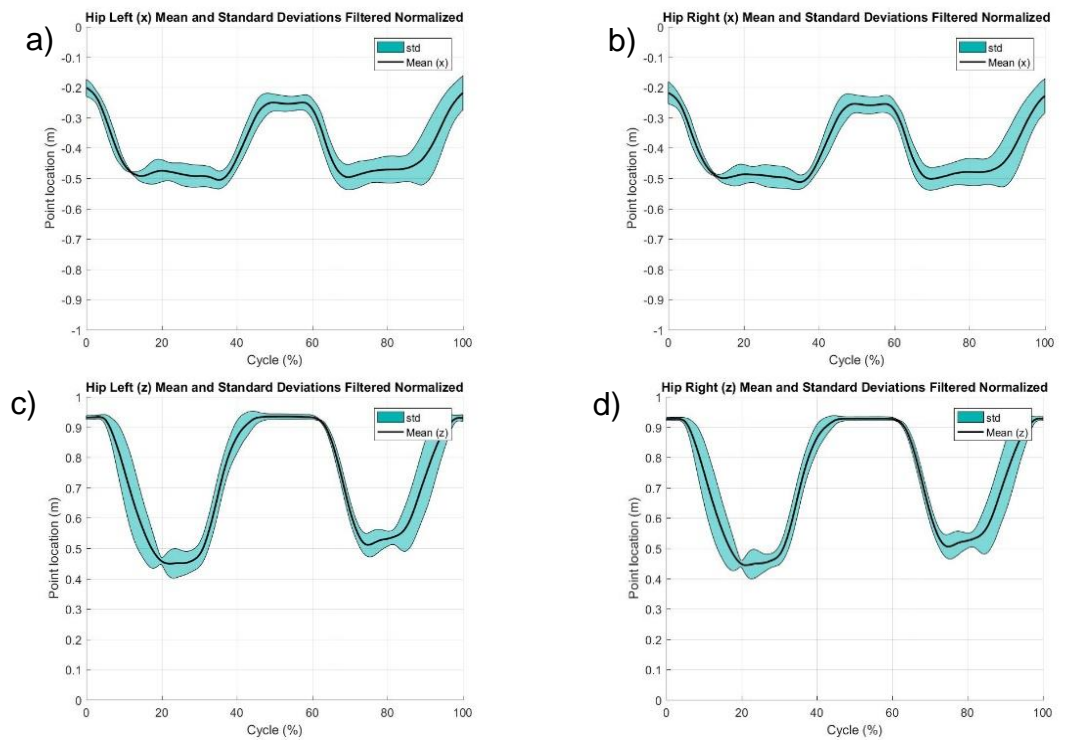
Figure 4.15 – Data for Hip joint trajectories during 'Object Lifting' motion
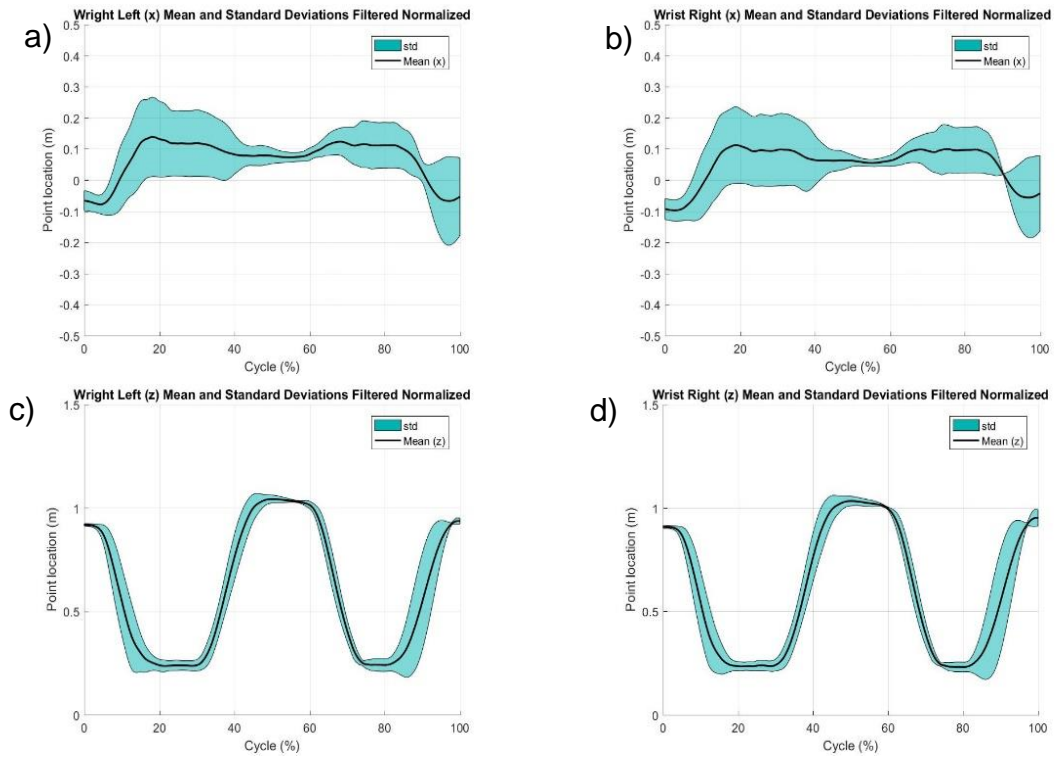
Figure 4.16 – Data for Wrist joint trajectories during 'Object Lifting' motion
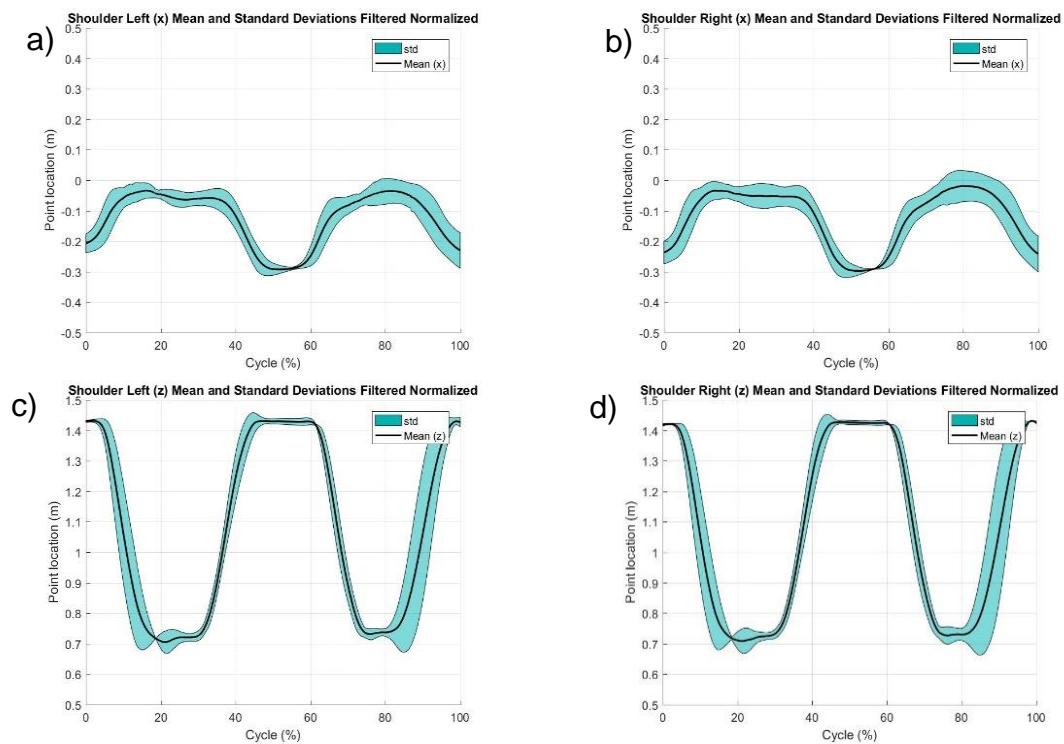
Figure 4.17 – Data for Shoulder joint trajectories during 'Object Lifting' motion
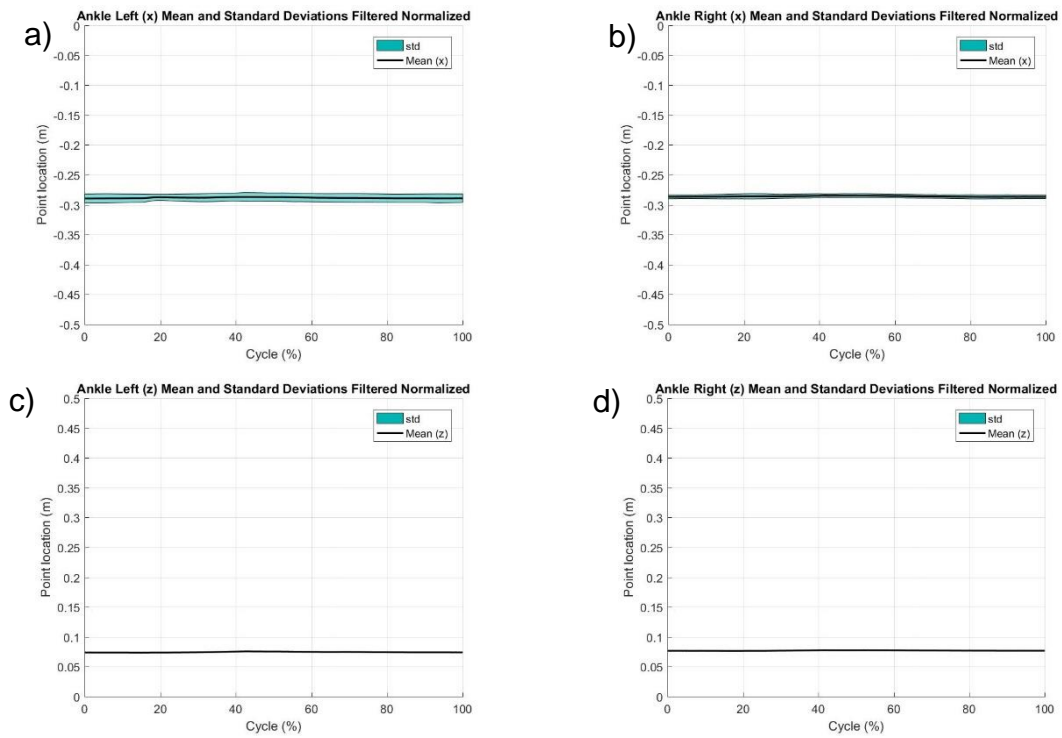
Figure 4.18 – Data for ankle joint trajectories during 'Object Raising' motion
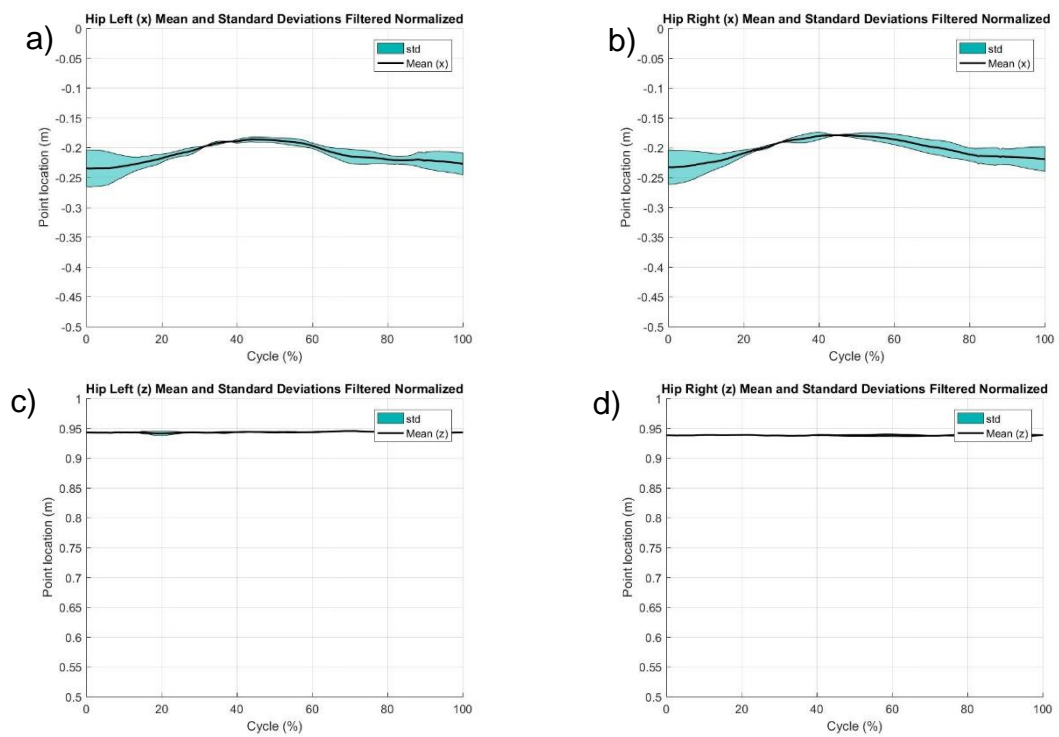
Figure 4.19 – Data for Hip joint trajectories during 'Object Raising' motion
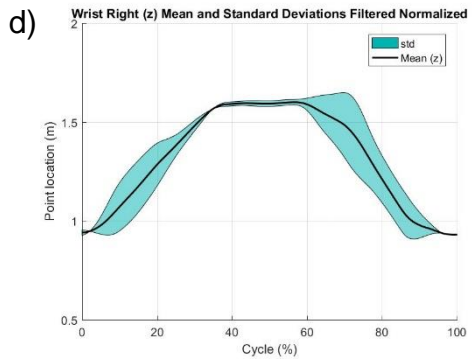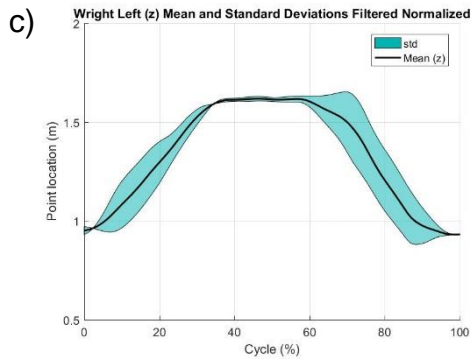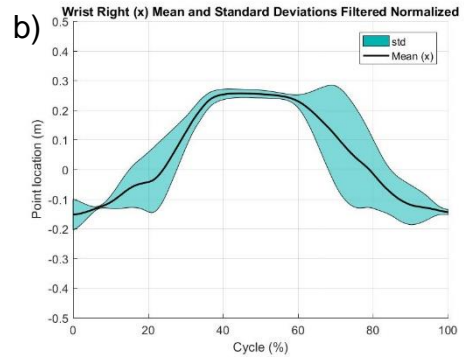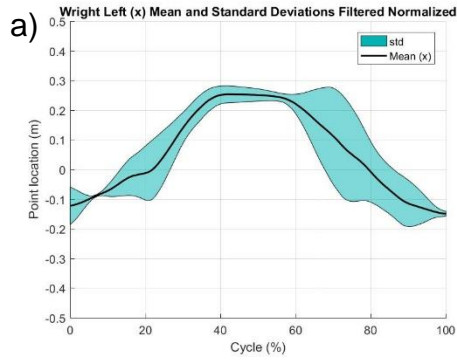
Figure 4.20 – Data for Wrist joint trajectories during 'Object Raising' motion
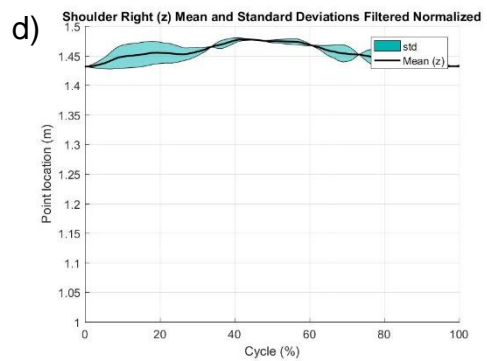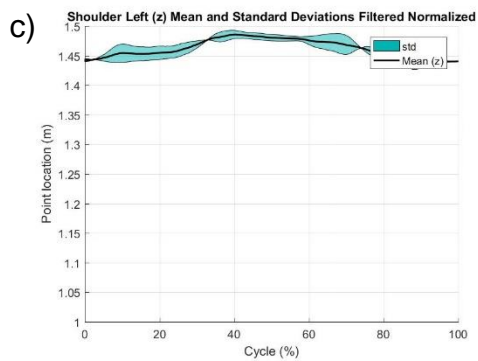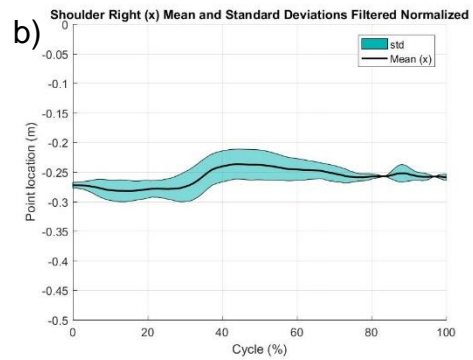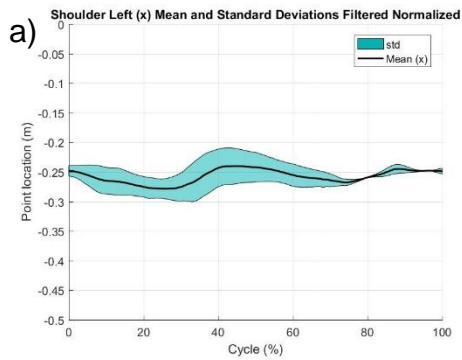
Figure 4.21 – Data for Shoulder joint trajectories during 'Object Raising' motion

4.5 Interaction Point Trajectory Analysis and Trajectory Simplification From Motion Capture Data

By investigating the interaction points motions from the motion capture data, the building of simulation environment may be simplified and broken down. Ideally the interaction points would be simplified to a single point, for each limb. It was shown however in Chapter 3 that this may not be the case for all motions. By looking at the trajectory of the ankle joint marker insight could be gained into how much information is lost if the trajectory was to be alter so that it retains certain key features when modelled as having only one interaction point. In this section this is done by looking at the 'Simple Gait' motion as a working example. The velocity magnitude or change in position with time is used as an indicator of (near) static periods of the ankle joint marker. This data can be used to indicate whether or not a simplification is needed, also how much of the data will be altered. The general characteristics of the motion are captured by analysing the trajectories in x (horizontal) and y (veritcal) directions on a 2D sagittal plane. For gait, known instances such as heel-on (ho) and toe-off (to) are used as markers for foot contact with ground.

4.5.1 Application of Re-Trajectory Work on 'Simple Gait' Motion

Research has been conducted in modelling the contact forces that occur in gait for humanoid robots (Mu and Wu 2006; Zheng and Hemami 1984). To simplify the analysis of the legs motion for robots some researchers have used an inverted pendulum model as the source of the motion trajectories for the hip with respect to the ankle joint during the stance phase (Bhounsule, Pusey and Moussouni 2016). In order to directly incorporate the human data in the simplifications a new exoskeleton trajectory is derived by simplifying the model to a point contact model. That is, the interaction points for the feet of the exoskeleton are represented by one point. Therefore the interaction point can be set to the ankle joint position for the sake of analysis. Effects of impact and contact in exoskeleton design are referred to in future works.

Using the data found in the previous section the right heel strike (rhs), right toe off (rto), left heel strike (lhs) and left toe off (lto) periods can be visualised on top of the graphs for marker trajectories, this is seen in Figure 4.22 for the right ankle marker. The marker is designated point A1, as the first ankle is simplified to an interaction point. By looking at the magnitude of the vector displacement [x ,y, z] with respect to time, static periods can be discerned, shown in Figure 4.22. The static period can be seen in Figure 4.22 and Figure 4.23 in between the green

bands. It can be seen that the complex gait motion only allows for a short span of time where the ankle is static. This occurs for approximately 40% of the time that the foot is in ground contact. For approximately 21% the foot is only in heel contact and for approximately 39% the foot is in toe contact only.
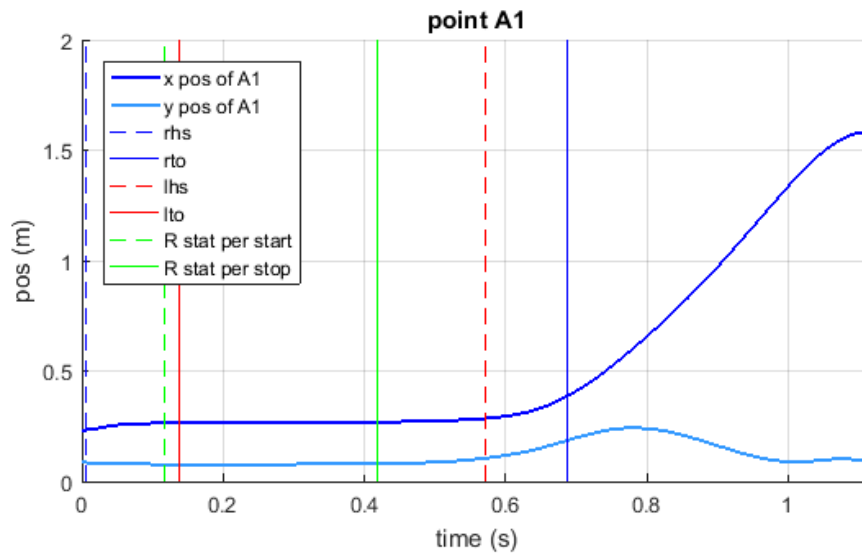
Figure 4.22 – Graph showing the X (horizontal) and Y (lateral) trajectories of the first (right) ankle joint location, A1 which is also an interaction point, using the mean motion capture trial data. The graph shows the span of the rhs to rto using blue vertical lines, hashed and solid lines respectively. The lhs and lto are also marked out. The interval where there exists double feel contact is visually clear. The green vertical lines mark the start and stop of a period where the motion of the ankle joint landmark is so negligible that it can be considered static.
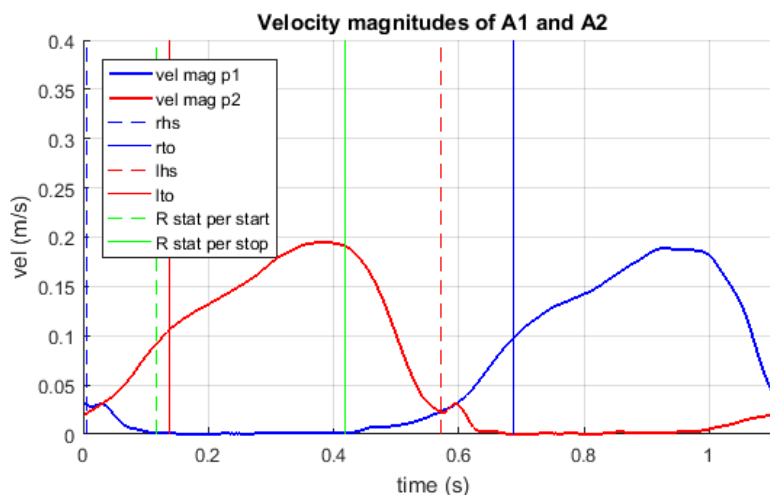
Figure 4.23 – The velocity magnitudes of vector [x, y, z] in 3D space for interaction points A1 (right ankle joint marker) and A2 (left ankle joint marker). The static period for the right ankle is marked with green vertical lines.

This means that a model which would be true to the human motion would have to accommodate the rolling of the heel. It also has to accommodate for when the heel is lifted and the foot is rested on the ball (that is the toes) of the foot.

As seen in the above example the gait pattern can become quite complex to model. To simplify this the interaction of the exoskeleton with the ground for the selected motions ('Simple Gait', 'Object Lifting' and 'Object Raising') is changed from being multi-contact to a single point contact. For 'Simple Gait' the assumption must be made that the exoskeleton foot (and by extension the ankle joint location) is static through the entirety of the stance phase, but otherwise retains the conditions which create the trajectory in the swing phase. Thereby a new trajectory for the ankle joint location can be generated.

What is needed to be retained in the exoskeletons trajectory is:

- Location of peaks and troughs (local minima and maxima of trajectory, that is when dx/dt = 0 and dy/dt = 0);
- Setting the initial and final location of gait cycle as well as the starting point in the swing phase to the static values of the ankle joint location during stance phase.

The data obtained will be used as the conditions for a new locus, which will be used as a simplified trajectory. The new gait pattern will assume that the foot is performing a point contact, as opposed to rolling contact like the human, whilst retaining the characteristics of human gait.

4.5.2 Pattern Analysis and Data Interpolation

In order to obtain the curve which satisfies the conditions for the locus, first the peaks and troughs are found. This is shown in detail in Figure 4.24, which illustrates the data for the ankle joint trajectory from toe-off to heel-strike for 'Simple Gait' motion with respect to sample step. Where the curve for y-position shows distinct curve, which are cyclical, the peaks and troughs are naturally occurring. The x-position curve is, for a forward walking human, always increasing. In this case the second derivative (speed) of the x-position curve is used to find suitable and corresponding x-position loci.

For the y-position the starting and ending value (corresponding to human toe-off, hto and human heel-strike, hhs) is set as the lowest value of the ankle joint location during the stance phase. The x-position however, being continuously increasing uses the starting and ending values of the ankle joint location.
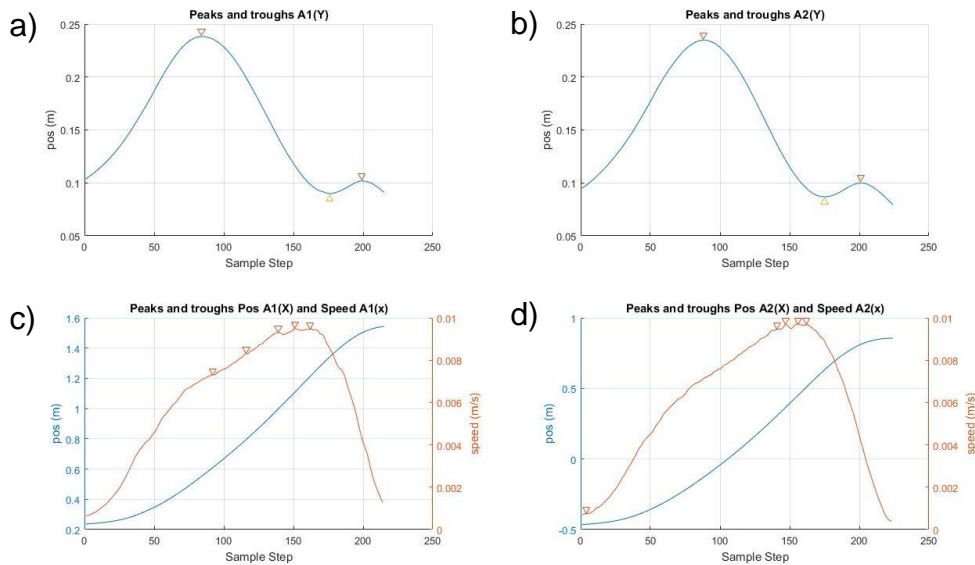
Figure 4.24 – Figure of graphs used for identifying peaks and troughs from ankle joint motion-capture space (x and y) vs sample step data from toe-off to heel-strike (swing phase). Graphs a) and b) show the left and right ankles y (lateral) trajectory in space. Graphs c) and d) show the x (horizontal) trajectory in space but also the calculated discrete speed of the marker at each sample step.

Now that the set of points has been gathered the data can be interpolated. This is shown in Figure 4.25. The data in Figure 4.25. a) and b) shows that for the x-position curves the interpolation, as is expected, removes the gradual increase in x-position of the ankle joint. It can also be noted that the trajectory for A2, left ankle joint, exhibits slight difference in motion between toe-off and the first peak in comparison to A1, right ankle joint. This is most likely an artefact of the interpolation, which occurs due to there not existing any further information about the curve behaviour between those loci. The graphs for the y-position, Figure 4.25. c) and d) shown very minimal deviation in behaviour, most notably is the slight difference in height for the A1 static period., which occurs most likely due to the rolling motion of the ankle joint producing a shift in motion-capture marker heights.

For the 'Simple Gait' motion there is an expected loss of information about the behaviour of the ankle joint during the stance phase and its transition to swing phase, specifically notable in the y-position curves, Figure 4.25 a) and b).
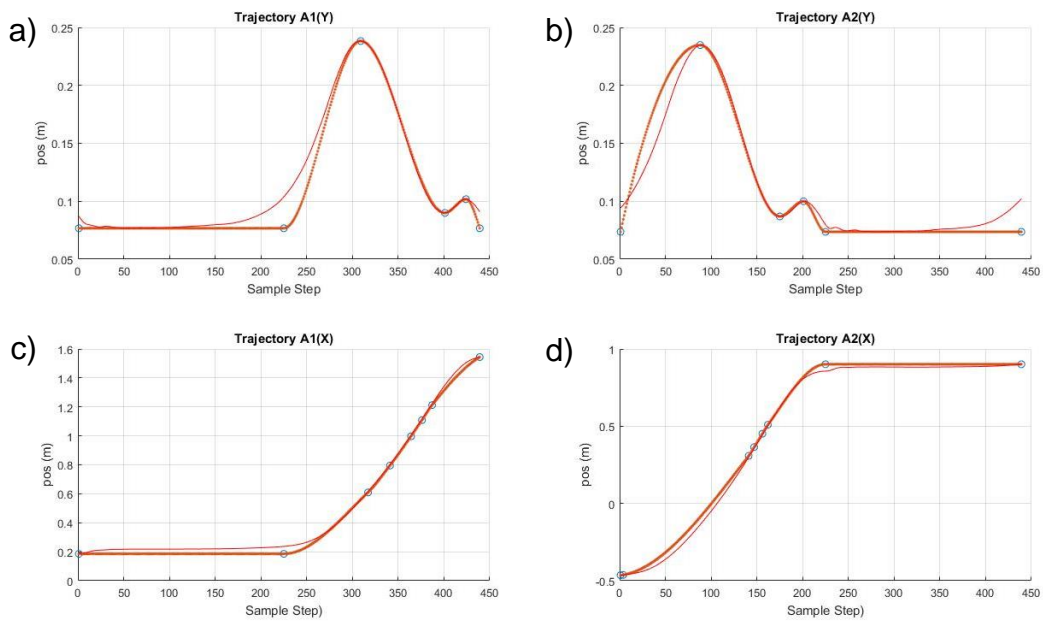
Figure 4.25 – The results of interpolation seen in orange, overlaid with the original motion in red for simple gait and blue circles identifying the sample step locations of the peaks and troughs.

4.5.2.1 Application on 'Object Lifting' and 'Object Raising' Motions

By looking at the graphs of the ankle joint marker trajectory in the previous section it can already be deduced that the subject is fairly static throughout the motions. This is confirmed by looking at the magnitude of the velocity. As an example the 'Object Raising' ankle joint position vs time and velocity magnitude vs time for one of the feet is shown in Figure 4.26.
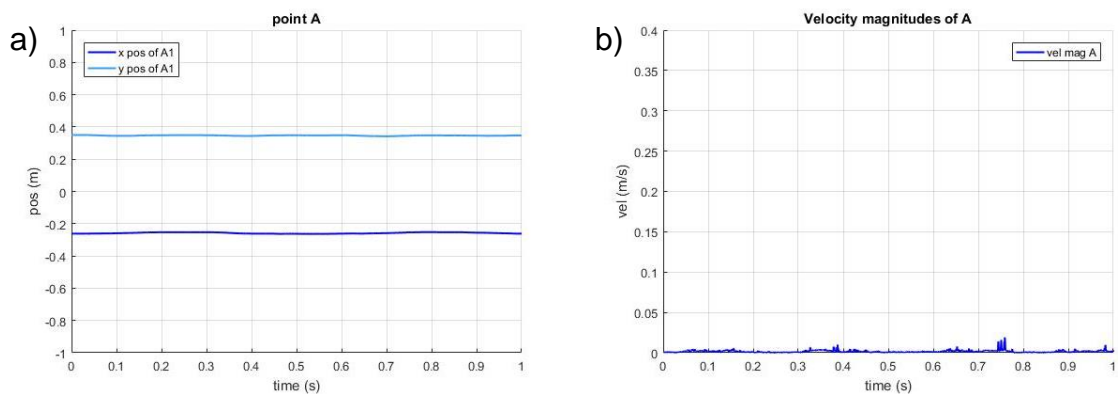
Figure 4.26 – graphs showing a) the X (horizontal) and Y (lateral) trajectories of the first (right) ankle joint location, A which is also an interaction point, using the mean motion capture trial data; b) the velocity magnitudes of vector [x, y, z] in 3D space for interaction point A (right ankle joint marker).

71

It can clearly be seen that the change in position over time is negligible. Although there are smaller spikes in the velocity magnitude graph, these can most likely be attributed to noise from derivation methods. Therefore the object lifting and raising ankle joint location can be set as static.

4.6 Applying Smoothing and Gradient methods to Inverse Kinematic Data

The effects of various methods of processing the data has so far been looked at individually. In this section it will be considered to use the gradient and smoothing techniques previously described on the velocities and acceleration from the joint position data which comes from the inverse kinematics.

The forward kinematic data used here is found in the previous section. The method of obtaining the inverse kinematics is discussed in Chapter 3. SimScape within the Simulink environment is used to simulate a two-link system which has base and end-effector trajectories that are set to the human ankle and hip joint marker trajectories from the motion.

Snapshots of the simulation is shown in Figure 4.27. It should be noted that for the structure of the links cylinders are used, and arbitrary values for thickness and radius are chosen as 2mm and 25mm respectively. In Chapter 6 the cross-section optimization of each link will be discussed in detail.
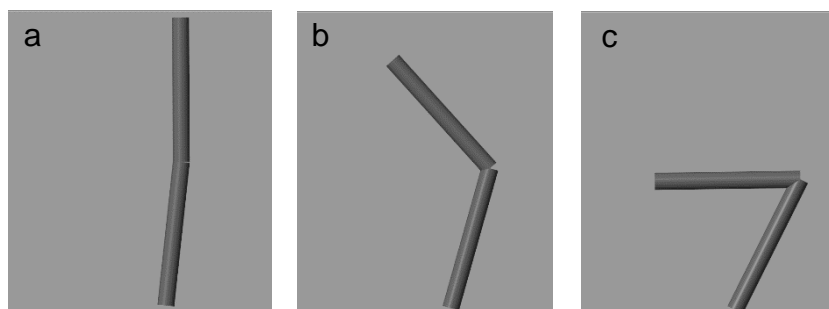
Figure 4.27 – Various stages in the two-link simulation of lifting motion, a) standing straight, b) mid-descent or ascent, and c) squatted position

The resulting data, for the joint trajectories, velocities, accelerations and torques as simulated by Simulink for both the ankle and the knee joint can be seen in Figure 4.28 and Figure 4.29 respectively. These figures show the unsmoothed velocity and acceleration data. It can be seen clearly that there is large amounts of noise that increases in amplitude depending on the data with the greatest noise showing in the torque data.

In Figure 4.30 and Figure 4.31 the same simulation can be seen but when the velocity and the acceleration data smoothed prior to simulation. The process by which smoothing and filtering is done is presented in APPENDIX O.
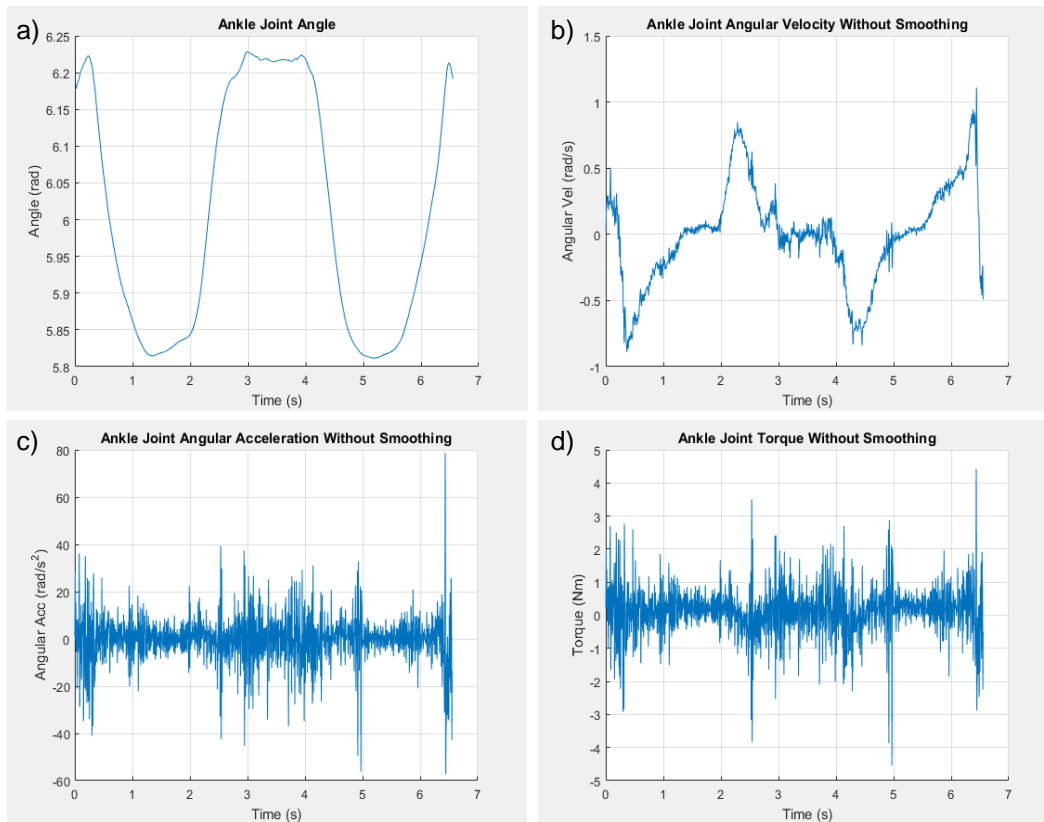
Figure 4.28 – Position, Velocity, Acceleration and Torque graphs for non-smoothed NA40 - 'Object Lifting' motion ankle joint marker
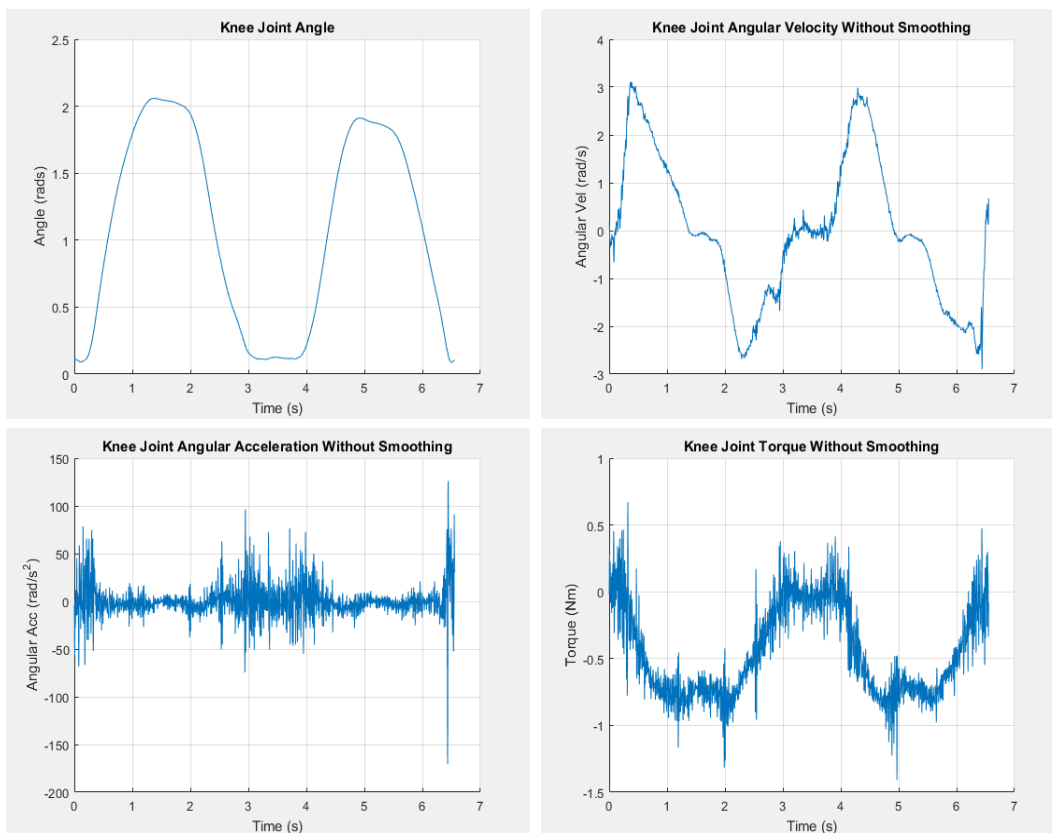
Figure 4.29 – Position, Velocity, Acceleration and Torque graphs for non-smoothed NA40 - 'Object Lifting' motion knee joint marker

74
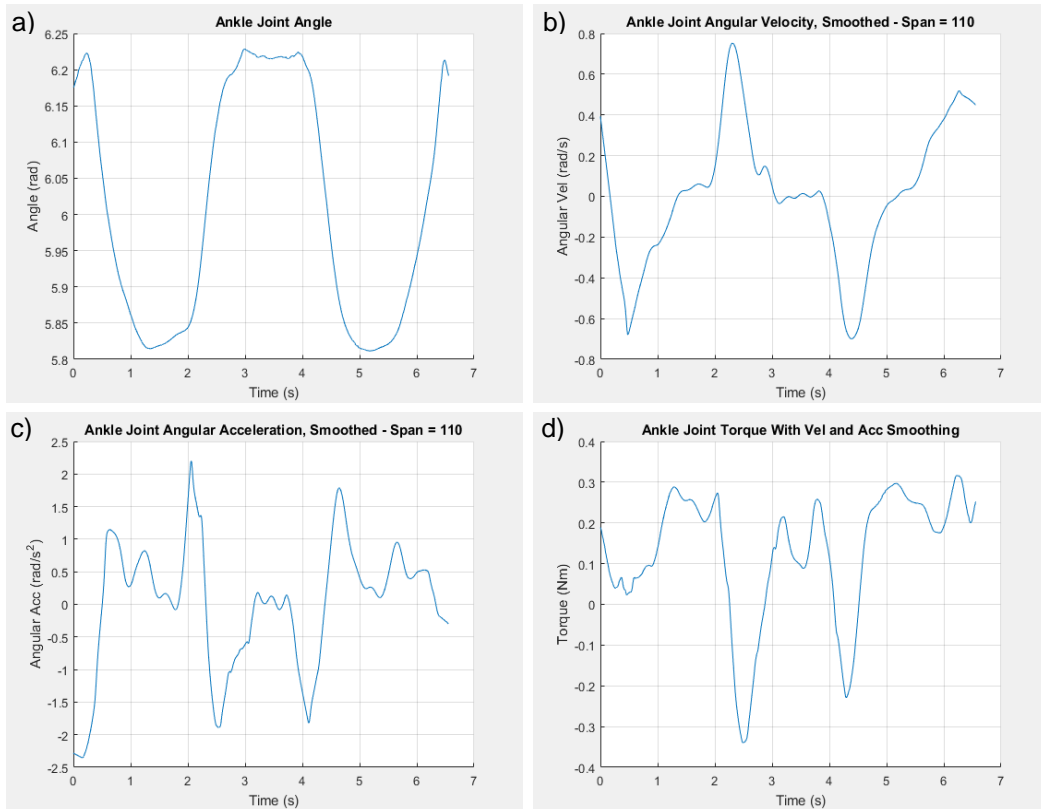
Figure 4.30 – Position, Velocity, Acceleration and Torque graphs for smoothed NA40 - 'Object Lifting' motion ankle joint marker
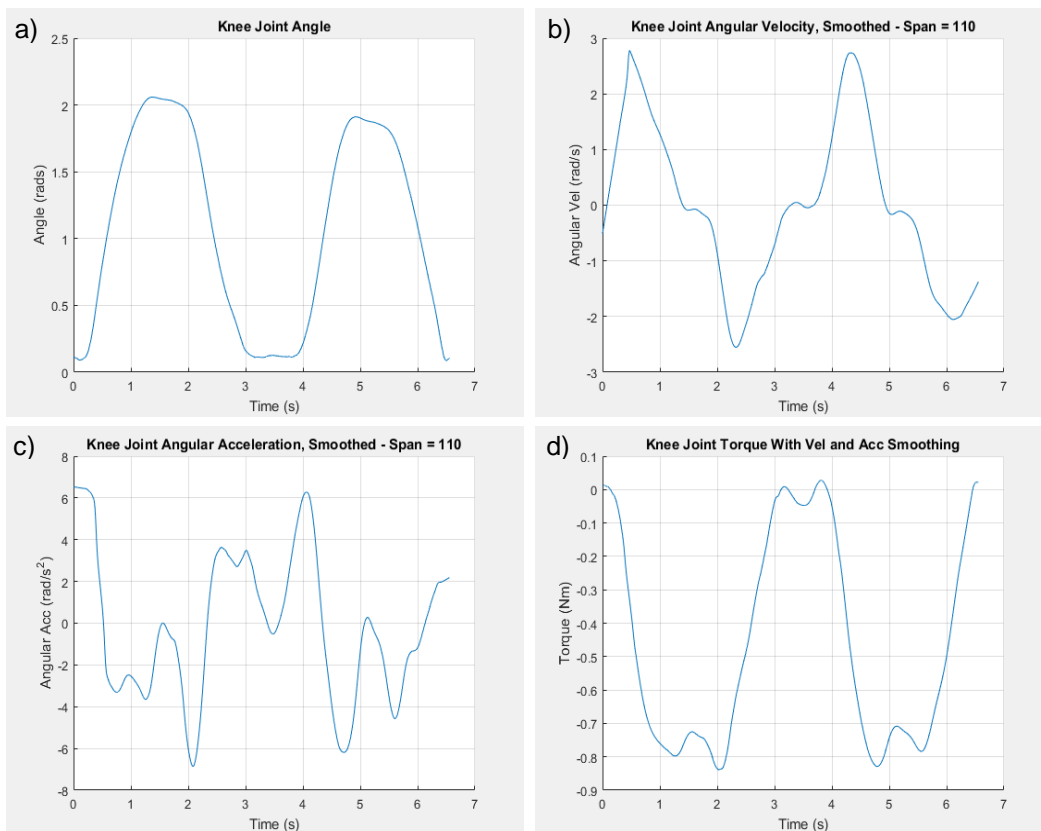
Figure 4.31 – Position, Velocity, Acceleration and Torque graphs for smoothed NA40 - 'Object Lifting' motion knee joint marker

In comparing the graphs it can be seen that the general pattern of the data sets are present. After smoothing the torque results are no longer noisy. Alternatively the data can be smoothed after the simulation, this is shown in Figure 4.32, where the torque simulation data shown in Figure 4.28 d) and Figure 4.29 d) has been smoothed. In comparing the torque results in Figure 4.30 and Figure 4.31 with that in Figure 4.32, the results are similar. It should be noted that in the ankle joint graph in Figure 4.32 (a) potential spikes in data can show themselves in unwanted ways, such as a major drop in torque, where the torque is expected to be minimal. It is due to this unwanted spikes that the velocity and acceleration data will be smoothed prior to obtaining torque values.
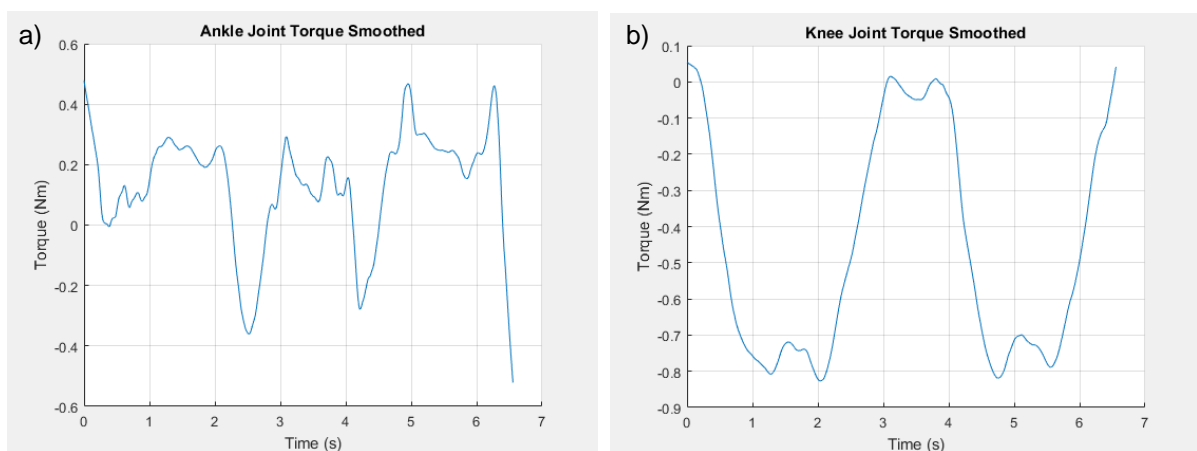
Figure 4.32 – Torques for ankle and knee, smoothed after simulation

4.7 Discussion

4.7.1 Cut-Off Frequencies for Joint Angles

The use of winters residual analysis in obtaining the cut-off frequencies for 'Simple Gait' for joint angles yielded mean results spanning from 5.4 Hz to 9 Hz. Taking into consideration 1 standard deviation the span ranges from 4.85 Hz to 9.25 Hz. Winter (Winter 2009b) shows that for marker displacements the range varies for 3 Hz for slow moving markers (hip and ribs) to 6 Hz for faster moving markers (on the ball of the foot).

Looking at 'Object Lifting' the obtained mean values are 6.33 Hz on the low end and 8.33 Hz on the high end. Accounting for 1 standard deviation the results are 5.75 Hz to 8.91 Hz.

For 'Object Raising' the obtained mean values are 5.5 Hz on the low end and 8 Hz on the high end. Accounting for 1 standard deviation the results are 4.38 Hz to 8.62 Hz.

Since the subject was healthy without any known injuries, and the cut-off frequencies for 'Simple Gait' correlates to that of the known literature. It would therefore be highly feasible that the frequencies for 'Object Lifting' and 'Object Raising' are reasonable to use for marker trajectory filtering when extracting data from Visual3D.

4.7.2 Verification of Motion Capture Pilot Study with Known Data

The joint angle data is also presented in this chapter principally to be used in conjunction with known data for verification. Comparing the data captured with the data used in the design of the BLEEX exoskeleton shown in Figure 4.33 the distinct patterns are seen. This is not unexpected as the subject was healthy without any known medical conditions. Since the research is concerned with the motions 'Object Lifting' and 'Object Raising' as well the data is presented for the joint angles. However there exist no clinical data in the literature known to the author at this stage on these motions that can be used for direct comparison, like 'Simple Gait'.
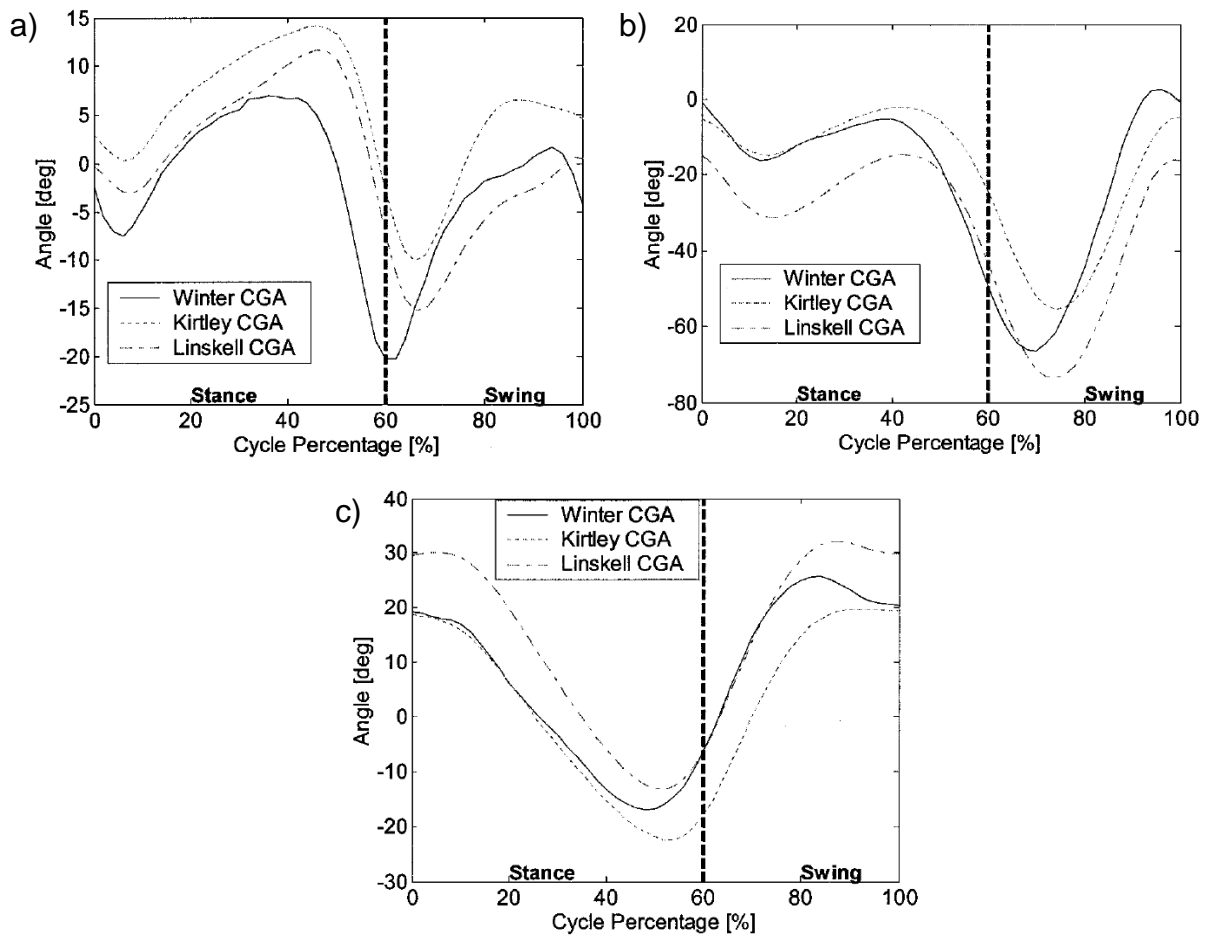
Figure 4.33 – The data for a) ankle, b) knee and c) hip flexion/extension used in the BLEEX design (Zoss 2006).

Though no trajectory data is known at the time this thesis is written to be used for comparison some visual comparison of the 'Object Lifting' motion can be made with known literature. As can be seen in Figure 2.3 in Chapter 2 where the squat posture has been demonstrated (Burgess-Limerick 2003), the final posture attained is similar to that of the 'Object Lifting' motion performed in this research, seen in Figure 4.7. It should also be noted that other research in correct posture during lifting present the squat as explained with photographs for illustration of the motion (Straker 2003). Some research have used reflective markers and photography to calculate joint angles for use in finding optimal postures in load lifting (Kothiyał, Mazumdar and Noone 1992), but no trajectory data is presented instead, maximum and minimum joint angles are discussed.

The main difference in the visual comparison with known research is that the subject in the pilot study kept his/her feet flat on the ground throughout the motion.

Much like in the squatting exercise. Sufficient to say that the data for 'Object Lifting' is satisfactory when compared the known literature discussed above, furthermore what is presented here are a collection of joint angle trajectories which can be used as a basis of comparison when more statistical data is gathered.

Due to the strictness of the motion criteria used in this research the exoskeleton will be designed for correct posture when lifting in a workplace. The comparison on the effects of the multitude of lifting motions that humans may produce are therefore omitted in favour of comparing a known set of motions.

The 'Object Raising' motion remains not compared. This is due to the fact that no data known to the author was found that could be used for verification. It is by means of logical deduction that it can be assumed that due to the healthy status of the subject and the validity of previous motions that no further statistical and comparative verification is required for this motion at this time. Like the 'Object Lifting' motion the joint angle trajectories can be used for comparison with a greater population when such data is gathered.

4.7.3 Trajectory data

It can be seen that in the 'Simple Gait' motion the subject's variability in his/her motion is small. Made clear by the smaller standard deviation in the results for both the joint angle and the landmark data seen in Figure 4.11, Figure 4.12 and Figure 4.13. This strengthens the point that there is some variety in the execution of lifting and raising motions. Potentially this variety may arise from these motions not being day to day activities like gait.

The common factor in both 'Object Lifting' and 'Object Raising' are the limited to almost non-existing motion of the ankle joint location, Figure 4.14 and Figure 4.18. This should be expected as they are both static motions. In 'Object Lifting' the ankle joint location does not seem to be fully static which can be seen in the median values of the lateral trajectories in Figure 4.14 a) and b). This is also made clear by the greater standard deviation bands in the lateral direction. As there is a greater turn performed at the ankle joint to bend the leg, it could be assumed that this would produce a small shift in the location of the ankle joint centre. This could be attributed to the fact that the ankle joint is not a perfect revolute joint which rotates about a pin. It could also be assumed that during the squatting movement, where there should have been perfect flat contact between the foot and ground, the limits of agility in the subject may have forced the posture out of shape.

The wrist joint locatation trajectory for 'Object Lifting', Figure 4.16, has a higher degree of sporadic behaviour, in comparison to the remaining joints which clearly

follow a pattern. Furthermore squat depth may also have contributed to this. It can be seen in Figure 4.15 c) and d) that there exists an approximate 10cm variety between the standard deviation bands. Though the wrist horizontal depth is not as discrepant, seen in Figure 4.16 c) and d), its horizontal movement seen in Figure 4.16 a) and b) show that the horizontal displacement has a discrepancy of an approximate maximum of 25cm.

Further improvement to the experiment could be to set static markers on the items for the subject to grab hold of for the 'Object Lifting' motion. For the 'Object Raising' motion a target could be set for where the item should be raised to.

4.7.4 Interaction point and trajectory simplification

The process by which the exoskeleton model is designed starts with the simplification of the exoskeleton interaction with the world. Firstly simplifications and assumptions are made. In this instance it is assumed that the interactions between the exoskeleton and the world could be represented by a single (contact) point. The analysis is done on the ankle joint marker trajectory data obtained from motion capture trials. Choosing the ankle joint allows the model to use a two-link leg structure for the exoskeleton leg model, for which there exist well studied and relatively simple kinematics (forward and inverse) and dynamics models and equations. By analysing the total velocity vectors of the contact point, static periods of the point could be found.

As a demonstration this is done in depth for gait as it is well studied in the biomechanics community. By splitting foot contact into only three phases, from initial contact to rest (heel strike, hs), rest and from rest to final contact (to) it was shown that out of the three phases the majority of the time the foot could be considered static approximately 40% of the time. However about 60% of the time the foot was in motion, meaning that for 40% of the time during stance phase the ankle joint could be considered as being static.

The re-trajectory work uses key events in the gait trajectory of the ankle joint, represented by peaks and troughs in x and y displacement (shown in Figure 4.24) together with the static values found during ankle joint rest phase. The points are used as conditions for generating a new locus/trajectory. The difference in the trajectories can be seen in Figure 4.25.

This method of obtaining expected exoskeleton trajectories, in comparison with the pendulum model is more cumbersome as it would entail actual experimental data. Furthermore not all motions are well studied, and therefore trajectory models may

not be known. Using motion capture data gives the ability to alter the complexity of the human motion and the models derived from them by using key loci.

The work done using the ankle as a contact point presents benefits in modelling by enabling the use of two-link legged model. This does however also mean that the full range of motions for the foot are not accounted for. In terms of exoskeleton design this could be likened to ski boots, it can be seen however from both the BE and the XOS-2 that the current enhancive exoskeletons have also not focused on intricate foot actuation (Army-Technology.com 2014; Lucchesi *et al.* 2010).

For certain motions the static period can be considered to last throughout the cycle. As seen in Figure 4.26 for the 'Object Lifting' and 'Object Raising' motions the ankle trajectory could be considered static. This should be expected as both tasks involve mainly upper body movements. The process is therefore twofold, first it verifies that there actually is a movement, second it detects the break points in phases.

4.7.5 Sample inverse kinematics example

In an example of a two-link 2D model of the exoskeleton leg the interaction point analysis, trajectory simplification and signal smoothing come together. Data is used from the 'Object Lifting' ankle and hip marker trajectories. The torque data smoothed without using the smoothing algorithm is compared with the torque data smoothed after using the algorithm. It is seen that the data it is very similar in the two cases. Some artefacts appear when not using the smoothing algorithm which can cause issues in calculations.

By knowing that the thigh link will be horizontal and almost perpendicular to the shin link at approximately 50% of the cycle time for 'Object Lifting' motion, it can be assumed that the knee will have a spike in torque. This is confirmed when looking at Figure 4.31.

The sample process of analysing motion data, selecting and applying filtering and derivation for motion simulation and post processing the torque data is confirmed in this section. The results are viable and as expected. However for more complicated motions further development needs to be made in order to incorporate complicated modes of contact forces. The same can be said about the impact forces during gait. The methods presented does not take into consideration any form of contact dynamics. Simulation using this method would enforce the assumption of perfect transfer of forces from the impacting foot (during hs) to the lifting foot (during to). Furthermore the model must be assumed to be perfectly inelastic as elastic behaviour and material considerations have not been taken into consideration.

4.8 Summary

4.8.1 Motion Capture Section

In the first part of the chapter the protocol for the motion capture pilot study is presented. The purpose of the pilot study is to gather data on a variety of human motions related to tasks which could be performed by a user of an enhancive exoskeleton. The data is set to be used by more than just his PhD thesis and therefore although a wide range of motions and sub motions, such as gait and turning during gait, are captured, three specific motions are focused on, 'Simple Gait', 'Object Lifting' and 'Object Raising'.

The software used for capturing and processing the motion capture data is described, so is the virtual environment where the human model is built. The three motions use the same global position, however 'Simple Gait' is performed 90 degrees to 'Object Lifting' and 'Object Raising' due to force platforms alignment in the laboratory. This was done to pick up the ground force reactions for both feet for the latter two motions.

Winters residual analysis is used to find cut-off frequencies. For 'Simple Gait' the span is found to be 5.4 Hz to 9 Hz with a maximum standard deviation of 1. For the 'Object Lifting' the span is 6.33 Hz on the low end and 8.33 Hz on the high end with a maximum standard deviation of 1. Finally for 'Object Raising' the span is 5.5 Hz on the low end and 8 Hz on the high end with a maximum of 1 standard deviation.

The results is presented filtered using a 12Hz low-pass filter, with encapsulates the entire range of cut-off frequencies. The data is also time normalized and presented with respect to percentage of the entire cycle time.

'Simple Gait' is used as the basis of comparison with known data, showing that the user is healthy and follows the normal range of motions expected. 'Object Lifting' motions are compared on a visual basis, and thus can be confirmed as well. 'Object Raising' motion remains not compared. However it is accepted as a motion on the basis of the aforementioned motions being statistically and visually sound with a distinct repeatable pattern emerging from the graphs.

'Object Lifting' and 'Object Raising' motions are found to be more sporadic in their patterns, made clear the not smooth standard deviation bands. The cause for this could be the user not being as used to perform the motions as with gait, lack of specific markings on the items the subject interacted with and there not being a specific target to reach when raising and placing the item.

Overall the pilot study is a success and the data is satisfactory. It would be interesting to correct some of the issues found here for a full scale statistic trial. This research has pointed to research on these topics as a basis of comparison to verify the motion capture results. It is also not in the scope of this research to compare the human conditions, however it would be interesting to compare squatting as a sport and for optimal working conditions with humans using their bodies as controllers for exoskeletons. These have been referred to in the future works section.

4.8.2 Interaction Point Trajectory Analysis and Simplification Section

In this section of the chapter the analysis of planar motion data is performed. It is shown that motion data can be used to generate alternative motion data, that suits simplified models of exoskeletons. Comparisons are made between the simplified interaction points and the human foot in the form of analysing the time when the ankle joint is static and when the foot is in contact with the ground. The analysis shows that some simplification must be made in the trajectory of the ankle joint in order to set this as static during the entire cycle (where the foot is in contact with the ground). This is done by obtaining key values which define the shape of the curve of motion trajectories as well as static periods of the interaction points. Using this information a new locus is generated, this represents the simplified trajectory.

Furthermore filtering, derivation and smoothing methods presented in MATLAB are investigated for the purposes of incorporating them into an automated process of optimization as well as for post-processing of data. Looking at the time for computation using FFT and designfilt function versus various smoothing methods, it is found that the actual filtering time of a noisy signal is less costly. The drawback with using filtering methods is the time for preparation and cumbersomeness for automation in comparison with the smoothing function. With the filtering the filter would need tuning. The 'rlowess' smoothing method is ultimately chosen as presented the most accurate results and was least time consuming of the smoothing methods.

A simple algorithm for the order in which the signal is to be smoothed and derived is looked at. It is found that it is acceptable to present signal data and its derivatives after smoothing using the methods and smoothing intervals found.

The new trajectory, smoothing and derivation algorithm is applied to a two-link 2D model simulation performing the 'Object Lifting' motion. The results are compared with the same motion without smoothing the derivation data and only smoothing the torque results. When comparing the torque data it is seen that when applying

the smoothing in the very end of the process some artefacts may occur which can skew the data significantly.

It is concluded that the results are viable as they have been verified and errors and deviations are controlled throughout the entire process. Further room for development exists and incorporation of contact and impact force models could improve the model simulation.

For the remainder of this research the simplified trajectory data is used as inputs for the simulated exoskeleton model to follow.

Chapter 5
Model Generation Using Motion Data

5.1 Introduction

In this chapter subdividing the exoskeleton into segments which are manageable in terms of simulation and equation simplicity will be developed and analysed. This includes a vector mapping of the way-point to the hip and shoulder joint, such that the relation between the exoskeletons hip and shoulder joint locations are statically defined with regards to the way-point. Then two ways of obtaining the orientation of the back structure for the simulation will be investigated. The new trajectories for the exoskeleton are derived using the orientation of the back structure and the vector mapping. The rigid-back structure for the exoskeleton is minimized by looking at two motions 'Object Raising' and 'Object Lifting' and closing the distance between the structure and the human back when the human is performing these tasks.

The human wrist and ankle trajectory data in Chapter 4 is used as input for the simplified exoskeleton models wrist and ankle locations. Shoulder and hip data together with spinal marker data found in APPENDIX N is used for the back-structure development and minimization. The DH-parameters and kinematic equations of the exoskeleton limbs are derived which will be used for the optimization.

The work in this chapter is discussed focussing on the orientation method, the back structure minimization and the difference in shoulder and hip joint location using the rigid-back structure and its implication on bulkiness.

5.2 Exoskeleton Subdivision

In Chapter 4 simplifying trajectories were looked at for motion capture data points following the assumption that the foot of the exoskeleton could be modelled being in single-point contact with the ground. Here the full implication of that on the exoskeleton model will be considered, as well as identify a method of creating a back model adapted to the motion capture data.

5.2.1 Exoskeleton Interaction Points

In order to start the design the model needs to be defined in terms of the way-points and peripheral-points described in Chapter 3. If it is assumed that the exoskeleton will be mimicking the human movement for all limbs in relation to some central point in the back, there will be 4 peripheral points and 1 way-point. This is shown in Figure 5.1. This description also correlates with the anthropomorphic kinematics used in XOS-2 and BE (Lucchesi *et al.* 2010; Army-Technology.com 2014). This will be adopted here this as the basis of the development of an optimal exoskeleton. More specifically, each way and peripheral point, is in relation to the human a location where the exoskeleton receives sensory input from the user, but needs not be a location where it receives direct sensory information from the external world. The physical implication of this is that there needs to be some sensor for the exoskeleton at this point where the human is connected.
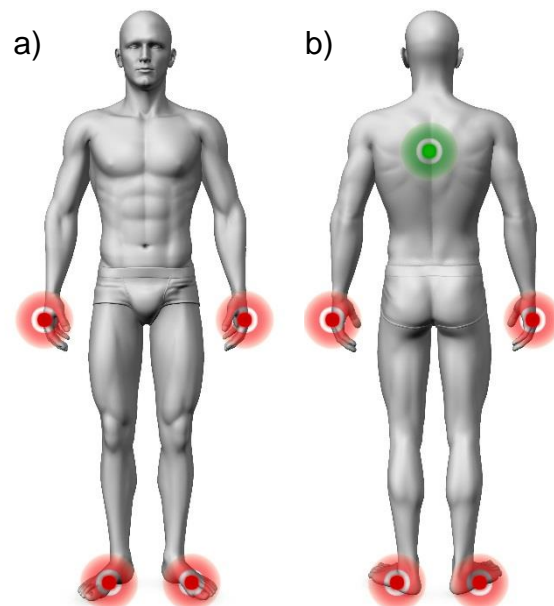
Figure 5.1 – Showing the estimated peripheral points in red
and way point in green for a) front and b) back

The input data at the arms of the exoskeleton, seen in Figure 5.2, is simplified by the assumption made that the user input is directly made on the wrist joint. At this point in the research it is not of interest to develop a gripper. Thus it is assumed that any external load the exoskeleton will carry will be on the endpoint of the arms.

From the findings in Chapter 4 on the trajectory simplification and continuing the assumption that the foot ground contact for the exoskeleton can be modelled as behaves as a point contact with the ground, it can be omitted to look at complex foot designs at the moment. This allows to model the entire leg as a two-link system, as the base case. This means that the interaction point will be set as the ankle location of the human.

As for the way-point, the connection is represented by the C6 motion capture marker. It lies beyond the scope of this research to find the optimal point to which the back should be connected to.

5.2.2 From Human to Structure

The exoskeleton model is built initially from a standing relaxed position of the human with arms to the side as seen in Figure 4.5 in Chapter 4, this is going to be called the neutral position of the exoskeleton. It is considered that the human forms the basis of the exoskeleton joint locations as well as the interaction points that the exoskeleton will follow. These are shown in Figure 5.2 (a). Lines can be drawn connecting each point as a rigid link shown in Figure 5.2 (b).

Knowing that the exoskeleton will be outside of the human, implicitly means that the rigid-back structure may have an exotic shape in comparison to the straight link. The rigid-back is connected to the shoulder and hip joint as well as the T3 marker position using 3 links. An external location is determined where two links from the T3 landmark and the Hip Joint meet shown in Figure 5.2 (c). This point is named Robot X, or rX.

Figure 5.2 d) shows how the model can be subdivided into three distinct problems.

1. The orientation in space of the rigid-back structure
2. The two-link inverse kinematics problem of the leg
3. The two-link inverse kinematics problem of the arm

The discrete (exoskeleton) shoulder and hip trajectories which are derived from the rigid-back structure, are used in the kinematic equations for the arm and leg to find the inverse kinematics.

The location of the exoskeleton hip and shoulder can be found using the relationship between the T3-marker and the human hip and shoulder markers, seen in Figure 5.3. The vectors that are drawn from T3-marker during neutral position are set in relation to eachother. This represents the set end locations of the rigid-body structure, which will therefore be known prior to shape minimization.

Once the orientation about T3-marker is found (shown in next section), this can be applied to the vector relationship of the rigid-back structure and a new trajectory for the exoskeleton hip and shoulder can be determined. These are the trajectories that will be used for points 2 and 3 mentioned above.
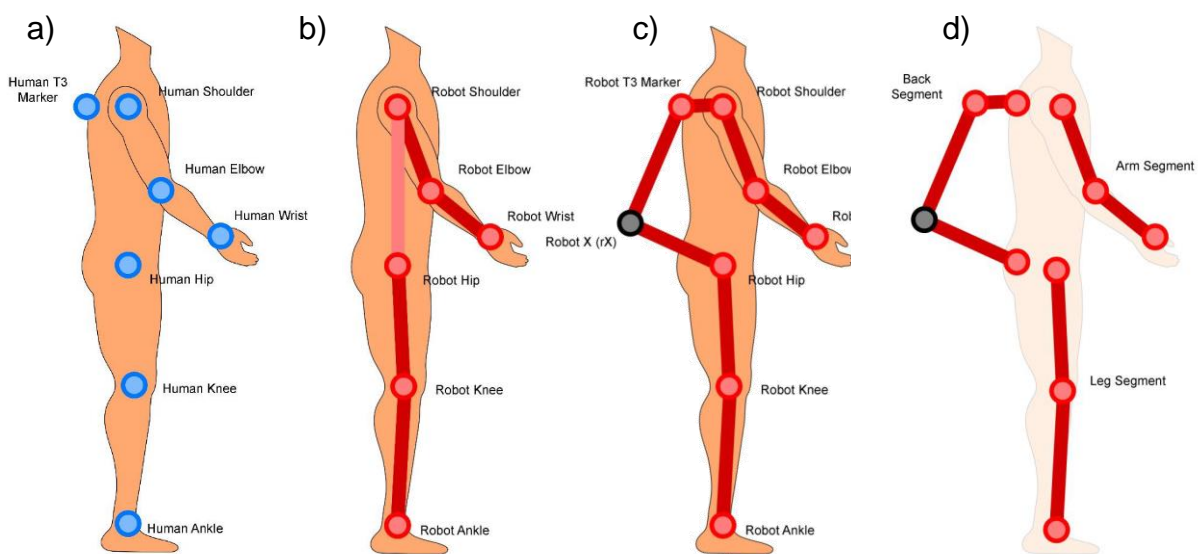
Figure 5.2 – Selected human joint and marker positions in a planar diagram used as a basis for exoskeleton modelling
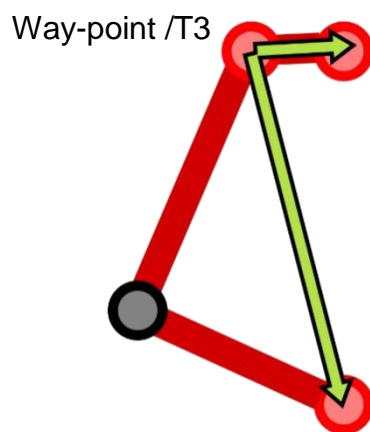
Figure 5.3 – Vector mapping shown in green arrows, with the way-point, which coincides with the T3 marker, as the origin. Using the neutral stance as starting point the vectors are locked with respect to the way-point. Once the orientation of the way-points reference frame alters due to user motion, so does the exoskeletons hip and shoulder joint locations by using the vector mappings constant relation to the way-point.

5.3 Exoskeleton Model Development

5.3.1 Methods of Generating Exoskeleton Rigid-Back Structure Orientation and Trajectories

The orientation of the rigid-back at its way-point is directly related to the orientation of the human back at the T3 landmark shown in Figure 5.1, Figure 5.2 and Figure 4.1 in Chapter 4. This will be obtained by looking at human motion capture data at the T3 landmark. By assuming that the rigid-back structure will always be tangential to that point on human the structures orientation can be found by looking at that (way) point in relation to its neighbouring points.

A couple of different methods of obtaining the orientation of the rigid-back structure are discussed in this section where generating the back orientation from the motion capture data will be looked at.

5.3.1.1 Using two Spine Motion Capture Markers, T3C6-method

If two points that are moving in planar space are kept at a uniform distance then the angular change of that line can be measured as a relative change in angle between the original location and a location some time after. In other words the line can be treated as a rigid body that has undergone some translation and some rotation over time and by knowing where the points are over time the rotation can be calculated. Figure 5.4 shows a visual representation of this in 2D space.
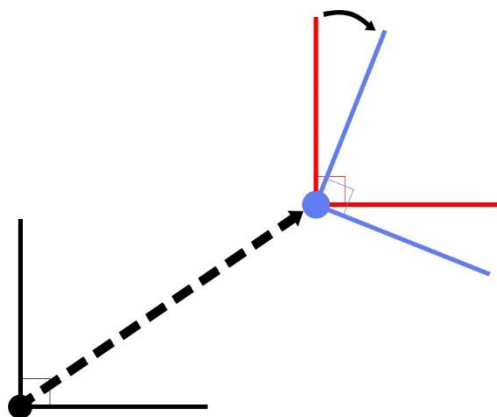
Figure 5.4 – 2D reference frame translation, from black to red, and rotation, from red to blue.

The way-point has been set atat the T3 mocap landmark, Figure 4.1 in Chapter 4 for landmark map. Ideally two points would be considered close enough for the displacements between them to be zero during motion capture. However this is somewhat impractical and can cause issues with the cameras picking up the landmarks. For this some points have been selected on the spine and the change in distances over a motion period compared. The results can be seen in Table 5-1.

Table 5-1 – Tabulated data on the relative distances of the T3 marker to the other spine markers for 'Object Lifting' motion. As can be seen the relative distance between T4 and C6 marker is shown to be smallest in all measures.

	T3 - C6	T3 -T12	T3 - L3	T3 - SM
Mean (m)	0.10533	0.20174	0.30908	0.42839
Standard Deviation	0.00205	0.00354	0.00867	0.02423
Max (m)	0.10053	0.193	0.29689	0.38525
Min (m)	0.10897	0.21017	0.32673	0.46015
Max - Min (m)	0.00843	0.01717	0.02984	0.0749

The couple T3C6 (shown in Figure 5.5) is the least changing couple and thus is used as for measuring the angular change of the rigid-back structure.
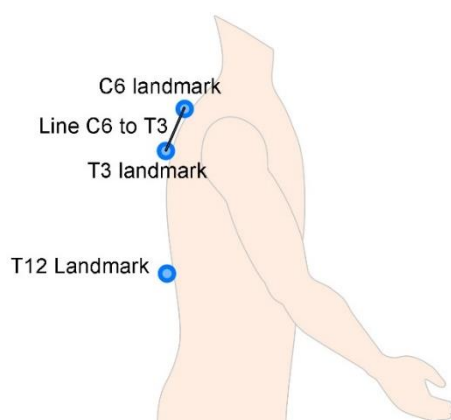
Figure 5.5- Showing the spine landmarks closest to the T3 landmark and the imaginary line connecting T3 and C6 landmark.

The difference between the T3C6-line to a reference frame at the way-point can be made at neutral position, shown in Figure 5.6. Once the angular difference between the T3C6 line is made the orientation can be found at any point in the simulation.
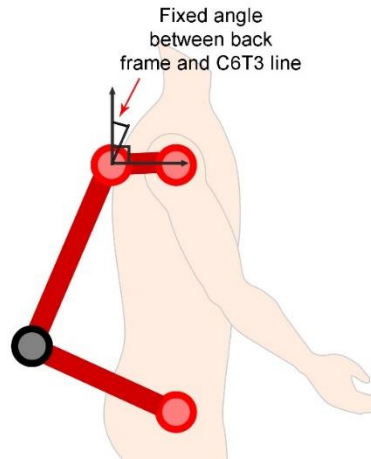
Figure 5.6 – The angle between the reference frame on the way-point and the T3C6 line is found at the neutral orientation of the rigid-back structure which occurs at standing position

5.3.1.2 Gradient Method

Mathematical solutions can be used to solve the problem for finding the gradient at the T3 landmark by using the first derivative of Lagrangian interpolation polynomial for three points, Equation 5-1, where the step size (change in x) is not uniform.

$$f'(x) \approx p'(x) =$$

$$y_{i-1}\frac{2x - x_i - x_{i+1}}{(x_{i-1} - x_i)(x_{i-1} - x_{i+1})} + y_i\frac{2x - x_{i-1} - x_{i+1}}{(x_i - x_{i-1})(x_i - x_{i+1})} + y_{i+1}\frac{2x - x_{i-1} - x_i}{(x_{i+1} - x_{i-1})(x_{i+1} - x_i)} \qquad \text{Equation 5-1}$$

For the case shown in Figure 5.7:

$$x = x_i = T3$$

$$x_{i-1} = T12$$

$$x_{i+} = C6$$

It is important to note that this is done in a reference frame local to the spine otherwise when $x_{i-1} = x_i$ or $x_{i-1} = x_{i+1}$ or $x_{i+1} = x_i$ then the equation will return undefined. This orthogonal reference frame is set at the T12 marker, with its horizontal axis pointing at C6.
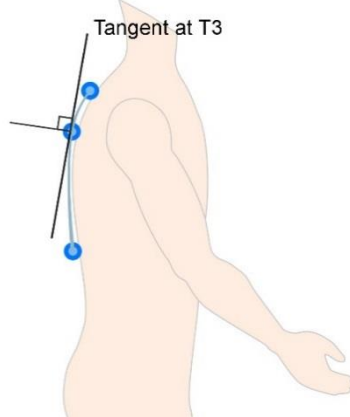
Figure 5.7 – The tangent method using Lagrangian interpolation polynomial
to find the tangent at location T3

Similar to the T3C6 method the angle between the tangent line and the frame of
the way point is found at neutral exoskeleton position this is shown in Figure 5.8.
This is set as constant and the tangent is calculated at each time instance of the
simulation. Using these two values the frame orientation is found.
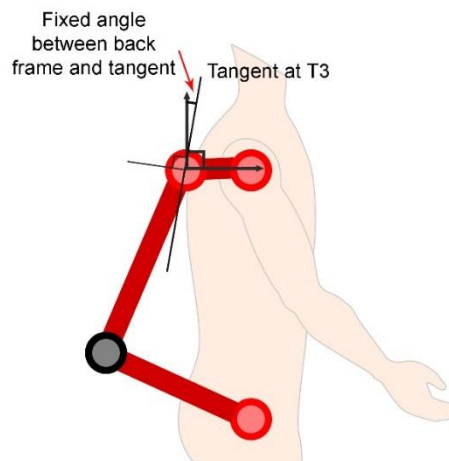
Figure 5.8 - The angle between the reference frame on the way-point
and the tangent line is found at the neutral orientation of the
rigid-back structure which occurs at standing position.

5.3.1.3 Exoskeleton Hip and Shoulder Trajectories

The two methods are compared by looking at the trajectories at three crucial points: shoulder, robot X, and hip for the back structure. The RMS error and maximum of the absolute difference values for the different trajectories using the two methods are shown in Table 5-2 for the motion.

Table 5-2 – The RMS error values and maximum absolute difference in both x and y direction when comparing T3C6 and Gradient method for 'Object Lifting' motion

	RMS(x)	RMS(y)	Max(abs(x))	Max(abs(y))
Shoulder (m)	0.0064	0.0071	0.0147	0.0206
Robot X (m)	0.00027	0.0008	0.0027	0.0083
Hip (m)	0.0064	0.0071	0.0147	0.0206

Figure 5.9 compares the angular change at T3 for 'Object Lifting' and 'Object Raising' motion. The angular change is the measure of rotation from starting point using the methods described. In the figure it can be seen that the general angular trajectory is similar between the two methods, and that the T3C6-method reaches a maximum angle which is approx. 3 degrees greater than the Gradient-method.
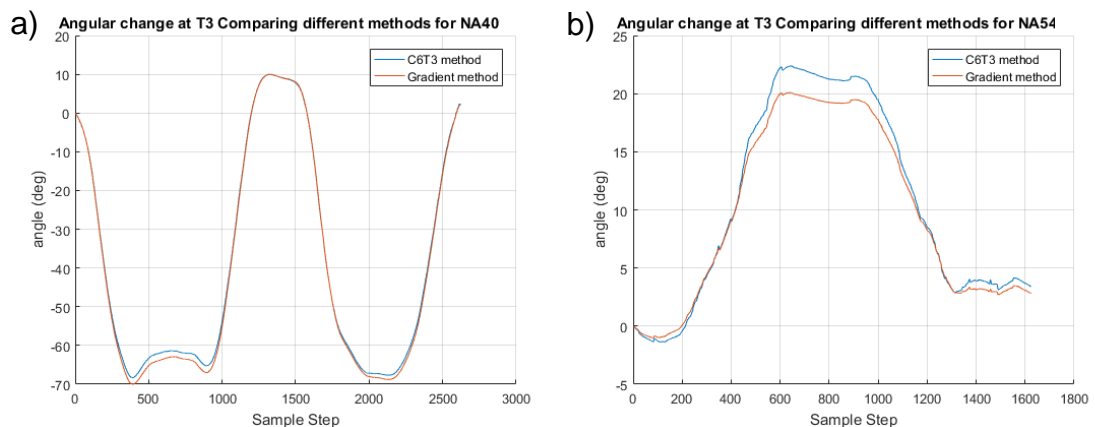
Figure 5.9 – Difference in the angular value at T3 for the two different methods considered shown for a) NA40 – 'Object Lifting' and b) NA54 - 'Object Raising'. It can be seen that theT3C6 method has at most a difference of approximately 3 degrees with the gradient method.

Using the rigid-back vector map shown in Figure 5.3, the exoskeletons hip and shoulder trajectories can be mapped out and compared to the humans, see Figure 5.10. The great differences in the very dynamic 'Object Lifting' and 'Object Raising' motion can be seen. For the former the joints start at the same location but have great discrepancies at full squat and for the latter the greatest discrepancy is for the hip joint location. It can be seen that using a rigid-back structure will change the centres of rotation for the exoskeletons joints noticeably.

a) Shoulder Hip Trajectories 'Object Lifting'

b) Shoulder Hip Trajectories 'Object Raising'
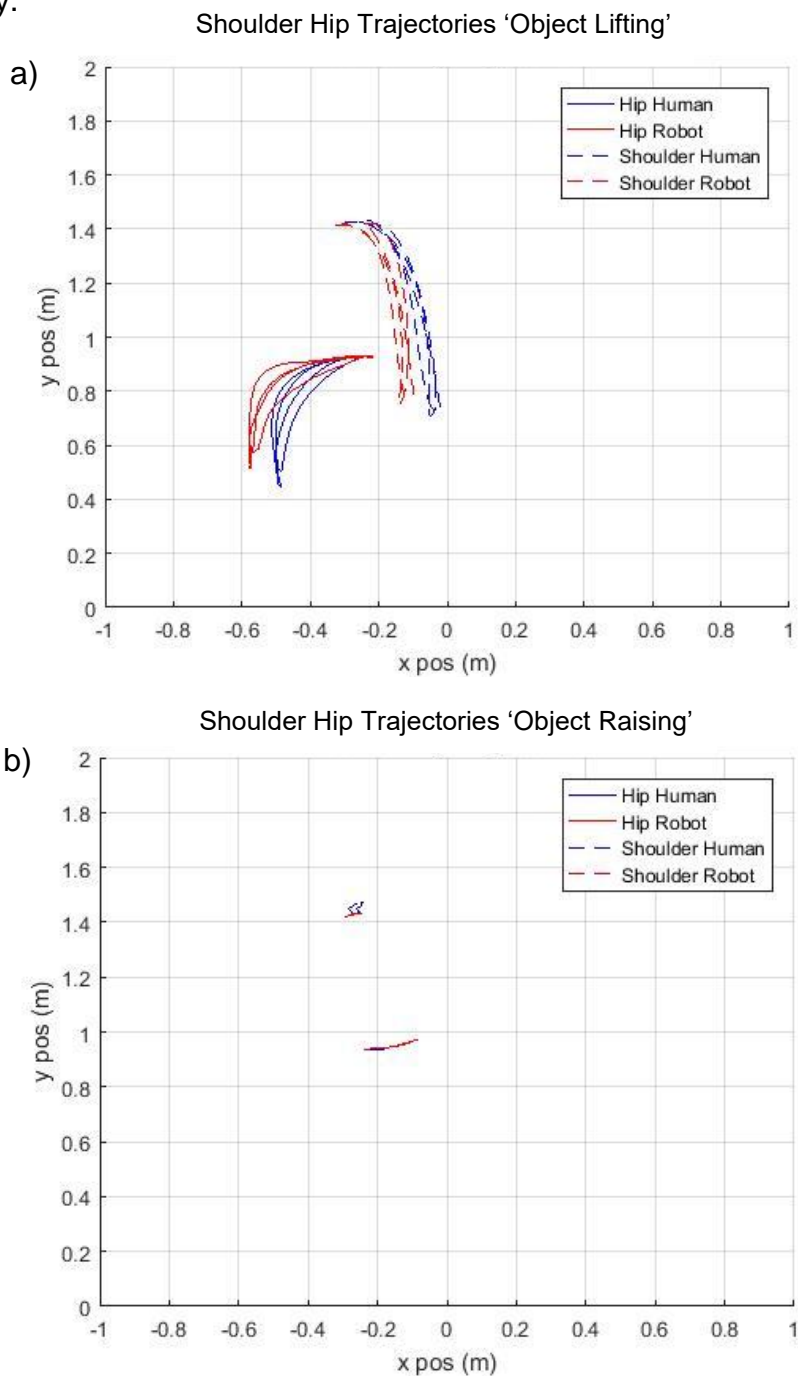
Figure 5.10 – Comparison of the human and exoskeleton robots shoulder and hip trajectories in space for lifting motions a) 'Object Lifting' and b) 'Object Raising'.

5.3.2 Rigid-Back Structure Minimization

As mentioned the back structure from point T3 to the hip is comprised of two links. This is an approximation of what can be expected to be a simplification of a detailed designed in terms of its shape. A common practise is seen in exoskeleton design to have a sturdy back structure (Army-Technology.com 2014; Lucchesi *et al.* 2010; Mosher 1967). The point of interest now is, where is the point rX going to be located.

Ideally, it is planned to keep the exoskeleton as close to the user as possible. This minimizes the bulkiness and in turn can aid to minimize the discrepancy in the centre of mass (COM) of the exoskeleton and the human. The latter is important as this aids in balancing the exoskeleton.

The distance magnitude of the link between rX and the exoskeletons hip is minimized using MATLAB function fmincon, shown in Figure 5.11. The condition of the minimization is that the vector made between rX and T3 may not cross the vectors made between, T3 and T12, T12 and L3, and SM and BR over the simulated motion (Figure 4.1 in Chapter 4). If this is violated the value for the rX and exoskeleton hip magnitude is invalid.
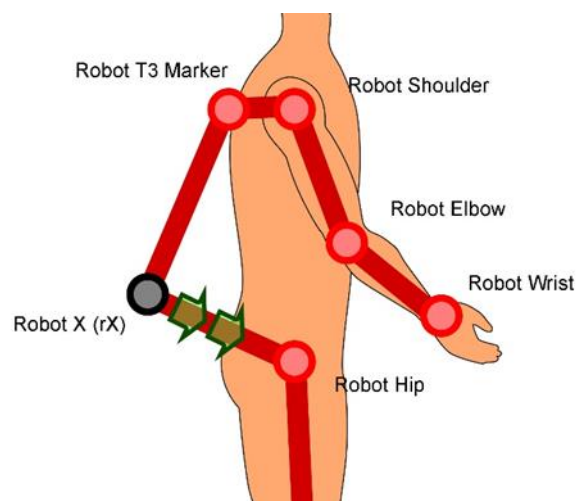
Figure 5.11 – Minimization of link connecting rX and exoskeleton hip.

The final results of the location of the rX point at neutral position can be seen in Figure 5.12 for two motions, NA40 – 'Object Lifting' and NA54 – 'Object Raising'.
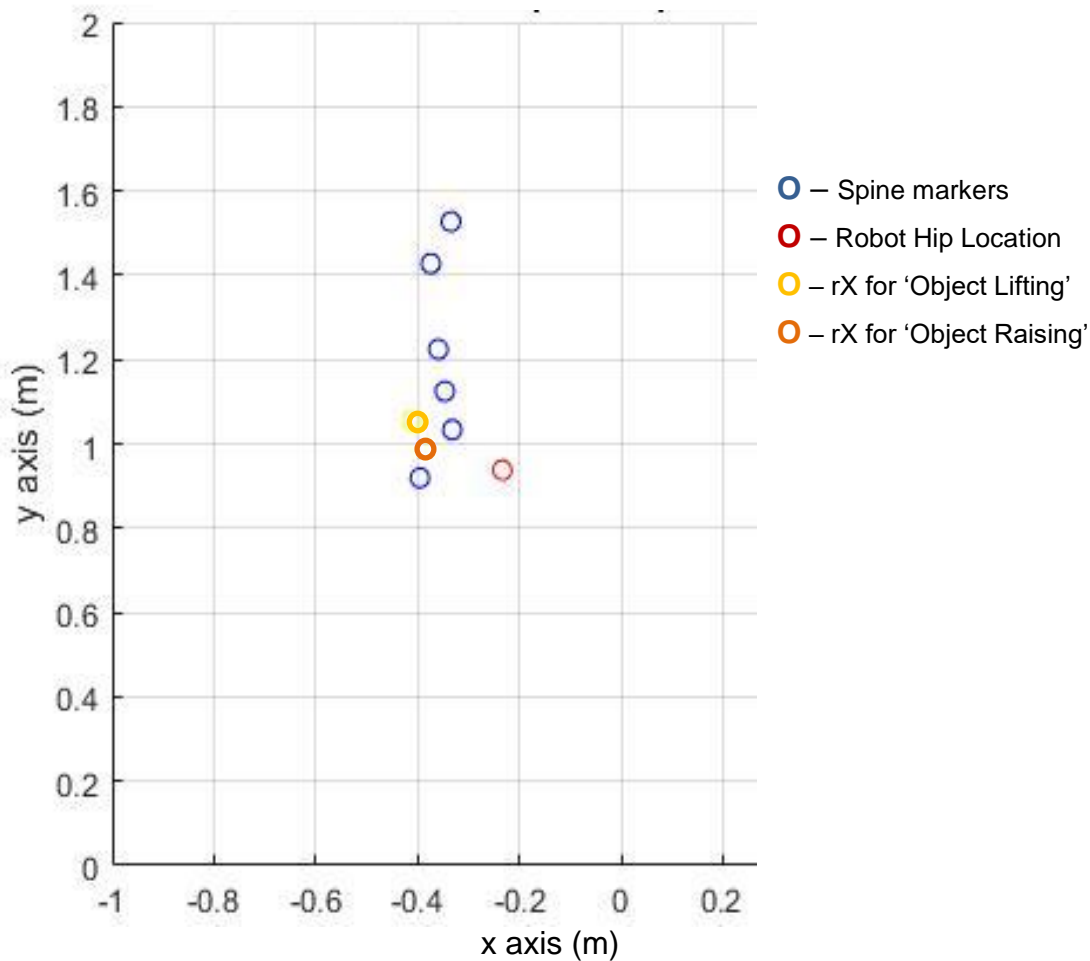
Figure 5.12 – The results of the minimization of the rX magnitude for two motions a) NA40 – 'Object Lifting' and b) NA54 - 'Object Raising' in neutral position. The back and spine markers are shown in blue circles and for reference from top down they are C6, T3, T12, L3, Sac and But.

Using the results a back geometry can be developed specifically for each motion where the lengths of the links and the angles between them are known. However it is interesting to note that the discrepancy between the two motions results are not that large. Even though they both differ quite radically in their motion patterns seen in Figure 5.10.

5.3.3 Inverse- Kinematics for Arms and Legs

As the leg and arm are simplified to two link models the inverse kinematics is well known for 2D models. Derivation of the equations can be found in APPENDIX P. For both the leg and arm case $\varphi_2 = 0$. For the leg $\varphi_1 = 90$ as it is desired that the ankle to be at 0 when standing straight, i.e. the shin is perpendicular to the foot segment. For the arm $\varphi_1 = -90$ as the shoulder is to be at 0 when vertical relaxed. The new *Dx* and *Dy* equations for the leg are:

$$Dx_{leg} = Px - \sin(\theta_1)l_1 - \sin(\theta_1 + \theta_2)l_2$$

Equation 7-8

$$Dy_{leg} = Py + \cos(\theta_1)l_1 + \cos(\theta_1 + \theta_2)l_2$$

Equation 7-9

Where:

Px and Py are x and y locations of reference frame of the ankle

$\theta_1 = \theta_1$ and is the ankle joint

$\theta_2 = \theta_2$ and is the knee joint

$l_1 = l_1$ and is the length of the shin

$l_2 = l_2$ and is the length of the thigh

And for the arm are:

$$Dx_{arm} = Px + \sin(\theta_1)l_1 + \sin(\theta_1 + \theta_2)l_2$$

Equation 7-10

$$Dy_{arm} = Py - \cos(\theta_1)l_1 - \cos(\theta_1 + \theta_2)l_2$$

Equation 7-11

Where:

Px and Py are x and y locations of reference of the shoulder

$\theta_1 = \theta_6$ and is the shoulder joint

$\theta_2 = \theta_7$ and is the elbow joint

$l_1 = l_6$ and is the length of the upper arm

$l_2 = l_7$ and is the length of the forearm

5.4 Discussion

The theories put forth in Chapter 3 regarding the way- and peripheral-points are applied in this chapter. The system is subdivided into manageable segments and each segment is looked at.

It is seen that the 2D exoskeleton model can be divided into 3 distinct segments. The lower limb, the back structure and the upper limb. This correlates with previous exoskeleton designs and is the simplest anthropomorphic design of the exoskeleton.

5.4.1 Differences in Back Orientation Methods

In order to commence the optimization work a continuation of the trajectory work presented in Chapter 5 needs to occur. Unlike with the human body, the exoskeleton back structure is rigid and is connected to the human at T3, its only way-point. This means that during motion the centres of hip and shoulder joints for human and exoskeleton will alter, therefore the hip and shoulder trajectories cannot be used as substitutes in the exoskeleton model simulation for trajectory information. As seen the orientation information for the back structure is obtained using two different methods, using spine motion markers, T3C6-method and by gradient method.

Using the T3C6 method means assuming that the distance between the two markers are near enough static that the line can be treated as a rigid bar in space with a reference frame at T3. In 2D scenario this is enough to obtain the orientation. The crucial issue here is that two vertebrae are not fused and therefor the markers will move relative to one another. This error can be minimized by moving the markers closer to one another. The limit of how close the markers can be is dependent on the motion capture equipment as too close will mean that discerning the marker locations will become impossible.

The gradient method uses the Lagrangian interpolation polynomial for three points. This method uses more information to obtain a gradient at the point of interest, which can be used to calculate the orientation. The primary difficulty with using this method is that it is an equation with denominators, therefore as the denominator goes towards zero the outcome will tend towards infinity, and when it is zero it will be undefined. Therefore a local reference frame is used, where the horizontal line is made by drawing a line from T12 and C6.

Comparing the two methods, by looking at the difference in the way point angular change for two motion (NA40 – 'Object Lifting' and NA-54 – 'Object Raising'),

found in Figure 7.9, it can be seen that there is some discrepancies in the methods. The largest error seems to occur at the peaks of the angular change curves.

Moving forward the methods could be verified by using motion capture markers closer to eachother and compare the effects of this. Certainly knowing how and where specifically the exoskeleton would be attached to the user in more detail might add to the model generation and selection of calculating the rigid back structure orientation. Furthermore the development of a test harness to be worn during motion capture trials would provide data about the position information of the actual module interface when performing motions. Overall, the methods only have a maximum of approximately 3 degree difference which may not be negligible, but is deemed not so large to have damaging effects on the simulation moving forwards as it corresponds to a 3 degree tilt which is considered for when performing the back structure minimization.

5.4.2 Back Structures Minimization

After obtaining the orientation data for the back structure, the data is used to obtain three pieces of information, a minimized back structure, exoskeleton hip trajectory and exoskeleton shoulder trajectory.

The minimization is purely geometric and focuses on minimizing the distance between the rX joint location and the human hip location. The constraint being that the vector between the way point and rX cannot lie on or be behind any of the vectors created when drawing a line between the back markers for any instance of time during the motion. The minimization runs through the entire motion and the smallest vector is selected which satisfies the above constraints.

When applying this method of optimization for two motions which is known to have a high bending of the back, it is seen that the resulting location of rX are quite similar. Though the back structure minimization does not directly focus on COM and beam bending, it could be assumed that by minimizing the lengths of the beams connected to rX, the beam bending and COM are considered indirectly. However, this method could be expanded by applying considerations of COM and beam bending, if only to verify. If the COM of the user is known from the motion capture models, this trajectory (through the motion cycle) could be used as the location to which the exoskeleton COM would be minimized towards. As will be shown in Chapter 6 the optimization methods will take into consideration the change in thickness of the structure for lower and upper limbs

as they are optimized with beam bending as constraints as well. Similar considerations could be made for the back structure during the minimization.

In this scenario the minimum structure is considered, where the back is a rigid one. An alternative would be to increase the number of way-points on the back structure to for example 2. This way some mechanism could be developed for the spine allowing the design to be more 'snug'. Using the back orientation methods described the unknown orientation of the exoskeleton segments could be found. Though the exoskeleton complexity would increase, it remains a research question whether or not introducing this extra complexity would be directly correlate with added bulkiness.

5.4.3 Difference in Hip and Shoulder Trajectories in Exoskeleton and Human and Impact on Bulkiness

Using the orientation data (Figure 5.9) and vectors (Figure 5.3) new trajectories for the exoskeleton hip and shoulder joints are derived. The back minimization takes into consideration that the user is safe from impact with the exoskeleton. The comparison, seen in Figure 5.10, shows that having a rigid back structure and using the standing relaxed position as starting point has a significant impact on the exoskeleton hip and shoulder trajectories. Interestingly bulkiness has so far been talked about in a static context. It is seen that this definition can be expanded into two classes, static bulkiness and active bulkiness. Where the static refers to bulkiness as is designed, by measuring the distance of the exoskeleton when in standing relaxed positon and active bulkiness refers to extreme cases in motion. This strengthens the notion that the exoskeleton should be designed with a task in mind, as it can then be guaranteed for that task.

5.4.4 Tip Rotation Effects

In this research the assumption is made that the weight of the external load is a point. When the link length changes, the orientation of the tip reference frame will not be the same as the users. Omitting the wrist rotation to compensate for a changing orientation of the load means that the effects of a load that is not a point load will not be considered. At this level of research the effects are accepted as the model uses a point load and "hand" segment with a gripper for the exoskeleton is beyond the scope of this thesis.

5.5 Summary

In this chapter the exoskeleton was subdivided using the methods of peripheral and way points and the results of the trajectory analysis of the motion capture data. By using the standing relaxed pose as the starting point the 2D model of the exoskeleton is simplified into 3 segments. The middle segment is looked at first, as its output will contribute to the other two.

A vector mapping and the orientation of the back structure is developed and analysed. The vector mapping is derived using the way point identified as the origin and the two vectors from the origin are to the hip and shoulder joints of the user. Two different methods of obtaining the orientation of the rigid back structure are compared. The first one looks at using only two points from the motion capture trials. Here the assumption is that the line connecting the two points are close enough to be considered static. The second method uses Lagrangian interpolation polynomial. This method although uses more points on the back and could therefore give a more accurate measure of the orientation, is dependent on selecting a reference frame in such a way that division by zero does not occur. Ultimately the discrepancy between the two methods are approximately 3 degrees. The vector mapping in combination with the back structure orientation is used to generate new trajectories for the exoskeleton hip and shoulder joint locations for the motions.

The back structure is minimized such that it never crosses the interconnecting lines of the back markers from the motion capture experiment, ensuring that for the specific motion, the exoskeleton does not collide with the user. Indirectly this may also stabilize the exoskeleton as the COM would be displaced towards the users own.

Kinematic equations for the two limbs which will be used in the optimization algorithm are presented as well. This information will be used together with the vector mapping of the back-structure and the method of obtaining orientation of the back-structure relative to the marker positions in the optimization to follow in Chapter 6.

Chapter 6
Optimization of Link Parameters

6.1 Introduction

This chapter will focus on and present two optimizations and their results. The first section focuses on optimization of both mass and cross-section geometries (specifically outer radius) of the exoskeleton links with constraint on beam deflection. The following section investigates the effects of altering the lengths of relevant links, that is to find the optimal position for the knee joint and for the elbow joint for minimizing power consumption. The cross-section/mass optimization is incorporated in the link-length optimization to find the optimal torque.

For the cross-section/mass optimization section the equations of simple geometries' (circle, square and rectangle) cross-sections are firstly compared. Specifically they are looked at from the perspective of their second moment of area. The focus is on the change in second moment of area when converting a circle to square or rectangle when maintaining the mass. The (multi-objective) optimization is demonstrated using an example, a simple pendulum with an external mass. Following the example the results for the full-system cross-section dimension and mass optimization are presented for NA40 - 'Object Lifting' and NA54 - 'Object Raising' motions. The results of the optimization are verified using simple FEA simulations. Following the optimization the cross-sections are reshaped using the relations presented in the beginning of the section and verified again using FEA.

The second section will explain the ratio, 'r', term that is used to relate the two link lengths being optimized to their total length. The mechanical work term which will be used as a basis of investigation together with maximum absolute torque is presented. Following this the results are presented for varying values of 'r'.

Finally the results will be discussed. Specifically the effects of cross-section dimensions and mass optimization will be discussed. The effects of solid vs. hollow links will be compared. The effects of the changing of link lengths will be discussed in detail. The results of geometry reshaping and the potential usage as an indicator of factor of safety is discussed. Lastly the chapter is summarized.

6.2 Link Cross-section Geometry Optimization

6.2.1 Simple Cross-section Geometry Comparison

The cross-section and mass optimization begins with a study into the effects of different cross-sections on the second moment of areas when constrained to an equal mass. As the complexity increases when using rectangular bars having to use two variables (four for hollow bars) when optimizing this study becomes important in order to select an appropriate starting point. The mass constraint is added as this is the inherent property of the material which will also increase power consumption. In the end of this section the results will be applied to the optimized results.

The second moment of area are shown in Equation 6-1, Equation 6-2 and Equation 6-3 for circles squars and rectangles respectively.

$$I_{2nd,C} = \frac{\pi}{4} * (r_0{}^4) \qquad\qquad \text{Equation 6-1}$$

$$I_{2nd,S} = \frac{1}{12} * (b_0{}^4) \qquad\qquad \text{Equation 6-2}$$

$$I_{2nd,R} = \frac{1}{12} * (b_0 h_0{}^3) \qquad\qquad \text{Equation 6-3}$$

The equations for masses of the links with the geometries are shown in Equation 6-4, Equation 6-5 and Equation 6-6

$$m_C = \rho_C l_C A_C \qquad\qquad \text{Equation 6-4}$$

$$m_S = \rho_S l_S A_S \qquad\qquad \text{Equation 6-5}$$

$$m_R = \rho_R l_R A_R \qquad\qquad \text{Equation 6-6}$$

Since the concern here is to obtain the second moment of area with a maintained mass, they are all equated as shown in Equation 6-7 and Equation 6-8.

$$m_C = m_S = m_R \qquad\qquad \text{Equation 6-7}$$

$$\rho_C l_C A_C = \rho_S l_S A_S = \rho_R l_R A_R \qquad\qquad \text{Equation 6-8}$$

When the densities and the link lengths are the same, $\rho_C \equiv \rho_S \equiv \rho_R$ and $l_C \equiv l_S \equiv l_R$, they will cancel out and we are left with Equation 8-9.

$$A_C = A_S = A_R$$

<div align="right">Equation 6-9</div>

First, the case of a circle compared to a square is looked at. The area equations are shown in Equation 6-10 and Equation 6-11.

$$A_C = \pi r_o{}^2$$

<div align="right">Equation 6-10</div>

$$A_S = b^2$$

<div align="right">Equation 6-11</div>

These are substituted into Equation 6-9 for the circle and the square, shown in Equation 6-12. The resulting manipulation can be seen in Equation 6-13 and Equation 6-14.

$$b_o{}^2 = \pi r_o{}^2$$

<div align="right">Equation 6-12</div>

$$b_o = \sqrt{\pi} * r_o$$

<div align="right">Equation 6-13</div>

$$b_o \cong 1.77 * r_o$$

<div align="right">Equation 6-14</div>

Substituting the b_o value into Equation 6-2 the second moment of area of a square can be expressed in terms of the outer radius of the circle, Equation 6-15.

$$I_{2nd,S} = \frac{1}{12} * \pi^2 * r_o{}^4$$

<div align="right">Equation 6-15</div>

The coefficients of Equation 6-1 and Equation 6-15 can be evaluated, shown in Equation 6-16 and Equation 6-17.

$$\frac{1}{12} * \pi^2 \cong 0.8225$$

<div align="right">Equation 6-16</div>

$$\frac{1}{4} * \pi \cong 0.7854$$

<div align="right">Equation 6-17</div>

This shows that Equation 6-18 is true.

$$I_{2nd,S} > I_{2nd,C}$$

<div align="right">Equation 6-18</div>

By substituting into Equation 6-18 the increase in second moment of area can be expressed as a ratio shown in Equation 6-19.

$$1.05 : 1$$

<div align="right">Equation 6-19</div>

Similar derivation using substitutions and manipulations can be done when relating the change in second moment of area of a circle to a rectangle. The key difference is that a rectangle's second moment of area for its two planar principle axes are different, due to the difference in height and width. Therefore an artificial

constraint must be placed such that either value of h_o or b_o can be found. The constraint chosen is to have the y direction second moment of area be greater than or equal to the second moment of are of the circle.

$$I_{2nd,R,y} \geq I_{2nd,C}$$

Equation 6-20

The area of a rectangle is shown in Equation 6-21.

$$A_R = b_o * h_o$$

Equation 6-21

Substitution of Equation 6-21 and Equation 6-10 into Equation 6-9 results in Equation 6-22. The equation is rearranged for r_o and shown in Equation 6-23.

$$b_o * h_o = \pi r_o^2$$

Equation 6-22

$$r_o = \sqrt{\frac{b_o * h_o}{\pi}}$$

Equation 6-23

Substituting the value of r_o into the second moment of area equation for a circle, Equation 6-1, gives Equation 6-24.

$$I_{2nd,C} = \frac{(b_o * h_o)^2}{\pi * 4}$$

Equation 6-24

Equation 6-20 can now be expanded to Equation 6-25

$$\frac{1}{12} * (h_0 b_0^3) \geq \frac{(b_o * h_o)^2}{\pi * 4}$$

Equation 6-25

This simplifies so that b_0 can be expressed in terms of h_o in Equation 6-26.

$$b_0 \geq h_o * 0.955$$

Equation 6-26

Substituting the b_0 into Equation 6-23 and rearrange for h_o, Equation 6-27.

$$h_o = \frac{r_o}{\sqrt{\frac{0.955}{\pi}}}$$

Equation 6-27

Now the two second moment of areas can be expressed in terms of h_o shown in Equation 6-28 and Equation 6-29.

$$I_{2nd,R,x} = \frac{1}{12} * (0.955 * h_0^4)$$

Equation 6-28

$$I_{2nd,R,y} = \frac{1}{12} * (0.955^3 * h_0^4)$$

Equation 6-29

Using Equation 6-27, the relationship with r_0 can be seen in Equation 6-30 and Equation 6-31.

$$I_{2nd,R,x} \cong 0.8612 * r_0{}^4$$

<div align="right">Equation 6-30</div>

$$I_{2nd,R,y} \cong 0.7854 * r_0{}^4$$

<div align="right">Equation 6-31</div>

So the coefficients show that in the principal x direction the second moment of area of the rectangle is greater than the circle Equation 6-32 and remains the same in the principle y direction.

$$I_{2nd,R,x} > I_{2nd,C}$$

<div align="right">Equation 6-32</div>

$$I_{2nd,R,y} = I_{2nd,C}$$

<div align="right">Equation 6-33</div>

Again the ratio is found and shown in Equation 6-34

$$1.10 : 1$$

<div align="right">Equation 6-34</div>

The equation manipulation done here serves as a proof that the simple geometry of a circle can be related to other simple geometries with greater second moment of area characteristics with relative ease. We also see that there is only a 10% increase in strength when using a rectangle over a circular shape. However optimization with two variables would mean more computation time and model complexity, therefor the optimization that ensues will use a circle as the cross-section geometry.

6.2.2 Single Pendulum Multi-Objective Optimization Example

The relationship between the mass and outer radius in a hollow cylindrical tube link will be considered. The tube is given an oscillatory sinusoidal trajectory to follow. The tube is fitted with an external load attached at its end. The system is illustrated in Figure 6.1.
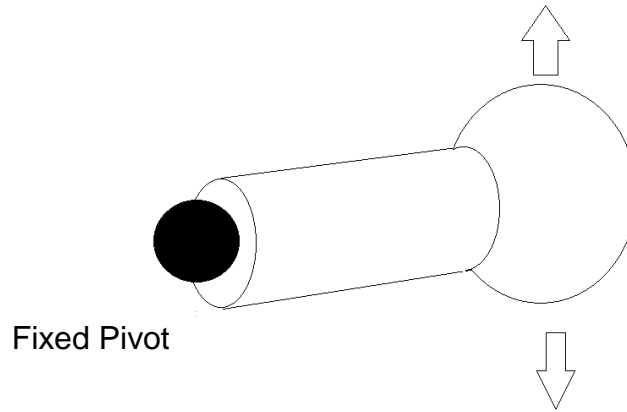
Figure 6.1 – Illustration of single link + external mass system.

As it is desired to compare the effects of two parameters the problem becomes a multi-objective optimization. The two objectives are minimizing both mass of the tube link and outer radius. The variables of the optimization are inner radius (r_i) and wall thickness (th). The constraint is the deflection (δ) of the link. The objective function equations are shown in Equation 6-35 which is used to find the outer radius and Equation 6-36 which is used to find the mass, Equation 6-37 is used to find the volume of the link. The constraints are calculated by looking at the second moment of area, Equation 6-38 of a hollow tube and the beam deflection equation shown in Equation 6-39 for a cantilever.

$$Objective1 = r_o = r_i + th$$
Equation 6-35

$$Objective2 = mass = V * \rho$$
Equation 6-36

$$V = l * \pi * (r_o{}^2 - r_i{}^2)$$
Equation 6-37

$$I_{2nd} = \frac{\pi}{4} * (r_0{}^4 - r_i{}^4)$$
Equation 6-38

$$\delta = \frac{F_y * l^3}{3 * E * I_{2nd}}$$
Equation 6-39

In the example simulation set here the link length, l, is set to 0.3 m, an approximate value of the arm links calculated by looking at the maximum distance from wrist to shoulder location in the motion capture trials. The external

mass is set to 45kg which is the required amount from the external requirements. and the density and young's modulus is set to that of aluminium 6061-T6. The maximum allowable deflection will be set to 0.001 m for this research. The effects of altering this constraints will be considered in the future works section.

The optimization is performed using MATLAB's global optimization toolbox. Specifically, the Genetic Algorithm (GA) optimization method is used (gamultiobj() function call in MATLAB). It allows for non-linear optimization at a large scale. This is made necessary as part of the optimization entails calling Simulink and running multibody physics simulation in Simulink. The work flow is shown in Figure 6.2.
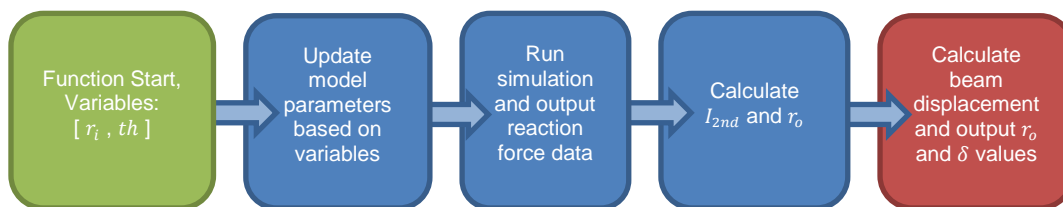
Figure 6.2 – Flow chart of the key steps in the constraint function used in the multi-objective-optimization

The options for using gamultiobj() are kept as standard, apart from the maximum time which is set for time constraint purposes as well as the option to vectorize the process. The vectorization allows for the variables to be passed as matrices and therefore the calculations can occur simultaneously as matrix calculations, the option can also be made to use parallel computing. Parallel and vectorized computation cannot both be select simultaneously. Vectorized computation is preferred at this stage over the parallel computing option as the version of MATLAB used for this research cannot simulate Simulink models in parallel. This creates a bottleneck in the program and is the greatest time drain in the optimization as all the simulations in the constraint function must occur in series.

The results of the optimization yields in a pareto-front shown in Figure 6.3. The figure shows that as the mass of the link increases the outer radius of the link decreases. This also means that the thickness of the link increases to accommodate for the volume needed to produce such increase in mass.

Although this served as an example to illustrate the procedure it can be seen that for a given motion that the system is expected to undergo with some mass similar

to what will be used in the simulations, 1) a pareto front exists and, 2) there might be some drastic changes in the mass of the links.
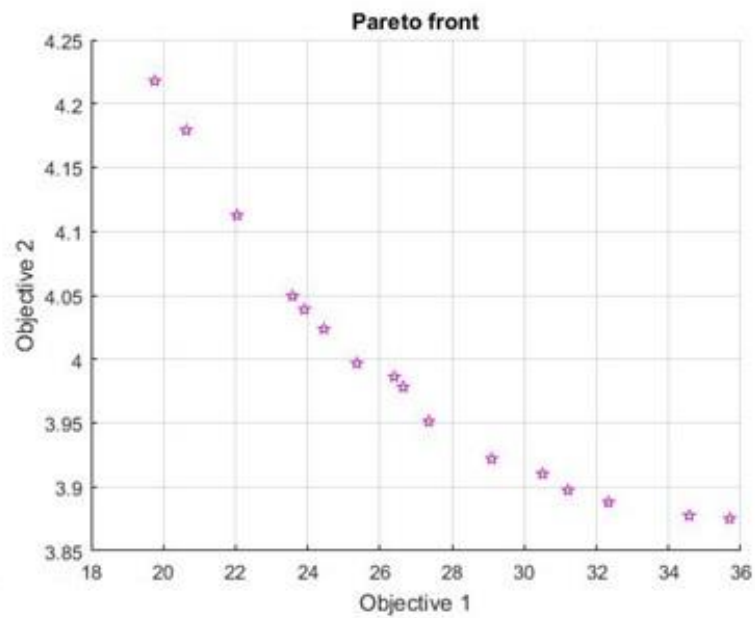
Figure 6.3 – Pareto front for single pendulum mass/diameter optimization

6.2.3 Full-System Cross-Section Dimensions and Mass Optimization

The example shown earlier is adapted to sequentially optimize the links of the exoskeleton model. By virtue of simplifying the model as described in Chapter 7 to a 2D problem it can be assumed for the 'Object Lifting' and the 'Object Raising' motions that the exoskeleton's dynamics and kinematics are mirrored about the central axis in the frontal plane. All of the exoskeleton models links are now in sequential order from external weight to ground.

It has previously been shown that depending on the cross-section geometry the strength of the link can increase, i.e. by changing its second moment of area whilst retaining a similar general mass. The optimizations will look at solid and hollow cylinders performing the same motion with and without an external load and the results will be compared. These two have significantly different optimization approaches due to the number of parameters being optimized and number of variables in the optimization. The multi-objective approach for the hollow tubes described previously utilized a GA approach. However for the cylinder, with one variable 'outer radius' and one goal, to minimize the mass it is sufficient to use MATLAB's fmincon().

As the goal is to find the geometries associated with a minimum mass an algorithm for avoiding using a full-scale approach, that is to optimize everything at the same time, is considered. One could argue that potentially the optimization could be done on the total mass of the system such as in Equation 6-40, where n is the total number of links.

$$M_{total} = \sum_{i=1}^{n} m_{link\,i}$$

Equation 6-40

This would yield in an optimization with multiple variables equalling the number of links. This number would be squared for hollow tubes. Stopgaps would need to be put in place for the issue of the overall mass being minimized but not the local link masses. Using a GA for a task like this could also create unnecessary overhead. The fact that the hollow tube already is a multi-objective problem significantly complicates this approach. Therefore to minimize time and to avoid the uneven distribution of the local masses, the optimization problem is subdivided to smaller pieces. Each link is optimized in sequential order.

The optimization algorithm is shown in Figure 6.4. The program starts by creating setting the model in Simulink. The model generation has been presented and discussed in previous chapters and it is those parameters found that are used when instantiating the exoskeleton model geometric properties.
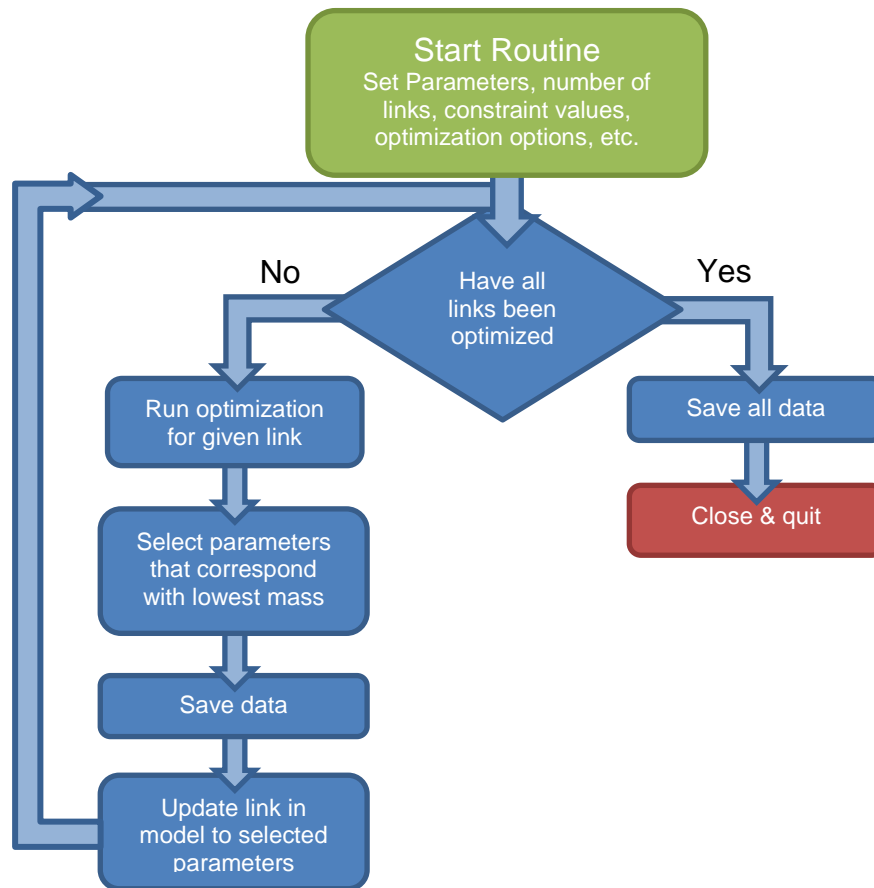
Figure 6.4 – Diagram of the general algorithm used for optimizing the exoskeleton model

During the process of assigning the exoskeleton model properties the start routine also sets the motion trajectories (including the velocity and accelerations), as developed in Chapter 4 and Chapter 5, for actuated joints. The optimization parameters are set as described above.

Once the start routine has finished the algorithm checks if all links have been optimized. As long as this is not true, the links will be iteratively optimized. The results of the optimization is saved, and the model is updated, using the parameters associated with the lowest mass value in the pareto front. This ensures that the overall weight of the model is minimized. Once all of the links have been optimized the algorithm saves all the relevant data and closes.

The results of the optimization are presented for each motion below.

6.2.3.1 Cross-Section Dimensions and Mass Optimization Results for Object Lifting Motion

It can be seen the optimized dimensions and masses of each link in Table 6-1 and Table 6-2 for the 'Object Lifting' motion. Table 6-1 shows the results for a solid cylinder and Table 6-2 shows the result for hollow tube optimization.

Table 6-1 - Link geometries for 'Object Lifting' motion using solid cylinder, the total mass of the links come to 6.5583 kg

	Length (mm)	Radius (mm)	Mass (kg)
ForeArm	300	14.63	0.5454
UpperArm	300	16.24	0.6696
Back Link 1	104.66	7.5	0.0513
Back Link 2	429.35	23.19	1.9602
Back Link 3	169.26	10.84	0.1701
Thigh	428	23.56	2.0142
Shin	428	17.77	1.1475

Table 6-2 - Link geometric properties for 'Object Lifting' motion using a hollow tube, the total mass is 0.26133 kg.

	Length (mm)	Radius (mm)	Thickness (mm)	Mass (kg)
ForeArm	300	15.19	5.63	0.0808
UpperArm	300	29.92	1	0.0025
Back Link 1	104.66	7.52	4.55	0.0184
Back Link 2	429.35	39.88	1.14	0.0047
Back Link 3	169.26	14.7	1.16	0.0019
Thigh	428	41.03	1.08	0.0042
Shin	428	31.1	6.4	0.1488

The pareto front for each link is shown in Figure 6.5. The torque values are shown in Figure 6.6 for the model with an external mass attached to it and in Figure 6.7 without any external load. Figure 6.8 shows the reaction forces at the base of each link in both the local x and local y direction.

Pareto-front results for 'Object Lifting' motion hollow tube geometry optimization
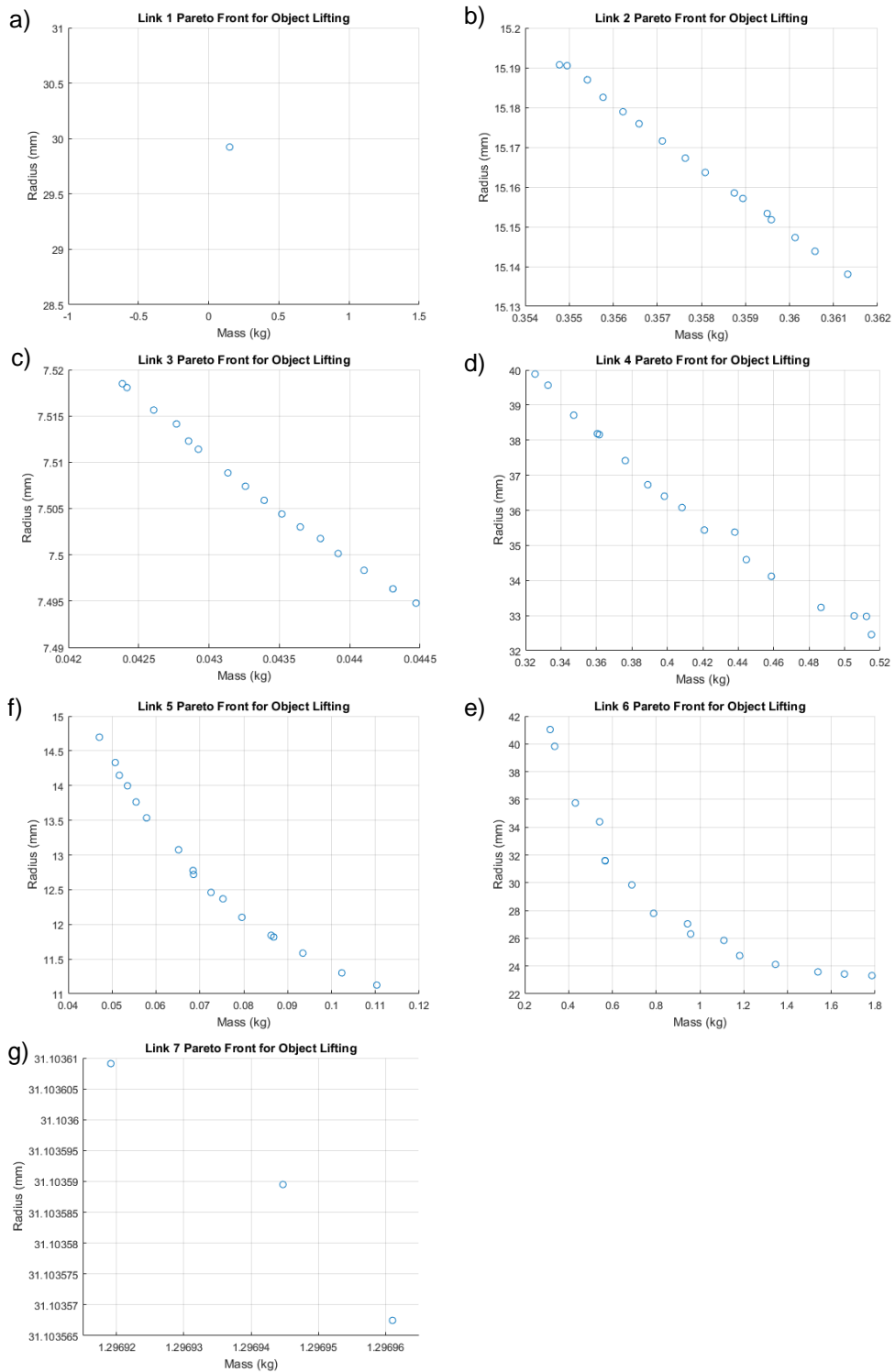
Figure 6.5 – Pareto optima graphs for 'Object Lifting' motion using hollow tubes. Graphs display the results of the multi-objective optimization, the objectives being minimizing radius and minimizing mass.

Torque results for 'Object Lifting' motion cross-section optimization
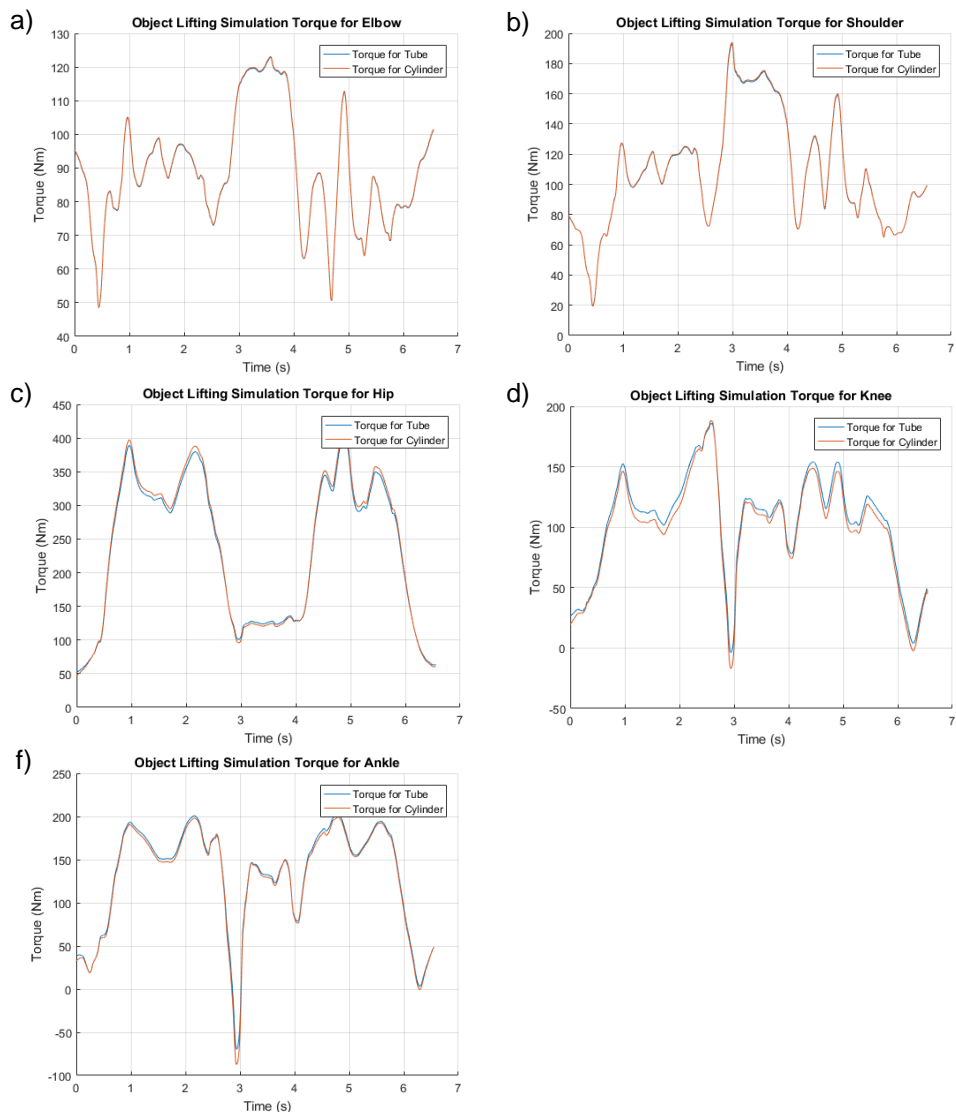
Figure 6.6 – Torque values of the actuated joints with an external mass of 45 kg attached at the end of the forearm link for 'Object Lifting' motion

Following the cross-section optimization the tube and cylinder models are simulated and the resulting torque data has been plotted in Figure 8.7. It can be seen that the variation in link masses has some relative significant effect on the torques experienced on the joints when there exists no influence of an external mass.

Simulation results for 'Object Lifting' motion with zero external mass
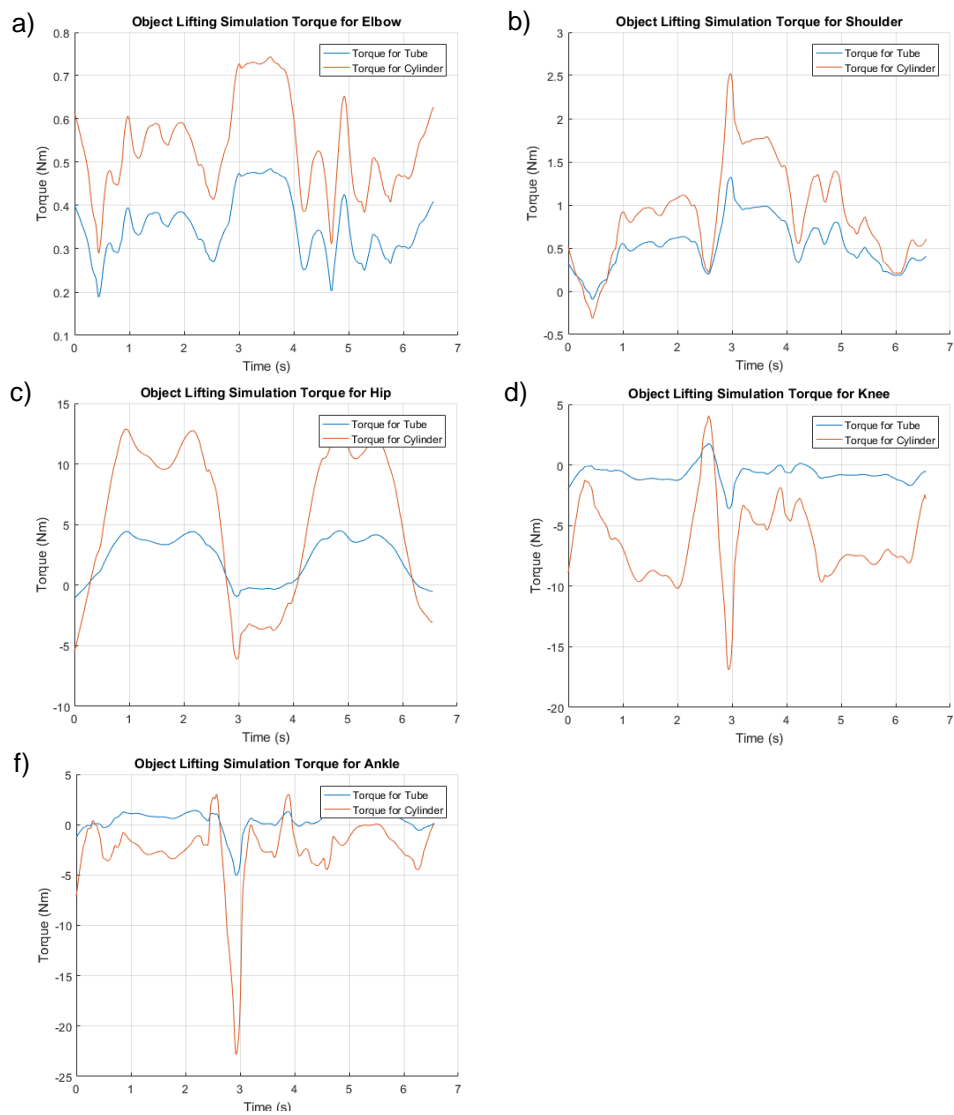
Figure 6.7 – Torque values of the actuated joints without an external load being carried for 'Object Lifting' motion

Reaction force results for 'Object Lifting' motion cross-section optimization
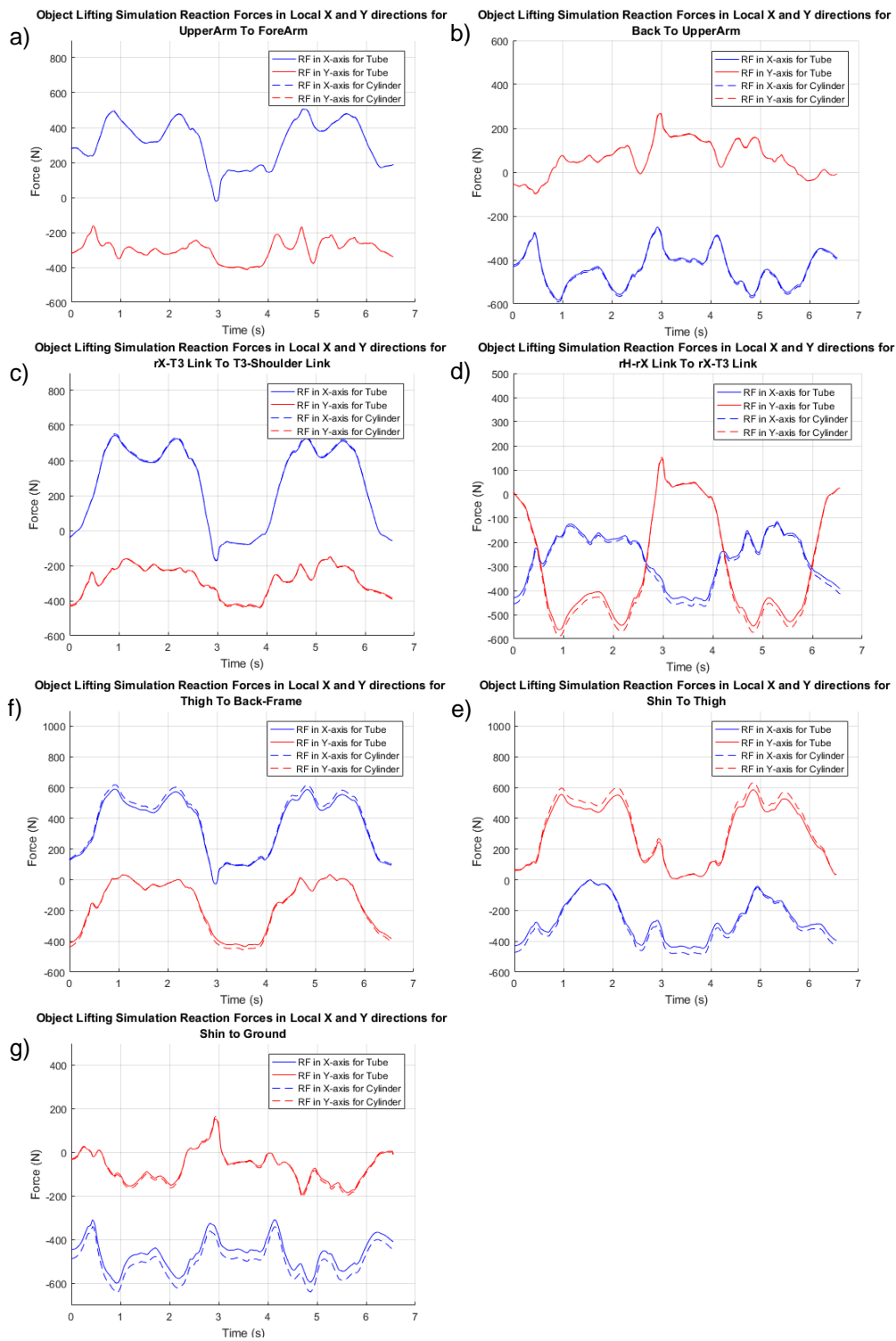
Figure 6.8 - reaction forces between links used to calculate beam bending of the model with an external mass of 45 kg attached at the end of the forearm link for 'Object Lifting' motion

Table 6-3 – Maximum and minimum reaction forces from the MATLAB simulation based on the 'Object Lifting' motion to be used in the FEA. The direction indicates weather the force is in the compressive (negative) or tensile (positive) direction for the X axis. For the Y axis direction the forces indicated downward (negative) or upward (positive) direction force which would result in either clockwise or counter-clockwise bending respectively about the base of the link.

Cross-section geometry	Tube Reaction Forces (N)				Cylinder Reaction Forces (N)			
Direction	Max X	Min X	Max Y	Min Y	Max X	Min X	Max Y	Min Y
Upper Arm To Forearm	505.41	-21.22	-162.45	-411.12	507.5	-21.31	-163.12	-412.85
Back Link 1 To Upper Arm	-249.61	-582.59	267.52	-96.87	-254.27	-591.35	272.72	-98.7
Back Link 2 To Back Link 1	542.84	-169.77	-148.82	-437.88	551.2	-173.21	-151.25	-444.65
Back Link 3 To Back Link 2	-113.9	-442.74	143.51	-561.99	-120.28	-465.65	151.76	-588.05
Thigh To Back Link 3	589.55	-27.92	33.34	-434.59	617.59	-28.03	34.45	-458.54
Shin To Thigh	-0.04	-446.61	585.85	5.87	-2.54	-487.61	632.13	6.69
Shin to Ground	-307.9	-597.98	154.08	-192.58	-339.08	-640.69	164.59	-204.7

6.2.3.1.1 Simple FEA analysis of the links for 'Object Lifting' motion

Following the link cross-section optimization the reaction force data is used to perform FEA static stress analysis of link models to verify that the constraint equations for the optimization has yielded feasible result. The CAD models of the links are developed using the geometries shown in Table 6-1 and Table 6-2 on SolidWorks.

The maximum and the minimum values of the reaction forces for both x and y directions found in the plots of Figure 6.8 have been tabulated in Table 6-3. It can be understood from both figure and table that certain links (upper arm, back link 2, thigh and shin) are in compression constantly. Table 6-4 shows the corresponding reaction forces for the absolute maximum Y and minimum X values shown in Table 6-3. The absolute maximum Y force will be the force that will cause the greatest amount of bending. The minimum X force is the highest compressive load the link will experience. Since the primary concern at this stage is the bending the FEA simulations are run with the maximum absolute Y force and the corresponding compressive (X direction) force.

Table 6-4 – The reaction forces corresponding to the maximum reaction forces for 'Object Raising' motion. Due to the uniformity of the cross-section the forces in the direction in the Y axis is inconsequential therefore the x direction force corresponding to the absolute maximum Y force is found. The minimum negative X direction force is chosen as this corresponds to compression of the link.

	Tube Reaction Forces (N)		Cylinder Reaction Forces (N)	
	Force X at Max Y	Force Y at Min X	Force X at Max Y	Force Y at Min X
Upper Arm To Forearm	154.31	-365	154.95	-366.69
Back Link 1 To Upper Arm	-265.5	49.73	-270.36	50.03
Back Link 2 To Back Link 1	-38.22	-338.94	-38.83	-345.28
Back Link 3 To Back Link 2	-176.64	3.25	-183.21	4.25
Thigh To Back Link 3	94.31	-379.63	99.31	-406.52
Shin To Thigh	-76.02	32.64	-85	35.65
Shin to Ground	-521.37	-94.5	-566.37	-102.62

The results of the simulations for cylinder links using the 'object lifting' motion reaction force data have been tabulated in Table 8-5. The plots of the stress analysis can be seen in Figure 6.9 for fore arm link, Figure 6.10 for upper arm link, Figure 6.11 for back link 1, Figure 6.12 for back link 2, Figure 6.13 for back link 3, Figure 6.14 for thigh link and Figure 6.15 for shin link.

Table 6-5 – Results of the FEA simulations for cylinder (solid) links, showing the maximum Von Misses Stress, maximum displacement and the minimum Factor Of Safety as calculated by SolidWorks.

Link	Von Misses Stress (N/m^2) x10^8	Displacement (mm)	Factor of Safety
Forearm	0.6206	1.498	4.431
Upper Arm	0.3075	0.6525	8.943
Back Link 1	1.729	0.9976	1.590
Back Link 2	0.3976	0.9919	6.917
Back Link 3	0.9944	0.9949	2.765
Thigh	0.4299	0.9916	6.397
Shin	0.2797	0.9900	9.833
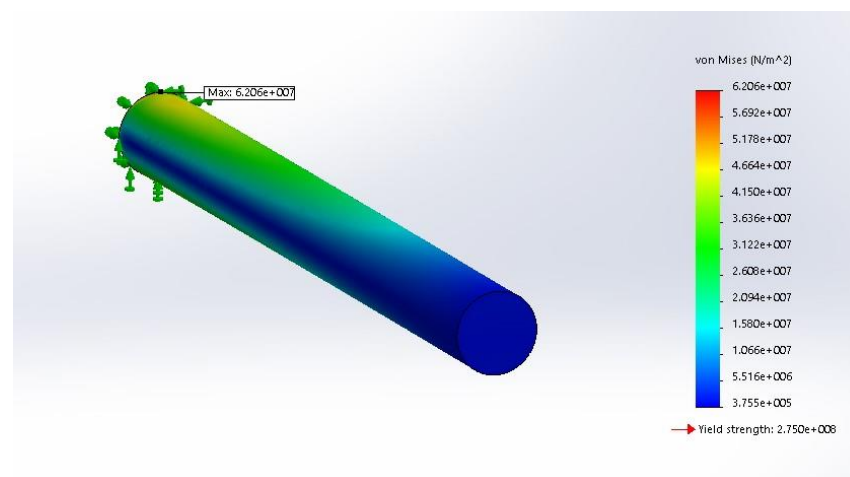
Figure 6.9 – Forearm cylinder link stress plot for 'Object Lifting', with max Y force direction and corresponding X direction force
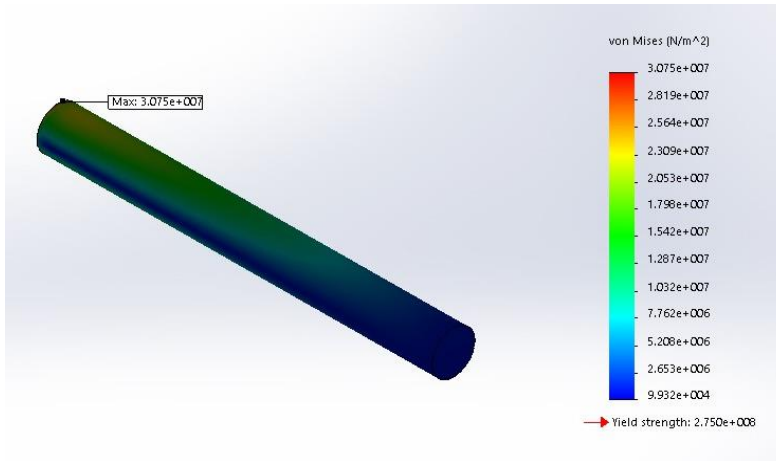
Figure 6.10 – Upper arm cylinder link stress plot for 'Object Lifting', with max Y force direction and corresponding X direction force
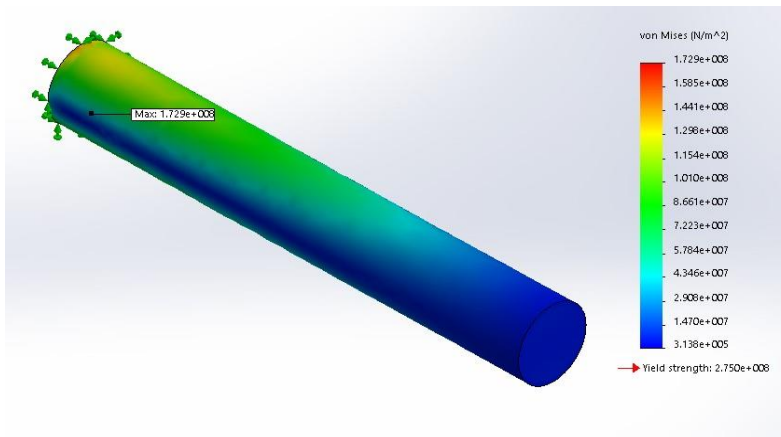
Figure 6.11 – Back cylinder link 1 stress plot for 'Object Lifting', with max Y force direction and corresponding X direction force
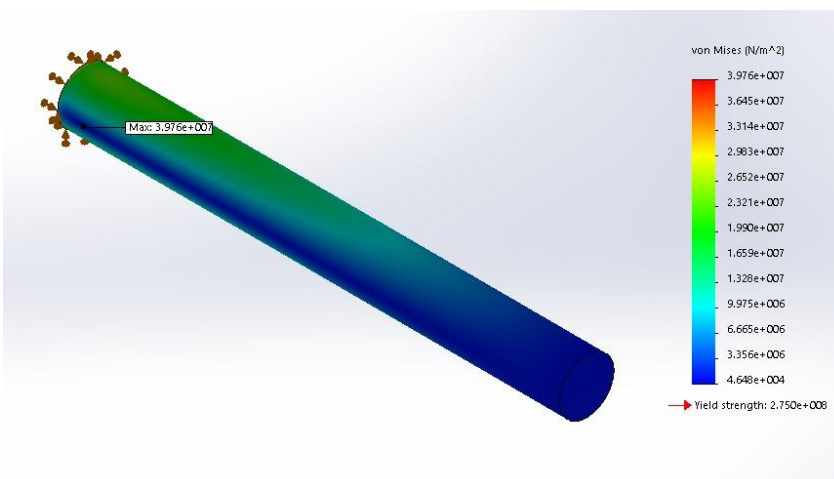
Figure 6.12 – Back cylinder link 2 stress plot for 'Object Lifting', with max Y force direction and corresponding X direction force
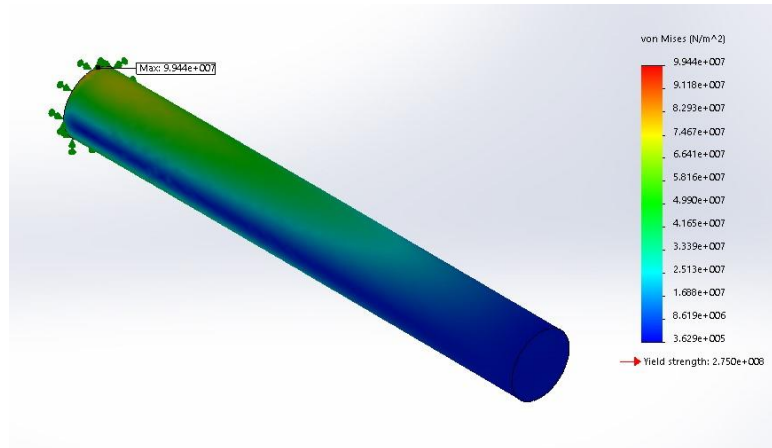
Figure 6.13 – Back cylinder link 3 stress plot for 'Object Lifting', with max Y force direction and corresponding X direction force
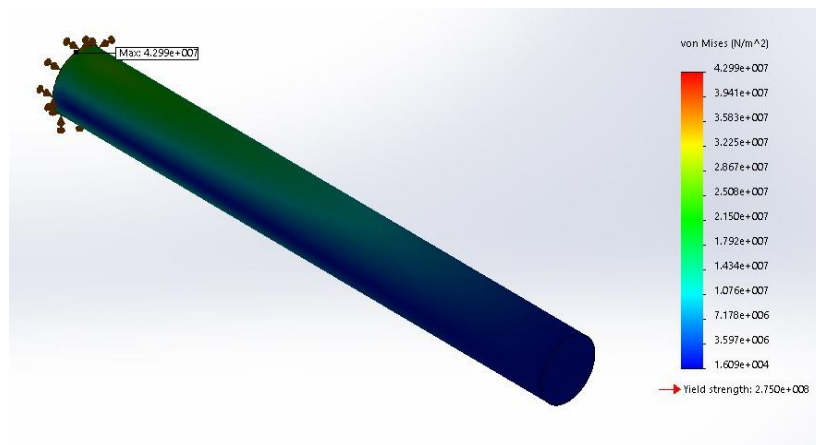
Figure 6.14 - Thigh cylinder link stress plot for 'Object Lifting', with max Y force direction and corresponding X direction force
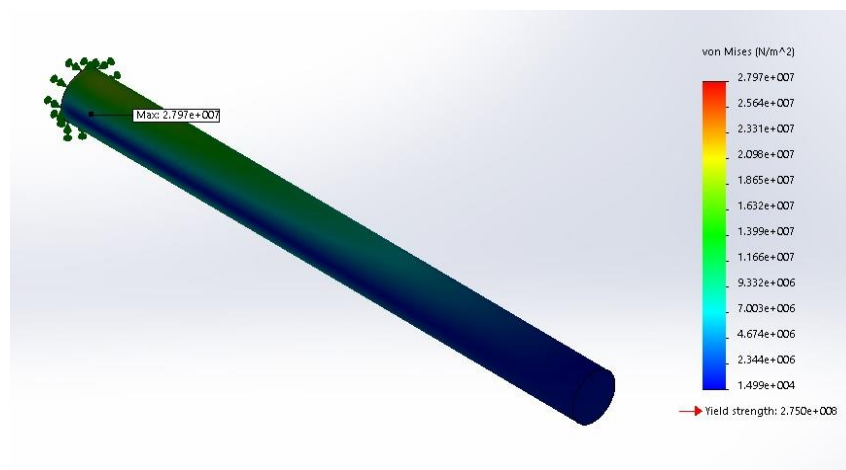
Figure 6.15 – Shin cylinder link stress plot for 'Object Lifting', with max Y force direction and corresponding X direction force

6.2.3.2 Cross-Section Dimensions and Mass Optimization Results for Object Raising Motion

The optimized dimensions and masses of each link can be seen in Table 6-6 and Table 6-7 for the object raising motion. Table 6-6 shows the results for a solid cylinder and Table 6-7 shows the result for hollow tube optimization.

Table 6-6 – Link geometries for 'Object Raising' motion using solid cylinder, the total mass of the links come to 5.7024kg

	Length (mm)	Radius (mm)	Mass (kg)
ForeArm	286	16.27	0.6426
UpperArm	286	16.45	0.6561
Back Link 1	101.36	7.7	0.0513
Back Link 2	374.44	15.43	0.756
Back Link 3	211.89	13.16	0.3105
Thigh	466.5	18.96	1.4229
Shin	466.5	21.7	1.863

Table 6-7 – Link geometric properties for 'Object Raising' motion using a hollow tube, the total mass is 0.089102 kg.

	Length (mm)	Radius (mm)	Thickness (mm)	Mass (kg)
ForeArm	286	24.21	1.31	0.0042
UpperArm	286	30.2	1.16	0.0032
Back Link 1	101.36	27.36	1	0.0009
Back Link 2	374.44	18.81	3.77	0.0451
Back Link 3	211.89	41.91	1.73	0.0054
Thigh	466.5	27.4	2.53	0.0243
Shin	466.5	36.42	1.14	0.0051

The pareto front for each link is shown in Figure 6.16. The torque values are shown in Figure 6.17 for the model with an external mass attached to it and in Figure 6.18 without any external load. Figure 6.19 shows the reaction forces at the base of each link in both the local x and local y direction.

Pareto-front results for 'Object Raising' motion hollow tube geometry optimization
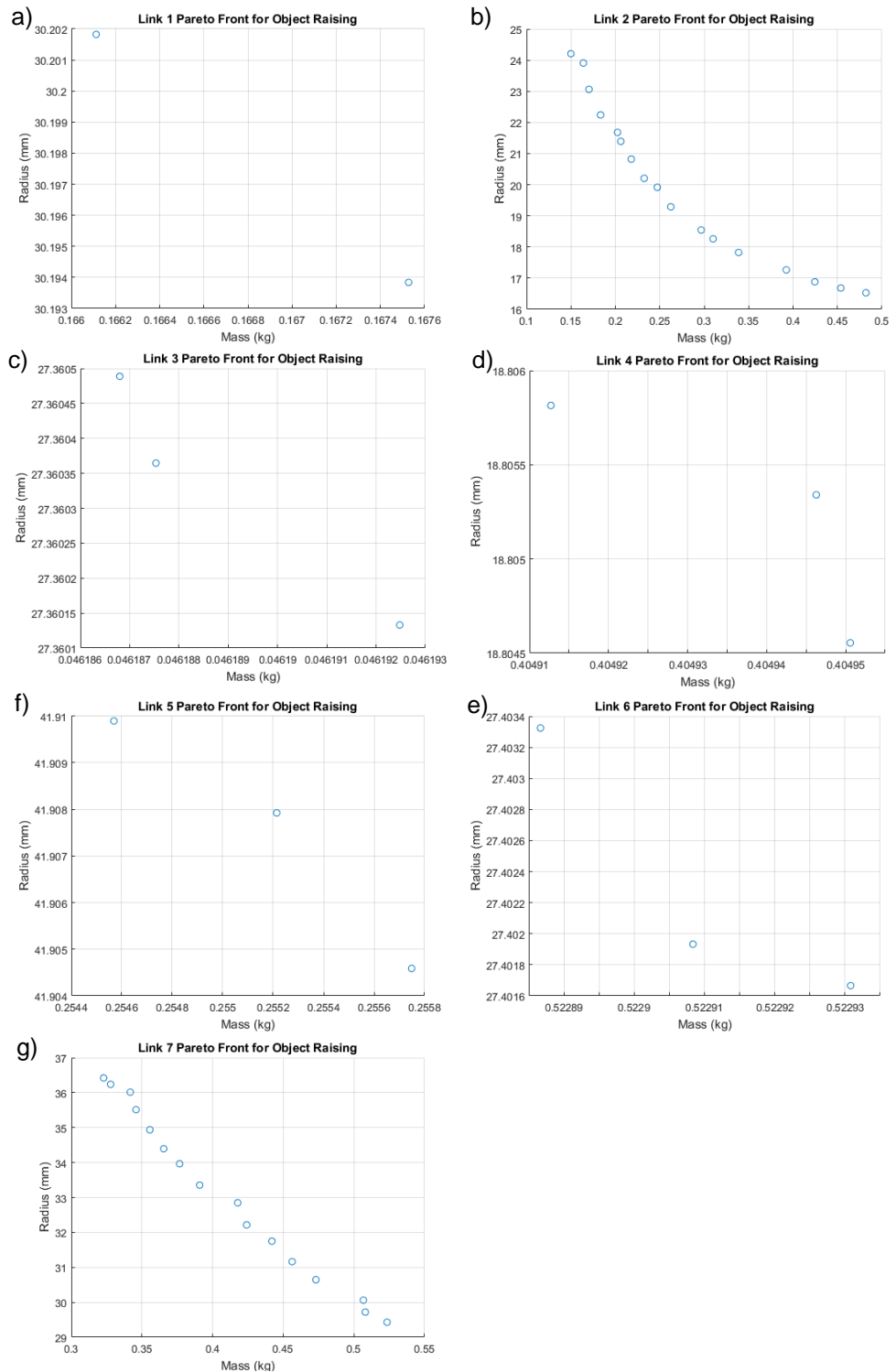
Figure 6.16 – Pareto optima graphs for 'Object Raising' motion.
Graphs display the results of the multi-objective optimization, the objectives being minimizing radius and minimizing mass.

Torque results for 'Object Raising' motion cross-section optimization
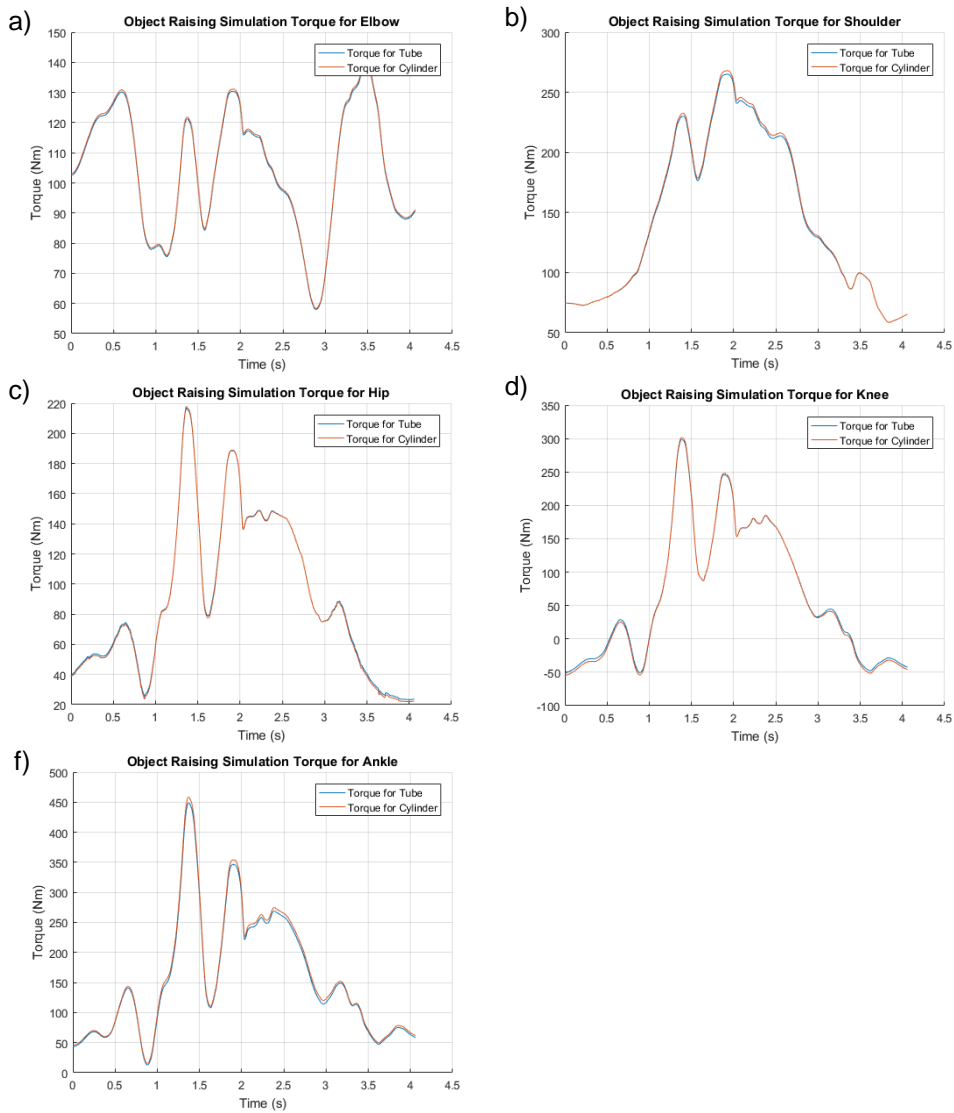
Figure 6.17 – Torque values of the actuated joints with an external
mass of 45 kg attached at the end of the forearm link

Simulating the optimized cross-section models again for 'object raising' motion shows similar characteristics as in the optimized cross-section models for 'object lifting'. The resulting torque data has been plotted in Figure 8.18. It can be seen that the variation in link masses again has some significant effect on the torques experienced on the joints when under no external load.

Simulation results for 'Object Raising' motion with zero external mass
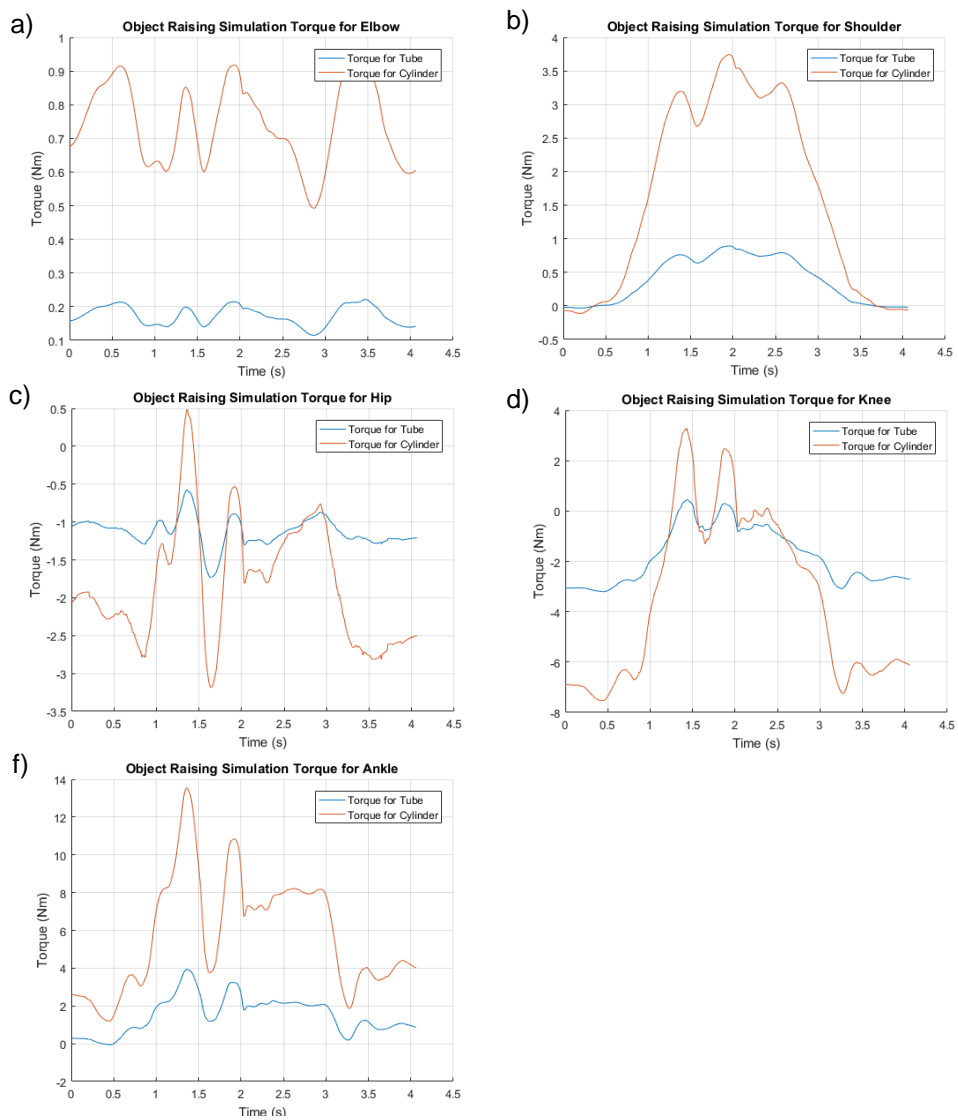
Figure 6.18 – Torque values of the actuated joints without an external load being carried

Reaction force results for 'Object Raising' motion cross-section optimization
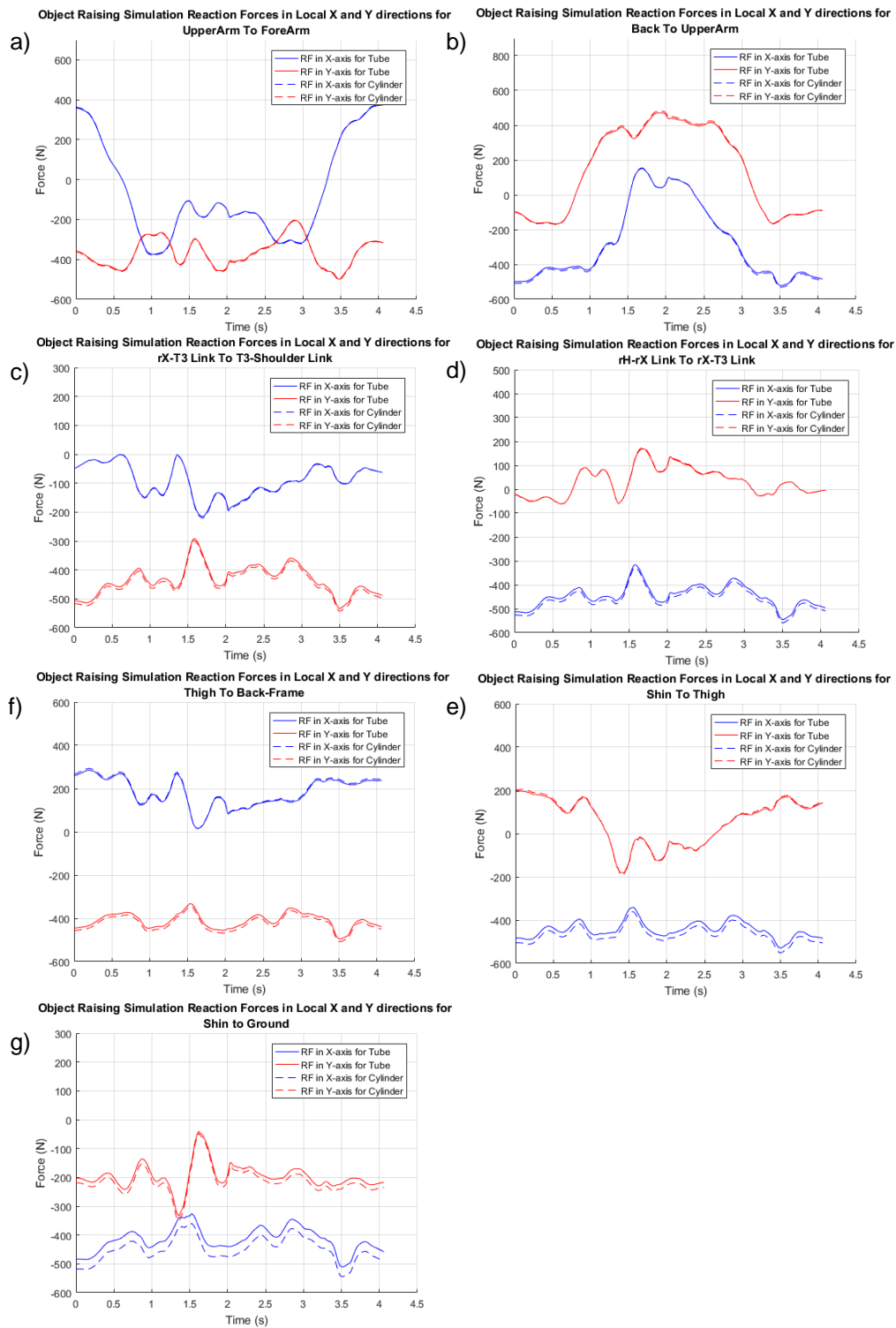
Figure 6.19 - Reaction forces between links used to calculate beam
bending

Table 6-8 - Maximum and minimum reaction forces from the MATLAB simulation based on the 'Object Raising' motion to be used in the FEA. The direction indicates weather the force is in the compressive (negative) or tensile (positive) direction for the X axis. For the Y axis direction the forces indicated downward (negative) or upward (positive) direction force which would result in either clockwise or counter-clockwise bending respectively about the base of the link.

Cross-section geometry	Tube Reaction Forces (N)				Cylinder Reaction Forces (N)			
Direction	Max X	Min X	Max Y	Min Y	Max X	Min X	Max Y	Min Y
Upper Arm To Forearm	374.06	-374.76	-203.51	-498.7	378.14	-378.9	-206.4	-503.59
Back Link 1 To Upper Arm	150.72	-521.98	472.36	-166.94	154.1	-531.58	482.24	-169.87
Back Link 2 To Back Link 1	-0.42	-215.51	-291.78	-533.42	-1.19	-220.32	-298.78	-543.3
Back Link 3 To Back Link 2	-315.81	-545.44	168.54	-61.51	-326.77	-558.88	173.47	-62.25
Thigh To Back Link 3	286.02	14.87	-332.65	-494.97	294.04	15.99	-344.39	-507.41
Shin To Thigh	-340.77	-529.2	196.91	-183.49	-361.33	-551.3	204.63	-188.31
Shin to Ground	-325.74	-510.48	-39.9	-332.69	-359.42	-544.22	-47.69	-351.07

6.2.3.2.1 Simple FEA analysis of the links for 'Object Raising' motion

Due to the similarity in the models, that is the feet are considered static, the number of linkages and joints are identical, the external load acts on the same point on the model, the work for the FEA static stress analysis can be duplicated. The CAD models of the links are developed using the geometries shown in Table 6-6 and Table 6-7 on Solidworks.

The maximum and the minimum values of the reaction forces for both x and y directions in this scenario can be found in the plots of Figure 6.19 and have been tabulated in Table 6-8. It can be understood from both figure and table that certain links (back link 1, back link 2, thigh and shin) are in compression constantly. Table 6-9 shows the corresponding reaction forces for the absolute maximum Y and minimum X values shown in Table 6-8. The absolute maximum Y force will be the force that will cause the greatest amount of bending. The minimum X force is the highest compressive load the link will experience. Since the primary concern at this stage is the bending the FEA simulations are run with the maximum absolute Y force and the corresponding compressive (X direction) force.

Table 6-9 – The reaction forces corresponding to the maximum reaction forces for 'Object Raising' motion. Due to the uniformity of the cross-section the forces in the direction in the Y axis is inconsequential therefore the x direction force corresponding to the absolute maximum Y force is found. The minimum negative X direction force is chosen as this corresponds to compression of the link.

	Tube Reaction Forces (N)		Cylinder Reaction Forces (N)	
	Force X at Max Y	Force Y at Min X	Force X at Max Y	Force Y at Min X
Upper Arm To Forearm	193.86	-277.17	195.62	-280.75
Back Link 1 To Upper Arm	40.54	-141.06	41.47	-143.86
Back Link 2 To Back Link 1	-95.86	-347.28	-97.5	-354.91
Back Link 3 To Back Link 2	-365.83	22.87	-377.46	22.97
Thigh To Back Link 3	233.55	-375.66	240.07	-388.48
Shin To Thigh	-483.06	161.98	-504.73	167.41
Shin to Ground	-338.78	-220.95	-371.08	-238.18

The results of the simulations for cylinder links using the 'object raising' motion reaction force data have been tabulated in Table 6-9. The plots of the stress analysis can be seen in Figure 6.20 for fore arm link, Figure 6.21 for upper arm link, Figure 6.22 for back link 1, Figure 6.23 for back link 2, Figure 6.24 for back link 3, Figure 6.25 for thigh link and Figure 6.26 for shin link.

Table 6-10 – Results of the FEA simulations for cylinder (solid) links, showing the maximum Von Misses Stress, maximum displacement and the minimum Factor Of Safety as calculated by SolidWorks for 'Object Raising' motion.

Link	Von Misses Stress (N/m^2) x10^8	Displacement (mm)	Factor of Safety
Forearm	0.5342	1.0370	5.148
Upper Arm	0.5271	0.9502	5.218
Back Link 1	1.7470	0.9981	1.574
Back Link 2	0.2905	0.9880	9.468
Back Link 3	1.5420	1.9880	1.783
Thigh	0.2664	0.9886	10.032
Shin	0.3037	0.9893	9.054
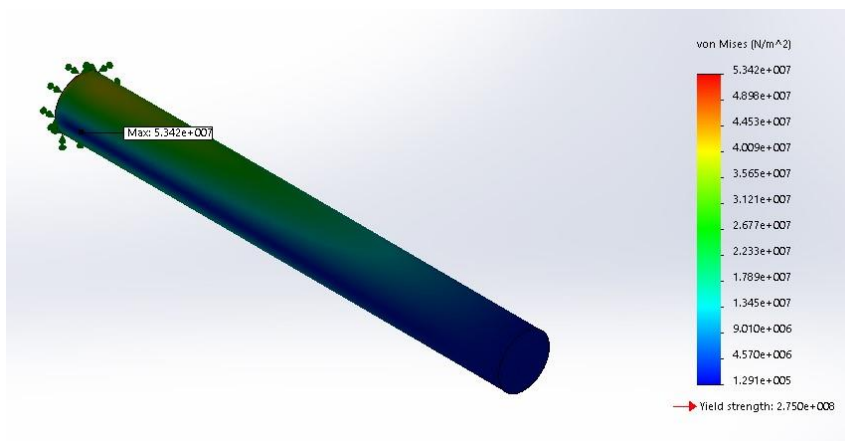
Figure 6.20 – Forearm cylinder link stress plot for 'Object Raising' motion, with max Y force direction and corresponding X direction force
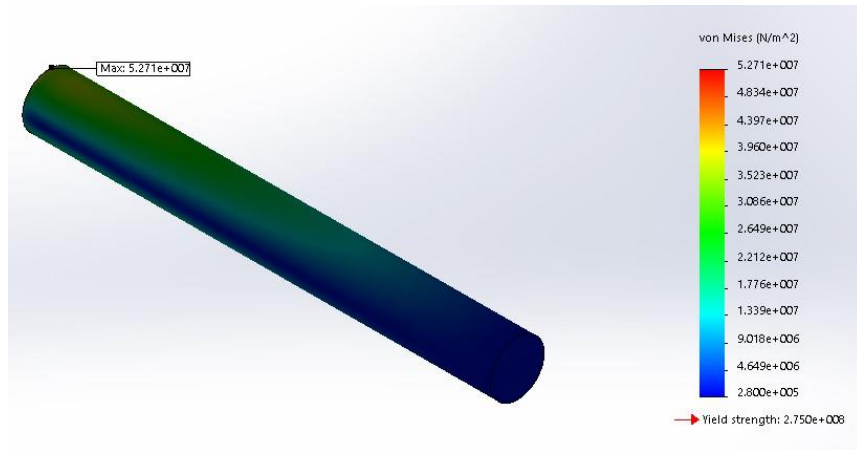
Figure 6.21 – Upper arm cylinder link stress plot for 'Object Raising' motion,
with max Y force direction and corresponding X direction force
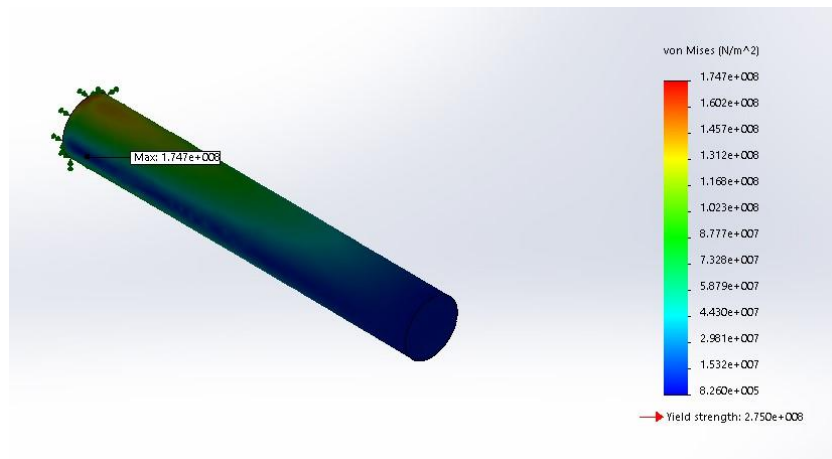
Figure 6.22 – Back cylinder link 1 stress plot for 'Object Raising' motion,
with max Y force direction and corresponding X direction force
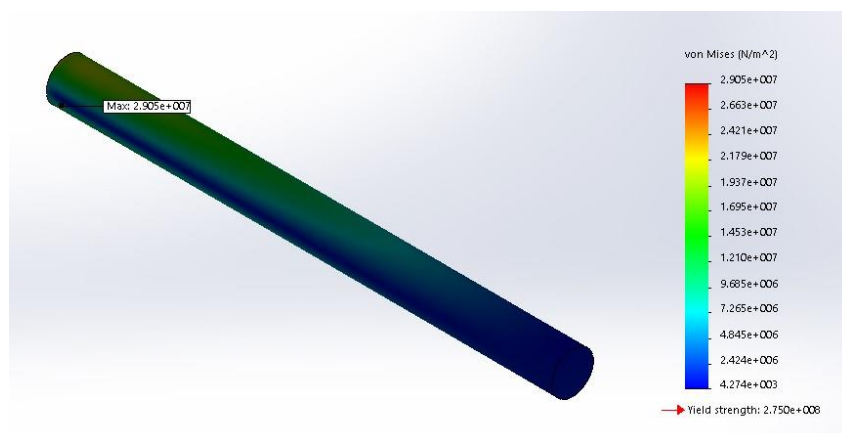
Figure 6.23 – Back cylinder link 2 stress plot for 'Object Raising' motion,
with max Y force direction and corresponding X direction force
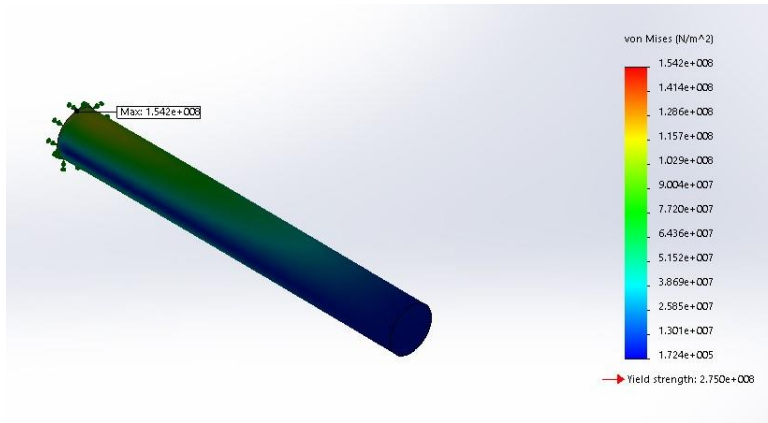
Figure 6.24 – Back cylinder link 3 stress plot for 'Object Raising' motion, with max Y force direction and corresponding X direction force
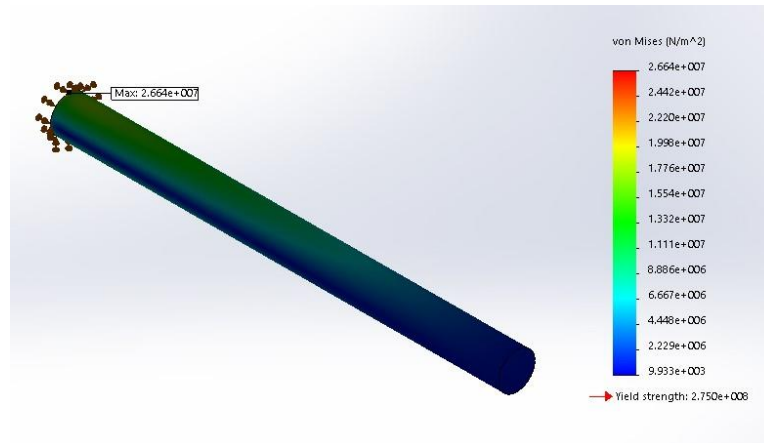
Figure 6.25 - Thigh cylinder link stress plot for 'Object Raising' motion, with max Y force direction and corresponding X direction force
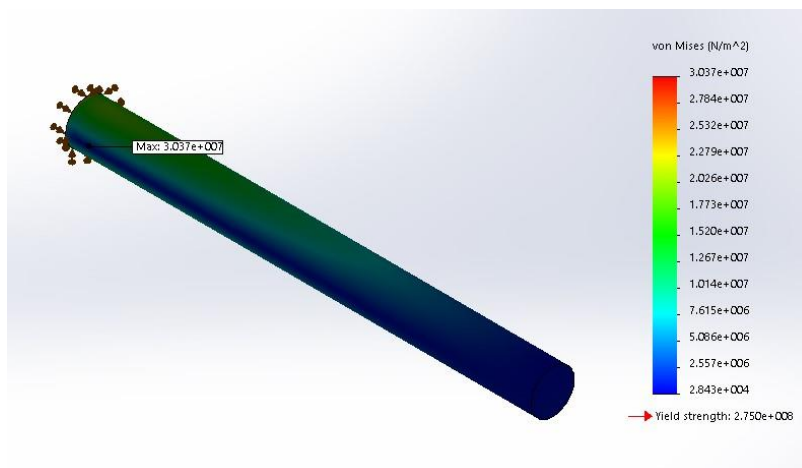
Figure 6.26 – Shin cylinder link stress plot for 'Object Raising' motion, with max Y force direction and corresponding X direction force

6.2.4 Geometry Reshaping Example

Using equations Equation 6-26 and Equation 6-27 the rectangular shapes which correspond to a greater second moment of area can be found post optimization. The values of the new cross-section dimensions are presented in Table 6-11 and Table 6-12 for 'Object Lifting' motion and 'Object Raising' motion respectively. The reduction in size column shows the decrease in the geometries dimension along specified axis. This can be viewed as a relative measure of bulkiness of the link. It can be seen in both tables that the conversion from circle to rectangle in cross-section has decreased the bulkiness of all links albeit in a small degree.

Table 6-11 – Tabulated results for reshaping of dimensions after optimizing the cross-section and mass for the 'Object Lifting' motion using cylindrical links. The diameters of the cylindrical links are presented calculated from Table 6-1. In the last column the reduction in size is also presented, showing the relative bulkiness of the rectangular shape compared to the circular one.

	Diameter, r_o x 2 (mm)	Height, h_o (mm)	Base, b_o (mm)	Reduction in size (mm)	
				X axis	Y axis
Fore Arm	29.26	26.53	25.34	2.73	3.92
Upper Arm	32.48	29.46	28.13	3.02	4.35
Back Link 1	15	13.60	12.99	1.40	2.01
Back Link 2	46.38	42.06	40.17	4.32	6.21
Back Link 3	21.68	19.66	18.78	2.02	2.90
Thigh	47.12	42.73	40.81	4.39	6.31
Shin	35.54	32.23	30.78	3.31	4.76

Table 6-12 - Tabulated results for reshaping of dimensions after optimizing the cross-section and mass for the 'Object Raising' motion using cylindrical links. The diameters of the cylindrical links are presented calculated from Table 6-6. In the last column the reduction in size is also presented, showing the relative bulkiness of the rectangular shape compared to the circular one.

	Diameter, r_o x 2 (mm)	Height, h_o (mm)	Base, b_o (mm)	Reduction in size (mm)	
				X axis	Y axis
Fore Arm	32.54	29.51	28.18	3.03	4.36
Upper Arm	32.9	29.84	28.49	3.06	4.41
Back Link 1	15.4	13.97	13.34	1.43	2.06
Back Link 2	30.86	27.99	26.73	2.87	4.13
Back Link 3	26.32	23.87	22.79	2.45	3.53
Thigh	37.92	34.39	32.84	3.53	5.08
Shin	43.4	39.36	37.59	4.04	5.81

6.3 Optimization of Specific Link Lengths

In this section the effects of the link lengths are investigated. The focus is on the links that undergo primary movement. For 'Object Lifting' the links are shin and thigh, and for 'Object Raising' the links are fore- and upper-arm. The cross-section optimization is incorporated into the investigation, such that each change in 'r' has been cross-section optimized. The geometry selected for the links are cylinders that are solid as they have least amount of variables, and as could be seen in previous section the disparity in torque data is minimal when loaded externally.

A ratio, 'r', is set between two links being compared. For 'Object Lifting' the relationship is:

L_{max} = Maximum distance between joint ankle position and hip position over the motion

$$L_{Shin} = r * L_{max}$$

Equation 6-41

$$L_{Thigh} = (1 - r) * L_{max}$$

Equation 6-42

Such that with a lower 'r' value the shin is shorter than the thigh, and for 'Object Raising' the relationship is:

L_{max} = Maximum distance between joint ankle position and hip position over the motion

$$L_{UpperArm} = r * L_{max}$$

Equation 6-43

$$L_{ForeArm} = (1 - r) * L_{max}$$

Equation 6-44

Such that with a lower 'r' value the upper arm is shorter than the forearm

The goal is to minimize power and thus the variables are:

r   Ratio between links
r_c Radius of cylinder
                cross-section

6.3.1 Results for Link Length Variation

This research looks at three different parameters mechanical work, peak torque and combined volume of the links being optimized. The mechanical work shown in Equation 6-45 has been used to investigate optimality in various robots (Bhounsule, Pusey and Moussouni 2016). As the data is sample based Equation 6-46 is used which is a discrete version of the mechanical work equation. It should be known that the product of the torque (T) and the angular velocity (ω) is power (P).

$$\int |T\omega|dt$$
<div align="right">Equation 6-45</div>

$$\sum_{i=1}^{n} |T_i\omega_i|$$
<div align="right">Equation 6-46</div>

Furthermore the maximum absolute torque is found for each r value and each joint of interest. The combined volumes of the links is used to determine at which 'r' value the local system will have the least weight.

Lower Link Length Optimization Results for Object Lifting
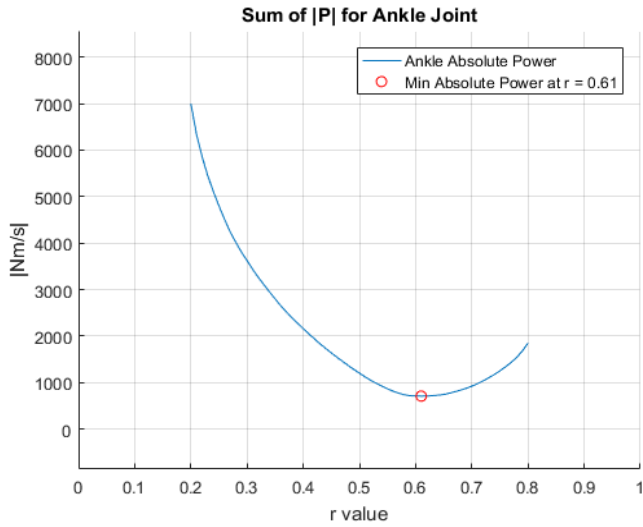
Figure 6.27 – Graph showing the sum of the absolute value of power generated by the ankle joint for each value of 'r' for 'Object Lifting' motion
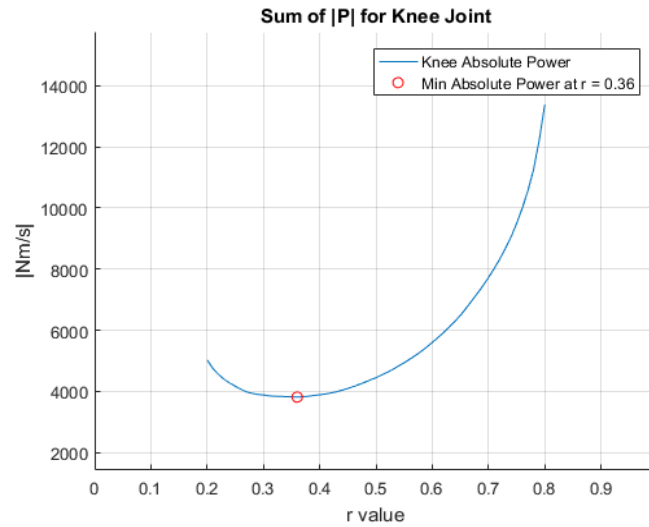
Figure 6.28 – Graph showing the sum of the absolute value of power generated by the knee joint for each value of 'r' for 'Object Lifting' motion
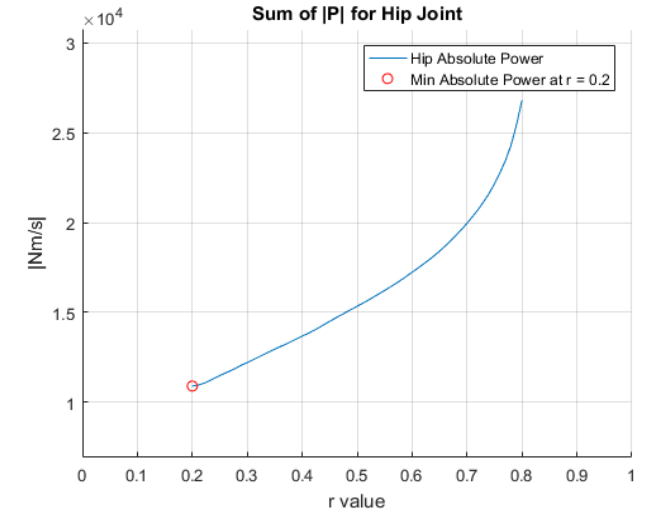
Figure 6.29 – Graph showing the sum of the absolute value of power generated by the hip joint for each value of 'r' for 'Object Lifting' motion
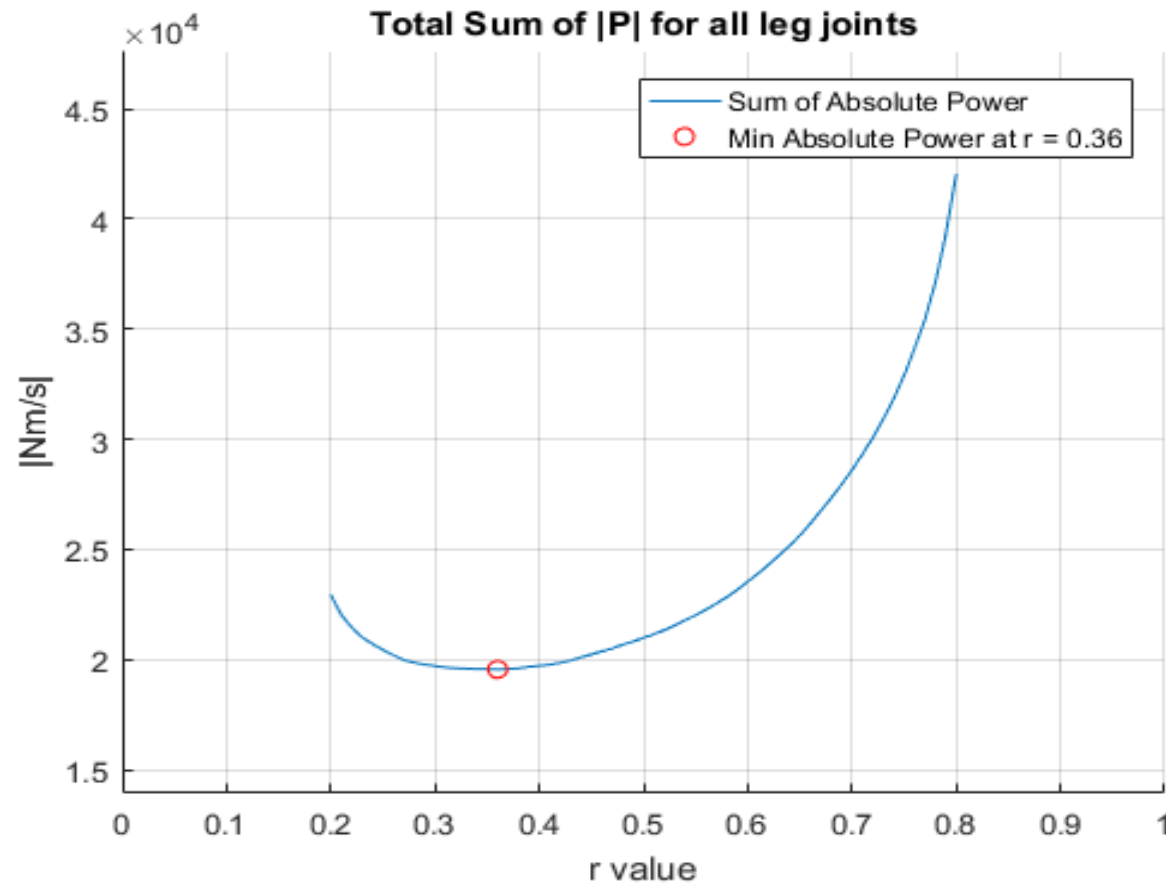
Figure 6.30 – Graph showing the sum of the absolute value of power generated by all
the joints 'Object Lifting' motion for each value of 'r'
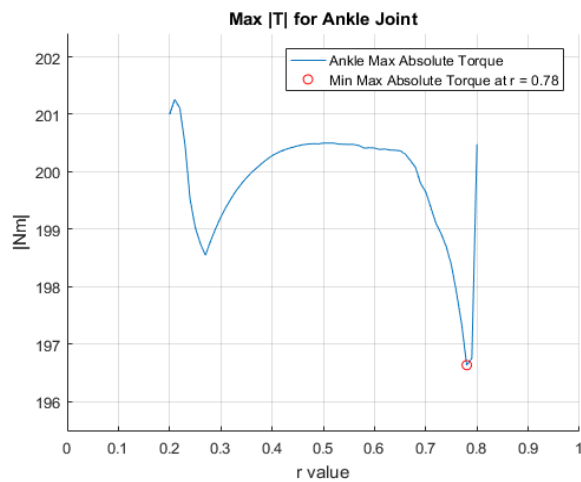
Figure 6.31 – Graph showing the maximum absolute value of torque (peak torque) generated by the ankle joint for each value of 'r' for 'Object Lifting' motion
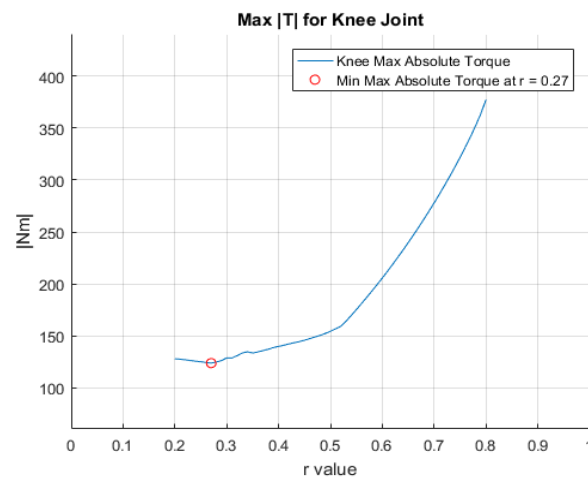
Figure 6.32 – Graph showing the maximum absolute value of torque (peak torque) generated by the knee joint for each value of 'r' for 'Object Lifting' motion
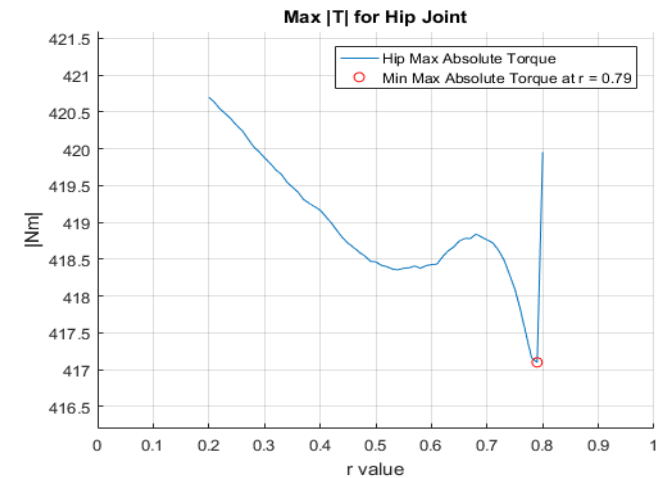
Figure 6.33 – Graph showing the maximum absolute value of torque (peak torque) generated by the hip joint for each value of 'r' for 'Object Lifting' motion
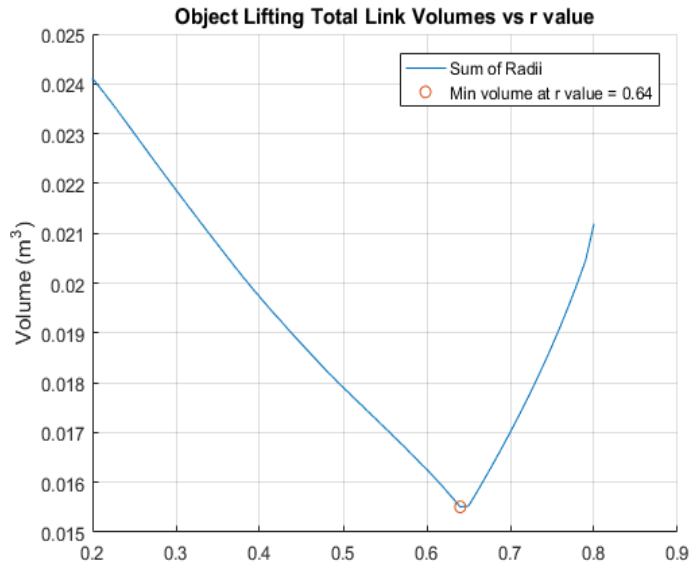
Figure 6.34 – Graph showing the relation between the total volume of the links and the link length ratio for object lifting motion, with the minimum volume circled at r = 0.64
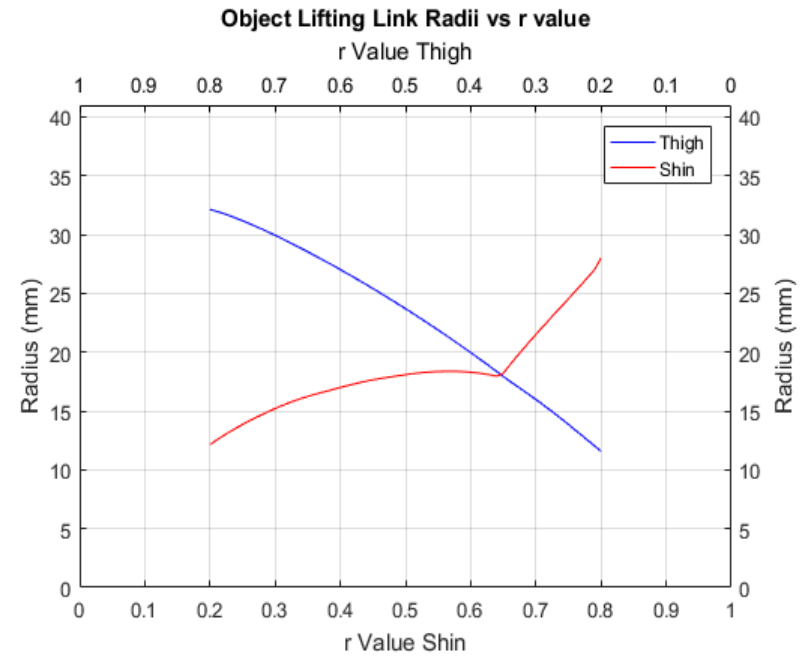
Figure 6.35 – Graph showing the relation between the link radius and the link length ratio 'r' for 'Object Lifting' motion, note that the r value for the thigh is 1 – r of the shin

Upper Link Length Optimization Results for Object Raising Motion
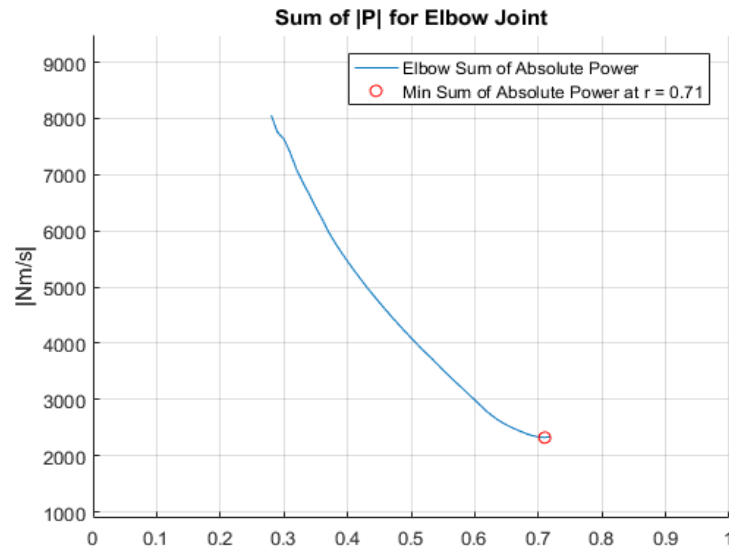
Figure 6.36 – Graph showing the sum of the absolute value of power generated by the elbow joint for each value of 'r' for 'Object Raising' motion
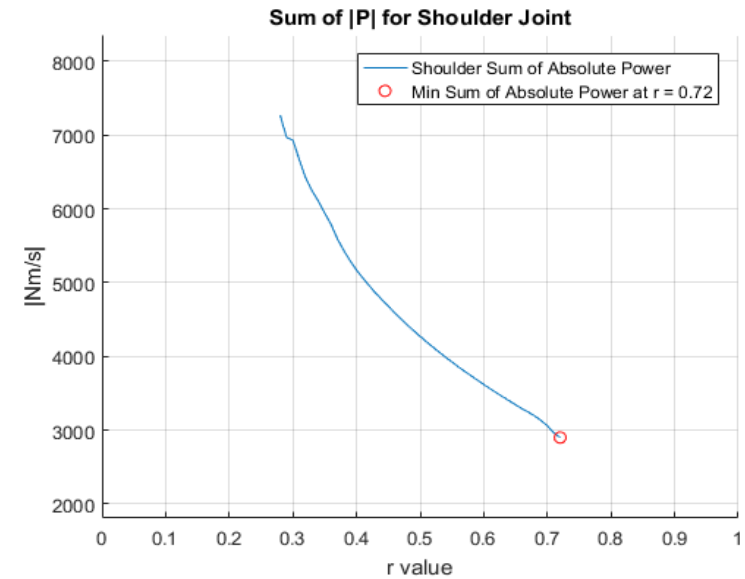
Figure 6.37 – Graph showing the sum of the absolute value of power generated by the shoulder joint for each value of 'r' for 'Object Raising' motion
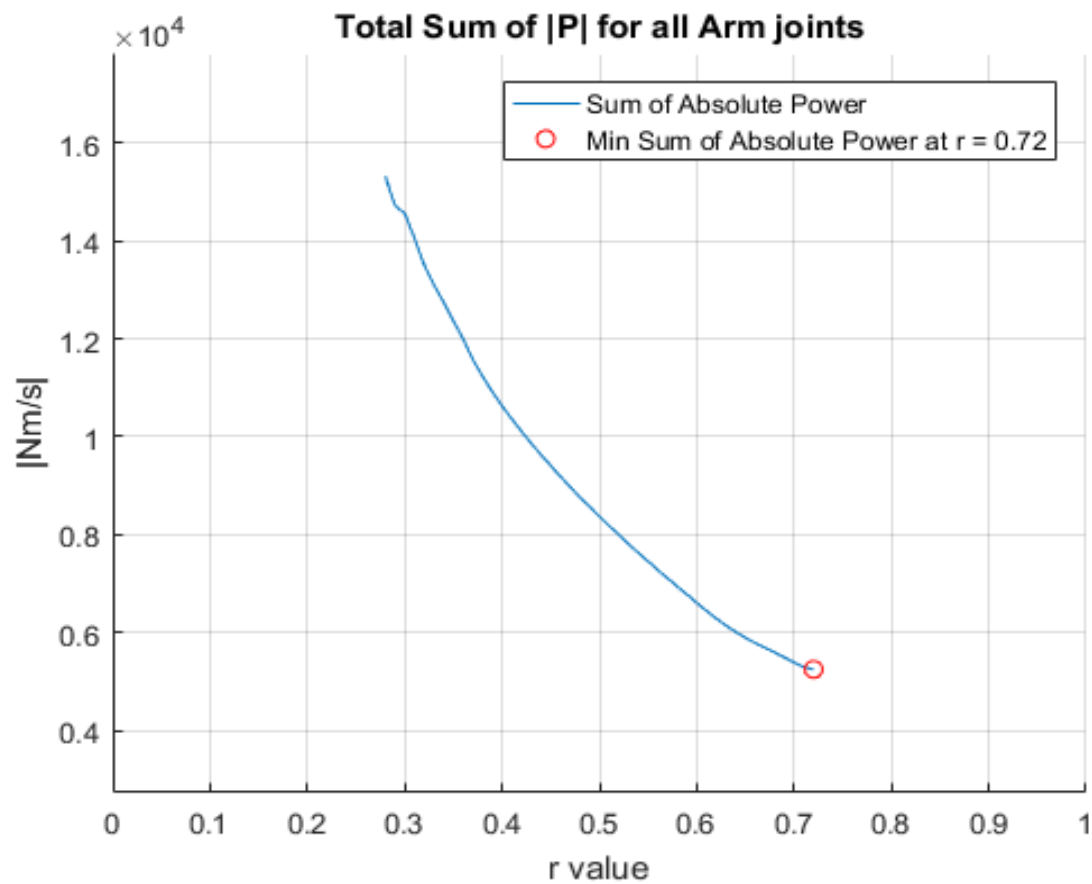
Figure 6.38 – Graph showing the sum of the absolute value of power generated by all the relevant joint in the arm for each value of 'r' for 'Object Raising' motion
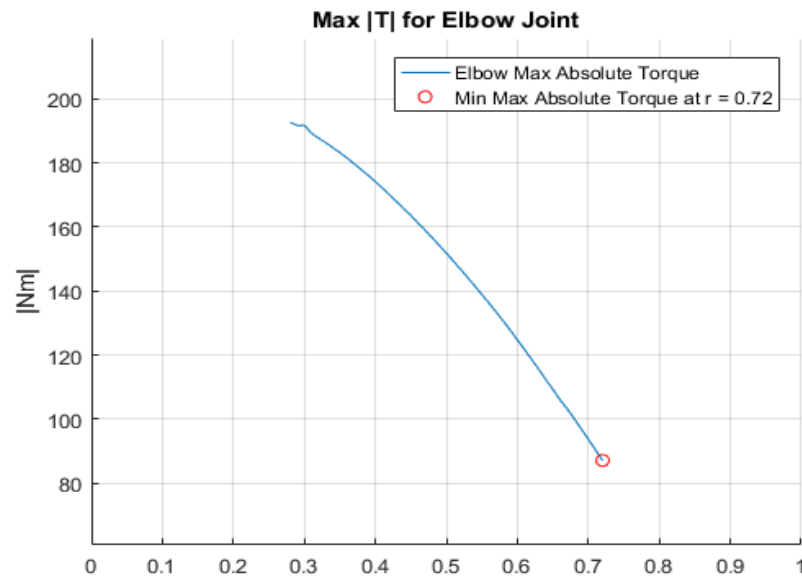
Figure 6.39 – Graph showing the maximum absolute value of torque (peak torque) generated by the elbow joint for each value of 'r' for 'Object Raising' motion
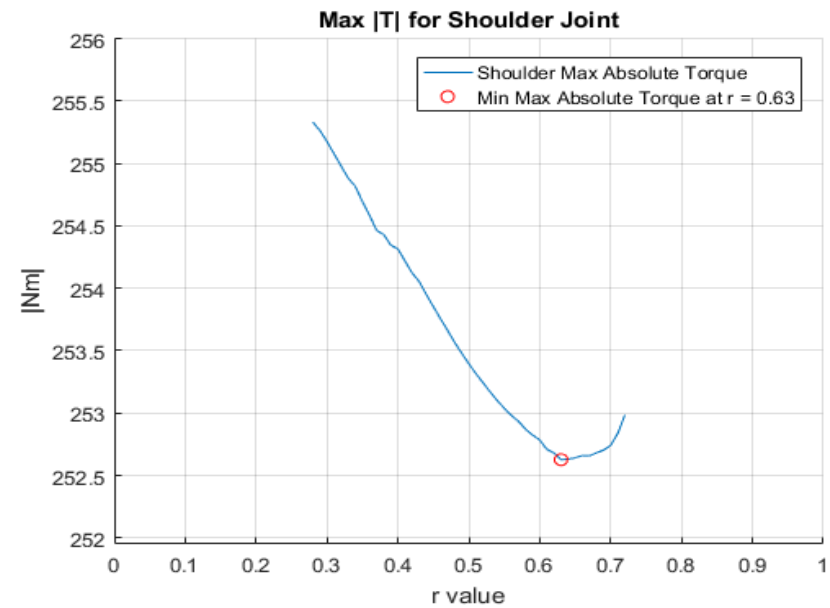
Figure 6.40 – Graph showing the maximum absolute value of torque (peak torque) generated by the shoulder joint for each value of 'r' for 'Object Raising' motion
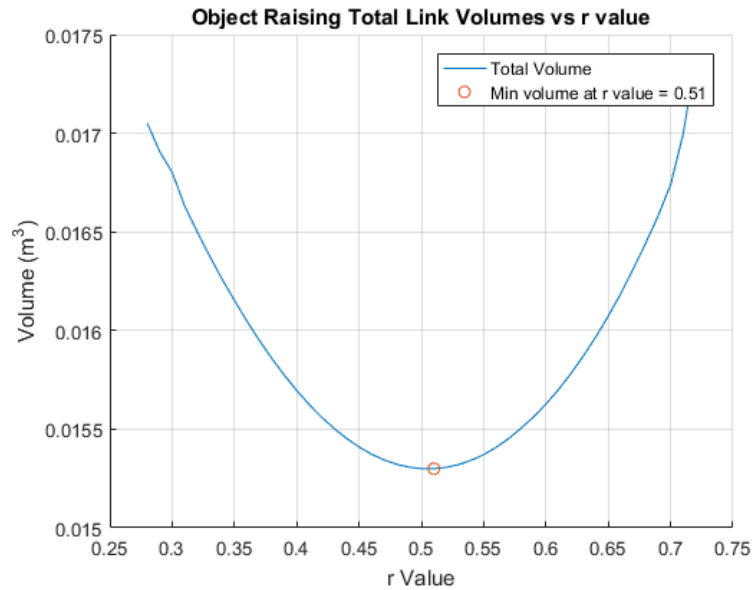
Figure 6.42 – Graph showing the relation between the total volume of the links and the link length ratio 'r' for 'Object Raising' motion, with the minimum volume circled at r = 0.51
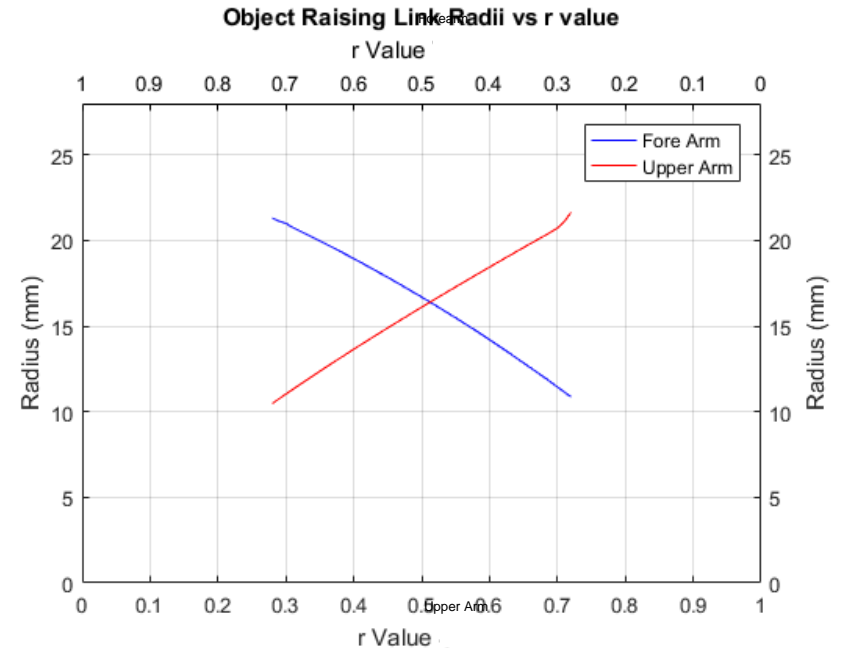
Figure 6.41 – Graph showing the relation between the link radius and the link length ratio 'r' for 'Object Raising' motion, note that the r value for the forearm is 1 – r of the upper arm

6.4 Discussion

6.4.1 Comparison Between Solid and Hollow Links

It can be seen that the mass of the exoskeleton links differ drastically, comparing the combined weights of the solid with the hollow structure it is found that it is approximately 24.1 times greater. The external weight (45kg) is approximately 6.9 times greater than the combined mass of the solid structure. It can be seen that when the exoskeleton is loaded with an external mass this becomes the prime influencer of the dynamic response of the joints, i.e. torque. Then the difference in mass between the different cross-section geometries has a significantly less impact in the dynamics. Such that it might be considered arbitrary. It is also no surprise that the reaction forces when model is under load, are similar for the two different structures.

6.4.2 Effects of Cross-Section Dimensions and Mass Optimization

The results of the FEA simulations are shown in Table 6-5 and Table 6-10. The dimensions found are feasible as far as not violating the static yield stress limits (yield strength in the simulation is set as 2.750 x10^8 that of aluminium 6061-T6 (United States. Department of *et al.* 2011)).

The results of the displacement show the average deflection of all links for 'Object Lifting' is approximately 1.02 mm with a standard deviation of approximately 0.25. For all links apart from the arm links the max displacement were just under 1 mm. For the upper arm the max displacement is 0.348 mm shy of 1 mm and for the forearm the displacement exceeds by approximately 50%. For 'Object Raising' the average deflection is approximately 1.13 mm with a standard deviation of approximately 0.38. In this motion the links that exceed the constraint are the forearm link which only exceeds by 0.037mm and the first back link which exceeds almost twice.

The results suggests that the driving influencer of the design is the deflection constraint and using this in the optimization was correct. Future work could include modelling the links and the forces dynamically in a FEA environment. This could further point to the accuracy of using a static worst case method on a dynamic model.

6.4.3 Application of Geometry Reshaping

It is also seen in Table 6-11 and Table 6-12 that the reshaping of cylinder links to rectangles reduces some of the volume. The change in shape is actually relatively small and it can be seen that the changes in the height and width are approximately 10% and 13%.

6.4.4 Effects of Link Length Optimization

The results of the link-length optimization for minimizing the sum of absolute power for all joints shows that the optimal link ratio for NA40 - 'Object Lifting' is 0.36 and for NA54 - 'Object Raising' is 0.72.

The results for NA40 - 'Object Lifting' shows that for an exoskeleton whose primary task is to lift object from the ground, it should be designed with a longer thigh than shank. Interestingly the curve shown in Figure 6.30 is displays convex properties. The convex portion occurs between 'r' values of 0.2 and approximately 0.58. The power consumption for the optimum case decreases below 50% in comparison to the maximum power expenditure. It can also be seen that after approximately 'r' = 0.58 the power consumption increases exponentially.

Looking at the joints individually it can be seen that ankle joint (Figure 6.27) favours a design with a higher 'r' value as compared to the knee Figure 6.28) and hip (Figure 6.29) joints. It is found that the hip joint is where most of the power will be consumed. In terms of magnitude its minima is 10 times higher than the ankle joint, this also explains why the combined power optima favours a value closer to the optima for the hip.

The peak torque graphs (Figure 6.31, Figure 6.32 and Figure 6.33) show an even less uniformity in results. It is found that for both ankle and hip joints there exists local minima. The minimum for the knee joint is located fairly close to the optima of the overall power optima, so too is the local optima for the ankle joint. It can be seen, however that only the knee joint will be greatly affected by changing the 'r' value further away from its optimum point. The torque range for both ankle and hip span from approximately 196.5 to 201 |Nm| and 417 to 421 |Nm| respectively whereas for the knee it spans from approximately 130 to 375 |Nm|. The optimal peak torque for the knee is at r = 0.27, at r = 0.36 (the optima for power consumption) the peak torque is approximately 140 |Nm|. At 'r' approximately 0.52 the peak torque for the knee is approximately 160 |Nm| after which its rate of change increases drastically to a value of approximately 375 |Nm|.

Figure 6.34 and Figure 6.35 show the geometric properties of total volume and link radii for changing 'r'. The total volume is the least at r = 0.64. This would also mean that the system would be (only considering the frame) the lightest at this point. The links exhibit an inverse relationship in the change in radii with respect to change in 'r'. It is observed that the shin radius has a very abrupt increase at approximately r = 0.64. The individual minima do not coincide, which is to be expected. And the span from r = 0.2 to r=0.64 in mm is approximately 12.5 to 18 mm. The same span for the thigh link (r = 0.8 to r = 0.36) is approximately 32 mm to 18 mm.

The results for the NA54 – 'Object Raising' shows that for an exoskeleton whose primary task is to raise an object from hip level to shoulder height, should be designed with a longer upper-arm than forearm. Unlike the curve for 'Object Lifting' the global optima shown in Figure 6.38 is found at the outer edge of the curve. The power consumption at the optimal point is approximately 35% of the least optimal point. It is noteworthy that the power consumption of the optimal point is approximately 65% that of the consumption at r = 0.50. This is important as the power consumption increases when decreasing the 'r' value to liken that of the human is not too costly. The increase is approximately 50%.

For both elbow (Figure 6.36) and shoulder (Figure 6.37) it is observed that the individual joint optima are located at r = 71 and r = 72. The magnitude and the span of the power curves are also similar. The peak torque for the elbow (Figure 6.39) also follows this pattern. The span for the peak torque of the elbow joint is approximately 85 to 190 |Nm|. Only the peak torque for the shoulder (Figure 6.40) has a local minima that is at r = 63. Though the span of the peak torque for the shoulder joint is too small, only approximately 3 |Nm|, to make a difference affecting the design process.

Figure 6.41 and Figure 6.42 show the geometric properties of total volume and link radii for changing 'r'. It can be seen that the minimum volume occurs at r = 0.51. The change in radii for both links is fairly linear throughout the span of 'r'. Both radii spans range from approximately 11 to 22 mm.

6.4.5 Implications on Design

Looking at what these results mean for design, the results for 'Object Lifting' motion indicate that there is some variability in the joints as to where the optimum should be. The hip joint having a higher power consumption, followed by knee and ankle becomes the primary contributor in the overall power consumption. Correlating this result with the peak torque, the span of the peak torques are

relatively small enough for the hip and ankle joints with varying 'r' that it may not be needed to worry about incorporating considerations of variant designs. Looking at the knee joint, the peak torque at r = 0.36 would only mean a 15 |Nm| increase from the optimum. The results although optimum in terms of power were not so much optimized for overall volume, not so much either for overall bulkiness. Interestingly this means that a heavier structure would, under load, consume less power.

The results of absolute power and peak torque for the 'Object Raising' motion were quite uniform. Interestingly it was found that changing the ratio of the links to be more human-like for the 'Object Raising' motion meant a direct increase in power consumption and peak torque. The power consumption at r = 50 would equate to an approximate 50% increase. This does however mean that the peak torque the elbow joint would have to handle would lie around 150 |Nm| which is an approximate increase of 75%. What effect that has on the actuation design is unknown at this stage, but an increase in peak torque would directly correlate to a need to increase structural integrity at the joint. As for the links this does mean that the overall weight would be lighter, and the base design would start with equal radii for upper arm and forearm links.

6.5 Summary

In this chapter optimization of the exoskeleton structure is done considering two motions, NA40 – 'Object Lifting' and NA54 – 'Object Raising'. First the link cross-section optimization is investigated. This optimization is incorporated into optimization of link lengths for some relevant links of each motion.

Looking at simple geometries, circle, square and rectangle, a relationship is established between them in terms of second moment of area. It is found that the circle could be used as a basic shape and post optimization converted to any of the other two shapes, with a known increase in the second moment of area. This would directly translate into an increase in structural integrity. The reduction in size is shown as well for the optimized cross-section results.

The optimization process is demonstrated using a cylindrical tube for a simple pendulum model with an external weight and an oscillatory motion. The choice of using genetic algorithms for optimization is discussed and the algorithm for the constraint functions in the optimization is presented as a flowchart. The constraint of the cross-section dimensions and mass optimization is the deflection of the link and is set at 1 mm. The resulting pareto front is also presented.

The full exoskeleton system cross-section dimensions and mass optimization is presented. The optimization is performed for both hollow and solid cylinders. Due to the serial nature of the linkages the optimization algorithm optimizes each link in succession. After each link is optimized the results with minimum mass is selected, the model updated, and the next link is optimized. This ensures that the minimum mass structure is found. The results are compared and it is found that the total mass of the solid tubes is approximately 24.1 times greater than that of the hollow tubes. It is also found that the external weight of 45 kg is approximately 6.9 times greater than the combined weight of the solid tubes. It could also be deduced that the difference in using hollow and solid tubes on torques and reaction forces were negligible in comparison to the effects of the external weight.

The optimization results are verified using FEA simulation models for each link for each motion. Overall it could be seen that the yield stresses were not violated for the links, however for the 'Object Lifting' the forearm link violated the constraint and the upper arm link bending 0.348 mm short of the 1mm constraint. For the 'Object Raising' motion the forearm link violated the constraint by only

0.037mm whereas the third back link had a displacement value almost double the constraint.

For the link length optimization the link lengths are defined as a ratio 'r' of the maximum distance between the two points of interest during the cycle of a motion. These points are ankle and hip for 'Object Lifting' and therefore shin and thigh links will be the affected links, and shoulder and wrist for 'Object Raising' and therefore the upper arm and forearm will be the affected links. For each instance of 'r' the cross-section dimension and mass optimization is performed for the relevant links. The mechanical work, peak torque and total volume of the relevant joints are analysed.

It is found that for the 'Object Lifting' motion the primary influencer in the power consumption is the hip. As for peak torque, changes in 'r' affected the knee substantially greater than the hip and ankle. The optimal design considering only mechanical work and peak torques point to a long thigh and a shorter shin. Considering overall volume the optimal design would have a shorter thigh and a longer shin.

For 'Object Raising' the results of mechanical work and peak torque correlate. It is found that the optimal design would be one with a longer upper arm and a much shorter forearm. Like the 'Object Lifting' motion the minimum volume does not correlate.

Looking at the link length optimization results and their implication on design, it can be seen that moving away from the power optimum, in both motions, means an increase in peak torques that would be experienced by the knee (NA40) and elbow (NA54). This would have a direct impact on the joint structure. The impact on the actuation design is unknown other than the actuator would need to support delivering a higher torque.

Chapter 7
Summary, Conclusions and Future Work

7.1 Summary

In Chapter 1 the research aims and objectives were outlined. The aim of the research was to find relationships between structural geometries of the exoskeleton and power and torque when following key trajectories of the human. Also to obtain optimum geometries which correspond to minimum power expenditure and peak torques for the joints relevant for the exoskeleton to perform given tasks with an external load. This information is to be used to design at least parts of an exoskeleton as verification of the optimum design methodology for enhancive exoskeletons. This section summarises the research objectives and results found.

1. Development of a design methodology for exoskeletons intended for specific load carrying tasks.

The design methodology was theorized and presented in Chapter 3. The theory is that an enhancive exoskeleton robot whose purpose is to mimic and enhance the user motions can be designed by finding an optimal configuration of joints and link dimensions such that the same task is performed as far as the trajectories of the connecting points between the exoskeleton and the human are concerned. The theory is derived from the gaps found in the literature review. The subsequent steps of the optimization and design process are derived and sub divided. In Chapter 5 the practical aspects of building the exoskeleton model are presented. Crucial aspects of subdividing the model into manageable sections are outlined and presented on a 2D sagittal model of the exoskeleton. The DH parameters of the 2D model are also presented.

2. Data collection and investigation into a greater spectrum of human motions to be mimicked by exoskeletons by use of motion capture.

Work was carried out to obtain the motion capture data as a pilot study for a group of tasks which would be used in this research in Chapter 4. The motions were verified where applicable with known data. In order to translate the motions to computer and mathematical models of the exoskeleton work was done to identify key events in the motions. It was crucially important to analyse the trajectories of interaction points of the human subject and the ground, in this case the feet. The analysis was performed in Chapter 4. This was done to secure the amount of time that the feet were in contact with the ground so that a relationship could be established between a simplified model of the foot and the real foot. The motion is then simplified to allow the use of a simpler exoskeleton model when optimizing. It was seen that for the 'Simple Gait' motion, the ankle joint location could be considered static a portion of the time the foot was in contact with the ground. For the 'Object Lifting' and 'Object Raising' motion the motion of the ankle was small enough to be considered static.

3. Demonstrate by comparison to FEA results that using a simple beam bending equation as a constraint within cross-section optimization is feasible.

The work on optimization performed in Chapter 6 starts by looking at the cross-section optimization of hollow and solid cylinders. Using deflection of bending cantilever beams as a design constraint the shapes are optimized for minimum mass and minimum radius. Using the results from the MATLAB model the geometric values for minimum mass models are used in CAD models and the deflection constraint verified. It can be seen that in a few cases the deflection constraints are violated by a small amount. Using beam bending as a constraint also alleviates the need to incorporate stress testing in the cross-section optimization.

4. Evaluation of the cross-sections role in the effects of link masses and in turn their effects on the overall power and torque characteristics of the exoskeleton joints.

The results for the cross-section optimization in Chapter 6 were compared with loaded and unloaded scenarios of the motions. Looking at the effects of hollow

vs solid cylinders in loaded scenarios it can be seen that the effects of the link masses are minimal, almost indistinguishable from eachother. On the other hand when unloaded it was found that the difference in mass plays a larger roll.

5. Optimal ratio of link lengths when considering a simple sagittal plane exoskeleton model for two load-carrying tasks. For lifting object from ground the exoskeleton's thigh-link ratio should be larger and for raising an object from hip height to shoulder height the upper-arm-link ratio should be larger.

Chapter 6 finishes with an investigation on the effects of the link lengths will have on the exoskeleton design, that is a link-length optimization on relevant links for two motions 'Object Lifting' and 'Object Raising'. The cross-section optimization is integrated into the study. A ratio term between the two links being examined is defined. The relevant links for 'Object Lifting' are considered to be the thigh and shin and relevant joints ankle, knee and hip, and for 'Object Raising' the upper arm and forearm and relevant joints shoulder and elbow. For 'Object Lifting' the optimal design in terms of mechanical work is one with a longer thigh and shorter shin. The knee joint is the only of the three joints that experiences a large shift when altering the ratio. The other two joints, ankle and hip, have local minima when altering the link ratio term. For the 'Object Raising' motion the optimal design is also one with a longer upper arm and a shorter forearm. The mechanical work and peak torques for both joints support this.

7.2 Conclusions

Looking at the summary it can be concluded that the research has successfully presented a design methodology for enhancive robotic exoskeleton design incorporating motion data of the user for optimization of basic link properties as outlined in Chapter 3. The work clearly has shown that the motions need to be taken into consideration in designing exoskeletons in order to obtain optimal working conditions of the mechanism.

For the motions that were used in the optimization, 'Object Lifting' and 'Object Raising' it was clearly seen that the the optimal link length configuration, as far as power consumption is concerned, is one with longer thigh and shorter shin and longer upper-arm and shorter forearm respectively. Furthermore, comparing the effects on power consumption when using hollow tubes and solid cylinders it is found that the actual weight of the exoskeleton chasi (using Aluminium) is negligible when simulated with an considerable external load (90kg for entire exoskeleton).

The results presented in this research justifies studies into global optimization research of exoskeletons considering a wider variety of tasks. These tasks can come from operations in search and rescue, building sites and warehouse locations, where work is repetitive and potentially harmful due to heavy loads and unstable environments. Further improvements and considerations will be discussed in future works section.

The research has also presented outcomes which where indirectly used in solving the objectives, these include:

1. A practical analysis using Maple and MATLAB software for analytic and numeric inverse kinematic calculations is discussed in Chapter 4.
2. Motion capture data joint angle and marker trajectory data from 'Object Lifting' and 'Object Raising' motions in Chapter 4.
3. Review of appropriate methods of filtering, smoothing and obtaining signal time derivatives in Chapter 4.
4. Comparing different methods of obtaining gradient for the exoskeleton model in Chapter 5.

7.3 Future Work

The following expansions on the current research are suggested for the future work:

1. Increasing the span of the motion capture experiment from a pilot study to a full scale study would increase the statistical variance of the motion data. The scope of the optimizations could include subjects conducting a greater variety of the motions as well.

2. As it was seen in 'Object Lifting' the depth of the squatting motion was very low. This might not be the case for all people whom lift objects, even though research has shown that it can be damaging for the back to stoop (Burgess-Limerick 2003; Gallagher and Unger 1990; Straker 2003). Looking at different levels of squat depth could potentially give rise to the pattern of optimal structure depending on the variability of user motion performing the same task, but with difference in motion. Specifically the competitive form of squatting could be compared with optimal working conditions.

3. Further research could be made into the model description of the exoskeleton, by expanding the number of interaction-points of the foot.

4. Contact dynamics could be incorporated into the model for the interaction points as well, so that the forces and torques during impact prone motions reflect these events.

5. The optimization at the current stage did not take into account internal loads such as joints and actuation systems. It remains a research question where and how to best incorporate this in the design process so that the structure reflects the effects of these necessary components.

6. As seen in previous research for robots (Bhounsule, Pusey and Moussouni 2016), the length of the links for gait is found to be optimal when the leg resembles an inverted pendulum. If it is assumed that this result is directly translatable to the exoskeleton, it would mean that the optima would be conflicting. It remains as future work to investigate what the potential effects of combining gait and lifting would be on the optima. By performing a similar optimization using the simplified gait trajectory, presented in Chapter 4, the optimal design for gait for an exoskeleton could be confirmed. Furthermore the gait optimal data can be used in a multi-objective optimization where the solution may present itself as a pareto front.

7. Furthermore research into the environment that the exoskeleton will be used in might give rise to an indication of the time it will spend performing certain amount of operations. This information can be used to the tasks in a multi-objective optimization.

List of References

ABATE, A., J. W. HURST and R. L. HATTON. 2016. Mechanical antagonism in legged robots. *In: Robotics Science and Systems (RSS).*

ANDERSON, C. K. and D. B. CHAFFIN. 1986. A biomechanical evaluation of five lifting techniques. *Applied ergonomics,* **17**(1), pp.2-8.

ARMY-TECHNOLOGY.COM. 2014. *Raytheon XOS 2 Exoskeleton, Second-Generation Robotics Suit, United States of America* [online]. [Accessed 02/02/2015]. Available from: http://www.army-technology.com/projects/raytheon-xos-2-exoskeleton-us/.

BERGAMASCO, M., F. SALSEDO, S. MARCHESCHI, N. LUCCHESI and M. FONTANA. 2010. A novel compact and lightweight actuator for wearable robots. *In: Robotics and Automation (ICRA), 2010 IEEE International Conference on,* 3-7 May 2010, pp.4197-4203.

BEYL, P., M. VAN DAMME, R. VAN HAM, B. VANDERBORGHT and D. LEFEBER. 2014. Pleated Pneumatic Artificial Muscle-Based Actuator System as a Torque Source for Compliant Lower Limb Exoskeletons. *Ieee-Asme Transactions on Mechatronics,* **19**(3), pp.1046-1056.

BHOUNSULE, P., J. PUSEY and C. MOUSSOUNI. 2016. A comparative study of leg kinematics for energy-efficient locomotion. *In: Conference: IEEE International Conference on Simulation, Modeling, and Programming for Autonomous Robots (SIMPAR), San Francisco, California.*

BROWN, E. W. and K. ABANI. 1985. Kinematics and kinetics of the dead lift in adolescent power lifters. *Medicine and science in sports and exercise,* **17**(5), pp.554-566.

BURGESS-LIMERICK, R. 2003. Squat, stoop, or something in between? *International Journal of Industrial Ergonomics,* **31**(3), pp.143-148.

C-MOTION. *Marker Set Guidelines* [online]. [Accessed 02/02/2016]. Available from: https://www.c-motion.com/v3dwiki/index.php?title=Marker_Set_Guidelines.

ČAPEK, K. and N. PLAYFAIR. 1923. *R.U.R. (Rossum's Universal Robots): a play in three acts and an epilogue.* London U6 - ctx_ver=Z39.88-2004&ctx_enc=info%3Aofi%2Fenc%3AUTF-8&rfr_id=info%3Asid%2Fsummon.serialssolutions.com&rft_val_fmt=info%3Aofi%2Ffmt%3Akev%3Amtx%3Abook&rft.genre=book&rft.title=R.U.R.+%28Rossum%27s+Universal+Robots%29&rft.au=%C4%8Capek%2C+Karel%2C+1890-1938&rft.au=Playfair%2C+Nigel&rft.date=1923-01-01&rft.pub=Oxford+University+Press&rft.externalDocID=b19528589&paramdict=en-US U7 - Book: Oxford University Press.

CEMPINI, M., S. M. M. DE ROSSI, T. LENZI, N. VITIELLO and M. C. CARROZZA. 2013. Self-Alignment Mechanisms for Assistive Wearable Robots: A Kinetostatic Compatibility Method. *Ieee Transactions on Robotics,* **29**(1), pp.236-250.

CENCIARINI, M. and A. M. DOLLAR. 2011. Biomechanical considerations in the design of lower limb exoskeletons. *IEEE Int Conf Rehabil Robot,* **2011**, p5975366.

CHESTNUTT, J., M. LAU, G. CHEUNG, J. KUFFNER, J. HODGINS and T. KANADE. 2005. Footstep planning for the honda asimo humanoid. *In: Robotics and Automation, 2005. ICRA 2005. Proceedings of the 2005 IEEE International Conference on*: IEEE, pp.629-634.

CRAIG, J. J. 2005. *Introduction to robotics: mechanics and control.* Pearson/Prentice Hall Upper Saddle River, NJ, USA:.

DONGHAI, W., L. KOK-MENG, G. JIAJIE and Y. CAN-JUN. 2014. Adaptive Knee Joint Exoskeleton Based on Biological Geometries. *Mechatronics, IEEE/ASME Transactions on,* **19**(4), pp.1268-1278.

DONGHAN, K., C. PYUNG HUN, S. MIN KYUN and S. JI-HYEON. 2011. Shoulder mechanism design of an exoskeleton robot for stroke patient rehabilitation. *In: Rehabilitation Robotics (ICORR), 2011 IEEE International Conference on,* June 29 2011-July 1 2011, pp.1-6.

ERGIN, M. A. and V. PATOGLU. 2012. ASSISTON-SE: A self-aligning shoulder-elbow exoskeleton. *In: Robotics and Automation (ICRA), 2012 IEEE International Conference on,* 14-18 May 2012, pp.2479-2485.

ESCAMILLA, R. F., A. C. FRANCISCO, G. S. FLEISIG, S. W. BARRENTINE, C. M. WELCH, A. V. KAYES, K. P. SPEER and J. R. ANDREWS. 2000. A three-dimensional biomechanical analysis of sumo and conventional style deadlifts. *Medicine and science in sports and exercise,* **32**(7), pp.1265-1275.

FICK, B. and J. MAKINSON. 1971. Final report on Hardiman I prototype for machine augmentation of human strength and endurance. *United States Army Project No. IM62410105072, General Electr. Co., New York, DTIC Accession Number: AD0739735.*

GALLAGHER, S. and R. UNGER. 1990. Lifting in four restricted lifting conditions: psychophysical, physiological and biomechanical effects of lifting in stooped and kneeling postures. *Applied Ergonomics,* **21**(3), pp.237-245.

GOIRIENA, A., I. RETOLAZA, A. CENITAGOYA, F. MARTINEZ, S. RIANO and J. LANDALUZE. 2009. Analysis of Bowden cable Transmission performance for orthosis applications. *In: Mechatronics, 2009. ICM 2009. IEEE International Conference on,* 14-17 April 2009, pp.1-6.

GOPURA, R. A. R. C., K. KIGUCHI and D. S. V. BANDARA. 2011. A brief review on upper extremity robotic exoskeleton systems. *In: Industrial and Information Systems (ICIIS), 2011 6th IEEE International Conference on,* 16-19 Aug. 2011, pp.346-351.

HAYASHI, T., H. KAWAMOTO and Y. SANKAI. 2005. Control method of robot suit HAL working as operator's muscle using biological and dynamical information. *In: Intelligent Robots and Systems, 2005.(IROS 2005). 2005 IEEE/RSJ International Conference on*: IEEE, pp.3063-3068.

HEALTH, M. A. A. R. P. 2013. *The human skeleton* [online]. [Accessed 16 feb].

HSCIC. 2013. *Health Survey for England - 2012* [online]. [Accessed 08-2014]. Available from: http://www.hscic.gov.uk/catalogue/PUB13218.

HYON, S., J. MORIMOTO, T. MATSUBARA, T. NODA and M. KAWATO. 2011. XoR: Hybrid drive exoskeleton robot that can balance. *In: Intelligent Robots and Systems (IROS), 2011 IEEE/RSJ International Conference on,* 25-30 Sept. 2011, pp.3975-3981.

JACOBSEN, S. C. and M. OLIVIER. 2009. *Contact displacement actuator system.* Google Patents.

JACOBSEN, S. C. and M. X. OLIVIER. 2014. *Contact displacement actuator system.* Google Patents.

JARRASSE, X, N. and G. MOREL. 2012. Connecting a Human Limb to an Exoskeleton. *Robotics, IEEE Transactions on,* **28**(3), pp.697-709.

KAWAMOTO, H. and Y. SANKAI. 2002. Power assist system HAL-3 for gait disorder person. *Computers helping people with special needs.* Springer, pp.196-203.

KAZEROONI, H. and R. STEGER. 2005. The Berkeley Lower Extremity Exoskeleton. *Journal of Dynamic Systems, Measurement, and Control,* **128**(1), pp.14-25.

KAZEROONI, H. and R. STEGER. 2006. The Berkeley lower extremity exoskeleton. *Journal of dynamic systems, measurement, and control,* **128**(1), pp.14-25.

KENNEALLY, G., A. DE and D. KODITSCHEK. 2016. Design principles for a family of direct-drive legged robots. *IEEE Robotics and Automation Letters,* **1**(2), pp.900-907.

KIGUCHI, K., K. KADO and Y. HAYASHI. 2011. Design of a 7DOF upper-limb power-assist exoskeleton robot with moving shoulder joint mechanism. *In: Robotics and Biomimetics (ROBIO), 2011 IEEE International Conference on,* 7-11 Dec. 2011, pp.2937-2942.

KIGUCHI, K., M. H. RAHMAN, M. SASAKI and K. TERAMOTO. 2008. Development of a 3DOF mobile exoskeleton robot for human upper-limb motion assist. *Robotics and Autonomous Systems,* **56**(8), pp.678-691.

KOTHIYAŁ, K., J. MAZUMDAR and G. NOONE. 1992. A biomechanical model for optimal postures in manual lifting tasks. *International Journal of Industrial Ergonomics,* **10**(3), pp.241-255.

LETIER, P., M. AVRAAM, S. VEILLERETTE, M. HORODINCA, M. DE BARTOLOMEI, A. SCHIELE and A. PREUMONT. 2008. SAM : A 7-DOF portable arm exoskeleton with local joint control. *In: Intelligent Robots and Systems, 2008. IROS 2008. IEEE/RSJ International Conference on,* 22-26 Sept. 2008, pp.3501-3506.

LISZKA, M. 2006. *Mechanical design of a robotic arm expskeleton for shoulder rehabilitation.* thesis.

LOW, K. H. 2011. Robot-assisted gait rehabilitation: From exoskeletons to gait systems. *In: Defense Science Research Conference and Expo (DSR), 2011,* 3-5 Aug. 2011, pp.1-10.

LUCCHESI, N., S. MARCHESCHI, L. BORELLI, F. SALSEDO, M. FONTANA and M. BERGAMASCO. 2010. An approach to the design of fully actuated body extenders for material handling. *In: RO-MAN, 2010 IEEE*: IEEE, pp.482-487.

MALOSIO, M., N. PEDROCCHI, F. VICENTINI and L. M. TOSATTI. 2011. Analysis of elbow-joints misalignment in upper-limb exoskeleton. *In: Rehabilitation Robotics (ICORR), 2011 IEEE International Conference on,* June 29 2011-July 1 2011, pp.1-6.

MAQBOOL, H. F., M. A. B. HUSMAN, M. I. AWAD, A. ABOUHOSSEIN, N. IQBAL and A. A. DEHGHANI-SANIJ. 2017. A real-time gait event detection for lower limb prosthesis control and evaluation. *IEEE transactions on neural systems and rehabilitation engineering,* **25**(9), pp.1500-1509.

MARCHESCHI, S., F. SALSEDO, M. FONTANA and M. BERGAMASCO. 2011. Body Extender: Whole body exoskeleton for human power augmentation. *In: Robotics and Automation (ICRA), 2011 IEEE International Conference on,* 9-13 May 2011, pp.611-616.

MARTINEZ, F., I. RETOLAZA, A. PUJANA-ARRESE, A. CENITAGOYA, J. BASURKO and J. LANDALUZE. 2008. Design of a five actuated DoF upper limb exoskeleton oriented to workplace help. *In: Biomedical Robotics and Biomechatronics, 2008. BioRob 2008. 2nd IEEE RAS & EMBS International Conference on,* 19-22 Oct. 2008, pp.169-174.

MATHWORKS. [online]. [Accessed 02-02-2016]. Available from: http://se.mathworks.com/help/symbolic/select-numeric-or-symbolic-solver.html.

MATHWORKS. *designfilt* [online]. [Accessed 20-04-2017]. Available from: https://uk.mathworks.com/help/signal/ref/designfilt.html.

MATHWORKS. *diff* [online]. [Accessed 02-03-2017]. Available from: https://se.mathworks.com/help/symbolic/diff.html?requestedDomain=true.

MATHWORKS. *gradient*.

MATHWORKS. *hampel* [online]. [Accessed 02-03-2017]. Available from: https://uk.mathworks.com/help/signal/ref/hampel.html.

MATHWORKS. *smooth* [online]. [Accessed 09-06-2016]. Available from: http://uk.mathworks.com/help/curvefit/smooth.html.

MINITEC. *Minitecframing* [online]. [Accessed 10-2014]. Available from: http://minitecframing.com/.

MINITEC. 2014. *Minitecframing* [online]. [Accessed 10-2014].

MOSHER, R. S. 1967. *Handyman to hardiman*. (0148-7191). SAE Technical Paper.

MU, X. and Q. WU. 2006. On impact dynamics and contact events for biped robots via impact effects. *IEEE Transactions on Systems, Man, and Cybernetics, Part B (Cybernetics),* **36**(6), pp.1364-1372.

NEF, T., M. MIHELJ, G. KIEFER, C. PERNDL, R. MULLER and R. RIENER. 2007. ARMin-Exoskeleton for arm therapy in stroke patients. *In: Rehabilitation Robotics, 2007. ICORR 2007. IEEE 10th International Conference on*: IEEE, pp.68-74.

NORDIN, M. and V. H. FRANKEL. 2001. *Basic biomechanics of the musculoskeletal system.* Lippincott Williams & Wilkins.

OPPENHEIM, A. Spring 2011. *RES.6-008 Digital Signal Processing* [online]. [Accessed 02-04-2016]. Available from: https://ocw.mit.edu.

PALASTANGA, N., R. SOAMES and D. PALASTANGA. 2008. *Anatomy and Human Movement Pocketbook.* Churchill Livingstone.

PERRY, J. C., J. ROSEN and S. BURNS. 2007. Upper-limb powered exoskeleton design. *Mechatronics, IEEE/ASME Transactions on,* **12**(4), pp.408-417.

PHEASANT, S. 1996. *Bodyspace: Anthropometry, Ergonomics And The Design Of Work: Anthropometry, Ergonomics And The Design Of Work.* Taylor & Francis.

RAMEZANI, A., J. W. HURST, K. AKBARI HAMED and J. W. GRIZZLE. 2013. Performance Analysis and Feedback Control of ATRIAS, A Three-Dimensional Bipedal Robot. *Journal of Dynamic Systems, Measurement, and Control,* **136**(2), pp.021012-021012-12.

SANKAI, Y. 2006. Leading edge of cybernics: Robot suit hal. *In: SICE-ICASE, 2006. International Joint Conference*: IEEE, pp.P-1-P-2.

SCHIELE, A. and G. HIRZINGER. 2011. A new generation of ergonomic exoskeletons - The high-performance X-Arm-2 for space robotics

telepresence. *In: Intelligent Robots and Systems (IROS), 2011 IEEE/RSJ International Conference on,* 25-30 Sept. 2011, pp.2158-2165.

SCHIELE, A. and F. C. VAN DER HELM. 2006. Kinematic design to improve ergonomics in human machine interaction. *IEEE Trans Neural Syst Rehabil Eng,* **14**(4), pp.456-69.

SHIGLEY, J. E. 1972. Mechanical engineering design.

SINGH, D. A. P. [online]. [Accessed 27-02-2018]. Available from: http://boneandspine.com/normal-gait-cycle/.

STEGER, R., S. H. KIM and H. KAZEROONI. 2006. Control scheme and networked control architecture for the Berkeley lower extremity exoskeleton (BLEEX). *In: Robotics and Automation, 2006. ICRA 2006. Proceedings 2006 IEEE International Conference on*: IEEE, pp.3469-3476.

STRAKER, L. 2003. Evidence to support using squat, semi-squat and stoop techniques to lift low-lying objects. *International Journal of Industrial Ergonomics,* **31**(3), pp.149-160.

TANG, Z., K. ZHANG, S. SUN, Z. GAO, L. ZHANG and Z. YANG. 2014. An Upper-Limb Power-Assist Exoskeleton Using Proportional Myoelectric Control. *Sensors,* **14**(4), pp.6677-6694.

UNITED STATES. DEPARTMENT OF, D., A. UNITED STATES. NATIONAL, A. SPACE, A. UNITED STATES. FEDERAL AVIATION, KNOVEL and J. H. T. C. WILLIAM. 2011. *Metallic materials properties development and standardization (MMPDS): MMPDS-06.* Washington, D.C.: Federal Aviation Administration.

VEPA, R. 2009. *Biomimetic robotics: mechanisms and control.* Cambridge University Press.

VITIELLO, N., T. LENZI, S. ROCCELLA, S. M. M. DE ROSSI, E. CATTIN, F. GIOVACCHINI, F. VECCHI and M. C. CARROZZA. 2013. NEUROExos: A Powered Elbow Exoskeleton for Physical Rehabilitation. *Robotics, IEEE Transactions on,* **29**(1), pp.220-235.

WHITTLE, M. W. 2014. *Gait analysis: an introduction.* Butterworth-Heinemann.

WINTER, D. A. 2009a. *Biomechanics and motor control of human movement.* 4th ed. Chichester;Hoboken, N.J;: Wiley.

WINTER, D. A. 2009b. *Biomechanics and motor control of human movement.* John Wiley & Sons.

ZHAO, H.-H., W.-L. MA, M. B. ZEAGLER and A. D. AMES. 2014. Human-inspired multi-contact locomotion with AMBER2. *In: ICCPS'14: ACM/IEEE 5th International Conference on Cyber-Physical Systems (with CPS Week 2014)*: IEEE Computer Society, pp.199-210.

ZHENG, Y.-F. and H. HEMAMI. 1984. Impact effects of biped contact with the environment. *IEEE Transactions on Systems, Man, and Cybernetics,* (3), pp.437-443.

ZHOU, L., S. BAI, M. S. ANDERSEN and J. RASMUSSEN. 2012. Design and Optimization of a Spring-loaded Cable-driven Robotic Exoskeleton. *In: Nordic Seminar on Computational Mechanics 25*, pp.205-208.

ZOSS, A. 2006. *Actuation Design and Implementation for Lower Extrimity Human Exoskeletons.* Doctor of Philosophy thesis, University of California, Berkeley.

ZOSS, A. and H. KAZEROONI. 2006. Design of an electrically actuated lower extremity exoskeleton. *Advanced Robotics,* **20**(9), pp.967-988.

ZOSS, A., H. KAZEROONI and A. CHU. 2005. On the mechanical design of the Berkeley Lower Extremity Exoskeleton (BLEEX). *In: Intelligent Robots and Systems, 2005. (IROS 2005). 2005 IEEE/RSJ International Conference on,* 2-6 Aug. 2005, pp.3465-3472.

ZOSS, A. B., H. KAZEROONI and A. CHU. 2006a. Biomechanical design of the Berkeley lower extremity exoskeleton (BLEEX). *IEEE/ASME Transactions On Mechatronics,* **11**(2), pp.128-138.

ZOSS, A. B., H. KAZEROONI and A. CHU. 2006b. Biomechanical design of the Berkeley lower extremity exoskeleton (BLEEX). *Mechatronics, IEEE/ASME Transactions on,* **11**(2), pp.128-138.

APPENDIX A

Exoskeleton Tasks

Table A-1 - Showing activities to be performed by the device

No.	Activity	Unique Identifier
1.	Walk on level ground	NA-1
2.	Walk on rough terrain	NA-2
3.	Run	NA-3
4.	Squat	NA-4
5.	Get up from a fallen position	NA-5
6.	Walk up the stairs	NA-6
7.	Walk up the slopes	NA-7
8.	Walk down the stairs	NA-8
9.	Walk down the slopes	NA-9
10.	Go through doorways	NA-10
11.	Walk on level ground with load	NA-11
12.	Walk on rough terrain with load	NA-12
13.	Run with load	NA-13
14.	Squat with load	NA-14
15.	Get up from a fallen position with load	NA-15
16.	Walk up the stairs with load	NA-16
17.	Walk up the slopes with load	NA-17
18.	Walk down the stairs with load	NA-18
19.	Walk down the slopes with load	NA-19
20.	Go through doorways with load	NA-20
21.	Deadlift	NA-21
22.	Overhead shoulder press (with bar)	NA-22
23.	Vertical jump	NA-23

24.	Bench press (with bar)	NA-24
25.	Horizontal push (full body)	NA-25
26.	Horizontal pull (full body)	NA-26
27.	Biceps curl (with bar)	NA-27
28.	Bent over row (with bar)	NA-28
29.	Pull down	NA-29

APPENDIX B

Customer Needs Document

(As for the end product)

Draft 4

Table B-1 - Customer needs document

No.	Need	Unique Identifier
1.	The device shall be a full body exoskeleton.	N-1
2.	The kinematic design of the frame shall allow the device to perform activities specified in the Appendix A.	N-2
3.	The frame shall be adjustable for different user size.	N-3
4.	The frame shall be modular.	N-4
5.	The joint and the actuator for each DOF shall be a separable module.	N-5
6.	The primary product shall be untethered, i.e. energetically independent.	N-6
7.	The load carrying capacity shall be the maximum achievable amount, considering the safety.	N-7
8.	The system shall be able to sense human motion (kinematics and dynamics).	N-8
9.	The device shall be easy to use.	N-9
10.	The device shall be easily adaptable to a new user.	N-10
11.	The device shall be safe.	N-11
12.	The device shall be reliable.	N-12
13.	The device shall be weight efficient.	N-13
14.	The power consumption of the device shall be efficient.	N-14
15.	The operation (as explained in the Appendix A) duration time shall be long.	N-15
16.	The system shall be cost-effective.	N-16
17.	The appearance of the device shall be acceptable.	N-17
18.	The user shall not be burdened with any extra effort to carry the exoskeleton (while not carrying any payload).	N-18

19.	The device shall comply with University of Leeds standards.	N-19
20.	The device shall comply with BS EN ISO 13482:2014.	N-20
21.	There shall be a feasible maintenance scheme in place.	N-21
22.	The device shall have an acceptable life-cycle.	N-22
23.	The device should decrease the metabolic cost of load carrying task.	N-23
24.	The actuators of the device should be dynamically strong enough to perform activities specified in the Appendix A except for running.	N-24
25.	The device should not impede movements.	N-25
26.	The device may be clean.	N-26
27.	The device may be easily put on and off by the user without any assistance.	N-27
28.	The noise produced by the primary product may be socially acceptable.	N-28
29.	The Type 1 variation of the device may be possible to achieve via modular changes (low cost, assistive, with the minimum possible actuators).	N-29
30.	The Type 3 variation of the device may be possible to achieve via modular changes (lower limb with a backpack frame, enhancive).	N-30
31.	The Type 5 variation of the device may be possible to achieve via modular changes (lower limb exoskeleton, hung from a frame or the ceiling, used for rehabilitation).	N-31
32.	The design should allow for subsystems of the product to be used as orthotic devices.	N-32

APPENDIX C

Customer Requirements Document

Draft 3

Table C-1 - Customer requirements document

Need (N-*X*)	Metric	Unit	Priority[1]	Marginally acceptable Value	Ideal Value	Unique Identifier
7	1. Mechanical Strength (weight of the user and load)	kg	1			M-1
2	2. Possible manoeuvres	-	1			M-2
4, 29, 31, 32, 30, 5	3. List of separate modules	list	1 (TBD)			M-4
3	4. Adjusting features	list	1			M-5
28	5. Noise	dB, subj.	3			M-6
26	6. Cleanliness	subj.	3			M-7
6	7. Untethered	-	1			M-8
7	8. Load carrying capacity without user effort while walking	kg	1			M-9
11	9. Maximum allowable angular speed of joints	rad/s	1			M-11
11	10. Maximum allowable angular acceleration	rad/s^2	1			M-12
13	11. Weight	kg	1			M-13
14	12. Power consumption	W	1			M-14

[1] Where '1' is the highest priority and higher natural numbers represent lower priorities

15	13. Operation duration	minute	1			M-15
16	14. Price	£, $, €	1			M-16
17	15. Appearance	subj.	1			M-17
32	16. The joint motions actively assisted by intended orthotic subproducts	list	3			M-18
10	17. Ease of control system adaptation	-	1			M-19
9, 10	18. Time to learn to operate the device	h	2 (TBD)			M-37
8	19. Human motions sensed	list	1			M-25
9	20. Ease of use	subj.	1			M-26
27	21. Ease of putting on and off	min. , subj.	3			M-33
18	22. Endurance augmentation (decrease of metabolic cost) without load.	%	1			M-20
23	23. Endurance augmentation (decrease of metabolic cost) with maximum load.	%	2			M-24
21	24. Maintenance scheme feasibility	subj.	1			M-21
11	25. Vibration	subj.	1			M-22
11	26. Safety	subj.	1			M-23
12	27. Reliability	subj.	1			M-27

11, 25, 2	28. Ranges of motion of joints	rad	1 (TBD)			M-28
19	29. University of Leeds standards compliance	subj.	1			M-29
20	30. Standard BS EN ISO 13482:2014 compliance	subj.	1			M-30
21	31. Maintainability	subj.	1			M-31
22	32. Life-cycle	TBD	1			M-32
29	33. Cost of the Type 1 variation	£, $, €	3			M-34
30	34. An option for a backpack frame	subj.	3			M-35
31	35. Rehabilitative capabilities	subj.	3			M-36
9	36. Time to learn to operate the device	h	1			M-37
2	37. Size of the longest dimension increase of the system	m	1			M-38

APPENDIX D

Metrics Document

Table D-1 - Metrics document

Unique Identifier	Metric	Unit	Marginally Acceptable Value	Ideal Value	Standard	Suggestion
M-1	Mechanical strength (weight of the load)	kg	45 (50% over average human)	90 (200%)	N/A	Marginal: 34, Ideal: 90
M-2	Possible manoeuvres	-	Appendix A to Customer Needs	Appendix A to Customer Needs		
M-4	List of separate modules	list	lower body with spine, upperbody exoskeleton	each motor, each link, each joint		
M-5	Adjustability features	list	limbs length, trunk length	limbs length, trunk length		
M-6	Noise	dB, subj.	safe for human	socially acceptable	Yet to be found	Comply with standards, and also keep it acceptable (subj.)
M-7	Cleanliness	subj.	no fume	no by products of energy production		
M-8	Untethered	-	tethered	untethered	N/A	unthethered
M-9	Load carrying capacity without user effort while walking	kg	45 (50% over average human)	60 (100% over average human) OR 90 (200%)		

M-11	Maximum allowable angular speed of joints	rad/s	safe	safe	Yet to be found	Comply with the standards
M-12	Maximum allowable angular acceleration	rad/s²	safe	safe	Yet to be found	Comply with the standards
M-13	Weight	kg	68	21		
M-14	Power consumption	W	lowest possible considering the other requirements	lowest possible considering the other requirements	N/A	minimise via optimisation
M-15	Operation duration (untethered)	h	1 h	2h 40 min		
M-16	Price	£, $, €	$30k	$10k		
M-17	Appearance	subj.	not a concern	socially acceptable		
M-18	The joint motions actively assisted by intended orthotic subproducts	list	none	each joint		
M-19	Ease of control system adaptation	-	1 - 2 Week	wear-and-use		
M-20	decrease of metabolic cost of walking without load.	%		Marginal: no excessive burden, Ideal: 5-12% without load, 15 with 36.7 kg (at 2MPH)	N/A	Marginal: no excessive burden, Ideal: 5-12% without load, 15 with 36.7 kg (at 2MPH)
M-21	Maintenance scheme feasibility	subj.	once/week (periodic check and operaion hours)	once/year		

M-22	Vibration	subj.	human safe	imperceptible		
M-23	Safety	subj.	safe for human	safe for human		
M-24	Endurance augmentation (decrease of metabolic cost) **with the maximum load (M-1)** as comapared to the case with the same load, without the exoskeleton	%	SF: 15%, MN: the controller should go to safe state if nominal operation value is exceeded	SF:50%, MN: the controller should go to safe state if nominal operation value is exceeded		
M-25	Human motions sensed	list				
M-26	Ease of use	subj.	trained users can use the exoskeleton	any user can naturally move within exoskeleton		
M-27	Reliability	subj.	reliable	reliable		
M-28	Ranges of motion of user joints	rad	as required by the manouvers listed in the Appendix A	full human range		
M-29	University of Leeds standards compliance	subj.	compliant	compliant		
M-30	Standard BS EN ISO 13482:2014 compliance	subj.	not-compliant	compliant		
M-31	Maintainability	subj.	maintainable by technician	maintainable by technician		
M-32	Life-cycle	TBD	2 years (quarantee)	10 years		
M-33	Ease of putting on and off	min. , subj.	additional 1 person to aid the user	no help required from another person		

M-34	Cost of the Type 1 variation	£, $, €				
M-35	An option for a backpack frame	subj.	yes	yes		
M-36	Rehabilitative capabilities	subj.	none	available for each joint		
M-37	Time for the user to learn to operate the device	h	one week training	immediate	N/A	0
M-38	Size of the longest dimension increase of the system	m	100% of aveage human	25% of average human		

APPENDIX E

Anthropomorphic Data

Table E-1 - Anthropomorphic data (Pheasant 1996; Peebles et al. 1998)

Number ID	Description	5th percentile (mm)	50th percentile (mm)	95th percentile (mm)	SD
1	Shoulder Height, from floor to acromion	1315	1425	1535	66
2	Elbow height, from floor to radiale	1005	1090	1180	52
3	Hip height, from floor to greater trochanter	840	920	1000	50
4	Knuckle height, from floor to metacarpal 3	690	755	825	41
5	Shoulder grip length, from acromion to object in hand	610	665	715	32
6	Forward grip reach, from back of shoulder blades to object in hand	720	780	835	34
7	Foot length, back of heel to tip of toes	240	265	285	14
8	Foot breadth, maximum horizontal breadth	85	95	110	6
9	Wrist height, from floor to wrist crease	783.8	854.9	926.0	43.2
10	Trunk depth at buttocks, from maximum protrusion to trunk	199.1	243.5	287.8	27
11	Knee cap height, from floor to upper border of patella	461.0	506.7	552.1	27.6

12	Shoulder breadth, bi acromial	365	400	430	20
13	Hip breadth, horizontal distance across maximum projections of the greater trochanters at head of femur	315.5	363.3	411.1	29
14	Rear of heel to outer ankle	47.3	55.5	63.7	5
15	Ankle height, from floor to maximum protrusion of inner ankle bone	64.7	76.8	86	5.5
16	Heel breadth	59.7	66.8	73.9	4.3

APPENDIX F

Actuation in Exoskeleton Design

Hydraulic Actuation

The BLEEX exoskeleton was initially designed utilizing linear hydraulic systems for ankle, knee and hip flexion/extension as well as hip adduction/abduction (Zoss 2006). The selection of actuators are derived from CGA, rotation of the hip joint was determined not to need an active actuation during walking.

The research considers the exoskeleton robot to be analogous to the human as far as joint kinematic characteristics are concerned. The torque of the joints that are actuated in BLEEX are designed based on human joint torque data. The CGA data used was normalized to the weights of the subjects participating. In designing the actuation system for BLEEX the CGA data was scaled to the expected weight of the exoskeleton and the external load, 75 kg total.

The torque produced by linear hydraulic systems was designed around the required torque from the scaled CGA data. The hip, knee and ankle joint designs can be seen in closer detail in Figure F-1.
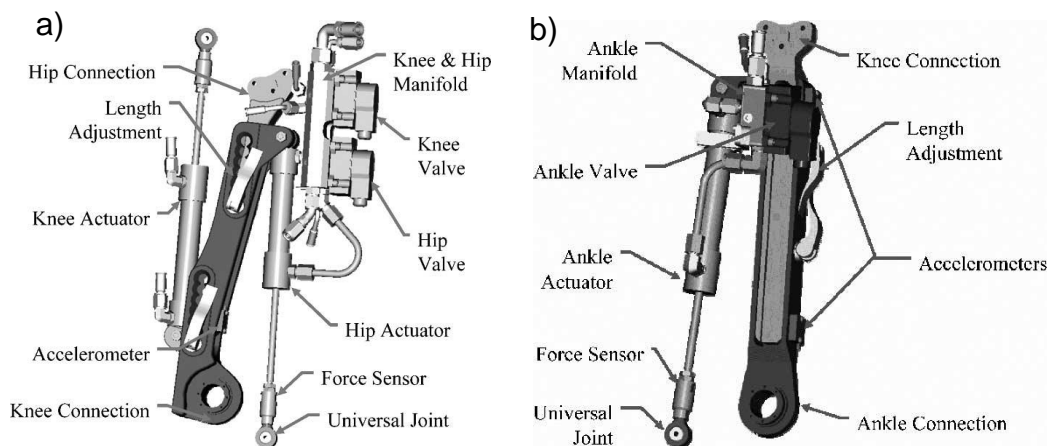
Figure F-1 - BLEEX hydraulic actuation systems for a) hip and knee and b) ankle (Zoss 2006).

Electric Actuation

Further analysis is made on replacing the hydraulic actuators with electric actuators (Zoss and Kazerooni 2006) shown in Figure F-2. It is shown that the joint weight (including the electric motor) is twice that of the hydraulic joint weight yet the power consumption in level walking is nearly half that of the hydraulic system. It is concluded that the electric system can be significantly more

desirable if the bulk weight of the electric actuator can be relocated so that the weight of the lower actuators would not contribute to the power consumption of the upper actuators. The use of actuator systems which incorporate harmonic drives and are placed on the joint axis directly has been considered as being bulky by some researchers (Liszka 2006).
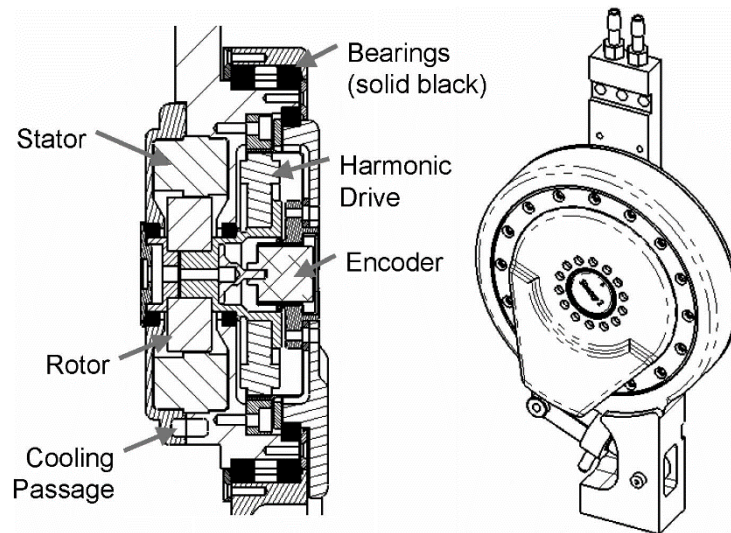
Figure F-2 - The BLEEX electrical actuation system
(Zoss and Kazerooni 2006)

The Percro Body Extenders actuation system shown in Figure F-3 includes electric rotary motors which are designed to provide up to 500Nm constant toque (800Nm stall torque) with a total weight of 6kg per unit (Bergamasco *et al.* 2010). The device is built to allow for dual direction drive using a pantograph mechanism. The actuation system of the BE is meant to be modular therefore it is replicated throughout the exoskeleton.

Figure F-3 - The Body Extenders actuation system
(Bergamasco *et al.* 2010)

Pneumatic actuators

Researches have shown that actuating exoskeletons with air muscles lead to a limited range of motion due to the contraction restriction of air muscles (Tang *et al.* 2014). Pleated pneumatic artificial air muscles shown in Figure F-4 used in combination with a four bar linkage system to alleviate the variable force characteristics as well as increasing the range of motion of the rotary joint (Beyl *et al.* 2014). A system using air muscles would require two in an antagonistic combination, as they are unidirectional.

Utilizing a hybrid actuation system, electric motors and pneumatic air muscles, the XoR shown in Figure F-5 presents a middle point where the strengths of both systems can be used (Hyon *et al.* 2011), air muscles for their high power density and electric actuators for their short time high torque capacities. The results show that the system was lacking in power for the hip flexion/extension, but the concept was proven nonetheless.
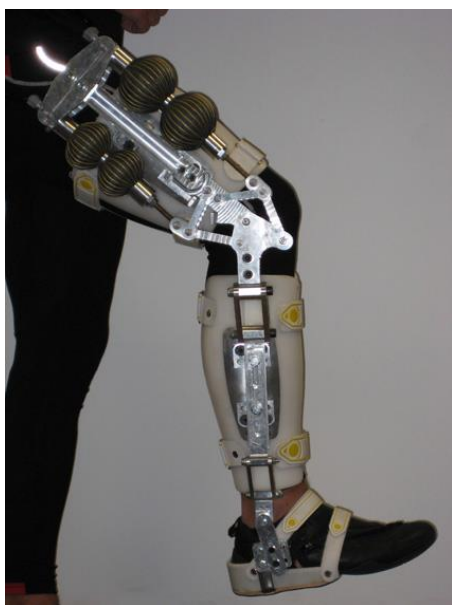
Figure F-4 - Pleated pneumatic actuators for a knee exoskeleton (Beyl *et al.* 2014)
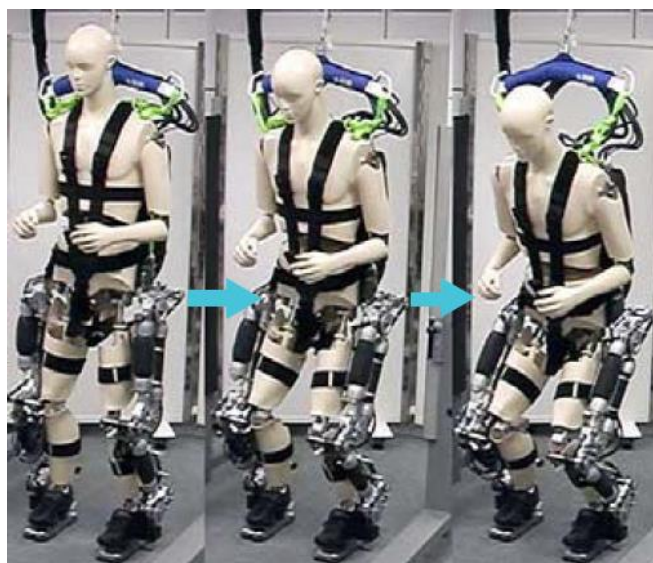
Figure F-5 - The XoR with a hybrid actuation system (Hyon *et al.* 2011)

Cable transmission

On several occasions cable transmission of force is used to drive an exoskeleton device. Only one research is known to the author that is developed with the purpose of enhancing the users capacity and allowing him/her to lift a 10kg load (Martinez *et al.* 2008). This upper body exoskeleton is shown being used in Figure F-6. Preliminary experiments show that for a two DoF system the Bowden cable transmission works, although thorough analysis needs to be done on the details of durability and efficiency.

Work has also been conducted in identifying the primary affecting factors when using cable transmission in orthotic exoskeletons. It was found that the most influencing factor is the cable flexion angle which reaches a load loss factor of 60% at 180 degrees bending (Goiriena *et al.* 2009).
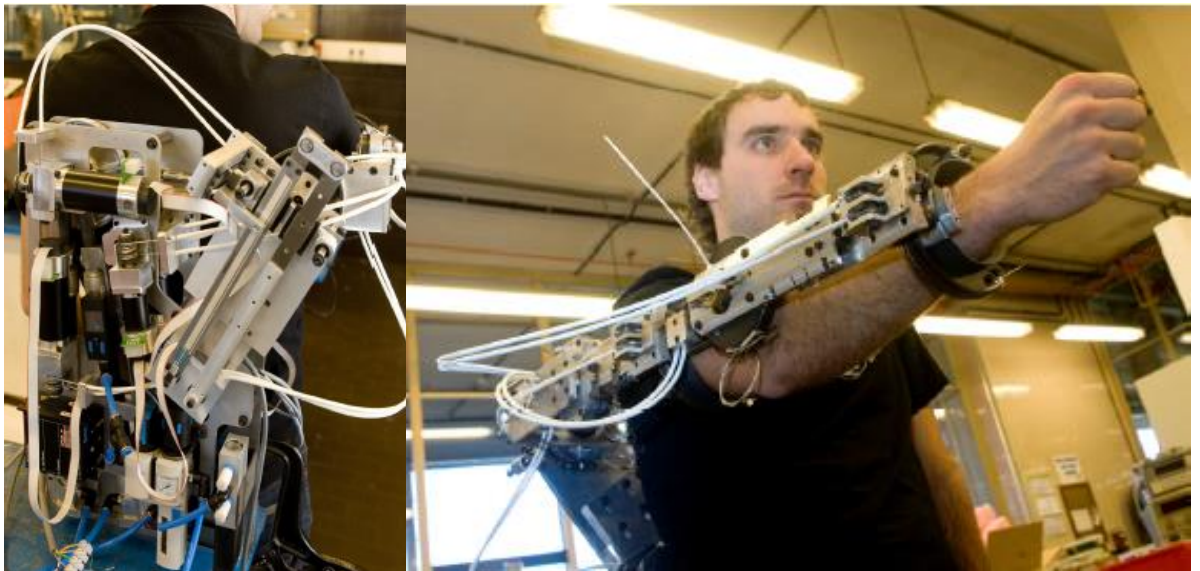
Figure F-6 - Bowden cables used to transmit forces in this exoskeleton a) the system back and b) the arm attached to user (Martinez *et al.* 2008)

Contributing factors from actuation methods in exoskeletons

Although the internal structure of the actuation system of the Body Extender is based on remotely locating the electric motor and the joint rotating component it is not as remotely located as the cable driven exoskeletons presented. This, and the fact that the same actuation system is used for most of the joints, adds to the bulkiness of the BE.

Research on BLEEX has suggested that electric actuation systems could potentially be better suited for an enhancive exoskeleton should the actuators be remotely located. The proof of this however has not been found in any literature. This consideration was made for the BLEEX which is a task dependant exoskeleton only designed for walking with a load.

Electric actuation systems have been utilized in full body enhancing exoskeleton BE. The more interesting comparison would be the characteristics of the BE against the XOS-2 that uses hydraulic systems. As for size visual comparison leads one to believe that the Body Extender using electric actuation, is larger and bulkier than the XOS-2.

APPENDIX G

Ethical Approval

Performance, Governance and Operations
Research & Innovation Service
Charles Thackrah Building
101 Clarendon Road
Leeds LS2 9LJ Tel: 0113 343 4873
Email: ResearchEthics@leeds.ac.uk

UNIVERSITY OF LEEDS

Abbas Dehghani-Sanij
School of Mechanical Engineering
University of Leeds
Leeds, LS2 9JT

MaPS and Engineering joint Faculty Research Ethics Committee (MEEC FREC)
University of Leeds

28 February 2018

Dear Abbas

| **Title of study** | Development of a full-body intelligent modular power enhancing robotic exoskeleton for humans. |
| **Ethics reference** | **MEEC 15-004** |

I am pleased to inform you that the application listed above has been reviewed by the MaPS and Engineering joint Faculty Research Ethics Committee (MEEC FREC) and I can confirm a favourable ethical opinion as of the date of this letter. The following documentation was considered:

Document	Version	Date
MEEC 15-004 Ethical_Application_Exoskeleton_Project_combined.pdf	1	25/09/15

The Chair made the following comments:
- Please ask *all* participants (phase M, 0 and 1) to sign a consent form.

Please notify the committee if you intend to make any amendments to the original research as submitted at date of this approval, including changes to recruitment methodology. All changes must receive ethical approval prior to implementation. The amendment form is available at http://ris.leeds.ac.uk/EthicsAmendment.

Please note: You are expected to keep a record of all your approved documentation, as well as documents such as sample consent forms, and other documents relating to the study. This should be kept in your study file, which should be readily available for audit purposes. You will be given a two week notice period if your project is to be audited. There is a checklist listing examples of documents to be kept which is available at http://ris.leeds.ac.uk/EthicsAudits.

We welcome feedback on your experience of the ethical review process and suggestions for improvement. Please email any comments to ResearchEthics@leeds.ac.uk.

Yours sincerely

Jennifer Blaikie
Senior Research Ethics Administrator, Research & Innovation Service
On behalf of Professor Gary Williamson, Chair, MEEC FREC

APPENDIX H

Design of Test-Rig and Modular 1 Degree of Freedom Joint For Exoskeleton Project

In this chapter the design of a test-rig and a modular 1 DoF joint is presented. The purpose of these are to aid in the analysis and testing of the exoskeleton to be developed for the larger project this research is a part of.

The chapter begins by looking at the design of the gantry test-rig. First the purpose of the test-rig is outlined. This is followed by outlining the constraints and requirements, which include the geometric constraints of the room which the test-rig will be in as well as load carrying capacity requirements at the time of the design of the test-rig.

The second section of the chapter will look at detailed design process of a single DoF joint. The purpose of the joint is to aid in the research in all aspects of the project including, control, actuation and design. Therefore some constraints are set which are beyond the scope of this research for a single joint system, which is developed by some members of the exoskeleton project.

The chapter will be concluded with a discussion and summary on the test-rig and joint.

Development of a Gantry for Testing of Exoskeleton Equipment

In order to perform work on the exoskeleton post production a test rig is developed. This is to keep the user and developers safe. The design of this gantry or support frame is described in this section.

Here are presented the justification of the selection of certain components by presenting the purpose of the support frame. It will then outline the various constraints in terms of operational area which includes the considered movements and maximum supported load. Force calculations will be carried out and components capable of handling these forces will be presented together with appropriate sliding systems.

Purpose

The primary purpose of the support frame is to allow for experiments to be conducted within a safe environment. The frame is to provide structural support within a given tolerance and requirements to any module, component or combination of the two which needs testing.

The requirement of the support frame is to allow support for a full exoskeleton prototype within a safe environment. In the event of malfunction or shut down of the exoskeleton it will be able to support, structurally, the full weight of the user, the exoskeleton and the load which it carries. It should allow for an array of user motions to be performed within the volume of the frame. The support frame should not hinder the user motion and thus will be equipped with sliders to allow for maximum compliance with user motion. These requirements can be found in the Customer Requirements document in APPENDIX C and the Metrics document found in APPENDIX D. Furthermore certain criteria for the exoskeleton are presented in the Customer Needs document in APPENDIX B. The Exoskeleton Tasks documents in APPENDIX A outlines the tasks intended to be performed by the exoskeleton.

Design Constraints and Requirements

The space constraints are defined which affect the geometry of the support frame; furthermore the operation-space is also defined. The maximum load to which the structure can withstand within a tolerable deflection is also defined.

The allowable area is the area in which the support frame can be built within the room. It is measured as 7.44 m length, 6.23 m width and 2.17-2.19 m in height;

the difference in height is due to an uneven floor or ceiling which is at the time this report was written unclear.

The room's walls and ceiling have uneven surfaces protruding, for example lamps, wiring etc. Therefor the walls cannot be used for attachment. These hindrances are taken into consideration when deriving the support frame dimensions but are too minute to be listed in detail. The most extreme protrusion from the wall is used as the base point and a line is drawn from that point normal to the wall which it protrudes from. Lamps that are located where the support frame is to be set up will be relocated. The ceiling also has a divide which makes approximately half the room shorter than the other, due to the location of sensitive equipment however the area with low roof will not be considered. Taking into consideration the above the allowable area is reduced to 7.30 m length, 2.9 m width and 2.19 m height.

In order to know which width to use for the support frame the consideration is given to all of the motions found in Customer Needs document as well as diagonal walking and circular walking. Due to height restrictions which are beyond control certain motions are automatically eliminated.

Operation Area

Using anthropomorphic data (found in APPENDIX E) a span of 1.86 m from arm to arm is used in the consideration of test-rig width. The width of the operation-space is therefor set as 2 m. This means the user will, when centred in the operation space, always be within the support frame. All motions that do not break the height restriction of the roof are possible to be tested within the boundaries of the support frame. Motions such as NA-22 (Overhead shoulder press), NA-23 (Vertical jump), NA 6-9 (Walk up the stairs, Walk up the slopes, Walk down the stairs, Walk down the slows) will not be testable.

The length of the operation-space is set as 7 m. In order to confirm that 7 m would cover a reasonable walking distance the length travelled in 6 steps (3 cycles) of 5 individuals whom are involved in the exoskeleton research are measured. The average walking distance was 3.99 m and thus within the operation area. It should be noted that although this was not an official experiment, the participants are team members who will be working within the support frame.

Maximum Supported Load

The support frame will need to structurally support 264 kg. This is a combination of three parameters, the human within the exoskeleton, the exoskeleton and the load the exoskeleton needs to support. The mean weight of a human male in the UK is 84 kg (HSCIC 2013), the maximum weight of the exoskeleton being built in this project is 90kg and the maximum load which it should be able to carry is given as 90kg (from Metrics document in APPENDIX D). The deflection constraint on the frame for deflection is set to 0.005m.

Force Calculations

Buckling

The equation for a fixed-fixed bar under pressure is given as:

$$Buckling\ Load = \frac{4\pi^2 EI}{L^2}$$
<div align="right">Equation H-1</div>

For an extruded 45x45mm aluminium bar (MINITEC) with a profile:

E = 69GPa

I = 9.953cm^4

L = 2.19m.

The buckling load is = 56'529.43 N or 5762 kg

These bars are considered sufficient for vertical support.

Deflection

To calculate deflection Macaulay's method is used. And it is found that the 5m sides needs four support beams on either side and the 2m slider by nature of its function is restricted to two. The beam that best supports the maximum load within the given tolerance is 45x90mm profile extruded aluminium.

A worst case scenario is that the entire max load is supported by only one side of the structure. This is a near possibility as the structure will allow for the user to move in all three axes therefor becoming closer to one side than the other.

The basic governing equation for slope and deflection of a beam is given as:

$$EI\frac{d^2 y}{dx^2} = M$$
<div align="right">Equation H-2</div>

Where,

y is deflection

x is distance along horizontal line

M is Moment as a function of x

For the case where one force is acting as two loads equidistant from either side the equation for deflection, y, is:

$$y = \frac{1}{EI}\left\{\frac{F}{k_F 6}[x^3 - (x-a)^3 - (x-b)^3] + A(x)\right\}$$
<div align="right">Equation H-3</div>

Where,

k is the number of points the force is divided between

a is distance from the point of reference to the first load

b is distance from the point of reference to the second load

With boundary conditions, x = L and y = 0, then:

$$A = \frac{F}{k_F x}[L^3 - (L-a)^3 - (L-b)^3]$$
<div align="right">Equation H-4</div>

Where,

L is total length of beam

Rewriting Equation H-3 for I, the second moment of area needed for a given load F and a given max displacement y at a location of the bar, in our case in the middle, can be found.

By dividing the length of the test-rig such that there is a pole every 1.705 m the needed second moment of area is 20.7 x10-8 m^4. The profile 45x90 has an I = 113x10-8 m^4 (MiniTec 2014) hence it is chosen as no other profile of the dimension 45x45 has a satisfactory second moment of area.

For the 2m slider the second moment of area needed for a single point load at its centre is 62x10-8 m^4 where again the 45x90 profile is more suitable.

Slider System

In order for the mechanism to move a slider system is needed. The LW45 is chosen for the 7 m beam. The slider system will be attached using 4 sliders. The slider LW 45's rated forces are 3500N and 1500N in the X and Y directions respectively. The slider, in either configuration, meets the weight requirement, the technical specs of the slider can be found in APPENDIX I.

The Assembled and Tested Test-Rig

The final 3D model of the test-rig can be seen in Figure H-1. The test-rig is visualized inside a space which corresponds the room it will be placed in together with a 3D model of a human in an exoskeleton mock model in Figure H-2.
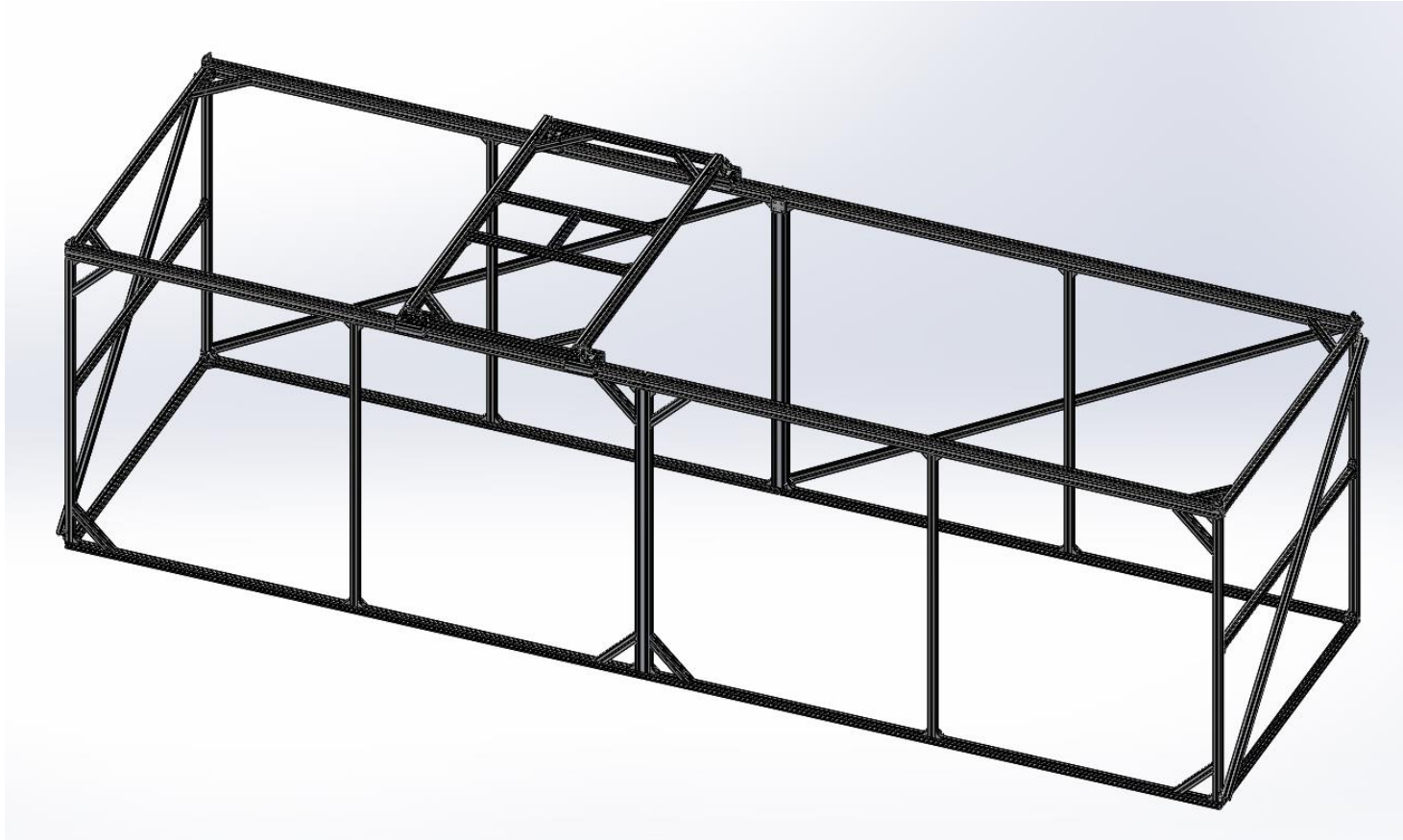
Figure H-1 – Full 3D model of the assembled test-rig with the sider.
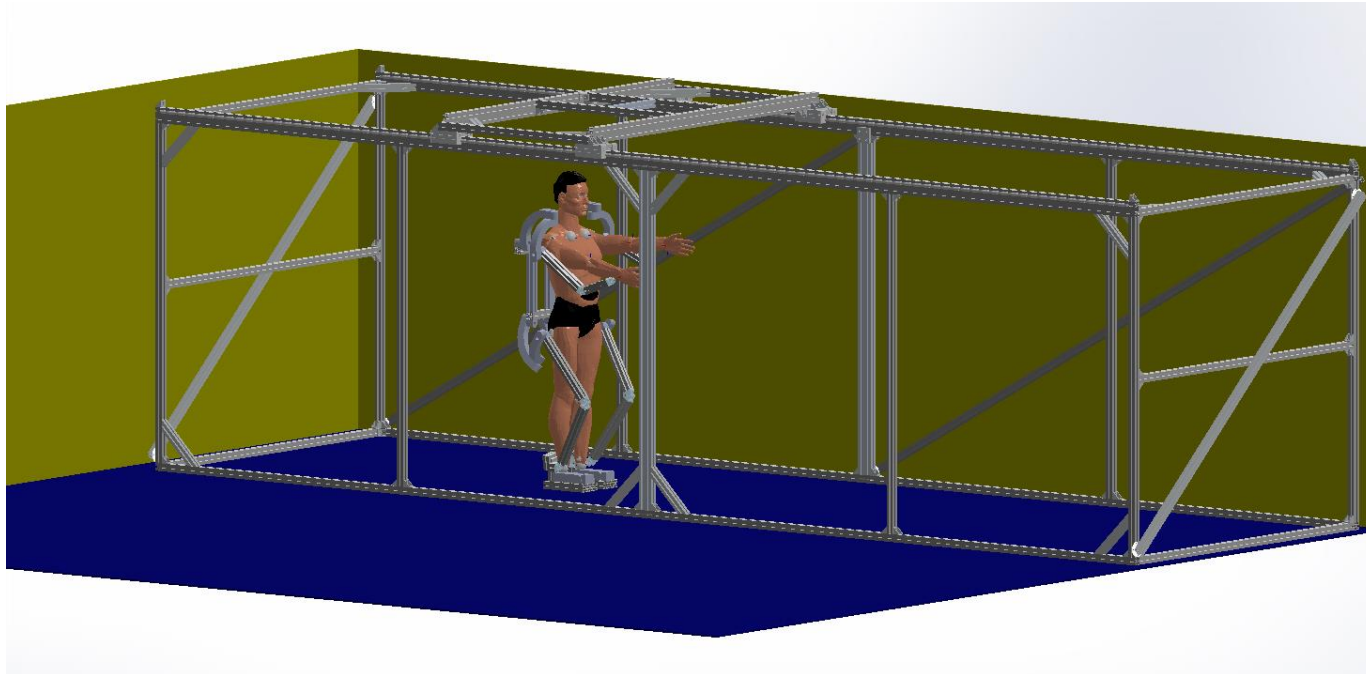
Figure H-2 – 3D visualization of the test-rig in the room with a human in an exoskeleton mock model

Single Joint Design to Aid Exoskeleton Research

Prior to the start of the work on optimization a modular joint is designed. The overall purpose of the joint is to have a starting point for the many streams of research in exoskeleton project. The joint is presented in this thesis to be used as a comparison to the optimization methodology which will be developed. As such the joint design will provide some insight into aspects of detailed mechanical design such as forces and stresses that need to be considered at component level, actuation input and geometric and physical restrictions coming from external components.

Development of the Single Joint Model

The design of the joint is done prior to and with exclusion of motion capture data. Together with the design of the joint an interface is designed for a single joint prototype. The actuation system for this single joint design is a planar two bi-directional piston hydraulic system. The system operates using two cylinders on either side of a single degree of freedom joint, this allows for a greater range of motion. The actuation system is designed by a member of the research team, whose research topic at the moment of writing this thesis is on hydraulic actuation system design for enhancive exoskeletons.

In order to estimate force, the process starts by looking at the motion of a single pendulum model; two links with a joint connecting them. Therefore some artificial constraints are produced for the velocity and load carrying capacity of the joint.

A. The joint will be designed to accommodate modularity, meaning that it should be able to take the full load (to be defined) in both horizontal and vertical configuration.
B. The angular velocity that will be used to calculate the forces and moments is set to a maximum 2*pi. This is deemed feasible within the project as it corresponds to 1 rps, or practically, lifting the arm in 0.5 sec.
C. The length 0.4479 m will be used for the length of the moment arm of the hydraulic system in the calculations (L in Figure H-3). This constraint comes from the actuation design, at the time of the design of the joint.
D. The length 0.15 m will be used for the flanges of the hydraulic system in the calculations (d in Figure H-3). This constraint comes from the actuation design, at the time of the design of the joint.
E. The total maximum weight that the joint needs to carry, and that should be used in the force calculations is 290 kg.

1. This is due to the following: The mass that the exoskeleton should be able to manipulate is found in the requirements is set to 90 kg.
2. The weight of the exoskeleton is estimated to lie between 90 and 200 kg at the time of designing the joint, this is taking into consideration the actuation system. Therefor the system will be estimated to lie at 200 kg.

F. The joint itself will house an angular encoder.

Kinetic Model of Single Joint System

In the chapters ahead, the equations for two link systems will be developed. However as only a single link system is concerned at the moment, the dynamic equations for it can be seen in Equation H-5. As it can be seen there exists an acceleration term which will be derived using the velocity constraint.

$$M(t) = \ddot{\theta}(t)I + mgl * \cos(\theta(t))$$

<div align="right">Equation H-5</div>

The free-body diagram in Figure H-3 shows the overall structure and the forces and moments relevant to the single joint system. The solid black lines represent the structural frame of the exoskeleton and the grey lines represent the hydraulic system.
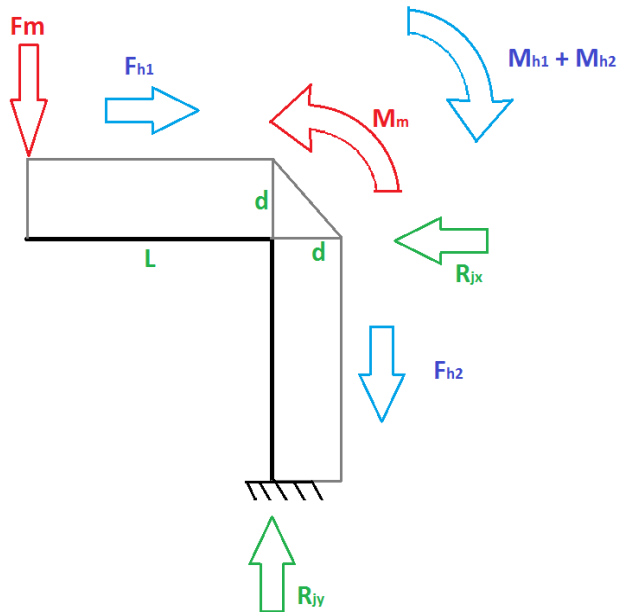
Figure H-3 – Diagram of the forces and moments experienced by the single joint hydraulic system. The diagram shows the system at the worst case scenario where the forces are expected to be at max.

Assuming a constant acceleration at the instance θ = 90 degrees, the value for $\ddot{\theta}$ =6.3 rad/sec^2. The highest possible load is estimated to be at the ankle, therefore m is set to 290 kg. Length l is already known as 0.4479. Substituting these values into Equation H-5, the torque is given as 2005.3 Nm. This calculation is done for varying external loads, the results can be seen in Table H-1.

Table H-1– The static and dynamic torques produced by varying external masses

Weight F_m (kg)	Static Torque M_m (Nm)	Dynamic Torque M_m (Nm)
90	882.9	622.3
180	1765.8	1244.7
290	2844.9	2005.3
580	5689.8	4010.6

The reaction forces R_{jx} and R_{jy} are calculated by first finding the hydraulic forces F_{h1} and F_{h2}. This is done for a varying range of external forces. Using d = 0.15, which is the external dimension from the hydraulic system. The results are shown in the Table H-2 for a static loads and Table H-3 for dynamic loads.

Table H-2 – The static forces and reaction forces as a result of the hydraulic forces plotted for varying external masses

Weight F_m (kg)	F_{h1} and F_{h2} (N)	R_{jx}	R_{jy}
90	1,318	2,201	1,318
180	2,636	4,402	2,636
290	4,247	7,092	4,247
580	8,495	14,185	8,495

Table H-3 – The dynamic forces and reaction forces as a result of the hydraulic forces plotted for varying external masses. The difference can be seen with the static loads to increase drastically as the external weights increase.

Weight F_m (kg)	F_{h1} and F_{h2} (N)	R_{jx}	R_{jy}
90	2,074	2,957	2,074
180	4,149	5,915	4,149
290	6,684	9,529	6,684
580	13,369	19,059	13,369

Component Selection and Joint and Actuator Interface Design

The design of the joint is highly constrained by the encoders, and the bearings chosen. As for the former, this lies beyond the scope of this research. The encoder that is used in the exoskeleton single joint is a Hengstler Absolute Encoder AC 36 – BiSS / SSI. The data sheet can be found in APPENDIX J. What might be relevant is that the size of the encoder (overall depth 48.1 mm and a diameter of 38.1 mm) makes it a quite large component. It would have been preferred to use Hengstler Absolute Motorfeedback Series AD 35 which has a diameter of 37.5 mm and a depth of 23.65 mm. The design decision must be made to save space axially, by mounting the sensor inside the joint, or radially, by mounting the sensor next to the joint. As bulkiness is a prime concern, the preference has gone to designing a joint where the sensor is housed inside (as much as possible) in the joint. A cross-section of the design can be seen in Figure H-4.
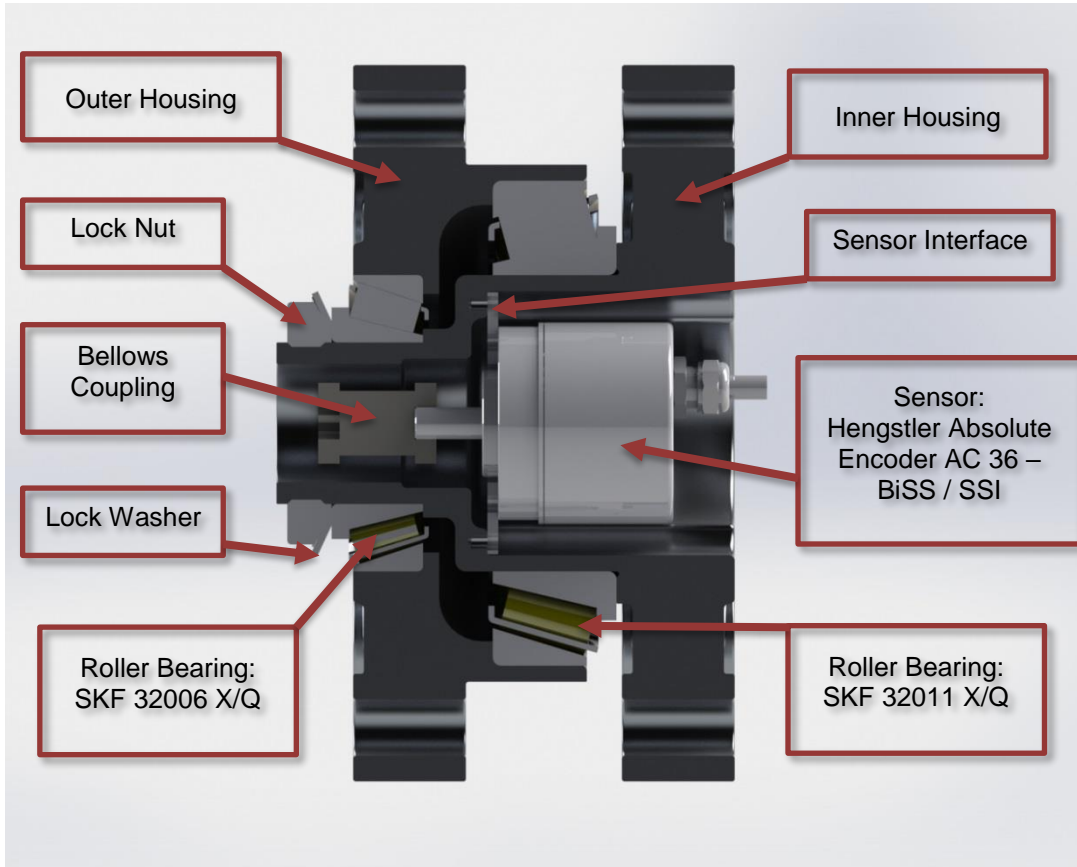
Figure H-4 – Cross section of joint design, showing all components

Bearing Selection

The decision of using tapered roller bearings over ball bearings was due to their superiority in dealing with radial as well as axial loads. As the joint is to be as modular as possible this was found favourable. Although they would have to come in pairs for each joint, in order to lock the two sections of the joint (inner and outer housing) similar options would not be possible with regular ball bearings. They also generally have a higher load carrying capacity over ball bearings due to their increased contact surface, this also means that there is more friction. However, friction in the relatively low speeds that the exoskeleton will be operating in, is deemed a non-issue at this stage of the research. Table H-4 shows the two tapered roller bearings selected in comparison with two equivalent ball bearings. As can be seen the masses of the ball bearings are approximately twice as high as their tapered counterparts but with much lower load ratings. It becomes clear that the weight and the load capacity of the tapered roller bearings make them more suitable

Table H-4 – The key properties and dimensions of the selected tapered roller bearings are compared with equivalent ball bearings.

	Load ratings (kN)		Mass (kg)	Inner diameter (mm)	Outer diameter (mm)	Total depth (mm)
	Dynamic	Static				
32006 X/Q	35.8	44	0.17	30	55	17
32011 X/Q	80.9	116	0.56	55	90	23
6006	20.3	11.2	0.475	30	55	13
6210	37.1	23.2	0.98	50	90	20

The decision was made to use SKF tapered roller bearings. Various companies where contacted and quoted however due to the short lead time, competitive prices and technical support SKF was ultimately chosen.

Lifecycle Considerations and Fatigue Limits

The fatigue life is estimated by calculating the maximum amount of steps which may be taken during the lifetime of this PhD research and one more PhD project at the time of inception of the single joint system in the lab during extreme usage. This is approximately 5 years. From the research on BLEEX walking speed was found to be 1.3 m/s (Zoss, Kazerooni and Chu 2006b), for an average step length 1.5 steps/m and a test area 7m long this gives approximately 20 steps (back and forth) assuming 1 step = 1 cycle. For research purposes, initially a working period of 3 hours of operation time/day is assumed. This will give 21,060 cycles/day. Alternatively, hours of use before failure can be found by dividing total cycle length by number of operation hours per day 8.7×10^3 hours of operation. For University of Leeds term time 49 weeks of 5 working days are assumed, which gives approximately 26×10^6 cycles.

For the prototype, aluminium 6061-T6 was selected due to its light weight compared to its strength and reasonable price. Data for fatigue life was derived from Metallic Materials Properties Development and Standardization (United States. Department of *et al.* 2011) and can be seen in Figure H-5. For bilateral loading the fatigue limit is approx. 143.1 MPa. Comparatively aluminium 7075-T6 has a fatigue limit of approx. 243.9 MPa. For a year's operation time for 6061-T6 , the fatigue limit is 176.6 MPa and for 100 hours of operation time 219.4 MPa.
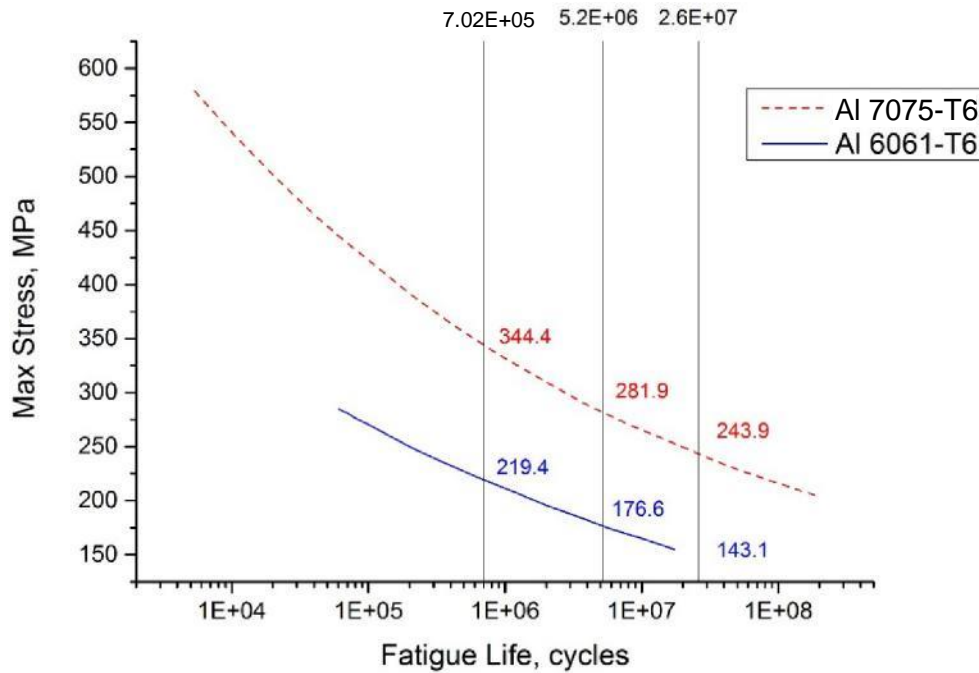
Figure H-5 – S-N Graph of aluminium 6061-T6 and 7075-T6 with key lifecycles plotted (United States. Department of *et al.* 2011)

Design Selections Based on Preliminary Stress Calculations

With the sensor and bearings selected, the loads defined and calculated, preliminary stress calculations for connections between joint and interfaces can be made. Different modes of failure in shear (Shigley 1972), which can be seen in Figure H-6 are examined. Specifically:

- bearing failure on the bolt from member (Equation H-6)
- bearings failure on member (Equation H-7)
- shear on bold from member (Equation H-8)
- shear tearout of member (Equation H-9), which assumes:
  - no tearout between bolts
  - entire bolt load acts perpendicular to nearest edge
  - tearout area is to be based on the closest distance from the edge to the bolt, seen in Figure 3.7, $A_{member} = 2at$
- and, tension failure of member (Equation H-10), where $A_{tension} = (w - d) * t$

$$\sigma_{bolt} = \frac{F/2}{t * d}$$ Equation H-6

$$\sigma_{member} = \frac{F/2}{t * d}$$ Equation H-7

$$\tau_{bolt} = \frac{F/2}{A_{bolt}}$$ Equation H-8

$$\tau_{member} = \frac{F/2}{A_{member}}$$ Equation H-9

$$\sigma = \frac{F}{A}$$ Equation H-10

Furthermore, using the equation for Hertz contact stress (Shigley 1972) shown inEquation H-11, the length of the contact surface can be found. Rearranged equation for length I can be seen in Equation H-12.

$$b = \sqrt{\frac{2F}{\pi l} * \frac{\left[1 - \mu_1^2 / E_1\right] + \left[1 - \mu_2^2 / E_2\right]}{\frac{1}{d_1} + \frac{1}{d_2}}}$$ Equation H-11

$$l = 2 * \frac{F * \left(\frac{1}{d_1} + \frac{1}{d_2}\right)}{\left(\left[1 - \mu_1^2 / E_1\right] + \left[1 - \mu_2^2 / E_2\right]\right) * \pi * b^2}$$ Equation H-12
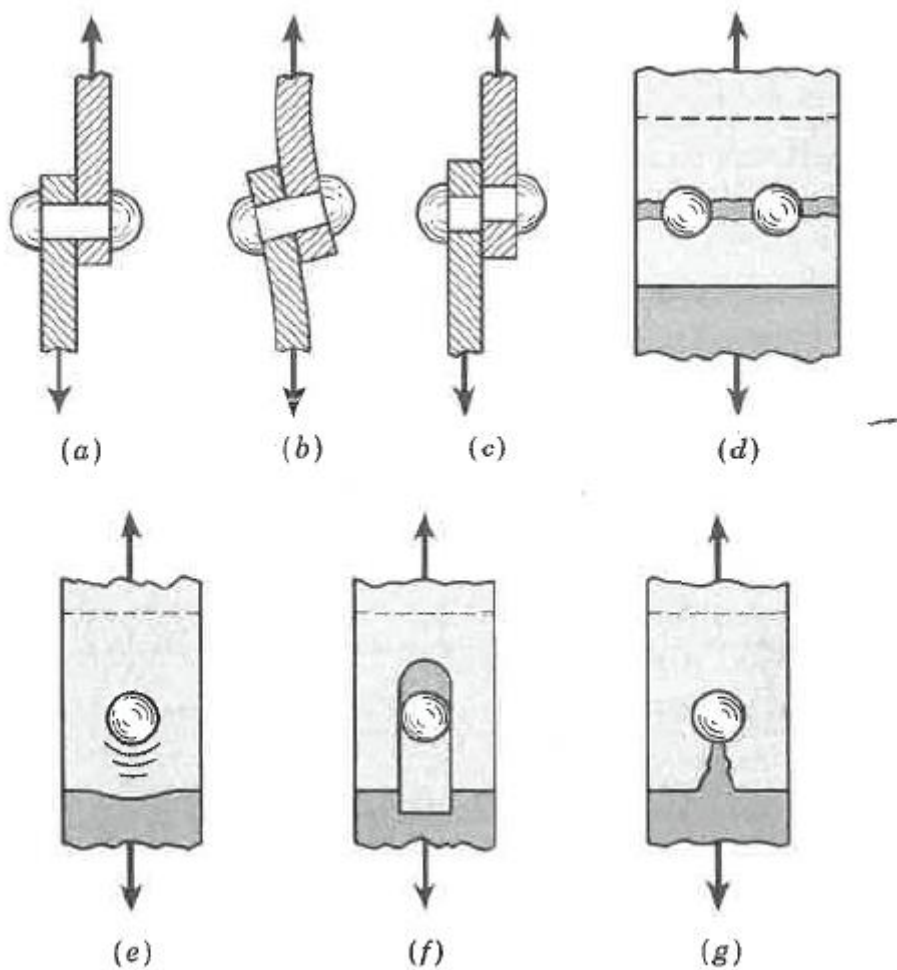
Figure H-6 – Different modes of failure in shear loading of a rivet or a bolt, a) shear loading, b) bending of rivet, c) shear of rivet, d) tensile failure of members, e) bearing of rivet on members or bearing of members on rivet, f) shear tearout and g) shear tearout (Shigley 1972)
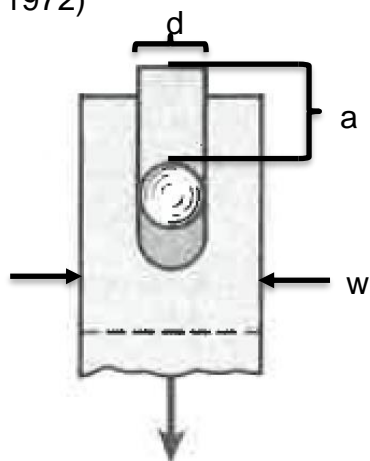
Figure H-7 – Figure of lengths used to calculate tear out area and tension failure, a distance of bolt to edge and t thickness of member (not shown in figure) (Shigley 1972)

The unknown parameters for the failure modes pertain to the diameters of the bolt, but for Hertz contact stresses are also for inner and outer diameter, d_1 and d_2. These will be made known when the bolt is selected. The youngs modulus terms E_1 and E_1 are known from the materials of the bolt and joint, the steel (200 GPa) of the bolt and aluminium 6061-T6 (69 GPa) (United States. Department of *et al.* 2011). Apart from the comparison of aluminium 6061-T6 and 7075-T6 which is a stronger grade of alumuminum when discussing fatigue, at this stage no further indepth material analysis is made. This is due to 6061-T6 is deemed sufficiently strong after the stress and fatigue analysis as well as the cost of materials and availability of 7075-T6 being higher.

The bolt type used for this design are shoulder bolts. Comparison of various bolts can be seen in context of the Hertz contact stresses, shown in Table H-5. Using the table as a basis of decision, M8 bolts are selected to move forwards on as they will offer a suitable balance between radial axial size.

Table H-5 – The length of the contact between two cylinders bolt shoulder and joint member, using Hertz contact equation, are calculated for various bolts and fatigue limits. Also shown are the shoulder diameters.

Bolt	Shoulder Diameter (m)	Length		
		Using fatigue limit 220 MPa at 100 hours (m)	Using fatigue limit 177 MPa at 1 year (m)	Using fatigue limit 144 MPa at 5 years (m)
M6	0.008	0.013	0.020	0.030
M8	0.010	0.009	0.013	0.020
M10	0.012	0.006	0.009	0.014
M12	0.016	0.004	0.006	0.008

The joint will be connected to the actuation system or other interfaces using flanges. In order to estimate the stresses at the base of the flange, it is assumed that each flange behaves a simple beam. The equation of the shear in a beam is given in Equation H-13 and Equation H-14.

$$\sigma = \frac{F * l_{beam}}{Z_{rectangle}}$$ Equation H-13

$$Z_{rectangles} = \frac{b * h^2}{6}$$ Equation H-14

Setting the breadth b to 0.02 m (found from Table H-6) we obtain the stresses can be obtained at the base for varying numbers of flanges. The results are shown in Table H-6. It can be seen that using 6 flanges would almost make a square shaped flange. However the decision to use 8 flanges is made as this would allow for a spread of the forces during operation.

Table H-6 – The value of h for the flange for a known force load for various number of flanges on the joint.

Number of flanges	Force per flange (N)	Value of b (m)
1	9529	0.0467
2	4765	0.0330
3	3176	0.0270
4	2382	0.0234
5	1906	0.0209
6	1588	0.0191
7	1361	0.0177
8	1191	0.0165

Using the selected bolt and knowing the number of flanges, for a fatigue limit of 144 MPa at the maximum cycles equations, Equation H-6, Equation H-7, Equation H-8, Equation H-9and Equation H-10 can be used to confirm the geometry and material. Looking at the results shown in Table H-7, we can see that all values are below the the values of the fatigue limit considerably.

Table H-7 – Verification of stresses using the methods shown in Figure 3.6.

Method	Stress (Pa)
Bearing stress on Bolt	6,018,934
Bearing stress on Member	6,018,934
Shear on bolt	16,859,799
Shear tearout	1,504,734
Tension Failure	48,151,474

The design must look at the constraints created from the components in order to estimate a minimum diameter. The values of the external diameter of the larger roller bearing (found in Table H-4) are used, a 0.005 m cylinder thickness is used for the cylinders which the bearings will be in placed in and around. Using the dimensions for the bearings and Equation H-13 for stress and the dynamic forces in Table H-3 the estimated stresses can be found for 0.005 m aluminium housing seen in Table H-8. It is found that the stresses are below the fatigue limit found earlier.

Table H-8 – Verification of stresses for the cylinder housings of the bearings.

Housing		Stress (Pa)
Large Bearing	Inner	21,165,569
	Outer	6,694,376
Small Bearing	Inner	79,850,484
	Outer	17,581,518

Having verified the housing dimension the minimum diameter between centres of the bolts can be found as a sum of, the large bearing outer diameter (0.09 m), thickness of the cylinder (0.005 m) multiplied by 2 and nut dimension (0.013 m). the total value is 0.113 m.

The values and dimensions found and confirmed in this section are used to design the two joint housings. The individual parts can be seen in Figure H-8. Full detailed engineering drawings of the housings and the sensor interface can be found in APPENDIX L.

a)

b)
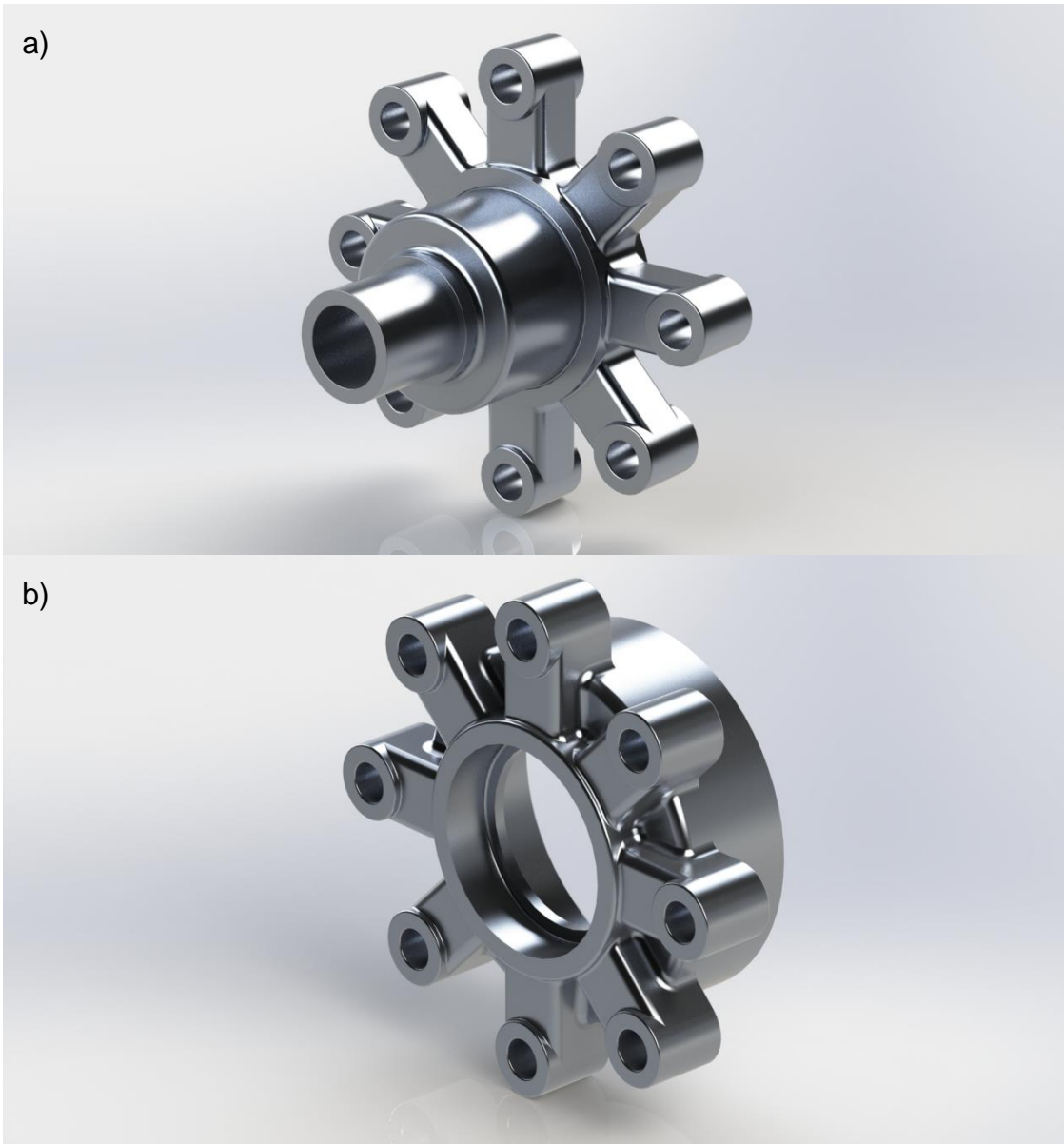
Figure H-8 – Isometric projections of the two main components of the joint
housing, a) the inner housing and b) the outer housing

Actuator Interface Design

Using the results of the previous subsection the interface for the joint and hydraulic actuator can also be designed. The results can be seen in Figure H-9. The design was made to allow for the two links of the single joint system to be fully parallel when closed (angle between the two links reaching zero). Which is also made possible because the joint is capable of rotating freely 360 degrees. This leads to the slightly bent, almost p shaped structure of the interface and an offset of the links centre line with the joint axis of rotation (seen in Figure H-10).

Figure H-9 – The finished actuator interface.
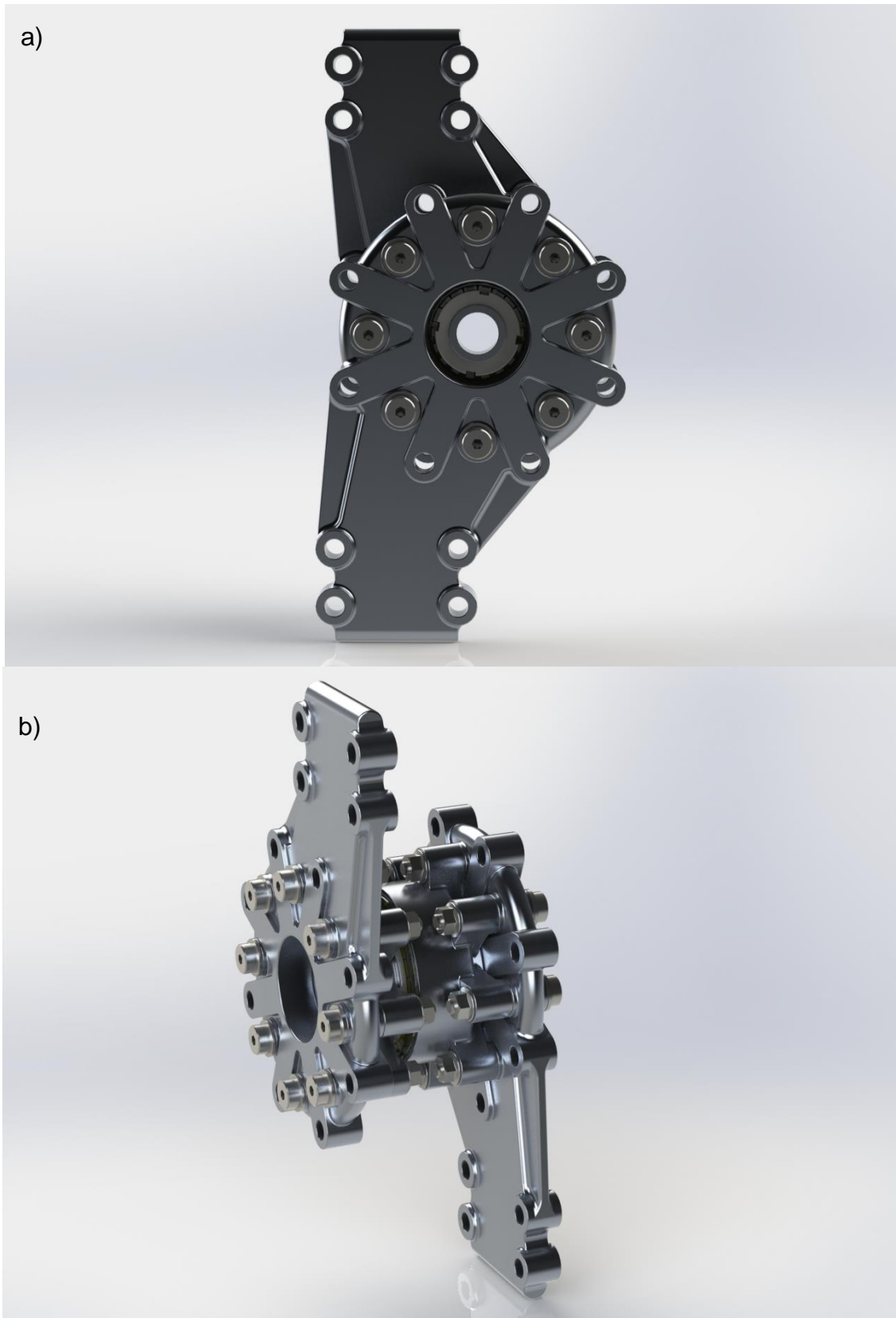
Figure H-10 – Assembled joint with joint interface. 180 degree open position, where the two links would be parallel and in serial configuration, a) side view and b) front side view.

FEA Verification for Joint and Actuator Interface

In order to verify and justify the production of this joint some FEA simulations are performed using SolidWorks. The simulations are performed for dynamic force shown in Table H-3. The results for the joint components are shown in Figure H-11. It can be seen that neither part yields. For the inner section there is however a stress concentration which has a value of approximately 154 MPa.

Figure H-12 shows the FEA results for the actuator interface for two cases, full compression and full tension. Firstly it will be noted that the design is altered slightly by removing some of the curved surfaces. This is done to ease the manufacturing process at University of Leeds. In both stress plots it can be seen that the maximum stress over-exceeds the fatigue limit (163 MPa in tension and 166 MPa in compression).

Upon closer inspection in all components, it is found that these stress peaks only occur at locations of stress concentration, such as edges. Whereas for the rest of the structure holds well under the fatigue limit.
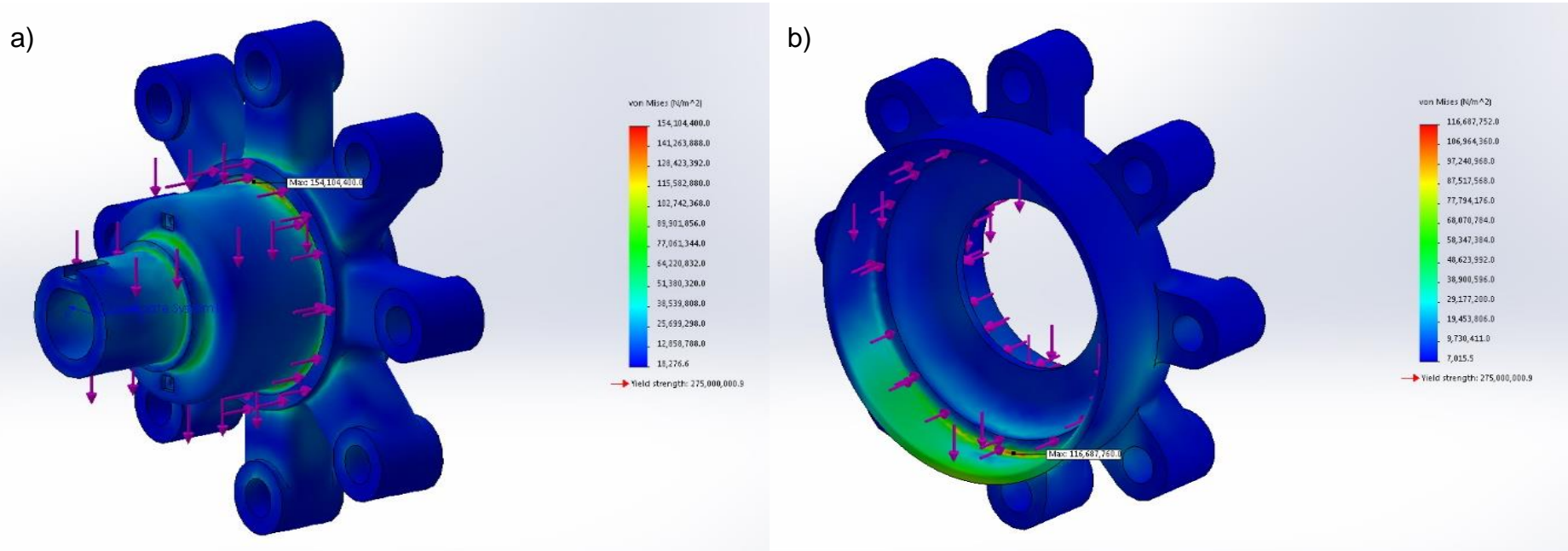
Figure H-11 – The FEA analysis results for stress for the joint model using 9529 N dynamic load found in Table H-3 as external load inputs; in a) the inner housing maximum yield point is approximately 154 MPa and for b) the outer housing is at approximately 117 MPa.
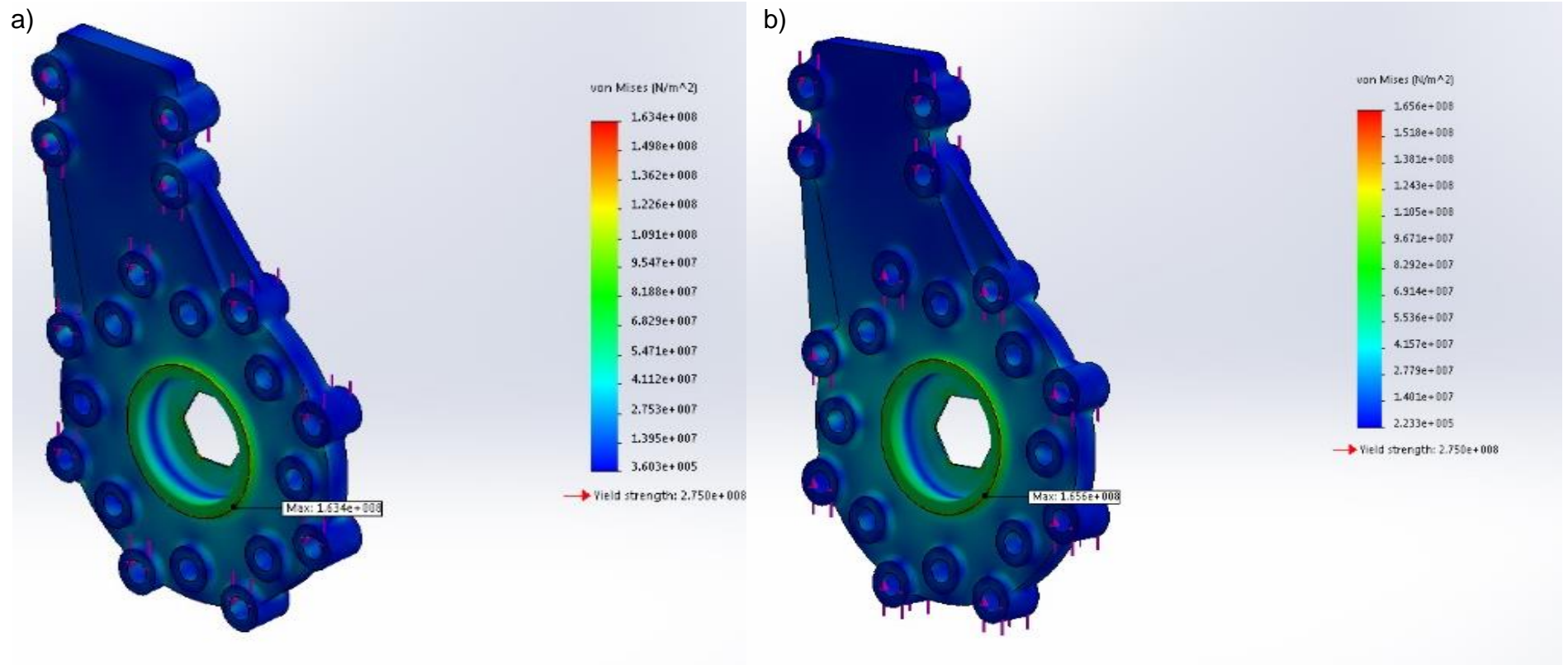
Figure H-12 – The FEA analysis results for stress for the actuator interface module using 9529 N dynamic load found in Table H-3 as external load inputs; in a) tension the maximum yield point is approximately 163 MPa and for b) tension it is at approximately 166 MPa.

Discussion

Test Rig

As has been shown using analytical calculations the frame structure will support a load of 264kg. The testing performed on the frame, shows that indeed it can support a much higher load (380 kg).

The test-rig was purposefully designed in such a way that it could be used for testing more than just the required exoskeleton. Therefore a key issue to note is that the interconnection between the support frame and the exoskeleton or other components to be tested on the rig will have to be designed.

The supporting beams for the long (7 m) side can be changed in any number of combinations to allow for changes in weight restriction. In that sense the test-rig is also rather modular. Care should be taken to test the rig after such changes.

Single Joint Design

The single joint design is started only after the torques and forces of the system and some understanding of the lifecycle of the machine are estimated. For this joint the material used is aluminium 6061-T6, due to its reasonable price, its light weight and high strength. After this various modes of failure seen in Figure H-6 are presented together with the Hertz contact stresses for cylinders in contacts.

Using the Hertz contact equation the length of the cylinder to hold the bolt was found for various bolts and compared. In this case an M8 shoulder bolt is used with an M10 shoulder. The equation for shear stress of a beam is used to estimate the dimensions of various amounts of flanges undergoing the found forces. The decision is made to use 8 flanges. Now the modes of failure can be used to verify the joint model, prior to design.

The equation for beam shearing is also used to estimate the thickness of the housings of the bearings. The total minimum diameter, from centre of bolts, was found to be 0.113 m. The values found were used to design the joint and actuator interface in SolidWorks. Figure H-13 shows the joint and the joint actuator interface used in the final full single joint system.

FEA is used to verify the design. It was found that in all components there exists stress concentration. In the inner housing as well as the actuation interface these strass concentrations are greater than the fatigue limit that was used to estimate the model dimensions analytically. However it should be noted that they were

not so great as to reach yield of the material used, in fact they did not break the 1 year fatigue limit.

Potential improvements could be made to the FEA model. Investigation could take place in the detailed design to potentially eradicate stress concentrations. A clear example is the rounding of edges, which was omitted (and considered acceptable for the prototype) for manufacturing ease. After these steps it would be prudent to compare the analytical design process and the FEA data with real life testing of the joints.

Furthermore, optimization software could be used to perform topology optimization of the structures. This could reduce the weight and materials used. In the light of optimization, external components could be considered which benefit the design as well, such as smaller sensors. As for the bearings, a larger investigation could be made into finding a suitable set of bearings. If could also be beneficial to look at how much bulkiness would be increased axially and decreased radially if the sensors were not placed inside the joint. As can be seen in Figure H-13 the actuation system is rather bulky, axially, itself.
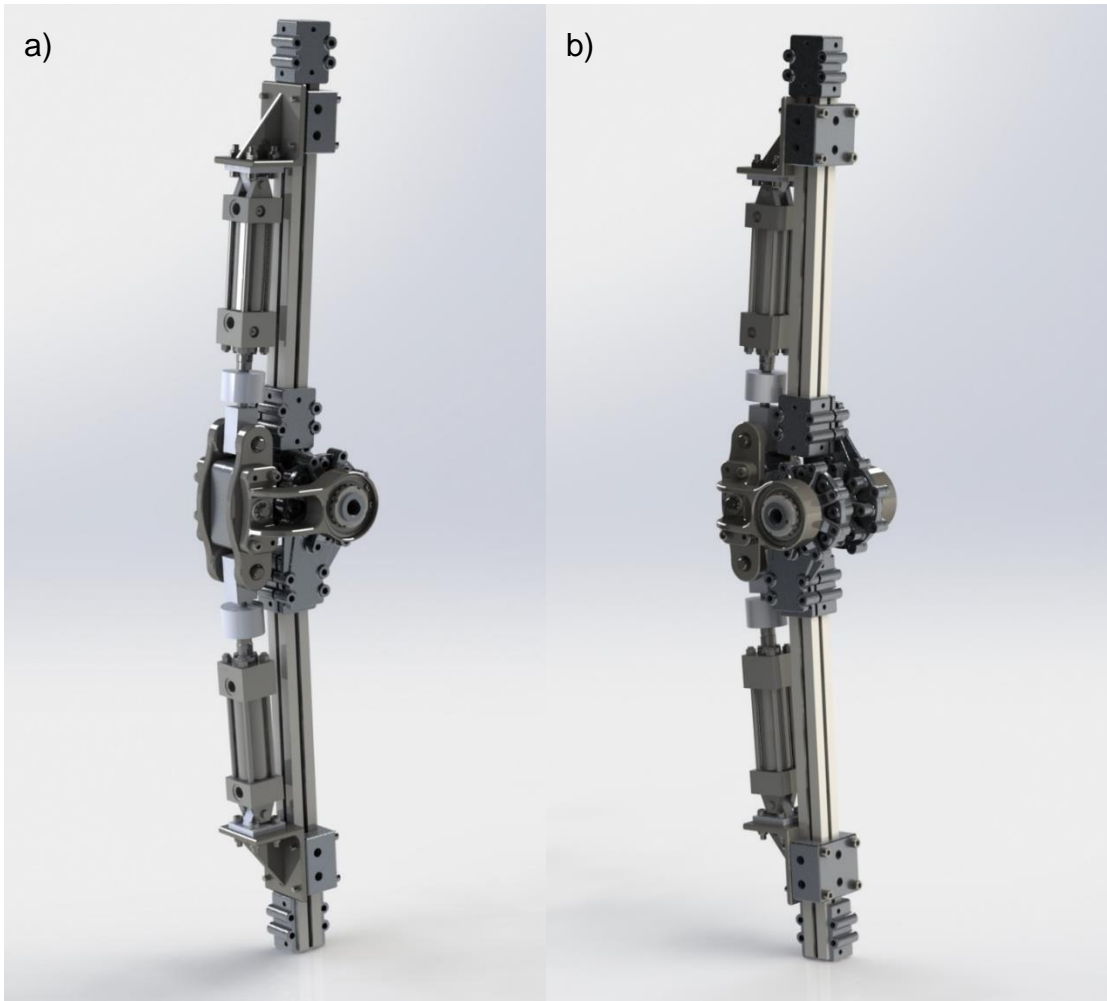
Figure H-13 – The full single joint system with all the fasteners, actuation system and angular sensors in place, a) side front view and b) side rear view.

Summary

This chapter looked at the design of a test-rig to be used for the exoskeleton project. It was initially design for the requirements set forth in the project. The length, width and height of the test rig is determined by the local constraints of the room it is to be placed in as well as some requirements of load carrying capacity and some of the motions that are desired to be performed inside. The materials used for the test-rig where purchased from MiniTec, and were predominantly aluminium extruded rods, 45x45 mm and 45x90 mm. The test rig also has a slider system incorporated in order to be able to move the support system with the exoskeleton as it walks. Testing is carried out on the rig and it is found that it can hold the load it was designed for.

After the design of the test-rig a single joint is designed together with an interface for a single joint hydraulic system. Torques and reaction forces are estimated together with the lifecycle of the joint. Fatigue limits for 5 years, 1 year and 100 hrs are looked at. Aluminium 6061-T6 is used as the material of the joint. Various modes of failure, Hertz contact stress and beam shear stress are reviewed and used to derive key dimensions which are used in CAD models

The models are simulated using FEA and it is found that the stress concentrations of the joint inner housing and the actuation interface exceed the minimum fatigue limit set (5 years). However, they do not exceed the 1 year or 100 hour limits.

.

Slider Data

LINEAR SYSTEM LR

Load capacity

Calculation of max. moment loads as function of the slide length:

My max. = 0,89 · (L-45) Nm
Mz max. = 1,50 · (L-45) Nm

L = length of slide

Linear system Slides	**LR6** Slide LR 6 4 bearings L = 90 mm	**LR 12** Slide 45 4 bearings L = 180 mm	Slide 90 4 bearings L = 180 mm	Slide 135 4 bearings L = 180 mm	Slide 180 4 bearings L = 180 mm	Slide 180 8 bearings L = 360 mm
Mx max.	30 Nm	79 Nm	107 Nm	130 Nm	165 Nm	240 Nm
My max.	75 Nm	120 Nm	120 Nm	120 Nm	120 Nm	275 Nm
Mz max.	40 Nm	202 Nm	202 Nm	202 Nm	202 Nm	470 Nm
Fy max.	800 N	3500 N	3500 N	3500 N	3500 N	7000 N
Fz max.	640 N	1500 N	1500 N	1500 N	1500 N	3000 N

Linear system Slides	**LR 16** Slides LR 16-45	Slides LR 16-90
Mx max.	158 Nm	214 Nm
My max.	288 Nm	288 Nm
Mz max.	323 Nm	323 Nm
Fy max.	7000 N	7000 N
Fz max.	3000 N	3000 N

Maximal speed slide 45 - 180:   10 m/sec.
Maximal speed slide LR 6:   5 m/sec.

Figure I-1 - List of component properties from MiniTec for the railing sizes LR6 and LR12 for sliders of size 45 and 90 (MiniTec 2014)

APPENDIX J

Report of Load Test

PCL
PETER CASSIDY (LEEDS) LTD

PETER CASSIDY (LEEDS) LIMITED
Holbeck Lane, Leeds, LS11 9XA
Tel: 0113 245 5457   Fax: 0113 242 6456
Email: sales@petercassidy.co.uk
www.petercassidy.co.uk

LEEA

REPORT OF LOAD TEST

Please note: This test does not certify the equipment, but the results of this test & this document should be kept in the equipments technical file for reference.

Company for whom Test was made	Address where Test took place	Certificate No.		77341
UNIVERSITY OF LEEDS FACULTY OF ENGINEERING WOODHOUSE LANE LEEDS LS2 9JT	ROOM G52 MECHANICAL ENGINEERING	Date of Test		25.02.16
		Date of Report		26.02.16
		Customers Order No.		EM14500849850

ID No.	DESCRIPTION OF ITEMS	QTY	TEST LOAD	RESULT
N/A	EXOSKELETON SUPPORT FRAME & GANTRY	1	380 kg	N/A

Any part found to have a defect:

NO DEFECTS NOTED.

Company Appointed Examiner	Signature
G Tegerdine	

Page 1 of 1

213

APPENDIX K

Henstler Encoder

(Kübler

Absolute encoders - singleturn

Compact optical	Sendix F3653 / F3673 (shaft / hollow shaft)	SSI / BiSS

Electrical characteristics

Power supply	5 V DC (±5 %) or 10 ... 30 V DC
Current consumption (no load) 5 V DC	max. 60 mA
10 ... 30 V DC	max. 30 mA
Reverse polarity protection of the power supply	yes (only with 10 ... 30 V DC)
Short-circuit proof outputs	yes [1]
UL approval	file 224618
CE compliant acc. to	EMC guideline 2004/108/EC RoHS guideline 2011/65/EU

SSI interface

Output driver		RS485 transceiver type
Permissible load / channel		max. +/- 30 mA
Signal level	HIGH	typ. 3.8 V
	LOW with I_{load} = 20 mA	typ. 1.3 V
Resolution		10 ... 17 bit
Code		binary or gray
SSI clock rate		50 kHz ... 2 MHz
Monoflop time		≤ 15 µs

Note: If the clock cycle starts within the monoflop time a second data transfer begins with the same data. If the clock cycle starts after the monoflop time the cycle begins with the new values. The update rate is dependent on the clock speed, data length and monoflop time.

Data refresh rate	resolution ≤ 14 bit	≤ 1 µs
	resolution ≥ 15 bit	4 µs

BiSS interface

Resolution	10 ... 17 bit
Code	binary
BiSS clock rate	50 kHz ... 10 MHz
Max. update rate	< 10 µs, depends on the clock rate and the data length
Data refresh rate	≤ 1 µs

Note: – bidirectional, factory programmable parameters are: resolution, code, direction, alarms and warnings
– CRC data verification

Incremental outputs (A/B)

	SinCos	RS422 TTL compatible
Max. frequency -3dB	400 kHz	400 kHz
Signal level	1 Vpp (±20 %)	HIGH: min. 2.5 V LOW: max. 0.5 V
Short circuit proof	yes [1]	yes [1]
Pulse rate	2048 ppr	2048 ppr

SET input

Input		active HIGH
Input type		comparator
Signal level	HIGH	min. 60 % of +V, max: +V
(+V = power supply)	LOW	max. 30 % of +V
Input current		< 0,5 mA
Min. pulse duration (SET)		10 ms
Input delay		1 ms
New position data readable after		1 ms
Internal processing time		200 ms

The encoder can be set to zero at any position by means of a HIGH signal on the SET input. Other preset values can be factory-programmed. The SET input has a signal processing time of approx. 1 ms, after which the new position data can be read via SSI or BiSS. Once the SET function has been triggered, the encoder requires an internal processing time of typ. 200 ms; during this time the power supply must not be switched off.
The SET function should be carried out whilst the encoder is at rest.

Power-ON time

After Power-ON the device requires a time of approx. 150 ms before valid data can be read.
Hot plugging of the encoder should be avoided.

DIR input

A HIGH signal switches the direction of rotation from the default cw to ccw. This inverted function can also be factory-programmed. If DIR is changed when the device is already switched on, then this will be interpreted as an error. The status output will switch to LOW.

Response time (DIR input)	1 ms

Status output

Output driver		open collector, internal pull up resistor 22 kOhm
Permissible load		max. 20 mA
Signal level	HIGH	+V
	LOW	< 1 V
Active		LOW

The status output serves to display various alarm or error messages. In normal operation the status output is HIGH (open collector with int. pull-up 22 kOhm).

An active status output (LOW) displays:
LED fault (failure or ageing) – over-temperature – undervoltage
In the SSI mode, the fault indication can only be reset by switching off the power supply to the device.

---

1) Short circuit proof to 0 V of to output when power supply correctly applied.
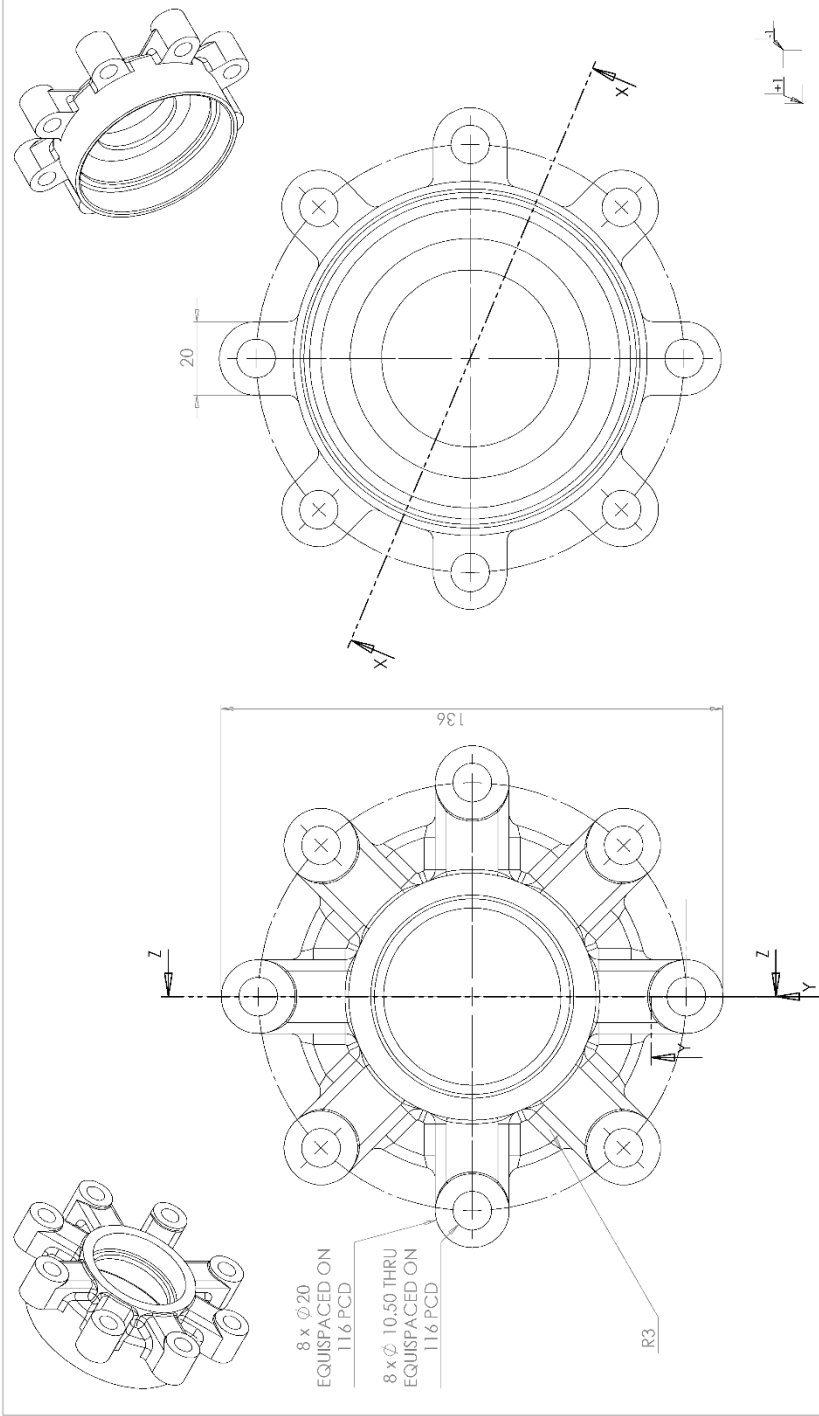
214

APPENDIX L

Engineering Drawings

External Member of
Joint 004

2 Required

DO NOT SCALE DRAWING

REVISION 3

136

20

R3

8 x Ø20
EQUISPACED ON
116 PCD

8 x Ø 10.50 THRU
EQUISPACED ON
116 PCD

UNLESS OTHERWISE SPECIFIED:
DIMENSIONS ARE IN MILLIMETERS
SURFACE FINISH:
TOLERANCES:
   LINEAR: 0.02
   ANGULAR: 0.1

DEBURR AND
BREAK SHARP
EDGES

FINISH:

	NAME	SIGNATURE	DATE
DRAWN	Douglas Friel		12/4/16
CHK'D			
APP'VD			
MFG			
Q.A			

MATERIAL:
Aluminium 6061-T6

TITLE:

DWG NO.
PF_J005_P002_D001_r3_Man

A3

WEIGHT:

SCALE:1:2

SHEET 1 OF 2

216

SECTION Z-Z

SECTION Y-Y

112.12

27.94

20 x ⌀20

84.96

77.40

35.62

2.32

73.84

119.40

20

12

4

3

R3

R3

16

(12)

8 x ⌀20
EQUISPACED ON
116 PCD

8 x ⌀20
EQUISPACED ON
146 PCD

30

22.50°

75

10

⌀20

R3

113

143

163

2 x R5

6 x R6

6 x 3.20 THRU ALL
EQUISPACED ON
38 PCD

20 x ⌀10.50
THRU ALL

6

6

(12)

4 x R3

	UNLESS OTHERWISE SPECIFIED: DIMENSIONS ARE IN MILLIMETERS SURFACE FINISH: TOLERANCES: LINEAR: ANGULAR:	FINISH:			DEBUR AND BREAK SHARP EDGES		DO NOT SCALE DRAWING	REVISION 3

4 Required

TITLE:
**Vertical Conector Plate
for Joint 005**

DWG NO.
PF_J005_P007_D002_r3_Man

A3

SCALE:1:2   SHEET 1 OF 2

	NAME	SIGNATURE	DATE
DRAWN	Prometei Ernul		12/4/16
CHK'D			
APPV'D			
MFG			
Q.A			

MATERIAL:
Aluminium 6061-T6

WEIGHT:

APPENDIX M

Matlab and Maple Comparison for Inverse Kinematics of Two-Link Model

Maple Model and Analytical Inverse Kinematic Solutions

Once the model description has been developed, Maple allows for the inverse kinematics to be found analytically. Alternatively, the model can be built in MapleSim which is the multi domain simulation environment for MAPLE, it is analogous to Simulink and SimScape from MathWorks. MapleSim allows for extraction of kinematic and dynamic equations of a system which have been built using its GUI into a Maple worksheet. The system, or the equations of the system, can then be manipulated and worked with in several ways. Here the focus will be on the manipulation of those equations as opposed to the integration of MapleSim in the workflow.

The primary strength of this method is that the inverse kinematic equations are derived once. The resulting equations allow for parameterization of relevant variables and the remaining calculations are performed by substituting the variables. Equation 3-9 and Equation 3-10 can be defined in Maple manually. θ_1 and θ_2 can then be solved for simultaneously using the built in solve function. The function, in the case of the two-link model, returns two pairs of solutions, that is two variations for each joint. A simplified version of the first variation for the first joint is shown in Equation M-1.

$$\theta_1(t) = \text{atan2}(A * B + C, D * E)$$

<div align="right">Equation M-1</div>

Looking at some of these variables namely, A, C and D, shown below, it can be seen that they are fractions. When the denominators are zero the fraction is undefined.

A
$$= \frac{1}{2 * (2 * L1 * Dx - 2 * L1 * Px) * (Dx^2 - 2 * Dx * Px + Dy^2 - 2 * Dy * Py + Px^2 + Py^2)}$$

$$C = \frac{-Dx^\wedge 2 + 2*Dx*Px - Dy^\wedge 2 + 2*Dy*Py - L1^\wedge 2 + L2^\wedge 2 - Px^\wedge 2 - Py^\wedge 2}{2*L1*Dx - 2*L1*Px}$$

$$D = \frac{1}{2*(Dx^\wedge 2 - 2*Dx*Px + Dy^\wedge 2 - 2*Dy*Py + Px^\wedge 2 + Py^\wedge 2)*L1}$$

Furthermore, this occurs when Dx, Dy, Px and Py are all zero, in other words when link 2 folds over on link 1. Similarly, when Dx equals Px the equation has undefined terms. What is shown here, using Maple, is consistent with literature (Vepa 2009; Craig 2005). One conceivable way to overcome this issue includes incorporating limits algorithmically for when the equation is undefined. As it will be shown later there exists a hybrid method for when the analytical solution yields undefined results in this case.

As mentioned earlier there are variations for each joint. This means that a means of determining which equation is giving the most suitable answer needs to be devised. In the case of the two-link model it is known, by analogy of the human limbs, that one variation is when the knee joint bends forward. The other must therefore be when the knee bends backwards. Thus this issue can be solved algorithmically.

MATLAB and SimScape Model and Numeric Inverse Kinematic Solutions

In MATLAB, the inverse kinematics problem is solved by numeric methods. The main differences using the numeric approach is that the inverse kinematics must be solved in each instance of time for discretised Dx and Px signals. Being a numeric solver there is also an issue of precision, which is considered negligible in this work.

The numeric solver vpasolve is used to calculate the joint angles in Equation 3-7 and Equation 3-8. The vpasolve function uses variable-precision arithmetic (MathWorks).

For nonpolynomial equations vpasolve returns the first solution it encounters and unless the starting point is different it will return the same value. Therefore, from the knowledge of the equations derived in previous section it is expected to be two solutions for each joint, to find these vpasolve must be ran a few times with different starting points on each iteration. This is achieved by passing the parameter 'random' and setting it to true. Considering the cyclic nature of sinusoids and the limited range that is of interest for the joints in

question, the range needs to be set to between 0 and 2π (radians). By doing this it is ensured that vpasolve does not return solutions of the form $\theta + n * 2 * \pi$.

MATLAB Algorithm

Firstly, the symbol variables are defined, using capital letters for their first letter

```
syms Theta1 Theta2 L1 L2 Px Py Dx Dy
```

The input signals and link lengths are set to variables, the non-symbol variables are differentiated by having lowercase names, they are holders for numeric values

```
Posin = px py dx dy; % array containing the X Y coordinates of the
distal and proximal locations of the two-link chain for a given time
instance

Parin = l1 l2; % holder array for the link length parameter values
```

Equation 4-7 and Equation 4-8 are defined as symbolic equations

```
eqnX1 = Dx == Px - L1*sin(Theta1) - L2*sin(Theta1 + Theta2);

eqnY1 = Dy == Py + L1*cos(Theta1) + L2*cos(Theta1 + Theta2);

Eqn = [ eqnX1, eqnY1 ];
```

eqnX1 and eqnY1 are now symbolic and the variables can be replaced but in order to do this the arrays containing the values and symbols to which those values will be replaced with need to be defined.

```
Ptotin = [Posin Parin];

Params = [Px Py Dx Dy L1 L2];

Th = [ Theta1 Theta2 ];
```

The values are substituted into the kinematic equations

```
SubX = subs(Eqn(1), Params, Ptotin);

SubY = subs(Eqn(2), Params, Ptotin);
```

As mentioned earlier the vpasolve function is ran multiple times with random starting points to find all the solutions, this is done with a for loop

```
for idx = 1:Loop
```

```
    [ a, b ] = vpasolve([ SubX SubY ], Th, [ 0 2*pi; 0 2*pi ],
'random', true);

    aa(idx) = a;

    bb(idx) = b;

end
```

depending on the loop variable there will be a number of duplicate results, these results are trimmed to only contain the unique solutions

```
Uvec = unique([aa, bb], 'rows'); % Uvec, Unique vector constructed
using a matrix consisting of the two arrays of results
```

This constitutes the core of the MATLAB inverse kinematic algorithm. For ease of reading certain error handling operations are omitted, such as ensuring that input data is of the right format and expected size.

An appropriate loop size is found by running the loop and finding when all the solutions have been found. This is done 1000 times and the resulting frequencies are shown in Figure M-1. As can be seen in approximately half of the trials required the same amount of iterations as expected solutions. This is due to the methods dependency on the random selection of starting point. Considering this the 'for loop' can be reconstructed to break out when the two solutions are found within an acceptable loop iteration, minimizing the simulation time to find the solutions.

```
Uvec2 = zeros(2, 2); % define a new unique holder for the solutions

for idx = 1:Loop

    [ a, b ] = vpasolve([ SubX SubY ], Th, [ 0 2*pi; 0 2*pi ],
'random', true);

    abhold =  double([ a, b ]);

    % make sure that the solution hasn't been save, i.e. its unique

    if ~ismember(abhold, Uvec2, 'rows')

        count = count + 1;

        Uvec2(count,:) = abhold;

    end

    % break if all of the solutions have been found

    if isequal(count, 2)
```

```
        break;

    end

end
```
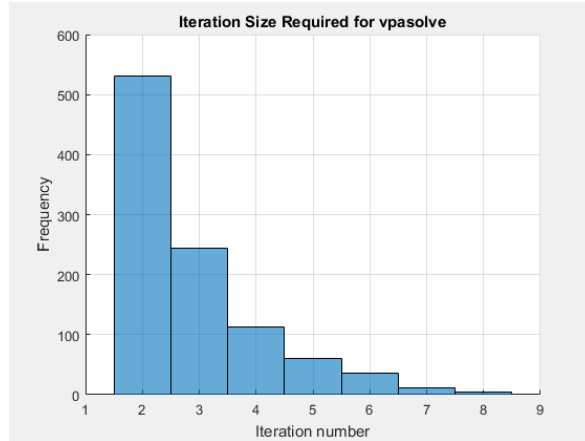

Figure M-1 - Histogram showing the frequency of the number of iterations to find all the solutions to the inverse kinematics problem, using vpasolve in MATLAB. 53.1% of the trials only required 2 iterations, whilst less than 2% of the trials required more than 6 iterations. Maximum iterations reached was 8.

Comparing Maple and MATLAB Calculations of Inverse Kinematics

A comparison is made between the two methods using the time to calculate the inverse kinematics of a given point and error between the two methods.

For the analytical method time taken is 0.118068 seconds to solve all four equations. For vpasolve method, using 15 iterations, mean time per function execution is 0.1748 seconds with a standard deviation of 0.0653. Using the mean value an estimate of the minimum (two) and maximum (fifteen) times required to solve can be acquired. The minimum amount of time 0.3496 seconds and the maximum amount of time is 2.622 seconds. This is based on serial computation, not parallel, in this stage parallel is omitted. It will instead be used when calculating the inverse kinematic for the given set of data points.

Finding the root mean square (RMS) error of the analytic and the numeric method for the joint pair it is found that the values are approx. 4.6×10^{-07} for joint 1 and 5.3×10^{-06} for joint 2. This leaves a debate whether these values are due to rounding and computational errors.

APPENDIX N

Motion Capture Filtered Data Results of Simple Gait, Object Lifting and Object Raising

The data from 'Simple Gait', 'Object Lifting' and 'Object Raising' is filtered using a lowpass filter with a maximum cut-off frequency found in Chapter 4. The full range of results are shown in this appendix.
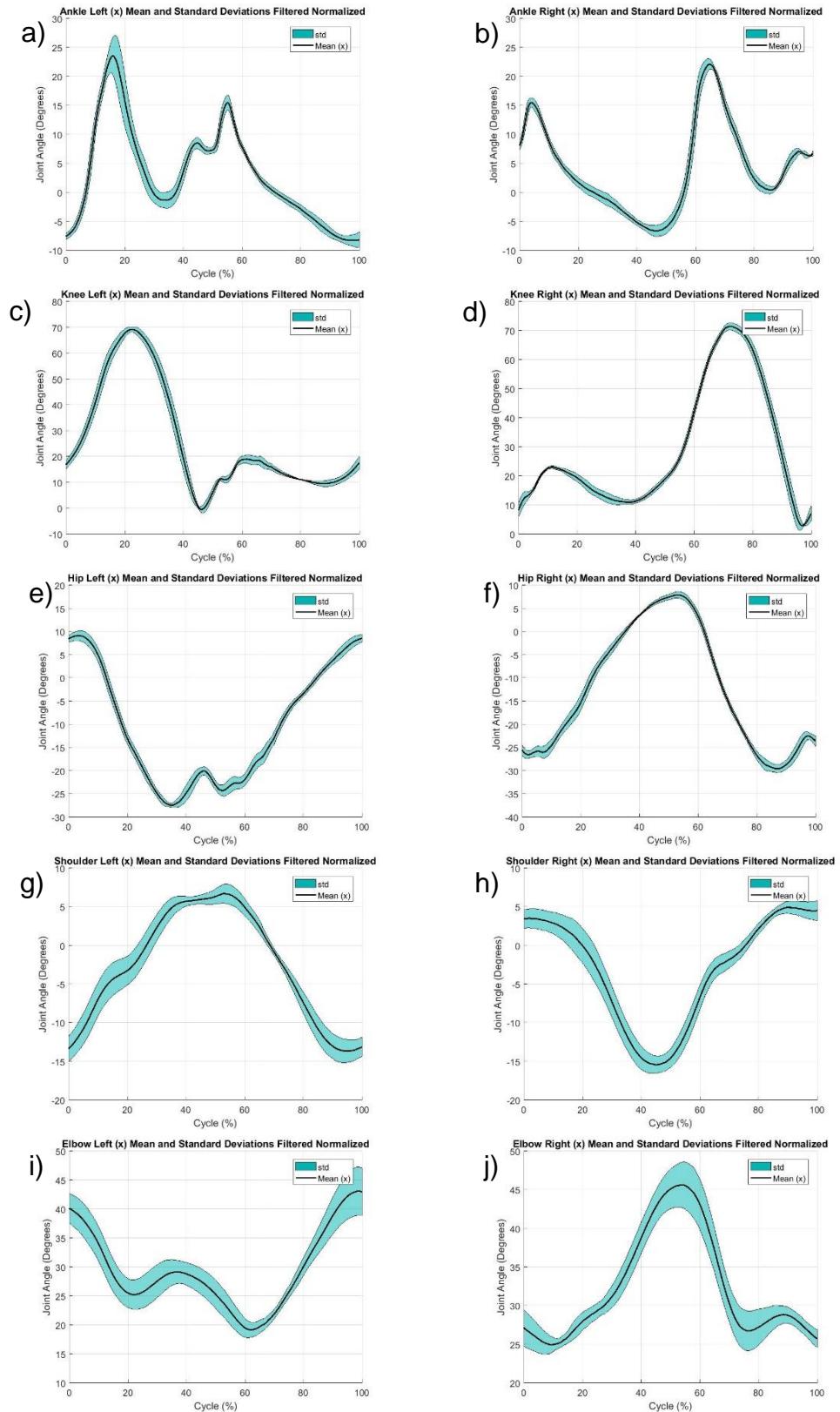
Figure N-1 – Joint angles mean and standard deviations for 'Simple Gait' for a) ankle right and b) left, c) knee right and d) left, e) hip right and f) left, g) shoulder right h) left, i) elbow right and j) left.
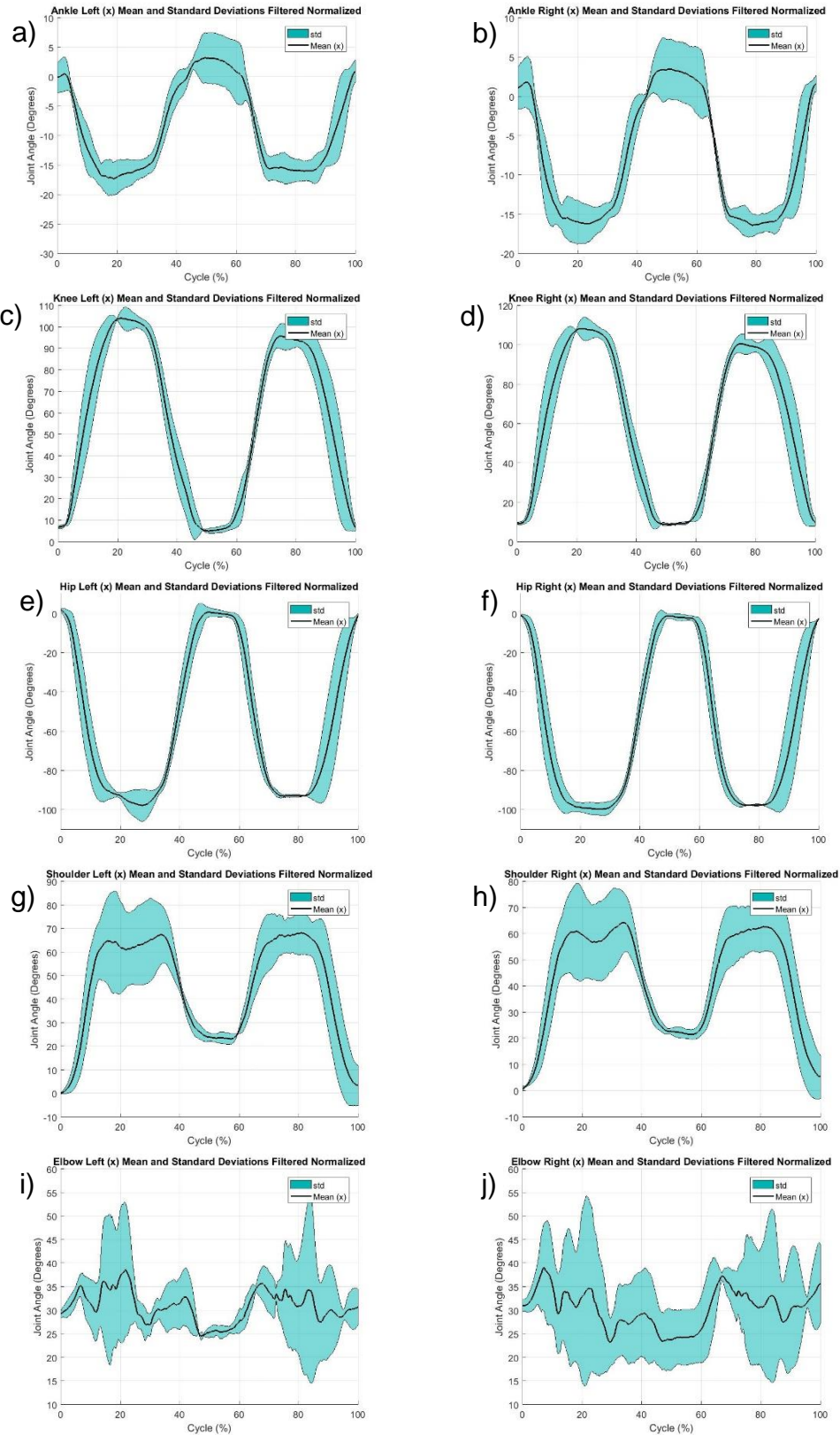
Figure N-2 - Joint angles mean and standard deviations for 'Object Lifting' for a) ankle right and b) left, c) knee right and d) left, e) hip right and f) left, g) shoulder right h) left, i) elbow right and j) left.

226
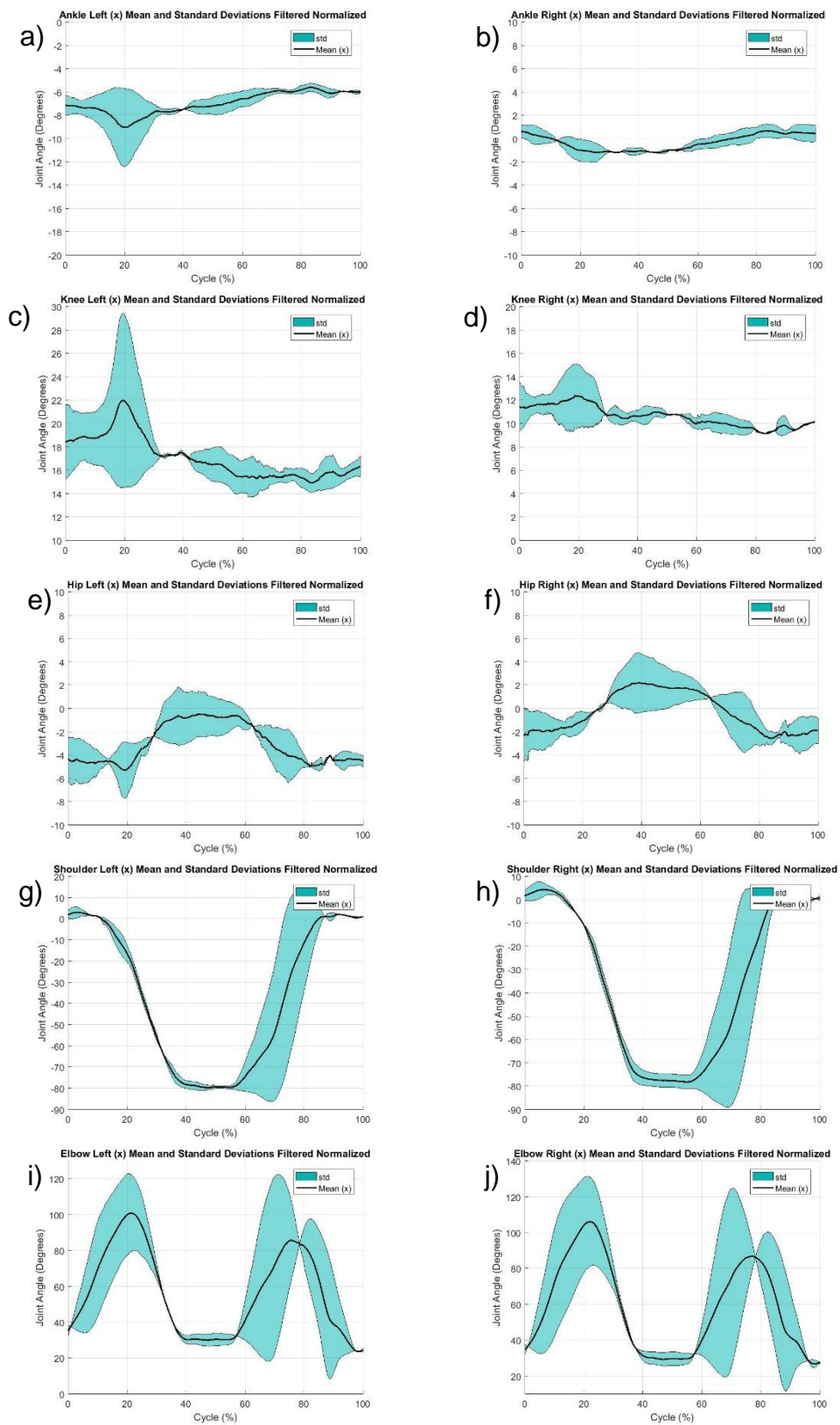
Figure N-3 - Joint angles mean and standard deviations for object raising for a) ankle right and b) left, c) knee right and d) left, e) hip right and f) left, g) shoulder right h) left, i) elbow right and j) left.
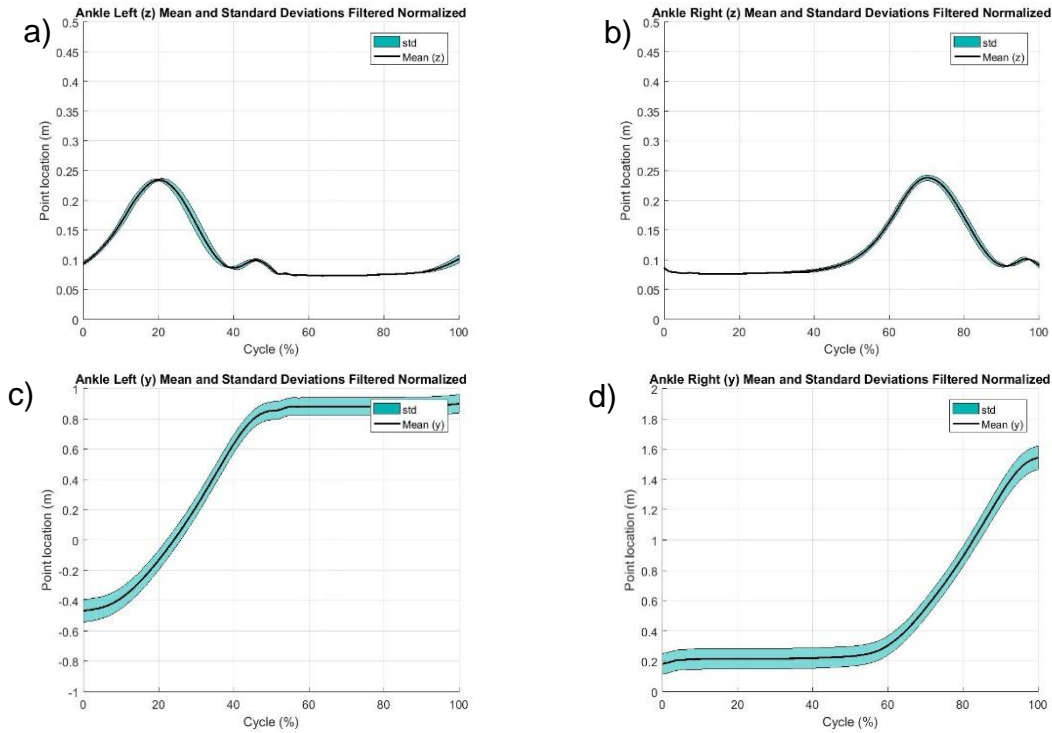
Figure N-5 – Data for ankle joint location during 'Simple Gait' motion
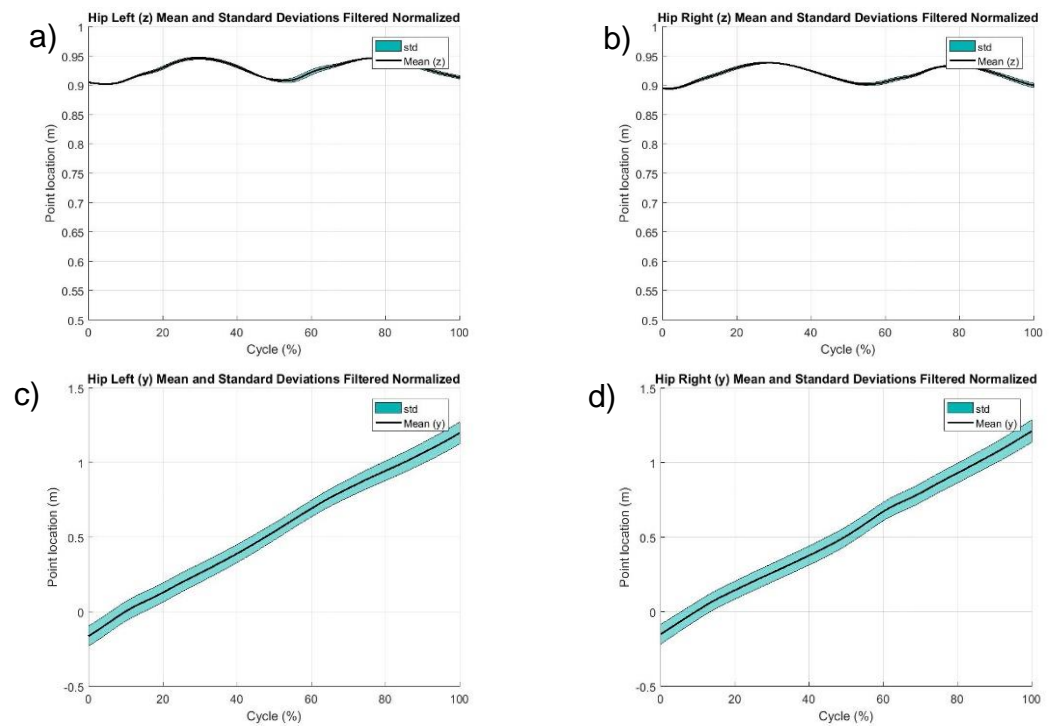
Figure N-4 – Data for Hip joint trajectories during 'Simple Gait' motion
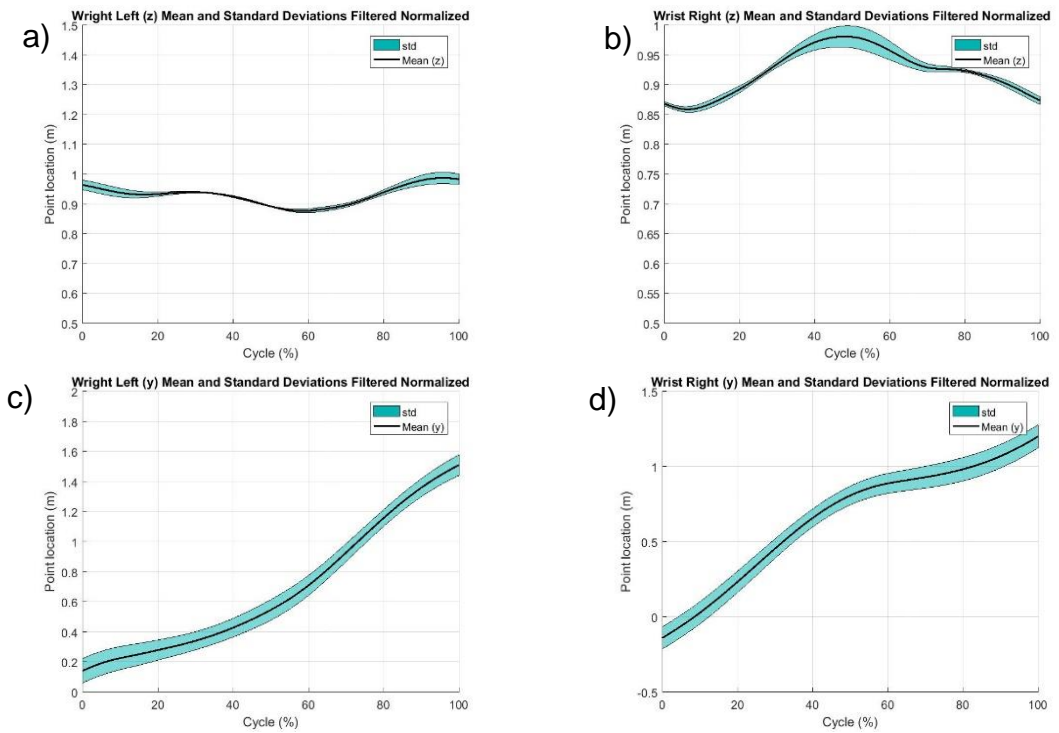
Figure N-6 – Data for Wrist joint trajectories during 'Simple Gait' motion
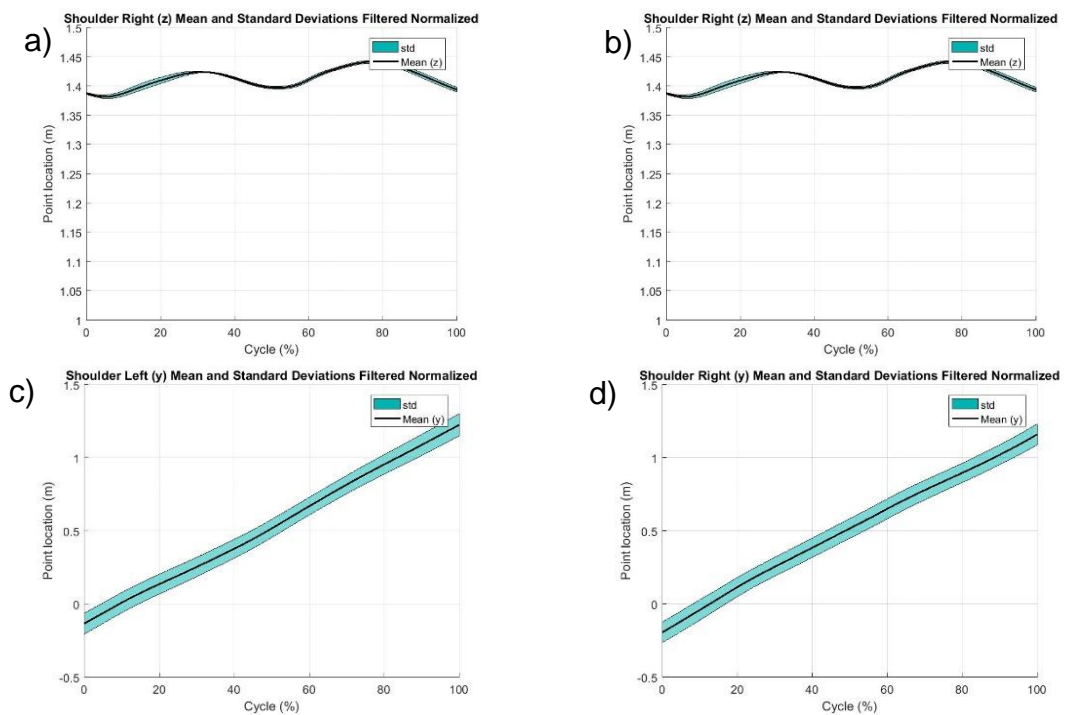
Figure N-7 – Data for Shoulder joint trajectories during 'Simple Gait' motion
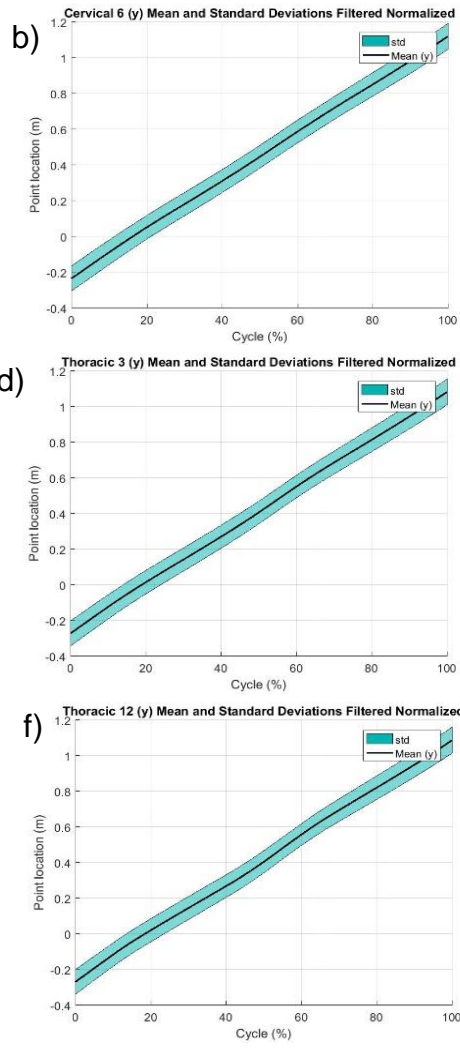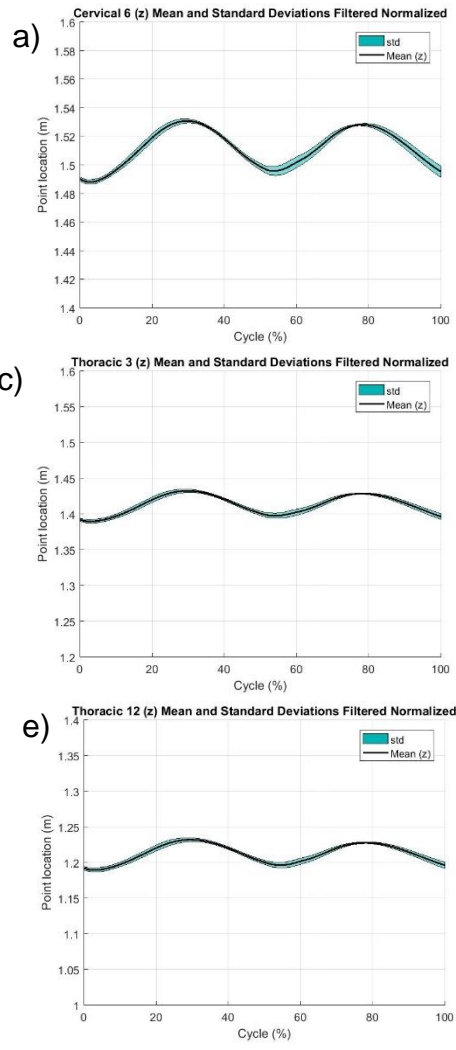
Figure N-8 – Data for the Spine landmarks trajectories during 'Simple Gait' motion, the Cervical 6 (C6), thoracic 3 (T3) and thoracic 12 (T12) landmarks.
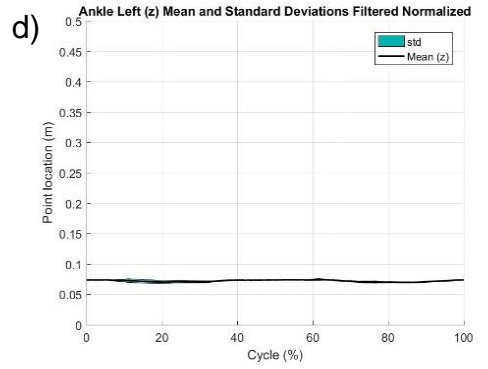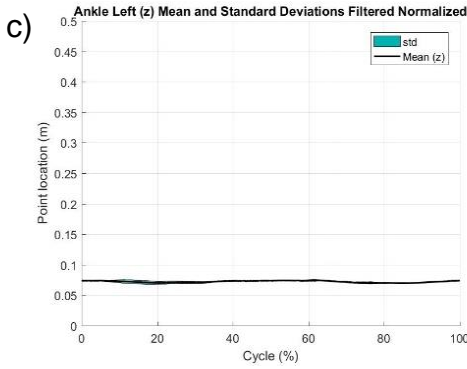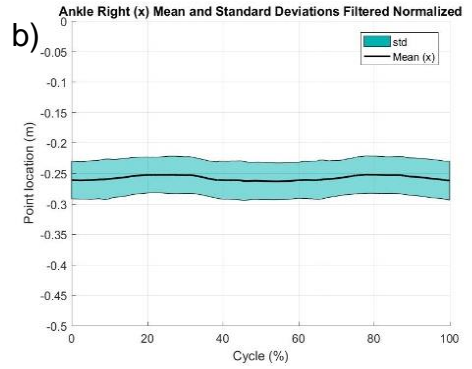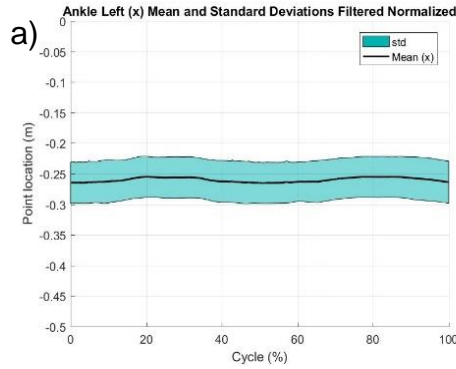
Figure N-9 – Data for ankle joint trajectories during 'Object Lifting' motion
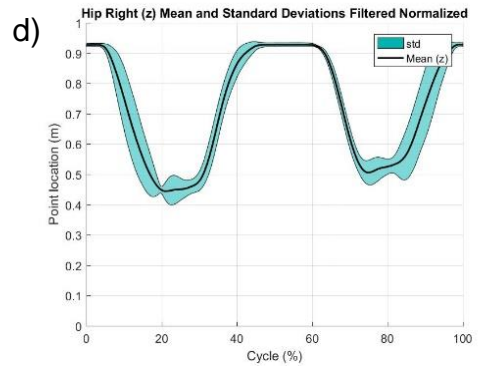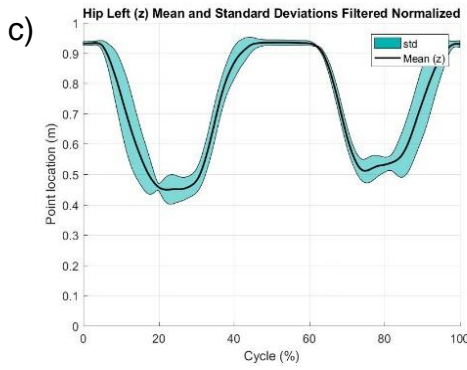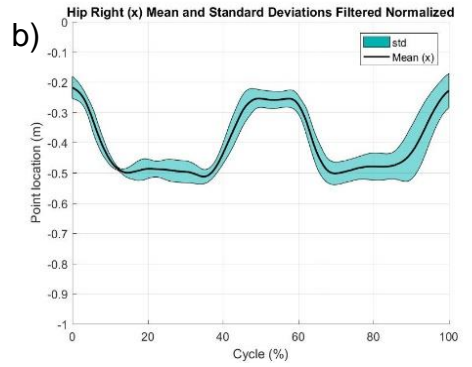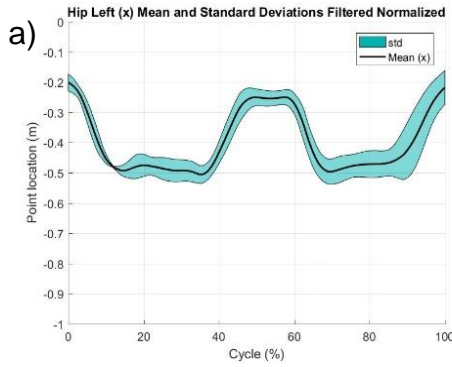
Figure N-10 – Data for Hip joint trajectories during 'Object Lifting' motion
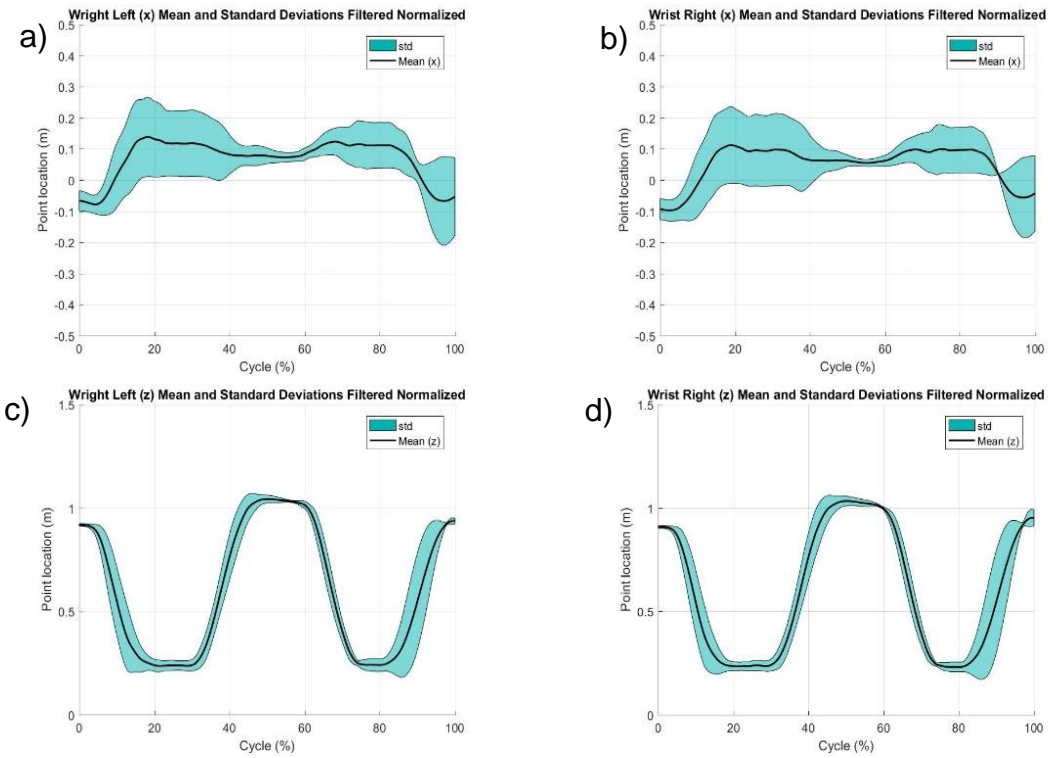
Figure N-11 – Data for Wrist joint trajectories during 'Object Lifting' motion
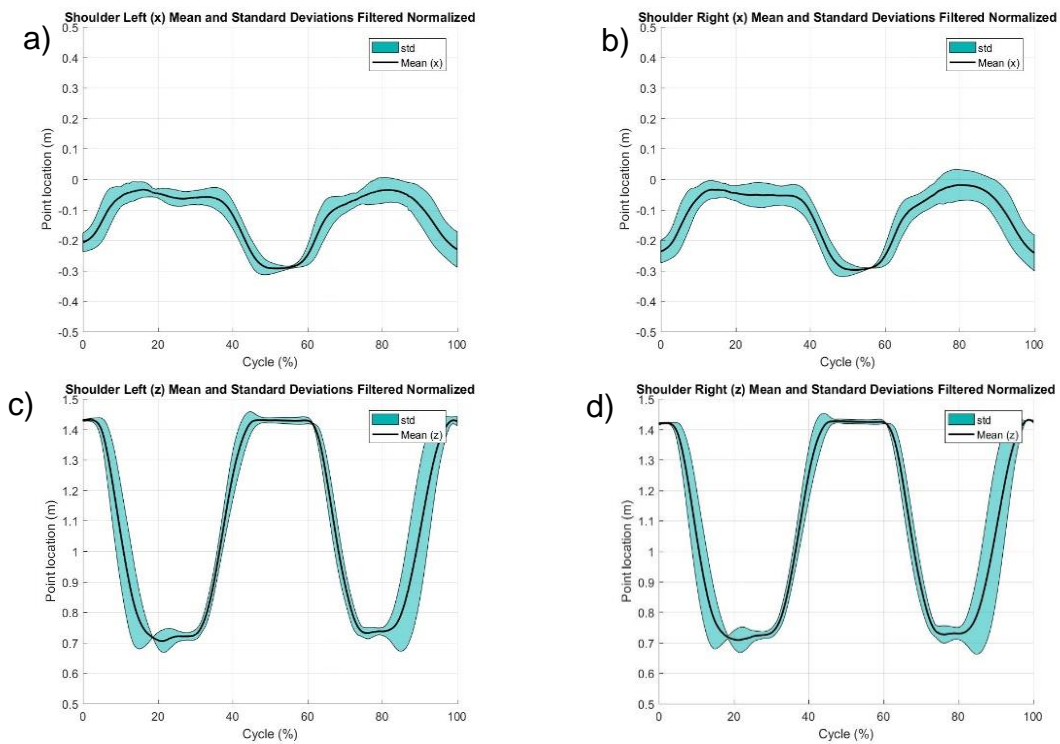
Figure N-12 – Data for Shoulder joint trajectories during 'Object Lifting' motion
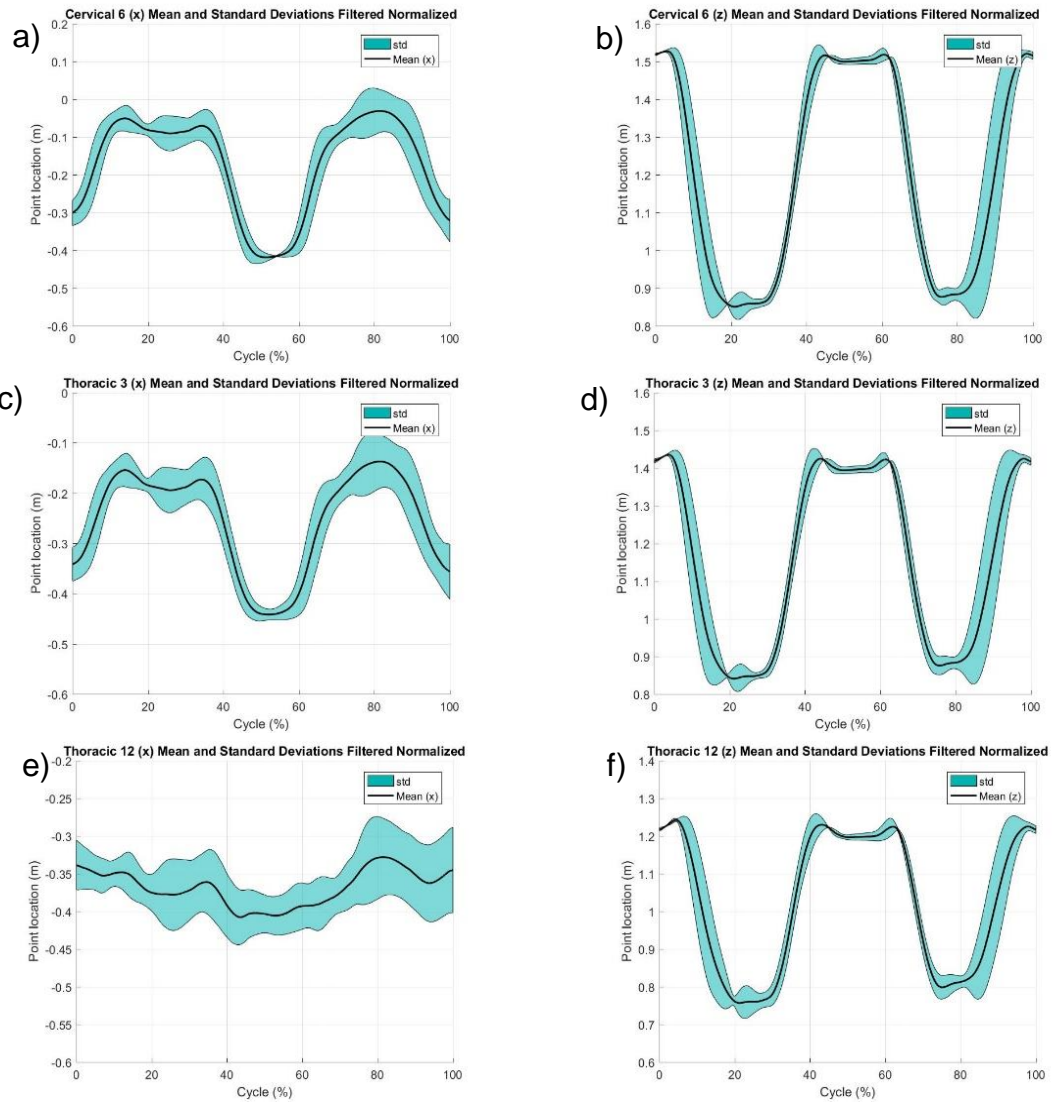
Figure N-13 – Data for the Spine landmarks trajectories during 'Object Lifting' motion, the Cervical 6 (C6), thoracic 3 (T3) and thoracic 12 (T12) landmarks
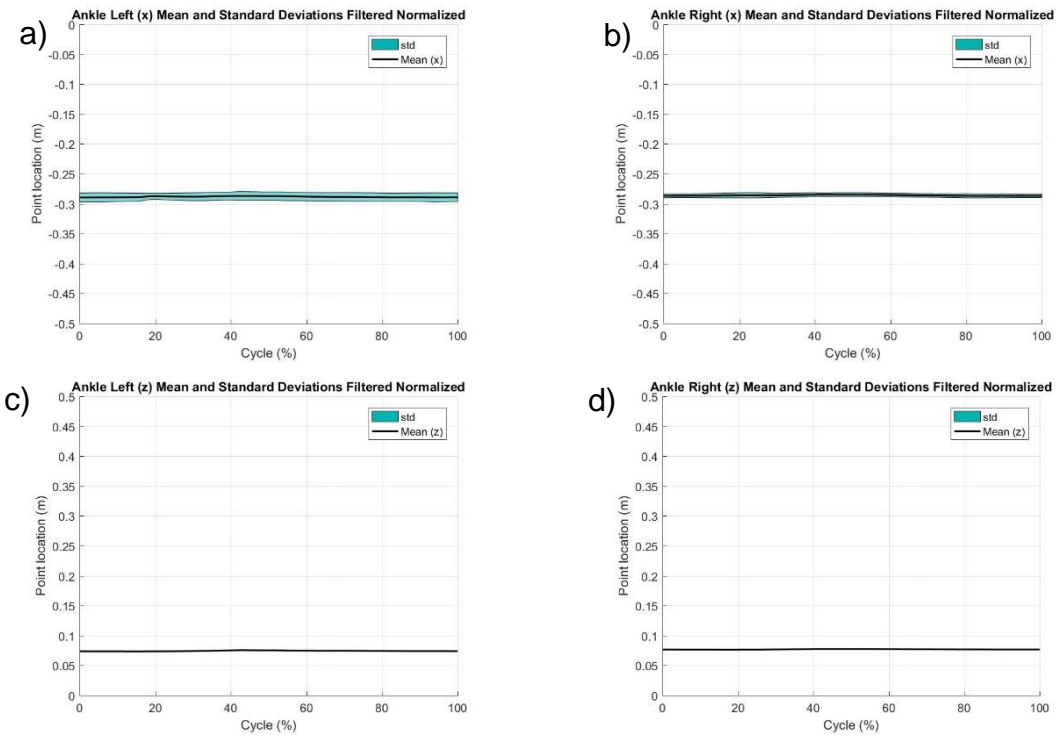
Figure N-14 – Data for ankle joint trajectories during 'Object Raising' motion
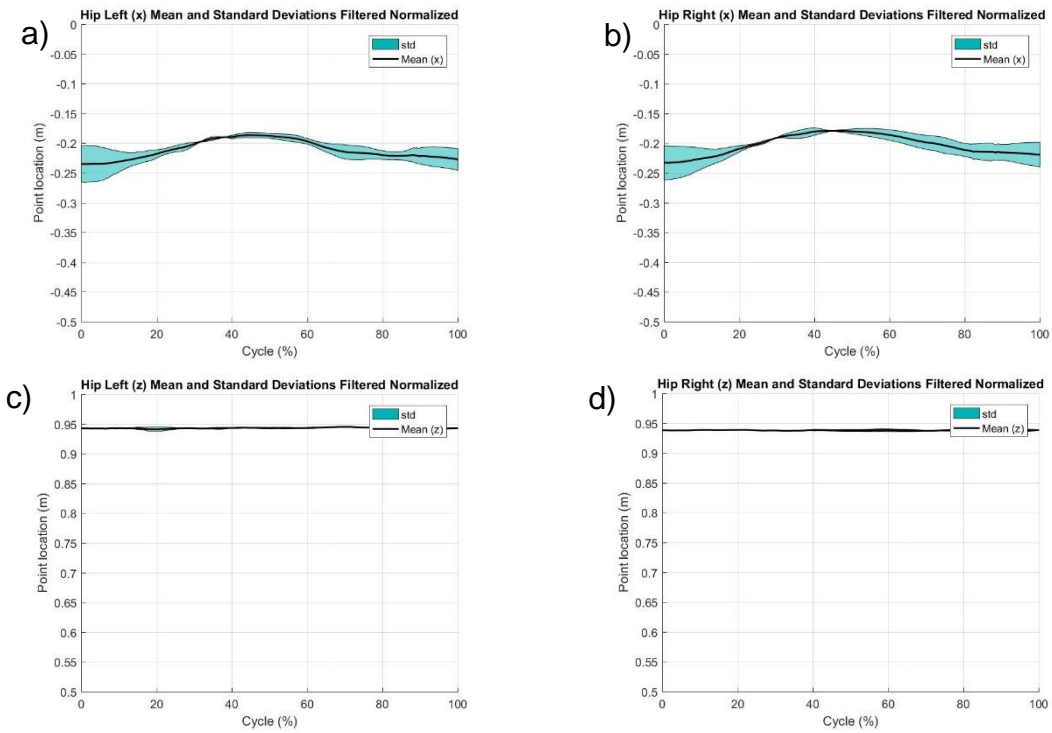
Figure N-15 – Data for Hip joint trajectories during 'Object Raising' motion
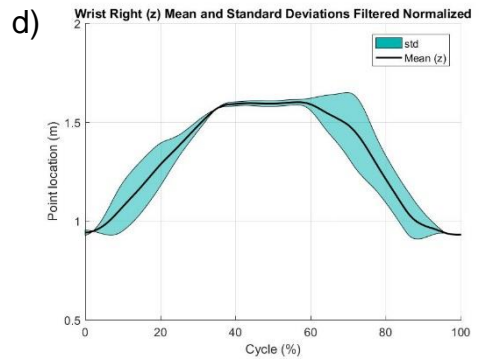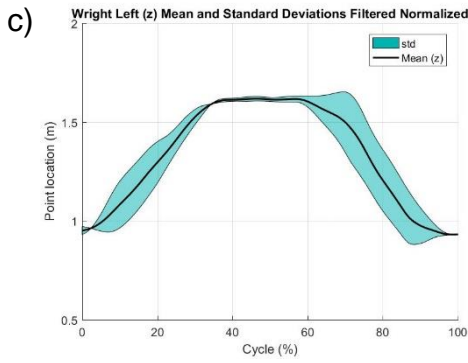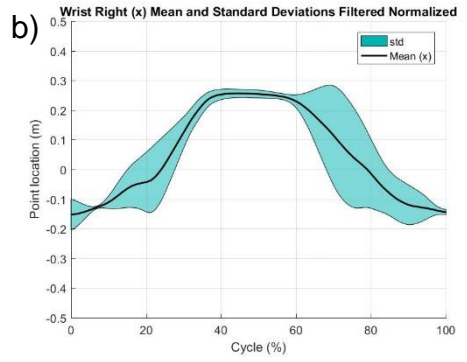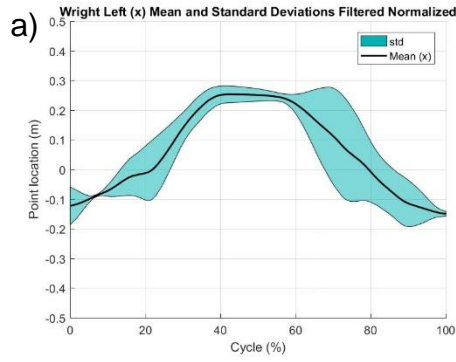
Figure N-16 – Data for Wrist joint trajectories during 'Object Raising' motion
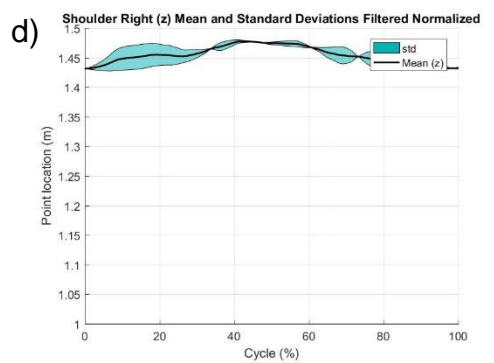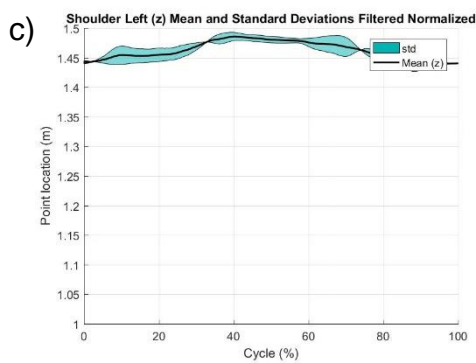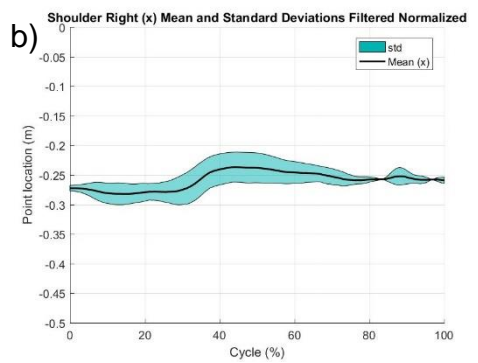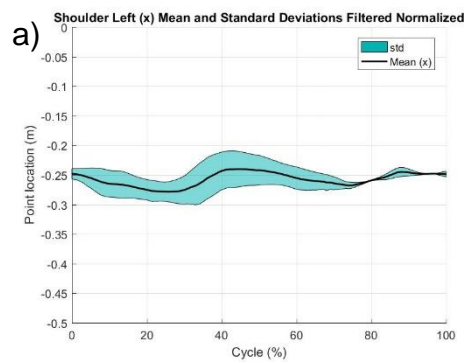
Figure N-17 – Data for Shoulder joint trajectories during 'Object Raising' motion
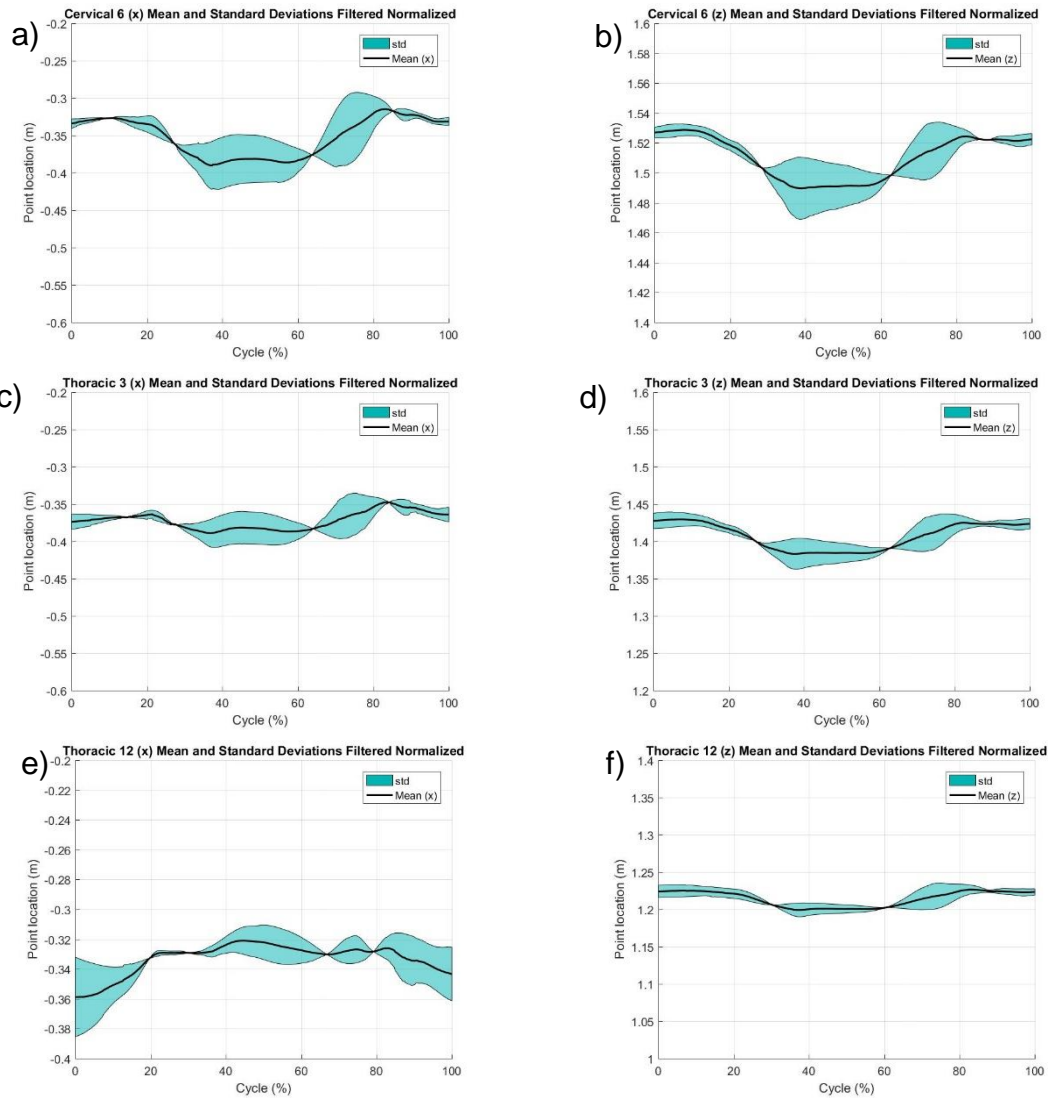
Figure N-18 – Data for the Spine landmarks trajectories during 'Object Raising' motion, the Cervical 6 (C6), thoracic 3 (T3) and thoracic 12 (T12) landmarks

APPENDIX O

Signal Filtering, Derivation and Smoothing from Inverse Kinematics
Results

Since the structure of the exoskeleton will undergo fundamental changes
during the optimization, some joint trajectories, velocities and accelerations
will be unknown. The only data that the inverse kinematics will yield is the joint
angle with respect to time. In this section, various methods for obtaining first
and second order derivatives of the trajectory are compared. Then various
smoothing and filtering techniques are also looked at and compared. A
simulation of a simple pendulum is carried out. Torque data from SimScape
using various methods are compared. It should be noted that this section will
not be an in depth explanation of each method rather an overview of the
results and how they fit in the scheme of this research.

Gradient method and Differentiator FIR Filter comparison

MATLAB has built in methods to derive the differential of data, the diff function,
gradient function (MathWorks) and by filtering methods. Due to being a
differentiator of symbolic expressions, the Diff function becomes unusable
when working with numeric data (MathWorks).

To compare the methods mentioned, a signal is produced which is well known
analytically. The analytical derivatives can be easily reproduced with the
highest accuracy. Initially a sine wave is created using the sample rate of the
motion capture. The analytical derivatives being known as cosine for the first
derivative and negative sine for second derivative. The number of samples is
set to $2 * \pi * sample\ rate$, to ensure a full sine wave cycle and enough
samples. The resulting angular displacement in radians can be seen in Figure
O-1.
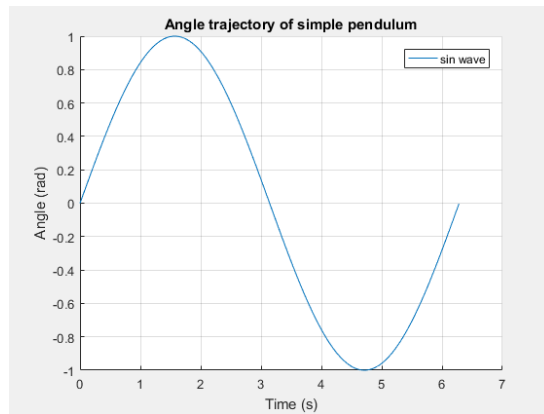
Figure O-1 – Angular displacement in radians derived from a sample rate of 400 Hz

Using the Fast Furrier Transform (FFT) the signal power can be seen in the frequency domain. By using the obw (Occupied BandWidth) function in MATLAB the 99% occupied bandwidth and bandwidth frequency bounds can be determined. The pwelch function measures the power spectral density. The results of the functions can be seen in Figure O-2 and Figure O-3 respectively and it follows that the identified bandwidth frequency bounds found with obw and pwelch coincide. The values are found to be below 0.238 Hz for the upper bound and 0.0804 Hz for the lower bound. The filter is designed with a passband frequency equal to that of the upper band and a stopband frequency near the passband. The filter order is set to 50 for initial investigation and the sample rate is of course set to 400.
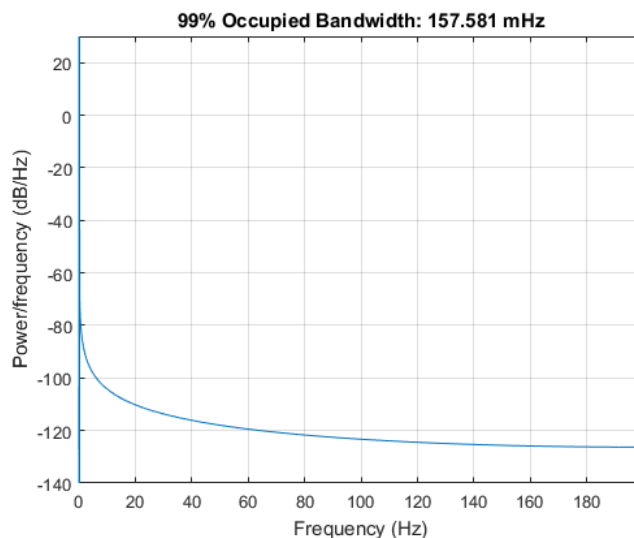
Figure O-2 – Occupied bandwidth of sine wave at 400 Hz sample rate
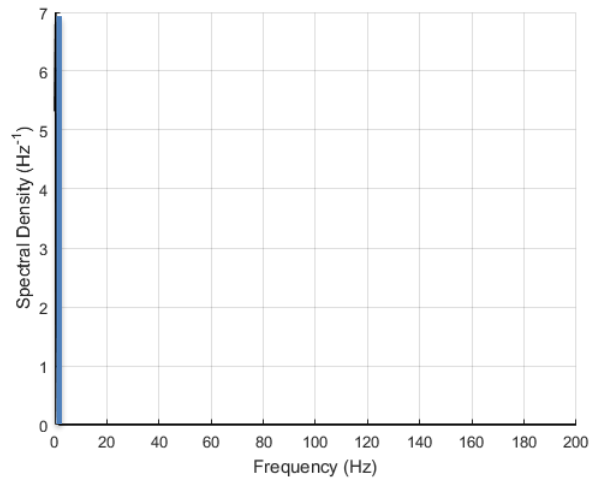
Figure O-3 – Plot for spectral density of sine wave at 400 Hz sample rate upper band highlighted with a blue line

The results of the gradient, analytical and filter method can be seen in Figure O-4 (a) and Figure O-4 (c). Figure O-4 (b) is a close-up of the sine curve of the first derivative, showing the discrepancy between the methods.
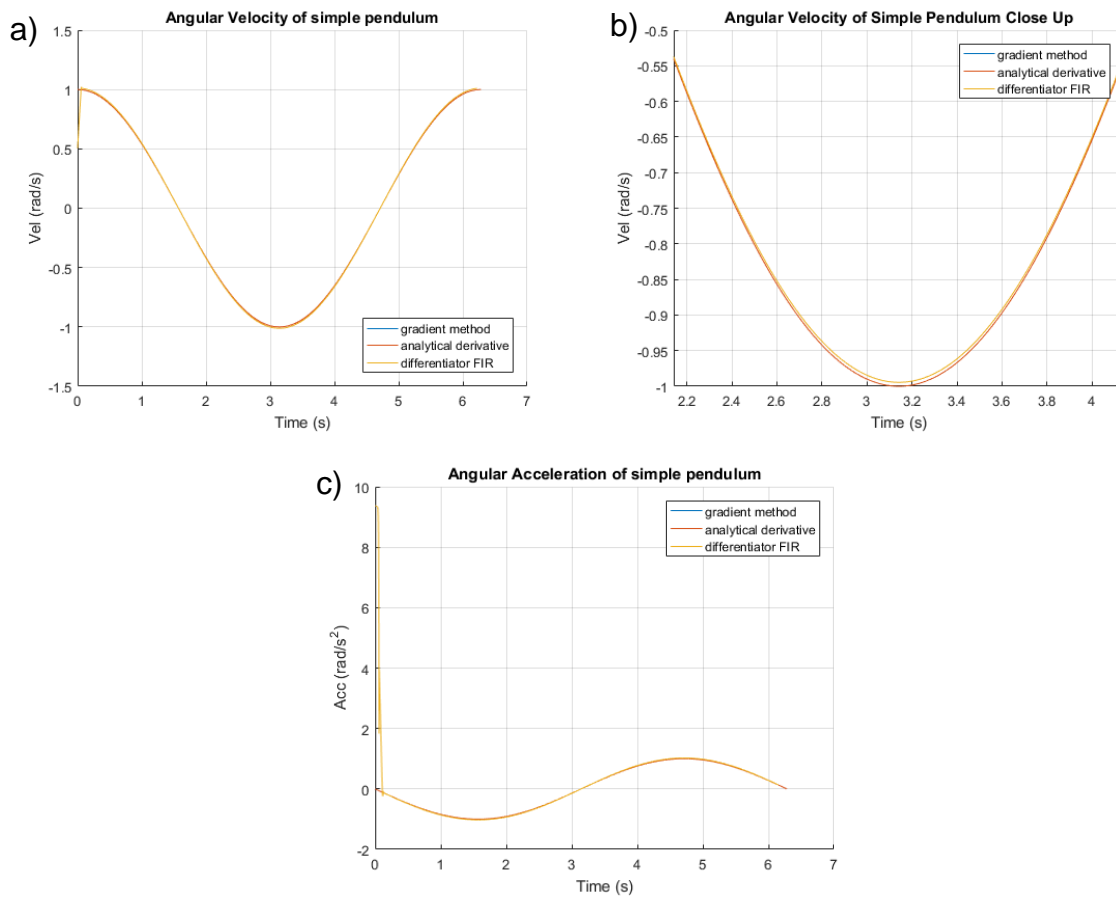
Figure O-4 – a) Angular Velocity plots, first differential of angular position, the gradient method is overlapped by the analytical derivative method. b) Angular Velocity plot, close up showing the discrepancy between filter method and analytical and gradient method. c) Angular Acceleration plots, first differential of angular velocity, the gradient method is overlapped by the analytical derivative method. It can be seen here that the filter method creates a large inconsistency in the beginning.

Unlike the gradient method, the filter method returns a truncated signal. This truncation is due to the delay caused by the filter which is compensated by shifting the signal forward. The truncation is doubled when differentiating the signal again.

The difference in the two methods is better illustrated by adding a disturbance in the form of overlapping sawtooth signal seen in Figure O-5. The sawtooth signals amplitude is 1% that of the sinewave and has half the frequency. These values are chosen to illustrate the effects of a non-smooth data in the simplest way possible. The effects on the first and second differentials can be seen in Figure O-6 (a) and Figure O-6 (c). Figure O-6 (b) showing a close up at the disturbance instance.
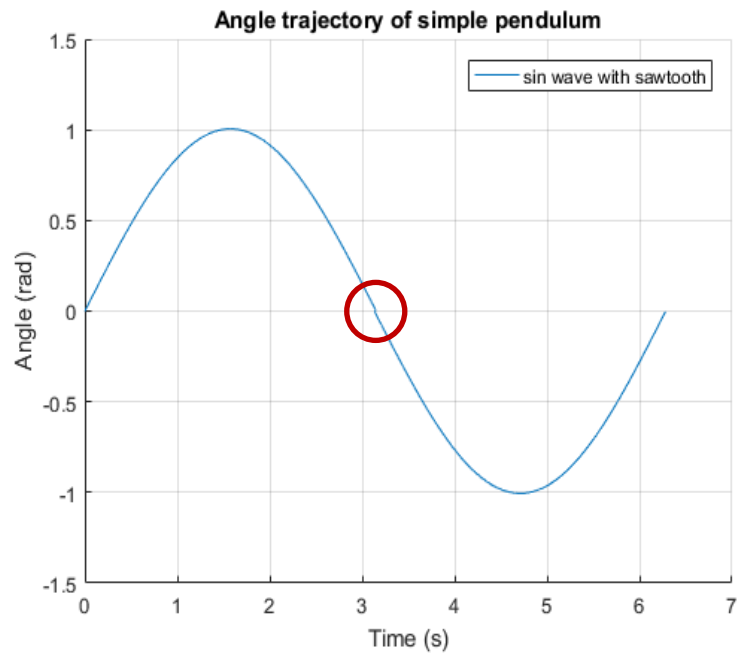
Figure O-5 – Angular trajectory with sawtooth overlap, the sawtooth frequency is selected so that it occurs only once with an amplitude 0.01 times the amplitude of the sine curve. It is marked by a red circle.
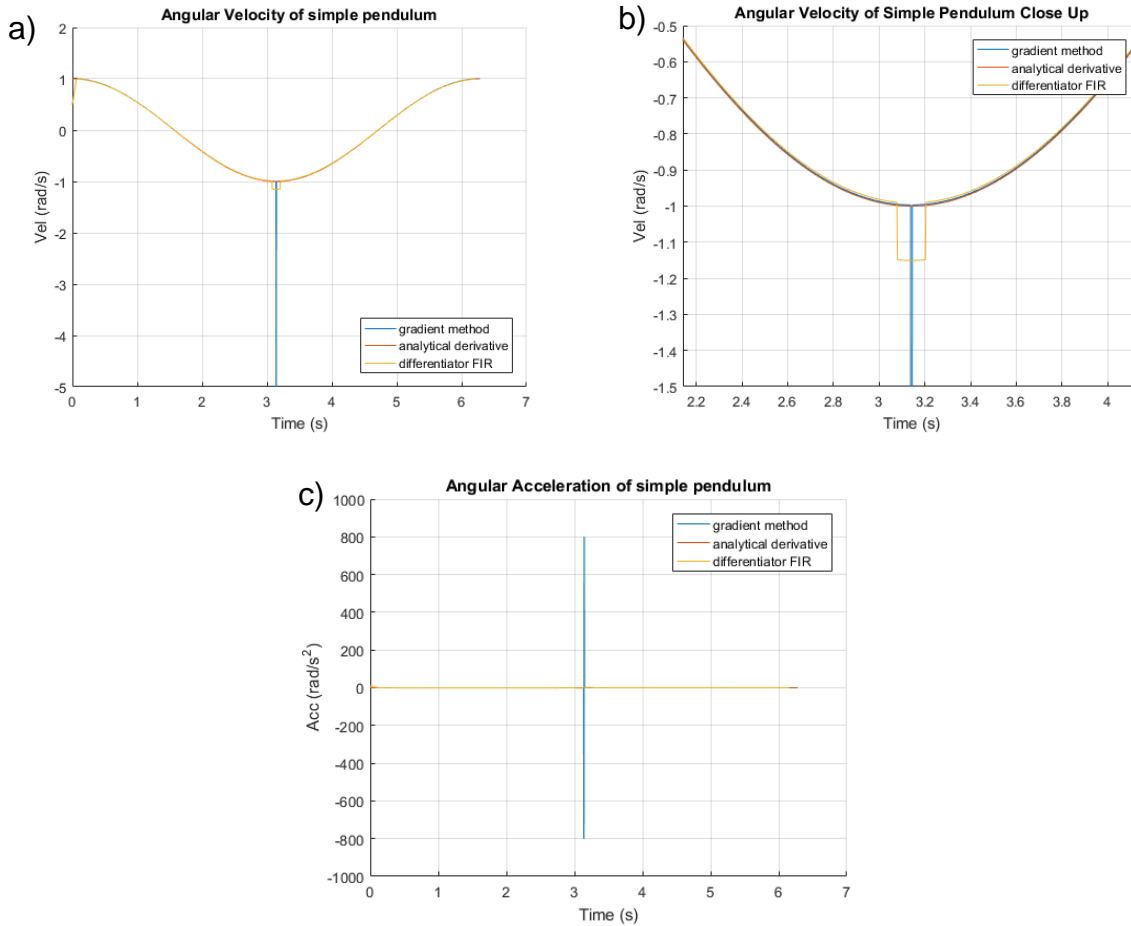
Figure O-6 – a) Angular velocity plots, first differential of angular position with sawtooth signal disturbance. The graph shows the effects of the disturbance on the gradient and filter methods. b) Close up of angular velocity plots, showing the difference in effect of the gradient and filter method. c) Angular acceleration plots, first differential of angular velocity with the sawtooth disturbance. The effects of the disturbance can be seen to have increased by a factor of approximately 200.

Removing outliers as a method of smoothing data

In order to manage the spikes in the data the hampel function can be used in MATLAB which removes outliers using Hampel identifier (MathWorks). For each sample of the signal the function computes the median within a given span on each side of that sample. It compares the value of that sample with the median and replaces it if the difference is greater than a set number of standard deviations (by default three standard deviations). This is done on the sawtooth example above and the filter results are shown in Figure O-7. After removing the outliers the filtered gradient derived velocity signal is used again with the gradient function to obtain the second derivative of the position data, acceleration. This is shown in Figure O-8 where the acceleration signal is compared with the analytical second derivative.
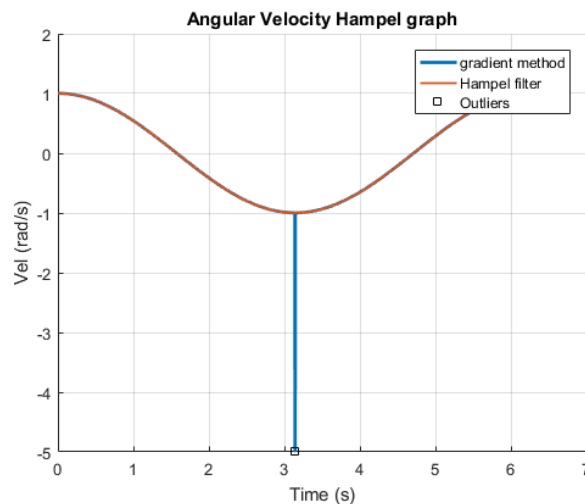
Figure O-7– Applying Hampel filter on the velocity signal derived by gradient method.
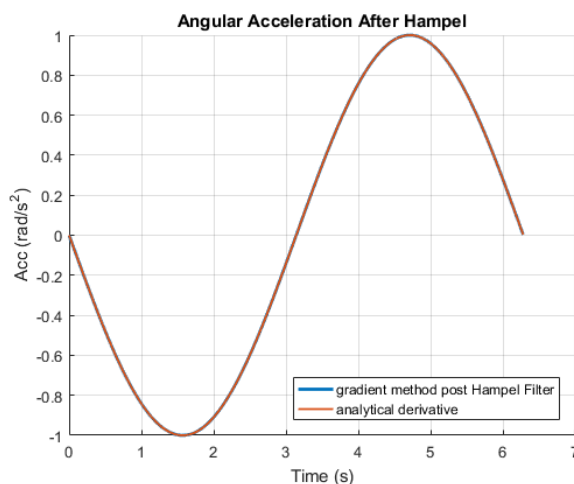
Figure O-8 – Applying the gradient function on the Hampel filtered velocity signal and comparing it with the analytical second derivative of the sine signal it can be seen that the curves overlap.

Filtering and Smoothing Signals with Noise

So far data which is smooth and smooth data with some singular disturbance has been looked at. Some data may not be smooth, or the derivatives of a semi-smooth data may yield noisy results. To simulate this white noise is added to a sine signal (Figure O-9).
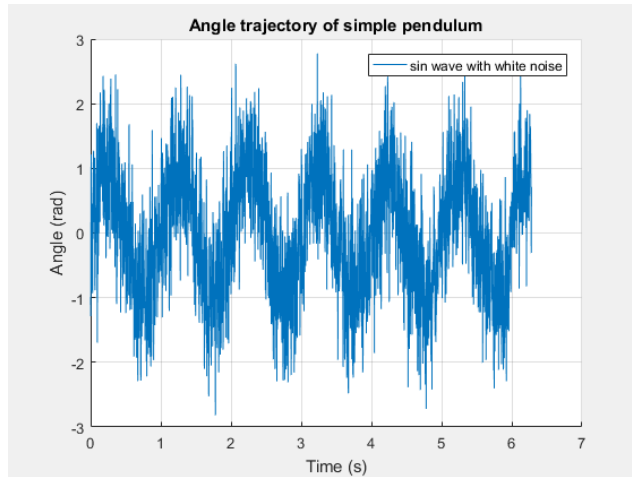
Figure O-9 – White noise added to sine signal.

Filtering

By way of Fast Fourier Transform (FFT) the signal frequency that may be most suitable for filtering can be identified (Figure O-10). The FFT graph confirms that the frequency of the signal is 1 Hz.
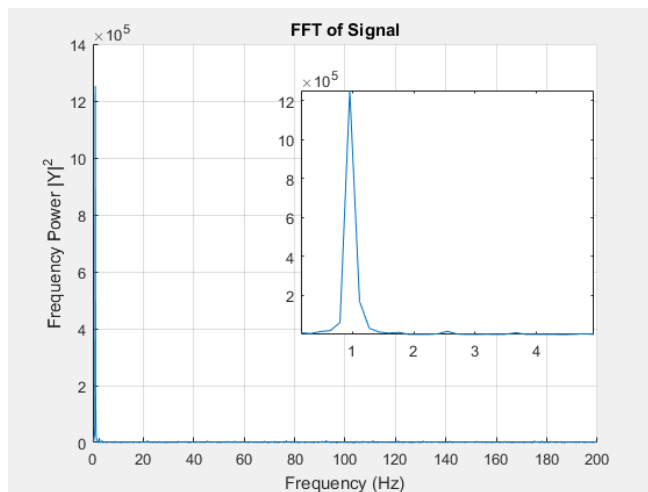
Figure O-10 – FFT of sine signal data. Plot shows signal power at respective frequencies. The plot zooms in on relevant section of the graph showing that the largest magnitude of the signal lies at frequency 1 Hz, as expected.

In the example scenario presented the percentage power of the signal of interest (at 1 Hz) compared to the total power is approximately 50%. Making the stop band frequency close to the pass band frequency is costly, therefor the stop band frequency is set to 10 Hz above the pass band frequency (Oppenheim Spring 2011). All other settings are kept as standard. The designfilt function is then used to design a filter (MathWorks). The magnitude response of the filter can be seen in Figure O-11.
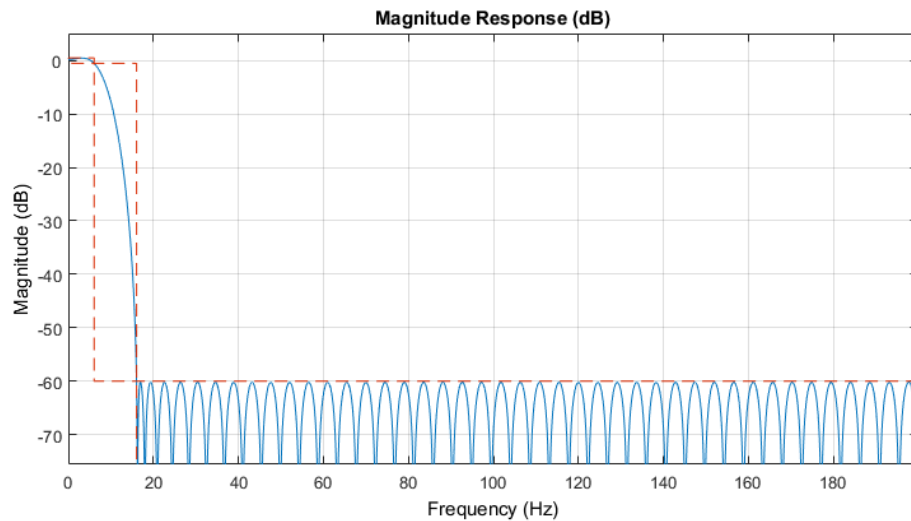
Figure O-11 - Magnitude response of the filter designed using the data from FFT of the noisy signal

Residual Analysis

Using residual analysis on this data (Figure O-12) shows that this method is not suitable for all kinds of noisy data. The results show that identifying the cut of frequency in this manner, for this type of noisy data is very difficult as there is not a clear region where the residual data diverges as seen in Figure 4.9.
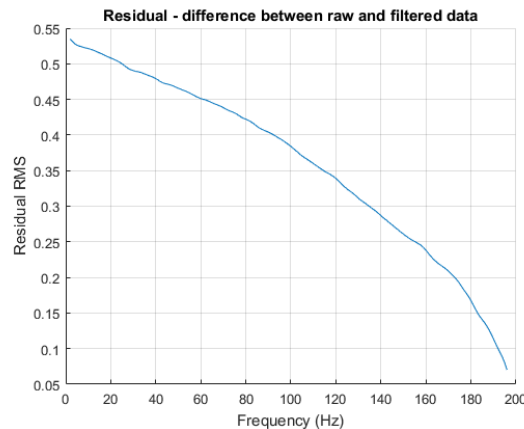
Figure O-12 – Residual against frequency for the noisy sine wave.

245

Data Smoothing

The smooth function in MATLAB smooths data using a moving average filter (MathWorks). This method of signal manipulation depends on the span and the method of moving average filter selected. The span signifies the number of data points that the moving average will use, the greater the number the greater the discrepancy between input and output. The smooth function can filter the data using various methods. First is the standard 'moving' method, which is a lowpass filter where the filter coefficients is equal to the reciprocal of the span. Second and third are the 'lowess' and 'loess' methods, which are local regression methods using weighted linear least squares and a 1st degree and 2nd polynomial model respectively. Fourth is the 'sgolay' method, which uses Savitzky-Golay filter. The fifth and sixth method 'rlowess' and 'rloess' are robust versions of 'lowess' and 'loess'. Difference being that these methods assign lower weightings to outliers in the regression and zero weighting to data six mean absolute deviations (MathWorks).

The results of smoothing the noisy sine signal is presented graphically in Figure O-13. The various methods are compared with the none noisy sine signal. The results of the root mean square (RMS) error of the sine signal and the smoothed signals can be seen in Table O-1.
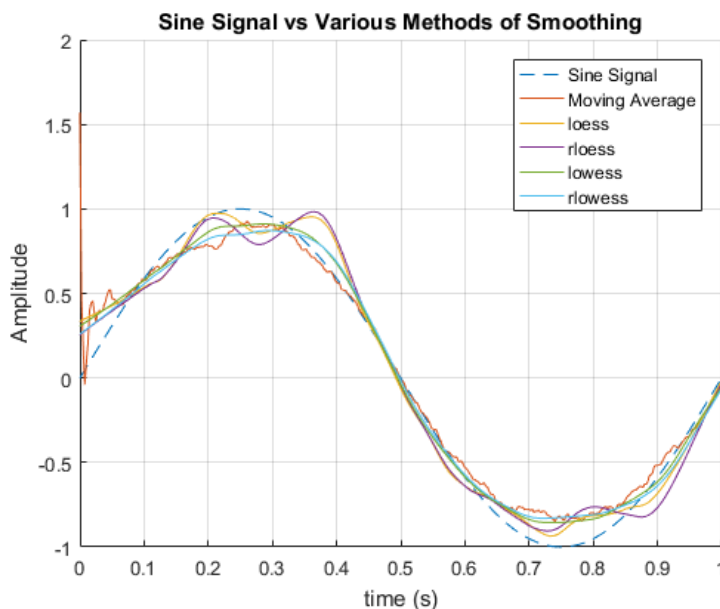
Figure O-13 – Graph showing various local regression methods for smoothing the noisy sine signal. All methods used a span of 100

Table O-1 – Table of RMS values for various smooth methods.

Methods	RMS values	Computation time (s)
'moving'	4.9548	0.0066
'loess'	5.4669	0.0190
'rloess'	5.8029	2.2722
'lowess'	4.1225	0.0076
'rlowess'	4.3444	1.4713

Comparing the 'robust' versions (rloess and rlowess) to their counterparts (loess and lowess) it can be seen that the rms error is smaller in the originals and not the robust versions. There is also a time cost associated with running the robust versions which is of the magnitude 50-70 times greater.

To investigate further over a range of various span numbers, the rms error is mapped as a function of span input variable for each method. Result is seen in Figure O-14. The rms value is obtained by looking at the difference of the smoothed signal and ideal sine signal (not the one that has noise). As can be seen in the figure, the loess methods converge to minimize the rms as the span value increases. The lowess methods both have a minimum value at approximately 100 span value. The simple moving average methods minimum is located at approximately 50 span values.
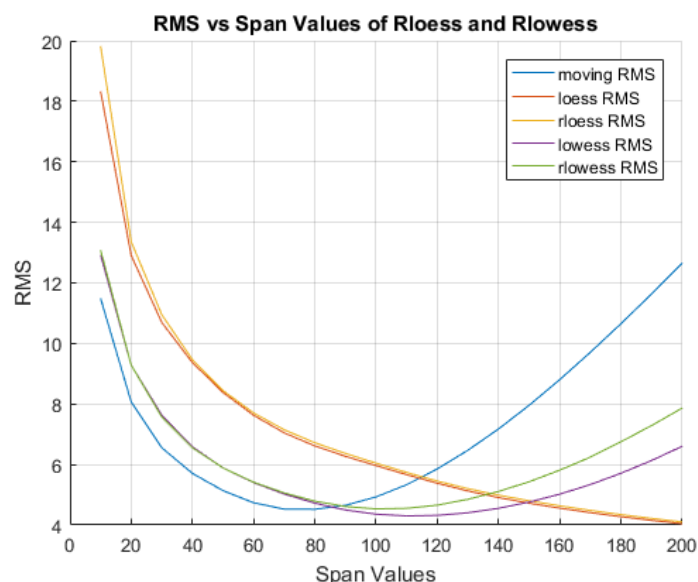
Figure O-14 – Root mean square (RMS) values of rloess and rlowess functions in MATLAB against span variable. The RMS value is against a sine signal without noise.

As outliers can cause a significant issue in the simulation result and during derivation (as seen in Figure O-6) 'moving', 'loess' and 'lowess' methods are automatically excluded. It is still interesting to see that the 'moving' method needs the least amount of span to reach a reasonable result, in terms of minimal rms value.

Since signal filtering or smoothing is expected to occur a significant amount of times during the simulation and optimizations, the final consideration will be to look at the time cost of increasing span number. From Figure O-14 it can be understood that the 'rloess' method reaches a similar rms value as the 'rlowess' method approximately two times the span number. The correlation of time cost and span number is shown in Figure O-15 for both methods. For the sine signal example the time cost is approximately twice as high using the 'rloess' method than using the 'rlowess' method.
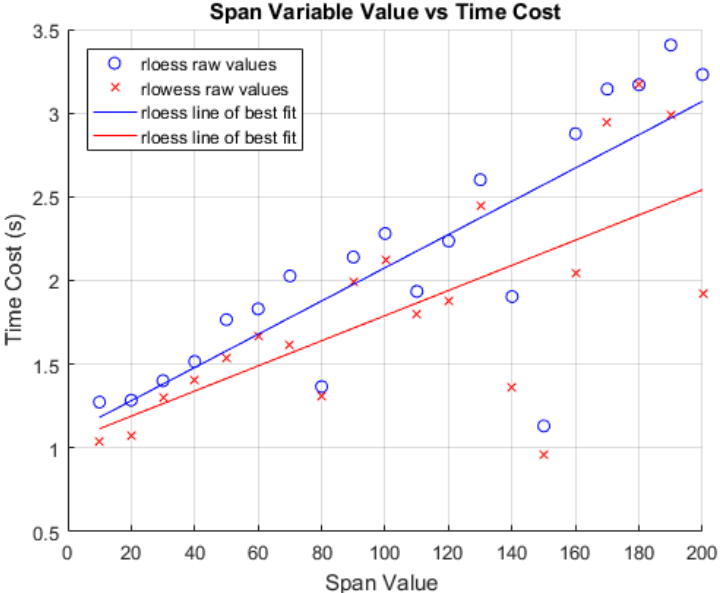
Figure O-15 – The time cost compared to the span number for rlowess and rloess methods of smoothing the sine signal.

Comparing Filtered and Smoothed Signals

As a final step the results of the filter developed previously and the rlowess-smoothing method are compared, sample results are shown in Figure O-16. The rms error value for the filtered signal compared to the desired sine signal is 6.1416, which should be noted is larger than the rlowess-filter. The time for filtering the noisy sine signal is approximately 0.0536 seconds. This is considerably smaller than using any of the smoothing techniques.

In this research the smoothing is deemed satisfactory. This is due to the process of obtaining the frequency and the required tuning to minimize the rms value, makes it less favourable to the smoothing method considering that it needs to be integrated into an automatic optimization routine.
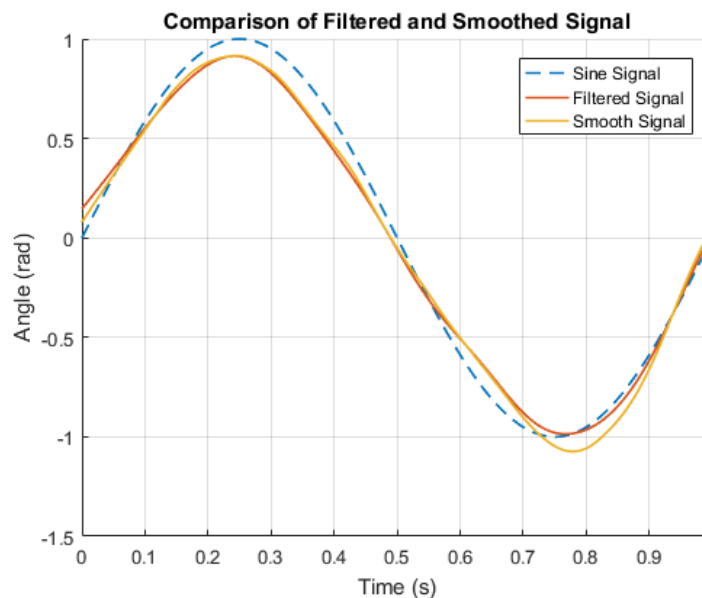
Figure O-16 – Comparison between smoothing using 'rlowess' method and filtering method

Signals with Noise, Smoothing and Derivation

So far consideration has been given to various methods of derivation of signals, filtering and smoothing. The purpose being to appropriately derive the velocity and acceleration data when smoothing or filtering from the inverse kinematic results. Figure O-17 a), b) and c) show the results of differentiating without the use of smoothing or filtering. As expected the noise error is carried on until the expected derivative results are negligible in comparison to the noisy ones.
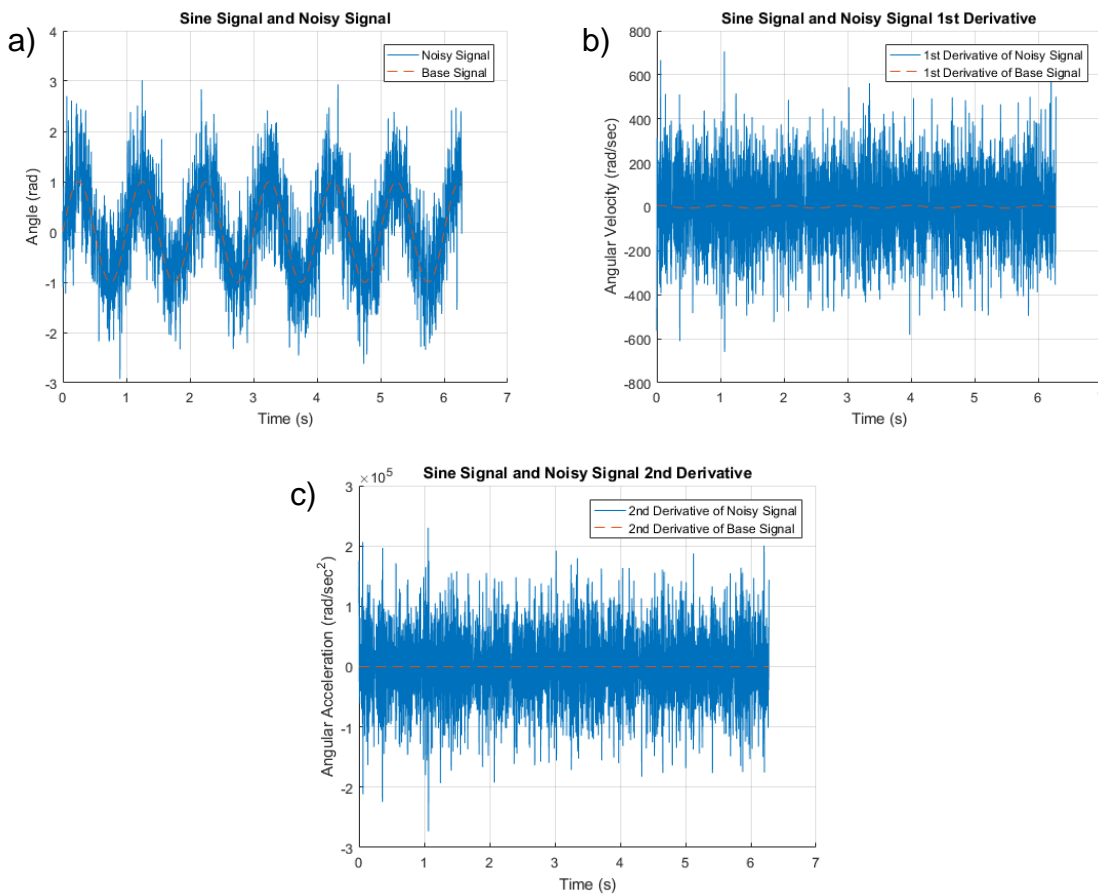
Figure O-17 – The sine signal and its derivatives shown with the noisy counter parts, a) shows the non-differentiated signal, b) the magnitude difference of a differentiation without smoothing shows itself to be several hundreds of magnitudes larger in this example, c) the magnitude difference for 2nd derivative is even greater, in the orders of 10^5.

The results of smoothing the post-derivation results above can be seen in Figure O-18. The base signal, as expected and seen in the previous example, retains the pattern and magnitude. The first derivative somewhat retains the pattern, although the magnitudes of the signal are not precisely the same. The

250

second derivative is very much not like what is to be expected, with magnitude order of 10^3 greater and chaotic amplitude.
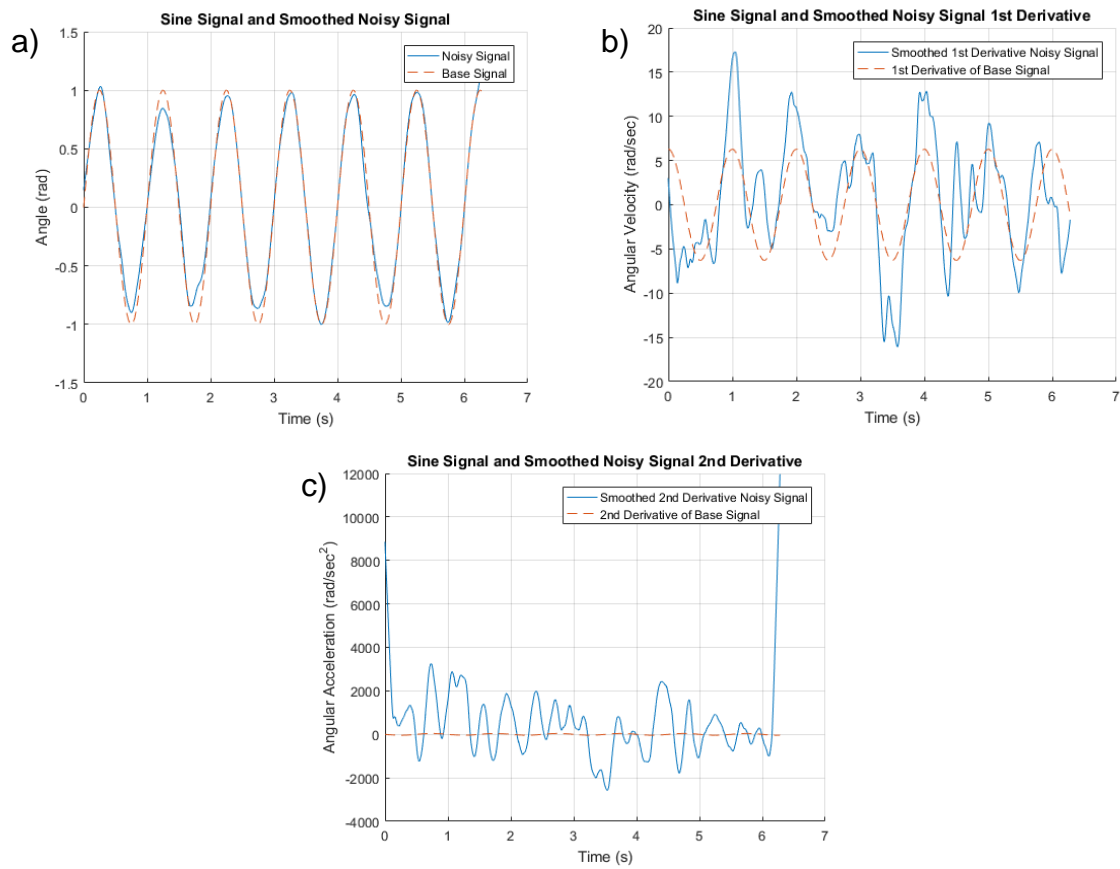
Figure O-18 – Smoothing of signal and derivatives, a) base signal b) first derivative and c) second derivative.

Deriving the gradient of the signal is considered after it has been smoothed. This is shown in Figure O-19. The curve after smoothing the 1st derivative of the smoothed signal is also shown. When calculating the rms error for the two derivatives the smoothed derivative has a smaller value.
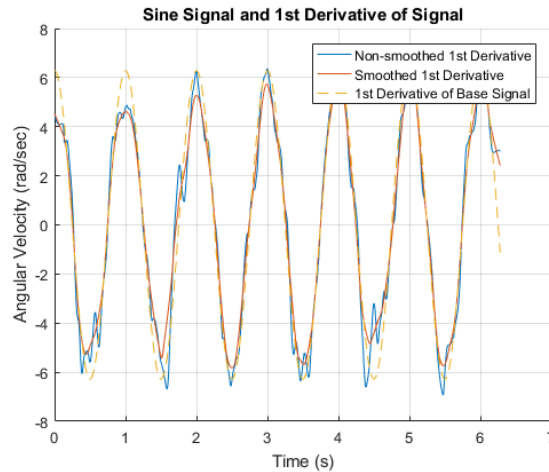
Figure O-19 – Comparison of the 1st derivatives of the sine (base) signal. The rms error of the smoothed 1st derivative being 41.8367 and 47.3923 for the non-smoothed 1st derivative.

The smoothed 1st derivative of the sine signal can be used to find the 2nd derivative by utilising the gradient function again. The results are shown graphically in Figure O-20. In contrast to the 2nd derivative in Figure O-17 and Figure O-18 the signal now demonstrates the traits that are expected, both in magnitude and frequency.
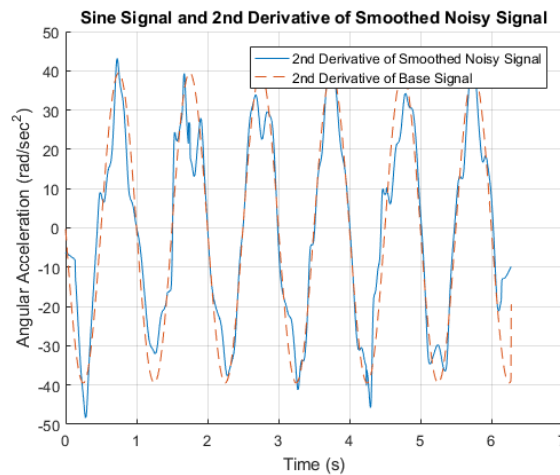
Figure O-20 – The derivative of the smoothed 1st derivative plotted together with the 2nd derivative of the base signal.

252

Filtering, derivation and smoothing

Investigation is carried out to obtain a suitable method of filtering, deriving and smoothing data. This is done in order to incorporate the best methods in the workflow and optimization algorithms. Since MATLAB and SIMULINK will be used for this research, the functions and methods available are examined.

The sine wave is used as a base signal for the comparisons, as it and its derivates are known. Initially the gradient method and the differentiator FIR filter are compared using the base signal. It was found that the gradient method is favourable. However when introducing a disturbance in the form of a chirp midway through the signal, the effects cascades and increase drastically to the point where in the gradient method the second derivate the disturbance is shown to have increased by a factor of approximately 200.

In order to deal with uneven data, smoothing and filtering of the signals is investigated further. White noise is introduced to the base signal. By way of FFT the frequency of the signal is obtained and the designfilt function is used in MATLAB to design a filter. The residual analysis method is also used but it is found that for this sort of signals the method is unsuitable.

MATLAB's smooth function is explored, and the noisy sine signal is filtered using various methods. Comparing the RMS values with a non-noisy sine signal and taking into consideration the computational time, rlowess method for smoothing with a span of approximately 100 is found to be the suitable choice.

When comparing the filtered data with the rlowess smoothed data it is found that the former has a higher RMS value. Filtering the data is however less costly in computation time. The main issue lies in generating the filter, and as such smoothing became the viable and chosen way moving forwards.

Finally smoothing the noisy data is looked at in conjunction with derivation of the noisy data. It is concluded that an acceptable method is to first smooth the data then derive in succession. The algorithm is shown in Figure O-21.
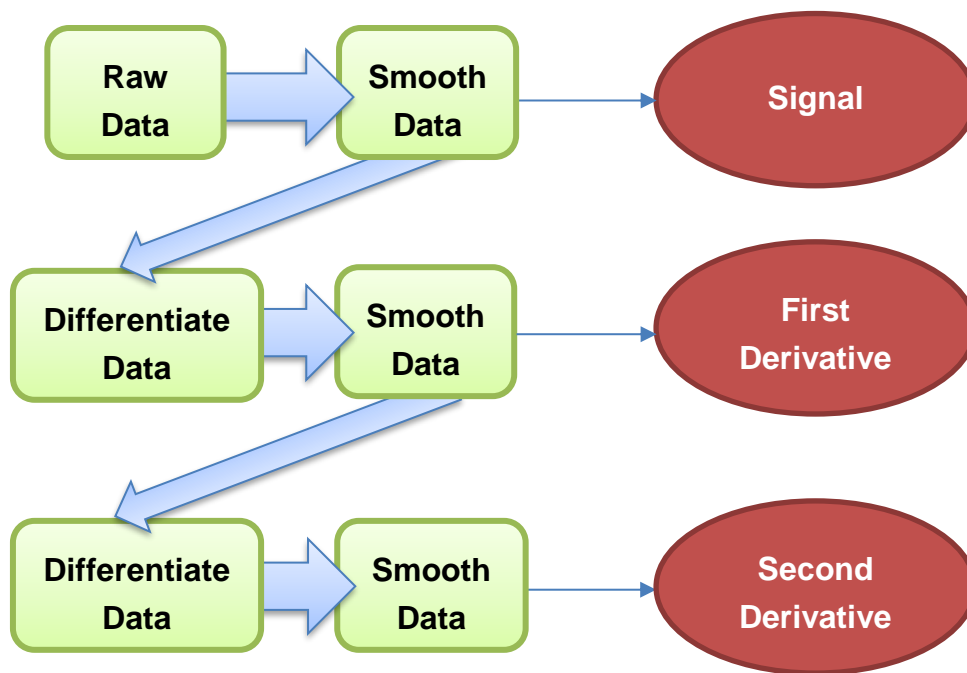
Figure O-21 – Visual representation of the algorithm to obtain
   signals and their first and second derivatives using smoothing
   and derivative functions in MATLAB

APPENDIX P

Denavit-Hartenberg Notation, Forward- and Inverse-Kinematics for Arms and Legs

The use of Denavit-Hartenberg (DH) notation is common in robotics to describe a robot (Vepa 2009; Craig 2005). Here using DH notation the derivation of the kinematic equations is shown for the model described in Figure 5.2. The equations were shown in part in Chapter 3 where the kinematic equations for a two-link planar system was used when comparing inverse kinematic methods.

Figure P-1 shows a diagram of the structure described in Figure 5.2 (c) with its link-frame assignments. The base frame is set to be the point contact between the first link and ground. Using this diagram the DH parameters of the exoskeleton planar model can be obtained in a manner described by Craig J. (2005). The DH-parameters are shown in Table P-1.
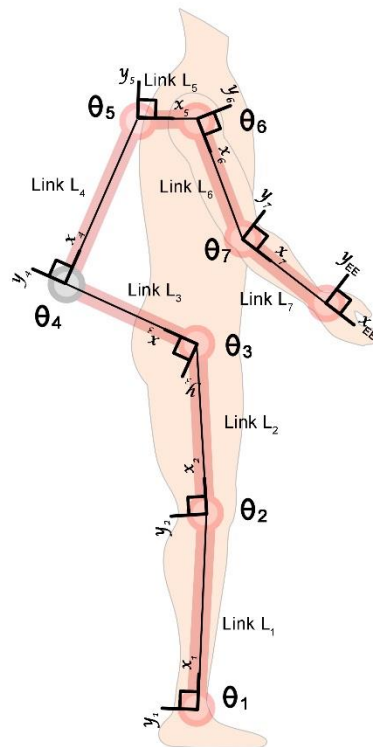
Figure P-1 – Kinematic chain of the 2D exoskeleton, with link and joints mapped out together with corresponding reference frames

Table P-1 – Link parameters for the exoskeleton

i	α_{i-1}	a_{i-1}	d_i	θ_i
1	0	0	0	θ_1
2	0	l_1	0	θ_2
3	0	l_2	0	θ_3
4	0	l_3	0	θ_4
5	0	l_4	0	θ_5
6	0	l_5	0	θ_6
7	0	l_6	0	θ_7
8	0	l_7	0	0

The link parameters found are inputted in Equation P-1 which is the transformation matrix from link i to link i-1 for each link.

$$T_i^{i-1} = \begin{bmatrix} \cos\theta_z & -\sin\theta_z & 0 & px \\ \cos\theta_x \sin\theta_z & \cos\theta_x \cos\theta_z & -\sin\theta_x & -\sin\theta_x\, pz \\ \sin\theta_x \sin\theta_z & \sin\theta_x \cos\theta_z & \cos\theta_x & \cos\theta_x\, pz \\ 0 & 0 & 0 & 1 \end{bmatrix}$$

Equation P-1

Where

$\theta_z = \theta_i$ (rotation about z axis)
$\theta_x = \alpha_{i-1}$ (rotation about x axis)
$px = a_{i-1}$ (translation along x axis)
$pz = d_i$ (translation along z axis)

The resulting transformation from base to end effector (EE) (in this case the wrist is where the exoskeleton interacts with the world and therefore both end effector and tool frame coincide) is calculated using Equation P-2.

$$T_8^0 = T_1^0\, T_2^1\, T_3^2\, T_4^3\, T_5^4\, T_6^5\, T_7^6\, T_8^7$$

Equation P-2

The resulting transformation matrix is given in Equation P-3.

$$\begin{matrix} \cos\theta_{1to7} & -\sin\theta_{1to7} & 0 & p1 \\ \sin\theta_{1to7} & \cos\theta_{1to7} & 0 & p2 \\ 0 & 0 & 1 & 0 \\ 0 & 0 & 0 & 1 \end{matrix}$$

Equation P-3

Where

$$p1 = \cos\theta_{1to7}l_7 + \cos\theta_{1to6}l_6 + \cos\theta_{1to5}l_5 + \cos\theta_{1to4}l_4 + \cos\theta_{1to3}l_3$$
$$+ \cos\theta_{1to2}l_2 + \cos\theta_1 l_1$$

$$p2 = \sin\theta_{1to7}l_7 + \sin\theta_{1to6}l_6 + \sin\theta_{1to5}l_5 + \sin\theta_{1to4}l_4 + \sin\theta_{1to3}l_3$$
$$+ \sin\theta_{1to2}l_2 + \sin\theta_1 l_1$$

$$\theta_{1to7} = (\theta_1 + \theta_2 + \theta_3 + \theta_4 + \theta_5 + \theta_6 + \theta_7)$$

$$\theta_{1to6} = (\theta_1 + \theta_2 + \theta_3 + \theta_4 + \theta_5 + \theta_6)$$

$$\theta_{1to5} = (\theta_1 + \theta_2 + \theta_3 + \theta_4 + \theta_5)$$

$$\theta_{1to4} = (\theta_1 + \theta_2 + \theta_3 + \theta_4)$$

$$\theta_{1to3} = (\theta_1 + \theta_2 + \theta_3)$$

$$\theta_{1to2} = (\theta_1 + \theta_2)$$

The variables θ_4 and θ_5 are constant angles that are used to define the rigid-back structure shape. The remainder of the angles are in this model analogous to the human joints, ankle (θ_1), knee (θ_2), hip (θ_3), shoulder (θ_6) and elbow (θ_7). As shown in Figure 5.2 d) the model can be divided into sections. The location of the start of the two-link system can be given by a translation from a point of origin. The point of origin for the data used to describe this translation co-insides with the motion capture setups origin as it was derived from the motion capture experiments.

The kinematic representation of the leg and arm section, is shown in the transformation matrix in Equation P-4

$$\begin{matrix} \cos\theta_{2link} & -\sin\theta_{2link} & 0 & Dx \\ \sin\theta_{2link} & \cos\theta_{2link} & 0 & Dy \\ 0 & 0 & 1 & 0 \\ 0 & 0 & 0 & 1 \end{matrix}$$

Equation P-4

Where

$$\theta_{2link} = (\varphi_1 + \theta_1 + \varphi_2 + \theta_2)$$

$$Dx = Px + \cos(\varphi_1 + \theta_1)l_1 + \cos(\varphi_1 + \theta_1 + \varphi_2 + \theta_2)l_2 \qquad \text{Equation P-5}$$

$$Dy = Py + \sin(\varphi_1 + \theta_1)l_1 + \sin(\varphi_1 + \theta_1 + \varphi_2 + \theta_2)l_2 \qquad \text{Equation P-6}$$

The φ term appears as a result of adding a constant rotation in order to change the reference frame. This is done to make sure the results are comparable with published data.

For both the leg and arm case $\varphi_2 = 0$. For the leg $\varphi_1 = 90$ as it is desired that the ankle to be at 0 when standing straight, i.e. the shin is perpendicular to the foot segment. For the arm $\varphi_1 = -90$ as the shoulder is to be at 0 when vertical relaxed. The new *Dx* and *Dy* equations for the leg are:

$$Dx_{leg} = Px - \sin(\theta_1)l_1 - \sin(\theta_1 + \theta_2)l_2 \qquad \text{Equation P-7}$$

$$Dy_{leg} = Py + \cos(\theta_1)l_1 + \cos(\theta_1 + \theta_2)l_2 \qquad \text{Equation P-8}$$

Where in Figure P-1:

Px and Py are x and y locations of reference frame 1

$\theta_1 = \theta_1$ and is the ankle joint

$\theta_2 = \theta_2$ and is the knee joint

$l_1 = l_1$ and is the length of the shin

$l_2 = l_2$ and is the length of the thigh

And for the arm are:

$$Dx_{arm} = Px + \sin(\theta_1)l_1 + \sin(\theta_1 + \theta_2)l_2 \qquad \text{Equation P-9}$$

$$Dy_{arm} = Py - \cos(\theta_1)l_1 - \cos(\theta_1 + \theta_2)l_2 \qquad \text{Equation P-10}$$

Where in Figure P-1:

Px and Py are x and y locations of reference frame 6

$\theta_1 = \theta_6$ and is the shoulder joint

$\theta_2 = \theta_7$ and is the elbow joint

$l_1 = l_6$ and is the length of the upper arm

$l_2 = l_7$ and is the length of the forearm